Pipeline Leak Detection Techniques and Systems: Comparative Assessment of Pipeline Leak Detection Methods

by

Javier Barrios Briceno

A thesis submitted in partial fulfillment of the requirements for the degree of

Master of Science

in

ENGINEERING MANAGEMENT

Department of Mechanical Engineering

University of Alberta

Abstract

Pipelines are one of the most reliable and environmentally benign ways of transporting liquid and gas commodities. However, pipelines are complex systems, with assets of varying ages, diameters, thicknesses, and materials. Furthermore, pipelines are tasked with carrying batches of product, each having different compositions, viscosities, and other properties. This variability makes pipeline evaluation and assessment challenging. Regardless of substantial investments in pipelines detection systems, as well as stringent regulations to the energy transportation industry, the annual average of pipeline leak incidents in the last ten years is 125 incidents (Transportation Safety Board of Canada, 2019). The characteristics of leak detection systems are widely different, resulting in limitations of practicality and reliability. For instance, deploying sensor suites can be prohibitively expensive because of their retrofitting costs, restricting their implementation to local high-risk areas or new pipelines. On the other hand, inaccurate and insufficient sensor data hinders accurate modeling complex of real-world pipeline systems, leading to uncertainties which often result in false-positive and false-negative alarms.

The present research aims to optimize the sensor suites of pipeline systems to determine the state of pipelines in situ. The proposal of this research is the design, development, and preliminary characterization of a testbed for laboratory-scale comparative assessment of leak detection methods. Additionally, the proposed testbed generates data that potentially can be used in the design of computational pipeline monitoring systems based on artificial intelligence.

A unique laboratory-scale apparatus which combines a wide variety of leak detection methods employed by the energy pipeline industry has been built and presented to address the shortcomings in existing leak detection techniques. Technologies tested are dielectric permittivity probes, temperature probes, thermal imaging, pipe vibrations, pressure profiles, and pressure transients. They were evaluated with the technological challenges proper of real-world pipeline systems.

Experimental results are varied because the relationship between factors (input) and responding variables is complex and multifactorial. However, experimental analysis elucidated some of the complexities that leak detection methods face. For instance, soil permeability substantially influences how the oil releases from a leak because it defines the leaked-liquids and soil relationship and consequentially the chances of the commodities reaching the probes. Soil moisture content also influences the probes' performance. For example, the dielectric permittivity probes perform inefficiently in saturated soils because the soil cannot absorb any more liquids. Thermal imaging is insensitive to soil permeability because its technology relies on rendering infrared radiation. Pressure transients are useful to detect leaks as proven through experiments. These findings help to select the most suitable leak detection method to improve the reliability of leak detection systems. More experimental conditions are suggested to evaluate additional uncontrolled variables that affect leak detection systems.

Acknowledgments

I want to thank Dr. Mike Lipsett for supporting and supervising this work, and giving me the opportunity to complete the Master in Engineering Management program. I am grateful for all his support, without which, this project could not have been completed. I was always pleased to hear his sensible thoughts.

I am also grateful to Dr. Scott Dick and Dr. Yuntong She for their guidance and supervising of this work.

I wish to express my gratitude to my wife Andreina, whose patience, love and support continue to make all of our endeavors possible, and to my son Javier Andres, who has been an endless source of motivation.

Table of Contents

List of Tables

List of Figures

List of Abbreviations

AI: Artificial Intelligence

ANN: Artificial Neural Network

API: American Petroleum Institute

CPM: Computational Pipeline Monitoring

DAQ: Data Acquisition

FLIR: Forward-looking infrared

LDM: Leak Detection Method

LDP: Leak Detection Principle

LDS: Leak Detection System

NDTs: Nondestructive Tests

NEB: National Energy Board

Re: Reynolds number

SCADA: Supervisory Control and Data Acquisition

SVM: Support Vector Machines

TSB: Transportation Safety Board of Canada

WSNs: Wireless Sensor Networks

WT: Wavelet Transform

Chapter 1: Introduction

1.1 Introduction

Pipelines are widely considered the safest method of transporting gas and oil because it is one of the most reliable and environmentally benign ways of transporting liquid and gas commodities (El-Abbasy, 2014). Their accident rate is lower than the railroad transportation, and pipelines are generally lower cost to convey liquid and gas commodities overland, only surpassed by rail under certain conditions (Verma et al., 2017). The National Energy Board (NEB) regulates pipelines in their life cycle with an objective of zero occurrences associated with their operation that results or could result in an adverse effect on property, the environment, or the safety of persons. Spills, leaks, and ruptures are rare, representing a tiny percentage of what is flowing through the pipelines. On average, 99.999 percent of the oil transported annually on the Canadian federally regulated pipelines moves safely (Natural Resources Canada, 2016). However, pipelines are complex systems which are inexorable aging; some pipeline infrastructures were constructed in the 1950s, becoming more susceptible to leaking with age (Transportation Safety Board of Canada, 2011). As a result, leak detection systems have to deal with many uncertainties thus some factors affect LDSs performance. API 1149 and API 1175 standards define several uncertainties such as SCADA scan rate, signal-to-noise ratio of the sensing element, repeatability of meter, meter accuracy, environmental effect on the pipeline hydraulics, telecommunication uncertainties, bias of the reference model, and so on.

Federally regulated pipelines had released, per year, in average 63 times oil or gas from 2008 to 2018 (National Energy Board, 2019). Environmental impact and public relations issues for pipeline operators are substantial. Therefore, more efficient pipeline condition monitoring systems are required to minimize pipeline occurrences. This research work presents an innovative leak detection technology for oil pipeline applications. This chapter describes the background and motivation to design and test a new leak detection system. Finally, research objectives and limitations are also described to outline the thesis research.

1.2 Background and Motivation

The Transportation Safety Board of Canada (2019) "examines and tests pipeline components involved in occurrences in order to identify and confirm safety deficiencies. TSB pipeline investigators monitor pipeline incident trends and promote the safety messages resulting from their investigations. TSB provides users with both data and statistics on pipeline occurrences." Figure 1.1 portrays pipeline's incidents involving the release of products in Canada, between 2008 and 2018.

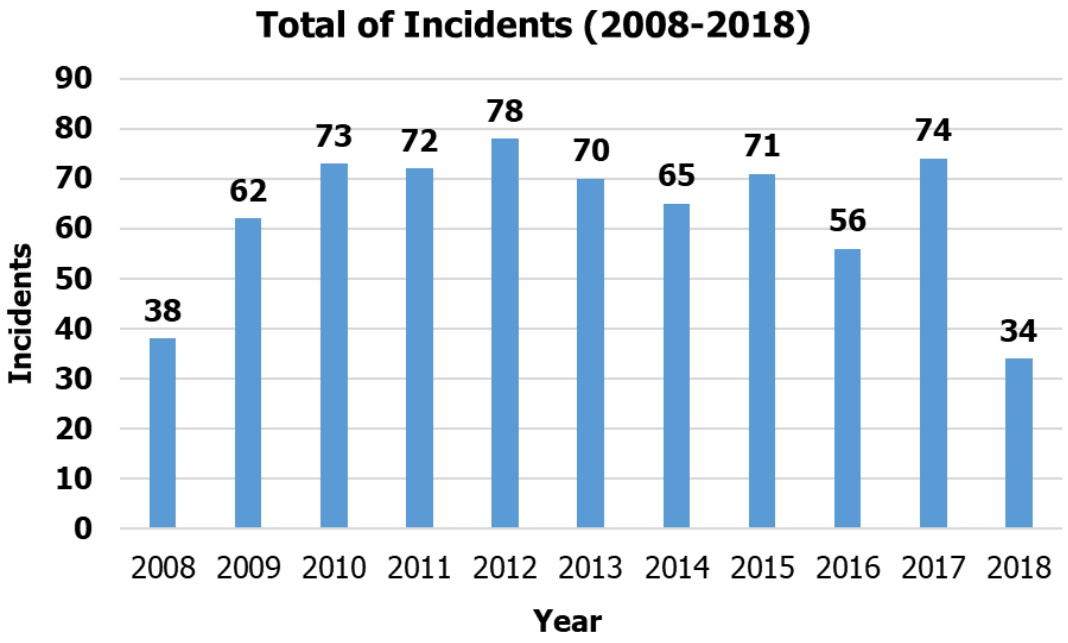

Figure 1.1: Pipeline accidents and accident rates in Canada (2008–2018)

The most common pipeline occurrence category, in 2018, was the release of products (32 of 34 occurrences). The most often product type released was hydrocarbon gas at 88% of all occurrences. Only 5.9% of occurrences involved a release of crude oil (TSB, 2018). Table 1.1 displays a breakdown of the release occurrences, whereas figure 1.2 plots Table 1.1 information.

Year	2018
Type of substance released	**Incident Number**
Gas	**30**
Natural Gas - Sour	8
Natural Gas - Sweet	21
Propane	1
Liquid	**2**
Crude Oil - Sweet	1
Diesel Fuel	1
Miscellaneous	**2**
Drilling Fluid	1
Glycol	1
Total	**34**

Table 1.1: Incidents and type of substance released in 2018

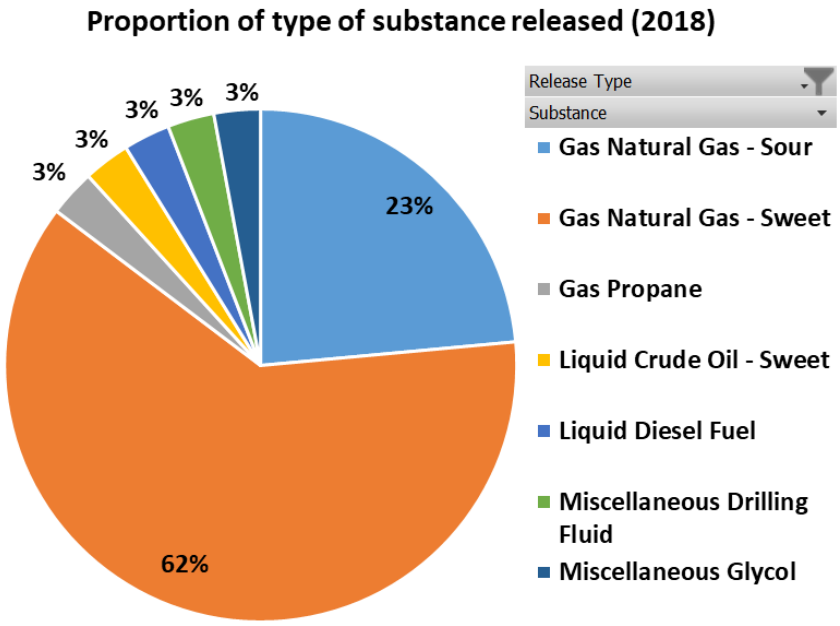

Figure 1.2: Proportion of type of substance released in 2018

Canada's pipeline network stretches for over 840,000 kilometers, whereas about 9 % of them are federally regulated (NEB, 2017). The Canadian pipeline system has been operating for approximately 100 years to convey different commodities. This system has been carrying batches of product with different compositions, viscosities, and other

properties; as a result, pipelines are of varying ages, diameters, thicknesses, and materials. Hence, evaluating and assessing the Canadian pipeline networks is a complex endeavor.

The main failure modes experienced by pipelines are mechanical damage (impact or accidental damage by third parties), external and internal corrosion, construction defect or material failure, and natural hazard (Drumond, 2018). These failures not only lead to economic and production losses but also affect public safety (Bin, 2017). Therefore, it is critical to design, implement, and maintain an accurate, reliable, and sensitive leak detection system to detect leaks effectively, thus assuring safe conditions and preventing economic losses.

Energy transportation companies invest heavily on leak detection systems to spot leaks of commodities on their pipelines, thus substantially minimizing the economic and environmental impact. The API acknowledges a wide variety of LDS employed by the energy pipeline industry, where each of them presents their particular up and downsides. As a consequence, current LDSs are imperfect systems which can flag false alarms or fail to detect actual leaks as aforementioned by the Transportation Safety Board of Canada. However, as scientific knowledge broadens new technologies can be applied on LDSs. Artificial Intelligence (machine learning) is the current breakthrough with high potential for detecting leaks on pipelines. Artificial Intelligence requires data to train and test the machine learning algorithms, which paired up with a physics model, will further feed the classifiers and issue whether there is a leak or not. Current data to feed the classifiers is scarce or unavailable.

1.3 Objectives

The main objective of the present research is to design and develop a characterization of a testbed as a method of laboratory-scale comparative assessment of leak detection methods and techniques, and to generate data sets by doing such comparative assessment.

1.4 Scope

This thesis aims to create a unique testbed in the use of hybrid leak detection principles, combining a direct observation of several individual technologies. As a result, data sets are created to potentially be used (in others researches) in inductive machine learning applications. Data sets required by machine learning algorithms are scarce at its best.

The scope of the investigation is limited to the following:

- Design, development, and fabrication of a testbed to evaluate several leak detection methods. The apparatus will recreate pipeline failures such as small leak and rupture. It also provides a platform to model external variabilities.
- Assess the responding variables under ideal conditions and in the presence of faults. Signal processing techniques in time and frequency domain will be applied to the resulting data sets, improving the evaluation of the leak detection methods.

1.5 Novelty of the Present Research

Implementing new leak detection technologies has both technological and economic challenges. A sensor's performance is evaluated by its sensitivity, reliability, accuracy, and robustness. The feasibility of implementing new leak detection systems depends on their deployment capital cost, operating and maintenance costs, and the technology maturity, which may entail sustaining capital to improve the implementation (Dawson et al., 2016).

The novelty of this study is to design and develop a system able to model the complexity of a real-world pipeline system, and to test sensor suites (leak detection methods) under different experimental conditions, resulting in a better understanding of the uncertainty that real-world pipeline systems face. On the other hand, the testbed generates data sets, currently inaccurate or insufficient, that can be used by CPMs based on artificial intelligence. This is the innovation that the present research intends to explore.

1.6 Thesis Outline

The present thesis is organized in five chapters: introduction, explanation of relevant techniques, a general methodology for assessing different detection techniques (including experiment and relevant statistical tests), a specific description of the experimental apparatus and methodology for testing, results, and conclusions.

The introduction chapter defines the problem that the current pipeline LDSs face as well as their operational impacts. Chapter two details previous research on leak detection systems and relevant techniques currently used in the transportation energy industry. This chapter works as a primer for the next chapters since it delivers a comprehensive review of LDSs, including their upsides and downsides, where the proposed solution aims to improve these systems.

Chapter Three summarizes the conceptual design of the proposed testbed; a pipeline loop recreates failure modes which are evaluated by a sensor suite in order to understand the system behavior, as well as the relationship between the factors (controlled variables) and responding variables, this relation sets the baseline for potential applications based on artificial intelligence technologies. Chapter Four details the specific description of the experimental apparatus as a method of laboratory-scale comparative assessment of leak detection methods, and a methodology for running the experiments. Chapter Four also includes a test plan defining the variables, measurement methods, systematic errors, and experimental matrix. Chapter Five shows the trial's results under different experimental conditions, namely, combinations of factors at different levels, e.g., using either sand or black soil as a medium, or employing medium at different moisture content. This chapter evaluates each leak detection method in isolation, including ANOVA analysis.

The conclusions, framework limitations, and recommendations chapter deliver the conclusions achieved from the experiments, as well as details the unexpected limitations of the testbed, and suggest guidelines for future research in leak detection systems.

Chapter 2: Literature Review

2.1 Introduction

This chapter reviews the relevant leak detection systems (LDS) and techniques currently employed by the energy pipeline industry. An initial examination to the LDSs categorizes them as external or internal systems, furtherly described as continuous or non-continuous. A thorough analysis of the LDMs' capabilities is done to understand the problems faced by the pipeline industry in order to propose an innovative solution.

This section is a primer for Chapter 3, as some of these methods are components of a laboratory-scale apparatus to test current LDS technologies, with applications of buried pipelines. Implementing LDMs is a multidisciplinary task because it includes, amongst others, evaluating the effect of noise on leak detectability, and implementing signal-denoising techniques to address this effect.

2.2 Leak detection systems and methods

The American Petroleum Institute acknowledges a wide variety of leak detection principles employed by the energy pipeline industry, defined as external or internal systems. The API also describes the LDM as continuous or non-continuous. A leak detection system is the end-to-end application of one LDT with one LDM (API RP 1175, 2017). As a result, LDSs are divided into four major groups: non-continuous externally based, non-continuous internally based, continuous externally based, and continuous internally based systems. Each system presents its particular capabilities. The API defines the criteria to select the most suitable method of LDSs (API RP 1130, 2012 and API RP 1175, 2017) based on the pipeline conditions and specifications. Table 2.1 lists and classifies the LDSs.

Table 2.1: List and classification of LDSs

	Externally Based		Internally Based	
	Physical Inspection	**Sensor-Based Monitoring**	**Manual Observations**	**Computational Pipeline Monitoring**
Non-Continuous	Aerial Surveillance	Ground-Penetrating Radar	Volume or Line Balance Calculations	
	Ground-Based Line Surveillance	Sniffer Tubes	Hydraulic Calculations	
	Hydro Testing	Tracer Chemicals	Pattern Recognition	
	Satellite	Intelligent Pigs	Shut-in Testing/Stand-up Testing	
	One Call System/ Public Awareness	Soil Sampling		
Continuous		Sensing Cables	Controller SCADA Monitoring	Conservation of Mass (real time)
		Cameras		Real-Time Line Balance
		Chemical Analyzers		Pressure Monitoring
		Acoustic Sensors		Pattern Recognition
		CP Monitoring		Digital Signal Analysis
				Statistical Analysis

Non-continuous externally based LDSs are direct measurement systems that operate on a non-algorithmic principle and rely on physical detection methods to spot escaping commodity. They are clustered in two prime groups: physical inspection and sensor-based monitoring. Physical inspection technologies are for example aerial surveillance, ground-based line surveillance, satellite and one-call system/public awareness; conversely, sensor-based monitoring LDSs are, for example, ground-penetrating radar, sniffer tubes, tracer chemicals, satellite, intelligent pigs, and soil sampling (API RP 1175).

2.2.1 Public awareness system

One call system/public awareness system is a system which leaks are detected and notified by stakeholders such as public entities, communities, operations staff, and excavators (API RP 1162). Ground-based line surveillance is a manual inspection, where field staff drive along the transportation pipes and perform the visual inspection of them, looking for leakages or pipe damages, yet this method is highly inefficient, expensive and can even have potential hazards for operators (Shukla and Karki, 2016).

2.2.2 Unmanned aerial vehicles (UAV or Drone)

Currently aerial surveillance or Unmanned Aerial Vehicles (hereafter, the "UAV" or "Drone") are gaining interest in the industry as they have the potential to supplement the ground-based surveillance because of its advantages, meaning, low cost, reliability, availability, redundancy, functional in adverse conditions, and suitable for high-risk tasks. Drones can be tooled with wireless sensors and be part of a more comprehensive system. UAVs are compatible with other sensing methods since they can be equipped with sensor payloads to detect leaks before they come to the surface by measuring plumes of volatile organic compounds. Drones can also measure temperature differentials between the oil and the soil, and ground subsidence or ground heave, yet government regulations may hinder their applications because sensors have to be fitted on the UAVs, and Transport Canada has yet to allow UAVs to fly out of line-of-sight. Figure 2.1 exhibits a drone-based monitoring system.

Figure 2.1: Drone-based monitoring system

2.2.3 Wireless sensor networks (WSNs)

Wireless Sensor Networks are continuous or non-continuous systems depending upon their sampling frequency, which ranges from real-time to discrete sampling. Sampling frequency establishes the power consumption and the lifetime of the network (Sadeghioon et al., 2014). WSNs has been improving their real-time monitoring capacity thus their

performance and reliability to detect leaks (Karray et al., 2016), yet the design of WSNs present challenges, e.g., selecting an adequate wireless mote, deployment topology, and data mining technique (Eze, Nwagboso, and Georgakis, 2017). Nevertheless, Multimodal Underground Wireless Sensor Network (UWSN) who uses low power sensors overcome some of these challenges because of their capabilities, i.e., concealment, ease of deployment, retrofitting, reliability, and acceptable level of redundancy when deployed densely (Sadeghioon et al., 2014). Figure 2.2 shows a WSN pipeline leak detection node.

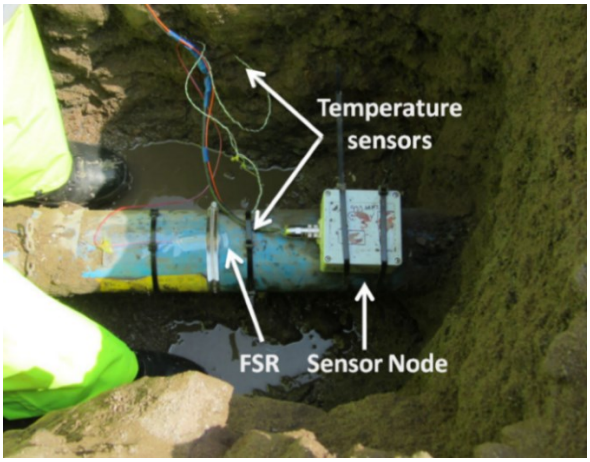

Figure 2.2: Sensor node attached to a pipeline

2.2.4 Ground-penetrating radar and sniffer tubes

Sniffer tubes and tracer chemicals are soil-monitoring approaches. A tracer compound (non-hazardous, highly-volatile gas) is injected into the pipeline, and its subsequent release from a pipe leak location creates a tracer plume which is detected by probes deployed in the soil above the pipeline. Samples are collected periodically and analyzed using a gas chromatograph (Murvay and Silea, 2012). The technology reliability and sensitivity of this technology is a comparative advantage, but its operational cost is expensive. As Kadri, Abu-Dayya, and Trinchero (2013) have argued, another disadvantage is that this process interrupts the pipeline operation to inject tracers. On the other hand, tracers cannot be used on overland pipelines because when the leak happens, the tracers disperse through the failure location's surroundings, diminishing the concentration of the

tracers, so the analysis of soil samples will unlikely detect the tracers. Figure 2.3 depicts an LD method based on sniffer probes; figure 2.4 depicts a soil monitoring LDS.

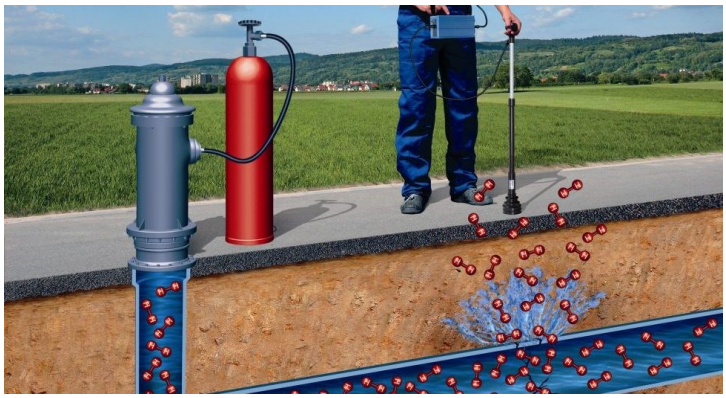

Figure 2.3: LDM based on sniffer probes.

Figure 2.4: Soil monitoring LDS

2.2.5 Smart pig

Smart pigs are instrumented packages that travel through the pipe with sensitive caliper tools, magnetic flux leakage detectors, and ultrasonic sensors for pipe wall integrity assessment. “Pigging” is a non-continuous method, externally based principle, broadly used due to its sensitivity to detect cracks, metal losses, and pipe geometries. “Intelligent Pigs” devices are inserted into the pipeline and propelled by the flowing liquid; they record physical data about the pipeline’s integrity as it moves throughout the pipeline (Kishawy, 2010), yet the technology has notable downsides. Pipeline piggability depends on many

factors: physical characteristics (pipeline design), line pipe grade, type of welds, length, fittings, internal diameter, elevation profile, tees, bends, valves, and spans. Department Of Transportation statistics indicates that 30% of the pipelines in the United States cannot be inspected using smart pigs (PHMSA, 2018). Figure 2.5 exhibits a pipeline pigging system. Since pigging has been in the market for decades, numerous providers are already inspecting thousands of pipe yearly, for instance, General Electric has been inspecting over one million kilometers of pipeline worldwide for the last 35 years (GE Oil & Gas, 2018).

Figure 2.5: Pipeline pigging system

SmartBall or sphere pig technology is another version of pigging, gravity allows the automated launching and receiving of spheres turning them very easy to deploy and very cost-effective attributable to its spherical shape (Elliott, 2008). This method is very sensitive and better suited to larger pipes since spheres are more maneuverable than standard smart pigs. SmartBalls as Smart Pigs requires specialized deployment-retrieval equipment (Po and Xing, 2011). Figure 2.6 shows the deployment of the SmartBalls.

Figure 2.6: Deployment of smartBalls

Pigging pipelines is expensive and labor-intensive. Deployment frequency depends on the operator's criteria, each run of this susceptible instrument may cost between $100k and $500k, hence pigging period in the industry ranges from one to five years, so pipeline shape data is unavailable throughout this period except in the event of a leak. Pigging inspection is done by nondestructive tests (NDTs) where the "ultrasonic pulse velocity (UPV) test" is widely used to detect defects (Saechai, 2012), but signal noise appears when the original signal travels through the commodity (Herlinawati, 2017) masking the original signal with unwanted features (Zhao, 2010).

2.2.6 Fiber optic sensors

Technologies such as sensing cables, video cameras, chemical analyzers, and acoustic sensors are continuous externally based LDSs which are deployed along the pipeline. The use of fiber-optic sensing cable has grown steadily in the industry because its comparative advantage over other sensors; burying optical fiber with new pipelines adds minimal cost (Baldwin, 2018). Fiber-optic technology measures how the temperature changes when the released substances come into contact with the cable. Distributed acoustic sensing (DAS) detectors surrounding the pipe detect the low-frequency acoustic signals caused by a leak. Fiber sensor cables can also measure variables such as electrical or presence of hydrocarbons, for instance, sensor cables change their electrical properties, i.e., resistance or capacitance when coming into contact with the released fluid. Optical-fiber cables are very sensitive, yet they must be deployed immediately adjacent to the pipe. Retrofitting long spans of existing pipelines is prohibitively expensive, limiting their application to local high-risk areas such as river crossings and highly populated areas, or new pipelines (Arifin et al., 2018). Another critical downside is the lack of redundancy in these sensors. If a section of the cable were to be damaged or requires replacement, the fiber optic system potentially would be put out of service along the whole pipeline run (Sadeghioon et al., 2014). Figure 2.7 exhibits the installation of a fiber-optic leak detection cable.

Figure 2.7: Installation of a fiber optic leak-detection cable

2.2.7 Computational pipeline monitoring (CPM)

Computational pipeline monitoring (CPM) is a continuously internally based LDS. It is a recommended practice for federally regulated pipelines (NEB, 2016) and a mandatory practice for Alberta regulated pipelines (Province of Alberta, 2014) due to its advantage of being relatively non-invasive to the pipe; it does not require the additional deployment of process instruments. CPM comprises two main parts, the inference engine, and the alert algorithm. The CPM system uses instrument data and calculated data from the inference engine to feed the alert algorithm. If these data exceed the alert algorithm threshold, the system generates an alarm that may indicate a leak (API RP 1130, 2002). Figure 2.8 describes the computational pipeline monitoring (CPM) system.

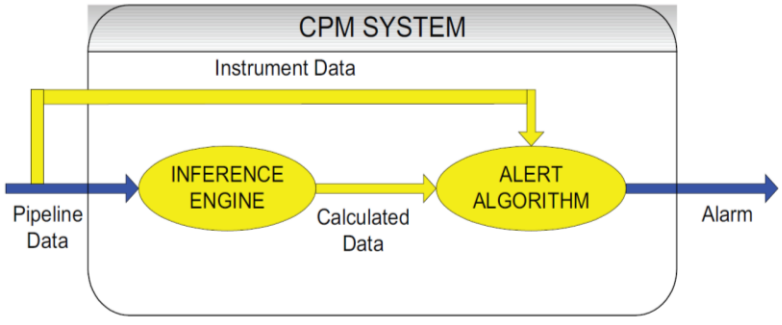

Figure 2.8: Computational pipeline monitoring (CPM) system

The SCADA system recollects data from field sensors. The number and type of sensors that have been deployed define the resolution of the sensor network, therefore the system's sensitivity to detect events, and the accuracy of the inference engine. The CPM inference engine varies widely on its complexity, from basic techniques such as volume or line balance calculations, through pattern recognition and hydraulic models, to data-driven models based on methods such as artificial intelligence, statistical analysis, artificial neural networks (ANNs), data mining and clustering technique, support vector machines (SVMs) and machine learning.

2.2.8 Real-time, transient-model-based, leak-detection method

The energy pipeline industry uses the real-time and transient-model-based method widely. The core of such a system is a sophisticated hydraulic model based on the physics of the flow, obtained by solving the partial differential equations of mass, momentum, and energy conservation. This method is alike to use radar waves to detect remote objects. An abrupt alteration of the flow condition such as closing a side-discharge valve generates transient pressure waves. The generated pressure waves propagate along the pressurized pipe at high speed (typically 1000 to 1300 m/s in metallic pipes), so if the wave finds a physical discontinuity such as a leak, then it generates a reflective wave to the signal source (Gong, et al., 2018). The remaining wave refracts and moves forward along the pipe, so a leak causes a transient event, where pressure waves propagate in both directions along the pipe.

Pressure sensors measure the wave reflection as a pressure variation, and the hydraulic model analyzes this data, triggering the 'leak alarm.' This effectiveness of this method is limited by (a) the ability of the computer model to reproduce the complexity of a real-world pipeline system accurately, and (b) the accuracy of the pressure measurements at multiple locations (Gong et al., 2018). Although the transient-based leak detection methods show potential, their effectiveness to pinpoint leak locations depends mostly on the properties of pressure transients, occasionally leading in false-positive and false-negative alarms. Moreover, these detection methods have safety issues that may affect the pipe integrity, diminishing their value when undertaking leak detection surveys (Gao et al., 2018).

Hydraulic models are sophisticated global models of pipeline behavior, but they cannot prescribe specific distributions for every source of noise along the whole run of the pipeline. Figure 2.9 displays a typical measurement arrangement for leak detection in a pipeline system.

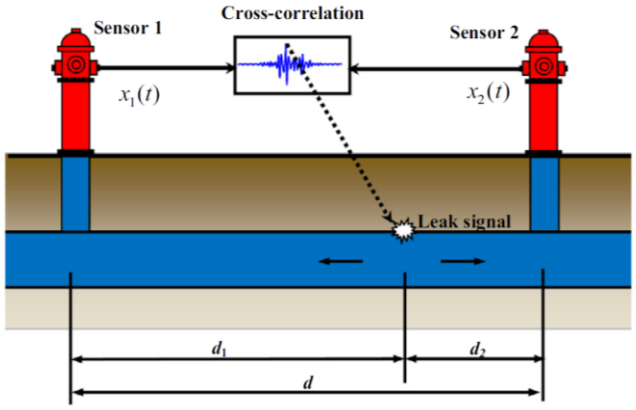

Figure 2.9: Acoustic-based LDM

The effect of leakage is to attenuate the transient pressure oscillations significantly. The leakage rate is correlated with the attenuation of the transient and that a small leakage of the order of a few percents will decrease the pressure amplitude significantly (Jonsson, 1994). Moreover, the attenuation effect is more pronounced the more significant the order of the oscillation period is. Figure 2.10 shows two examples of the calculated transient at the valve due to pump stop and check valve closure, 'a' case corresponds to a negligible leakage whereas 'b' represents a leakage of 4.8 % of the pipe flow (Jonsson, 1994).

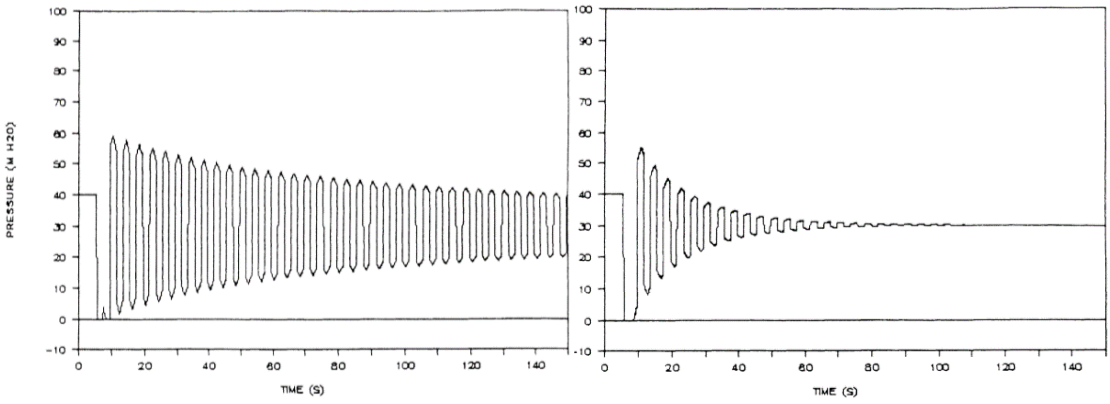

Figure 2.10: Pressure transient at the pump when stopped:
(a) Negligible leakage (b) Distributed leakage 4.8 %

The second way of studying the effect of a leak on the transient is related to the behavior of the pressure oscillations after valve closure (Jonsson, 1994). Figure 2.11 gives an example of the effect of a minimal leak on the transient. The top part of the figure shows an overall view of the transient and its bottom part an enlarged portion of the latter part of the transient, this also shows how a small leak causes, as Jonsson stated, “a growing disturbance of the pressure peaks, making even small leaks visible provided that a large enough number of oscillations occur.” Hence, the appearance of the disturbance can be used to locate the leak; Figure 2.11 bottom depicts clearly that the rate of change of the linearly decreasing pressure in a peak is suddenly changed (lowered).

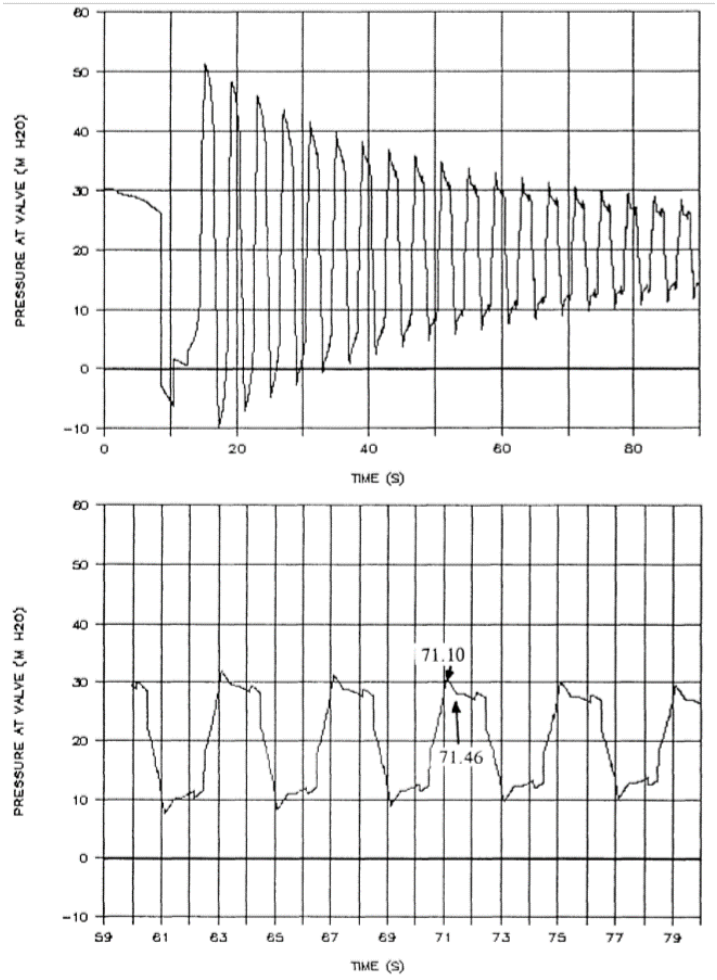

Top: Overall computed transient.

Bottom: Enlargement of pressure peak. Change at t = 71.46 s due to reflection at leak

Figure 2.11: Transient due to pump stop and automatic valve closure

2.2.9 Acoustic methods

Acoustic methods use vibration sensors to spot leaks in pipeline networks; these methods include listening-sticks, accelerometers, ground microphones, acoustic loggers, and leak noise correlators. When a leak occurs, it generates waves along both the pipe and its surroundings. Pressure sensors set through pipefittings measure the fluid motion. Rather than transient pressure waves, the continuous leak signals are used in the correlation analysis to calculate the time difference between their arrivals at different locations (where the vibration sensors are deployed); hence, current leak detection correlators operate by passive means (Gao et al., 2018). The correlation-based LDMs involve the problem of time delay estimation (TDE) of sensor signals in the presence of background noise. Waves travel away from the leak along the pipe wall (as radial vibrations) and through the water column (as pressure waves). Accelerometers on pipe fittings and hydrophones connected to hydrants measure them (Gao et al., 2018).

This method requires deploying sensors on each side of the suspected leak. Accelerometers are physically attached to the pipe wall, working well on metallic pipes; this array is known as a "dry" connection because the sensor is isolated from the fluid. Conversely, a ''wet" connection which uses hydrophones is more convenient for applications with substantial background noise, e.g., plastic pipes (Gao et al., 2018).

When a pipe leaks within a length d a distinct leak will be found in the cross-correlation estimator at the time delay τ_0. Referring to figure 2.9, the position of the leak relative to sensor 1 (d_1) is defined in equation 2.1, where c is the propagation speed of leak noise along the pipe.

$$d_1 = \frac{d - c\tau_0}{2} \qquad (2.1)$$

Leak detection correlators have not met their potential because background noise diminishes the cross-correlation effectiveness. Denoising techniques might eliminate critical signal features, leading to incorrect time delay estimates. Besides, reliable leak detection is accomplished when a distinct peak is identified in the cross-correlation; both signal reflection and resonance blur key signal's features (Gao et al., 2018). Probes must be

deployed every 50 to 200 meters apart because acoustic methods work effectively within these distances (Kadri et al., 2013).

2.2.10 Pressure profiles

Prihtiadi et al., (2016) contend that *the equation of continuity states* describes an incompressible fluid flowing in a pipe, where the rate at which mass enters the pipe is equal to the rate at which mass leaves it plus the accumulation of mass within the system. Through a circular pipe, this relation is:

$$v_i A_i = v_o A_o \qquad (2.2)$$

The Bernoulli equation describes the flow of an inviscid fluid flowing from inside the pipe, '*i,*' to outside of it, '*o,*' as:

$$p_i + \frac{1}{2}\rho {v_i}^2 + \rho g y_i = p_o + \frac{1}{2}\rho {v_o}^2 + \rho g y_o \qquad (2.3)$$

The liquids within the pipe are at an elevation y_i, with a pressure p_i and velocity v_i. Pipe diameter is usually much larger than the hole's, so $v_o >> v_i$. Elevation change 'y_o - y_i' for pipe leak applications is typically negligible compared to other terms in the Bernoulli equation, so $y_o - y_i = 0$. Thus, in a circular pipe with length. '*L'* and diameter '*D,'* and friction factor '*f*' according to Darcy-Weisbach. Pressure drop is related to velocity '*v*' as:

$$\Delta p = \left(\frac{fL}{D}\right)\frac{\rho v^2}{2g_c} \qquad (2.4)$$

$$\mathrm{Q} = CA\sqrt{\frac{2\Delta p}{S*\rho_{w,std}}} \qquad (2.5)$$

According to Rui et al., the dimensionless pressure drop is the ratio between the pressure drops through the pipeline under leakage and no-leakage conditions (2017), this is expressed as:

$$\Delta_{pD} = \frac{\Delta_{pleak}}{\Delta_{p\ no\ leak}} \qquad (2.6)$$

2.2.11 Dielectric permittivity method

Parameters such as soil type, density, void ratio, moisture content, specific surface area, cation exchange capacity, solute concentration, and solution pH influence the hydraulic conductivity of soils. The source, extent, and quality of the contribution of each soil component to the cation exchange capacity are varied and complex. Reactions between components alter the extent and quality of cation exchange. The pH of the soil-water system also influences the reactions strongly (Mohamed and Paleologos, 2018). However, the fundamental relationship between soil dielectric permittivity and volumetric water content is well understood because the dielectric of water is about eighty as opposed as other soil constituents which are between one and five; changes in soil dielectric permittivity are highly correlated with soil water content (Kizito, F., et al.). Table 2.2 shows the experimental results published by Overmeeren (1994) of dielectric permittivity of water and different types of soils. Kargas, George, and Konstantinos (2019) estimated the volumetric soil moisture versus dielectric constant of different types of soils, their saturation points plateau between 25 and 35 as graphed in figure 2.12.

Table 2.2: Dielectric permittivity of different types of soil and water

Substance	Permittivity
Air	1
Dry sand	4
Water-saturated sand	25
Clay	5–40
Peat	60–80
Water (fresh)	80
Water (saline)	80
Benzene	2.3
Diesel oil, fuel	2.1
Gasoline, gas	2.0
Jet fuel	1.7
Kerosene	1.8
Heavy fuel oil	2.2
Oil petroleum	2.1

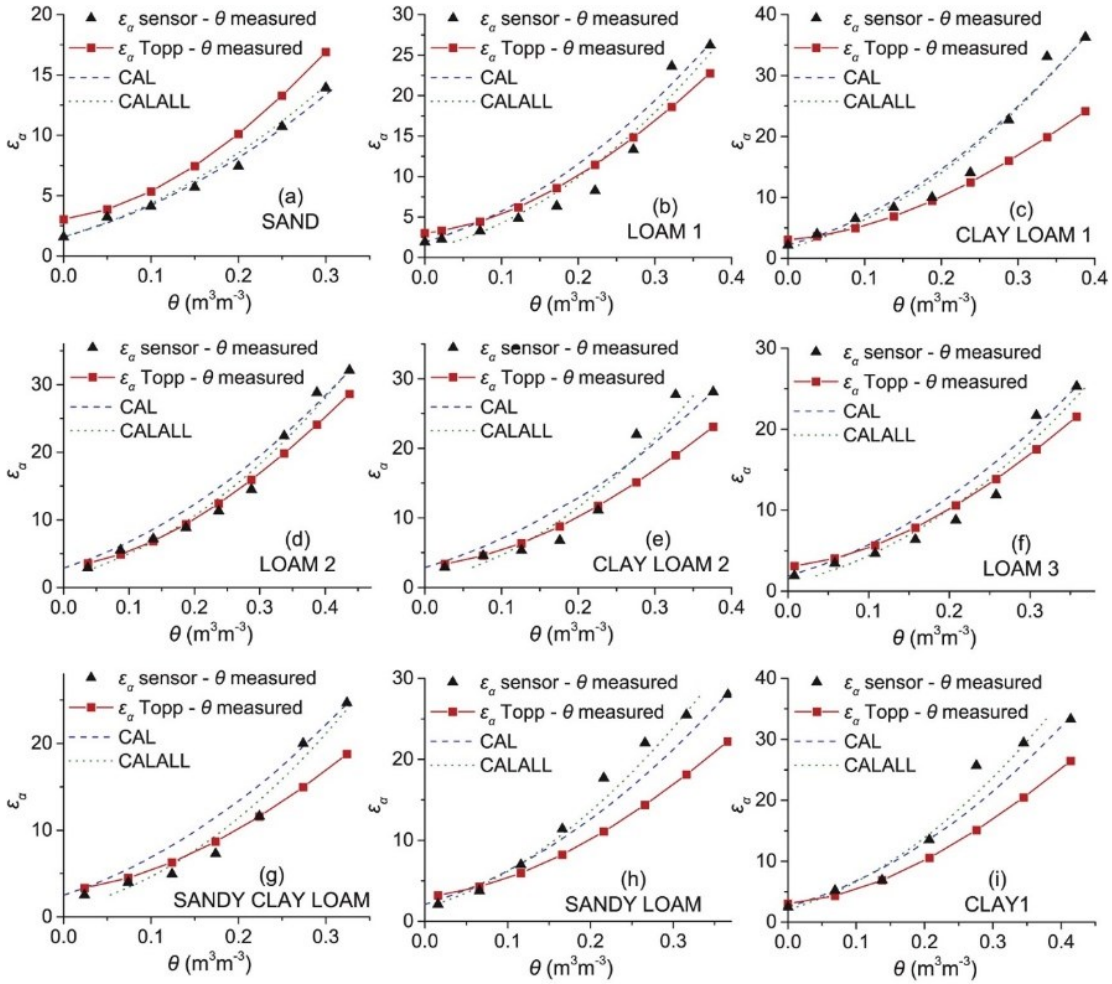

Figure 2.12: Volumetric soil moisture Vs. Dielectric constant

2.2.12 Thermal imaging

Thermal imaging detects the amount of radiation emitted by an object, which increases with temperature according to the black body radiation law, so thermographic cameras produce images of radiation detected as well as variations in temperature.

The sensitivity of the thermal imaging camera used in laboratory-scale work (E50) is 0.05 °C (FLIR, 2016). This technology senses changes in temperature because the simulant liquids emit more thermal energy than soil's, the "heat signature" between them are different, materializing their differences when sitting next to one another. UAVs can be equipped with FLIR payloads, as described in 2.2.2, to detect leaks before they come to the surface by

measuring temperature differentials between the oil and the soil (Barrios, J., She, Y., Dick, S., & Lipsett, M., 2018).

The Factors that determine the temperature of the ground are meteorological, terrain, and subsurface variables. Meteorological elements are primarily solar radiation and air temperature. Williams and Gold (1976) stated in the Canadian Building Digest Journal #180,

> "snow is probably the second most important factor affecting ground temperature. This influence is due not only to its insulating properties but also to the moisture it provides to the ground during the thaw period. Other terrain features such as slope orientation, can have significant effects. Water content is a variable property (…) heat capacity, thermal conductivity, and latent heat depend on water content; they also are variable; the larger the water content, the larger the heat capacity, thermal conductivity, and latent heat."

Figure 2.13 shows an example of a thermo-graphic inspection of a pipeline.

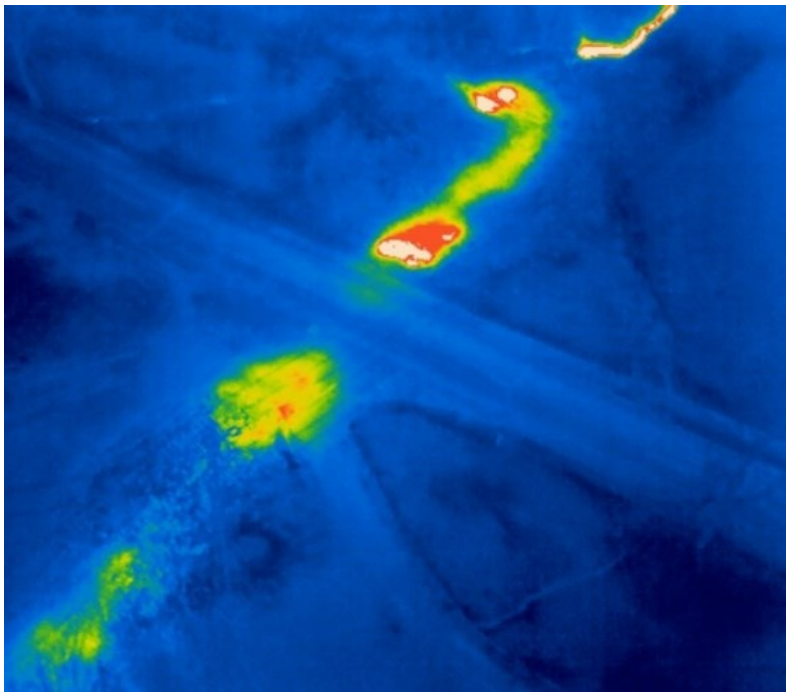

Figure 2.13: Thermo-graphic inspection of a pipeline

2.2.13 Statistical analysis

2.2.13.1 Hazard functions

Gas and oil pipelines usually follow common patterns when it comes to their failure or hazard rate. One of the most commonly adopted hazard patterns, $h_{(t)}$, for these networks is the bathtub pattern (Sun, Fidge, and Ma, 2011). Figure 2.14 shows a typical bathtub curve. According to Modarres (2010),

> "this curve can be divided into three regions. The burn-in early failure region exhibits a decreasing failure rate (DFR), characterized by early failures attributable to defects in design or construction. The chance-failure region exhibits a reasonably constant failure rate due to random failures. The third region, wear-out region, exhibits an increasing failure rate, mainly due to the aging phenomena."

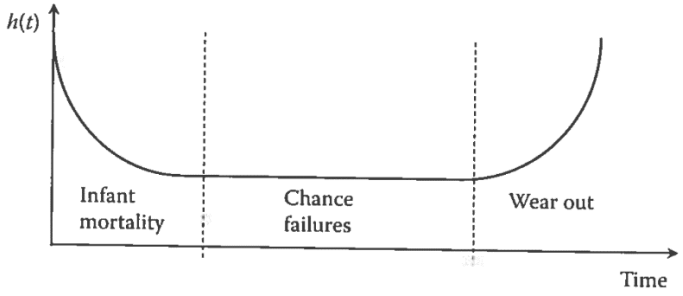

Figure 2.14: Typical bathtub curve

Several distributions can represent the hazard pattern, each one presents unique characteristics that have a wide range of applications in reliability analysis, so the distribution is chosen depending upon the case analysis. For example, the Weibull distribution, described in equation 2.7, covers all three regions of the bathtub curve.

$$h(t) = \frac{\alpha}{\beta}\left(\frac{\alpha}{\beta}\right)^{\beta-1}, \qquad \alpha, \beta > 0, t > 0 \qquad (2.7)$$

2.2.13.2 Nonlinear quantile regression

The statistical analysis calculates the probability of oil release against the probability of no-oil release. Sensors readings are statistically evaluated in real-time for the presence of

patterns associated with a leak. Prime techniques are the maximum likelihood method (MLR) and the linear (or nonlinear) least-squares regression method. The MLR criteria needs a distribution model to turn the leak detection analysis into an analytical optimization problem (Duru and Ani, 2017).

A probability threshold defines if the event is an oil release. The alarm algorithm acquires input data from the inference engine and field instruments and determines whether an alarm condition has occurred and what type of alarm should be generated, thus reducing the number of false alarms consequently. Algorithms data requirements vary widely; for instance, the maximum likelihood method requires an extensive database to describe the pipeline needs to produce credible results. Conversely, Least-squares regression obtains the mean response of the dependent variable as a function of the independent variable.

Both MLR and linear (or nonlinear) least-squares regression method struggle when the "leak pattern" is poorly identified, or the historical pipeline failure is scarce and generic, or they do not account for all the parameters and conditions associated with pipeline network. They fail to yield a complete picture of the variable's relationship. These situations are an issue in any data-driven supervised learning method that relies on fault events to train for fault classification. Besides, statistics-based methods do not account for all the parameters and conditions associated with the pipeline systems, and they are also sensitive to extreme outliers that can distort the results significantly (Pesinis, 2017). Conversely, the nonlinear quantile regression works well with heteroskedastic data, data with non-Gaussian error distributions, and data derived from sample selections of statistical analysis (Pesinis, 2017). The PSI Software AG company developed a model-based method paired with statistical analysis CPM system that was successfully implemented in DOW Central Germany, Kuwait Oil Company, Lukoil and Saudi Aramco (PSI Software AG, 2018).

Statistical LDSs are generally parametric models. For each uncertainty in the system, an assumed probability distribution is fitted to observed data by modifying specific parameters of the distribution, in case of little theory to guide choosing the probability distribution; parametric modeling reduces to a trial-and-error search through an infinite space of model forms.

2.3 Capabilities of current LDSs

Datta and Sarkar (2016) made a comprehensive analysis of the LDSs' capabilities currently used in the energy market. Table 2.3 exhibits them.

Table 2.3: Advantages and Disadvantages of the LDSs used in the energy market

Techniques/Approach	Advantages	Disadvantages
Vibration analysis	Satisfactory performance and easy to detect blockage in the pipe by using the relationship between the size of blockage and vibration signal	1. Good contact between accelerometer and pipe is necessary 2. Accuracy depends on the closeness of the fault to different measuring points
Pulse eco methodology	The methodology is efficient and fast; it can detect a large number of blockages simultaneously	Inefficient for short blockages
Acoustic reflectometry technique	The methodology is inexpensive, able to identify blockages and holes in pipes as small as 1% of their diameter	Fault detection is challenging due to noise through the pipe, and it requires signal denoising
Transient wave blockage interaction and blockage detection	The approach is precise and efficient	Difficult to detect multiple extended blockages
Stochastic Successive linear estimator	A straightforward approach to analyzing complex pipe geometries	Error due to size, length, and location of the blockage in a pipe
Impedance method	Applicable for blockage and leakage both in a pipe	Prediction to Locate blockage and leakage is challenging
Radioisotope technology	Sampling variables is fast	Skilled operators are required to measure the variables, environmental risks involved
Damping of fluid transient	The response given by the technique is fast and precise	The approach is unsuitable for old pipelines
Thermodynamic solid-liquid equilibrium model	Quality of results is excellent, particularly for crude oil pipelines	The methodology is inefficient for fluids with different characteristics
Negative pressure wave based leak detection	Simple performance, low cost, satisfactory leak location, and detection	The methodology is not appropriate for short pipeline systems

Techniques/Approach	Advantages	Disadvantages
Fiber sensor-based leak detection	Deployment of technology to new pipelines adds minimal cost	The technology relies on several conditions; it might turn inefficient when it does not meet conditions
SVM - based pipeline leakage detection	Excellent performance and precision for identification and locating the leakage in pipelines	For good accuracy, a large amount of data is required
Piezoelectric AE sensor	Online monitoring is effortless and able to locate time-dependent failure (leakage) in the pipeline	Technology is complex to use in complex pipeline networks
Harmonic Wavelet Analysis	Accurate and Reliable approach to detect small leaks in pipelines	The process is lengthy and slow
Genetic algorithm (GA) in combination with the inverse transient method	The GA method does not guarantee the best possible solution	Method binds its search in the parameter space
Computational fluid dynamic simulation	Good simulation results	Prediction of leakage in pipelines is difficult
Frequency Response Diagram	An efficient method to locate both single and multiple leaks	Technique application is complicated If leaks happen at the pipeline mid-point
GRA	Prediction of leakage in the pipe network is realistic	Technique application is complicated for large diameter pipes
Ground-penetrating radar (GPR)	A reliable approach for pressurized water supply pipes	1. Leakage detection is difficult for pipes surrounded with reinforcement bars in concrete pavement 2. A skilled operator is needed 3. Costly
Magnetic Flux Leakage detection	Data loss might be reduced	Computational complexity
Sparse flow measurement	Capacity to manage large amounts of data	Procedure is complex
Transient behavior of fluid	Methodology reduces error and research interval	On-line implementation is not possible
Ad-hoc wireless sensors	Easy maintenance and low power consumption	Limited communication range
Transient pressure oscillation	The methodology is efficient and simple	Methodology struggles in noisy environments

Each method displays its capabilities; for example, systems based on hard sensors are more expensive since they must be deployed along the pipeline, whereas soft sensors are low-cost because software-coding substitutes the hardware of hard sensors. Artificial Intelligence-based leak detection systems are minimal-cost and highly reliable systems while displaying high accuracy of fault detection. AI methods also take advantage of the sensors already deployed since their sampling data feed the soft-sensor system. Some CPM methods are more sensitive to measurement repeatability and drift, while other approaches may require extensive configuration efforts and tuning. No one technology will be suitable for all pipeline applications (API 1130, 2012).

2.4 Water movement in soils

API argued in 2017 that "Externally based leak detection systems are applications that use sensors to directly detect the presence of a hydrocarbon or physical changes in the environment due to a leak" (API RP 1175). Hence, how the liquid escapes from the pipe and permeates the medium (soil) affects the sensors' performance. The water movement in saturated and unsaturated soils is analyzed because water is used as simulant fluid.

Mohamed and Paleologos (2018) stated that soil-water relation is subjected to several force fields: capillary forces; adsorptive forces tying water onto solid surfaces; gravitational forces; and drag or shear forces at the interface of water-solid surfaces. These forces define soil water's total energy or equivalent potential energy, denoted the *total soil water potential*; kinetic energy is negligible because the water movement in the soil is slow. Depending on the acting forces, the soil water potential is split into pressure, gravitational, solute (osmotic), and air pressure potentials. The ***potential pressure*** results from pressure differences in soil water. If the soil is saturated the pressure potential (also denoted as hydrostatic pressure potential) is positive; if the soil is unsaturated, then the pressure potential (in this case referred to as matric potential) is negative (suction). The ***gravitational potential*** is the energy resulting from water elevation differences and can be positive or negative. ***Solute or osmotic potential*** refers to the concentration differences of a solution across a semipermeable membrane and is relevant mainly for flow into plant roots. The solute potential is always

negative as it is defined relative to pure H_2O. Finally, the ***air pressure potential*** accounts for changes in air pressure and can be positive or negative depending on whether it is higher or lower to the atmospheric pressure. Equation 2.2 represents the algebraic sum of these force fields. The minus sign comes about from the fact that potential decreases as, *m*, moves in the direction of the force.

$$\varphi_T = -\int_{S_0}^{S} \frac{\sum F_i}{m}.ds = \varphi_{Gravitational} + \varphi_{pressure\ or\ matric} + \varphi_{osmotic} + \varphi_{air\ pressure} \quad (2.2)$$

2.4.1 Soil-Water movement and flux density equations

Equation 2.3 relates the direction of water movement with gravitational and pressure potentials, on a volumetric basis:

$$\frac{\sum F^s}{m} = -\frac{\partial \varphi}{\partial s} = -\left(\frac{\partial \varphi_g}{\partial s} + \frac{\partial \varphi_p}{\partial s}\right) = -\left(\rho g \frac{\partial z}{\partial s} + \frac{\partial}{\partial s}(p - p_{atm})\right) \quad (2.3)$$

Here, 's' is the direction of water movement and φ_g, and φ_p, are the gravitational and pressure potentials. The term flux density expresses the rate of movement of water in soils. The flux density, q, is the volume of water moving along direction 's,' divided by a cross-sectional area perpendicular to the direction of motion 's' (Mohamed and Paleologos, 2018).

$$q\ \alpha \frac{\sum F^s}{m} \rightarrow q = -k\left(\rho g \frac{\partial z}{\partial s} + \frac{\partial}{\partial s}(p - p_{atm})\right) \rightarrow\ q = -K\left(\frac{\partial z}{\partial s} + \frac{\partial h}{\partial s}\right) = -K\frac{\partial H}{\partial s} \quad (2.4)$$

$$\text{Where } K = \rho g k \text{ and } H = h + z$$

Here the proportionality coefficient K is called hydraulic conductivity; it is a property of the medium and the fluid. Thus, the change of moisture in time dt is given by:

$$\frac{\partial \theta}{\partial t} = -\left(\frac{\partial q_x}{\partial x} + \frac{\partial q_y}{\partial y} + \frac{\partial q_z}{\partial z}\right) = -\nabla \cdot q \ \rightarrow\ \frac{\partial \theta}{\partial t} = \nabla \cdot (K \nabla h) + \nabla \cdot (K \nabla z) \quad (2.5)$$

In a saturated soil with an incompressible matrix, $\frac{\partial \theta}{\partial t} = 0$, the conductivity is usually assumed to remain constant, assuming isotropic soils, that is, when the hydraulic conductivities in the x, y, and z directions are all equal (and constant), so movement in saturated soil is given by equation 2.6:

$$\frac{\partial^2 H}{\partial x^2} + \frac{\partial^2 H}{\partial y^2} + \frac{\partial^2 H}{\partial z^2} = 0 \quad (2.6)$$

2.4.2 Water movement in unsaturated soils

As explained in point 2.4.1, water flow in saturated soils is caused by a driving force resulting from an effective potential gradient. Darcy's law can be written as $q = -K(\theta)\nabla H$, where ∇H is the hydraulic head gradient that accounts for suction and gravitational components. The resulting flow has following characteristics: (a) it takes place in the direction of decreasing potential, (b) the rate of flow is proportional to the potential gradient, and (c) it is affected by the geometric properties of the pore channels through which the flow takes place. The following principles apply in unsaturated flow as well as in saturated soils: Water in unsaturated soils is subject to matric suction, so its gradient constitutes a moving force. The matric suction is due to the natural affinity of water to the soil-particle surfaces and capillary pores. Water tends to be drawn from a zone where the hydration envelopes surrounding the particles are thicker to where they are thinner. In other words, water tends to flow from where the suction is low to where it is high (Mohamed and Paleologos, 2018).

Soil structure influences soil moisture-energy relationships; a well-granulated soil has more pore space than one with sparse granulation or one that has been compacted. The reduced pore space may result in a lower water-holding capacity. The compacted soil also may have a higher proportion of small- and medium-sized pores, which tend to hold water with greater tenacity than do larger pores. The term permeability, k_s, characterizes the porous medium. Figure 2.15 correlates the permeability as a function of the porosity for different types of soils (Mohamed and Paleologos, 2018).

Permeability coefficient (m/s)	10^{-1} 10^{-2} 10^{-3} 10^{-4} 10^{-5} 10^{-6} 10^{-7} 10^{-8} 10^{-9} 10^{-10} 10^{-11}				
Degree of permeablity	V.high	High	Moderate	Low	V.low
Soil type	Gravel	Sands	V. fine sands, sills, glacial trills, statfied clays	Homogeneous clays	

Figure 2.15: Permeability as a function of the porosity for different types of soils

Chapter 3: General methodology for detection techniques

3.1 Introduction

This chapter develops a framework to characterize the pipe's observability by testing a variety of sensors and simulating a liquids pipeline under different failure modes. This framework is expected to generate a methodology to device a laboratory-scale apparatus to stream the data required, in further researches, to evaluate candidate inferential sensors. This data sets the ground to design an LDS based on inferential sensing. Several procedures and standards are followed when evaluating several failure scenarios to ensure safe laboratory conditions while minimizing experimental errors.

3.2 General methodology

3.2.1 System concept: Process flow diagram

The proposed system (to be developed in further research) improves the inference engine of the internal based CPM system by using artificial intelligence; current methods are basic volume, line balance calculations, and hydraulic models. The design relies on inferential sensing, which is a modeling approach which estimates challenging-to-measure responding variables from direct measurement variables. Figure 3.4 pictures the experimental design for evaluating such a system. The scope of this research focuses on boxes one and two.

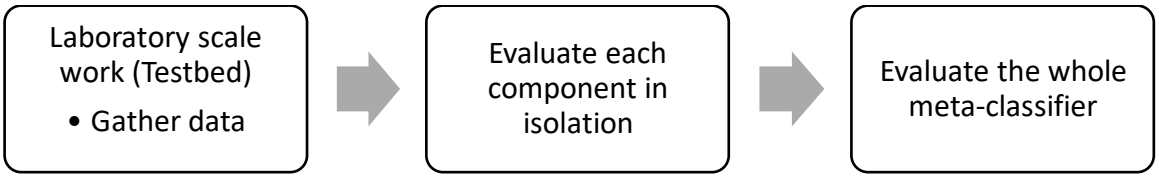

Figure 3.4: Experimental design for evaluating the concept

Figure 3.1 depicts an adapted general methodology of product development for assessing different LDSs. The methodology has three phases. Lam (2010) defines on its

research that a systematic approach is required to design a process capable of fulfilling the design functions stated in the early stages. Figure 3.2 describes his methodology adapted to the present research, and figure 3.3 illustrates the path from the customer needs to the system concept that lays out the baseline for the specification development, project planning, and conceptual design.

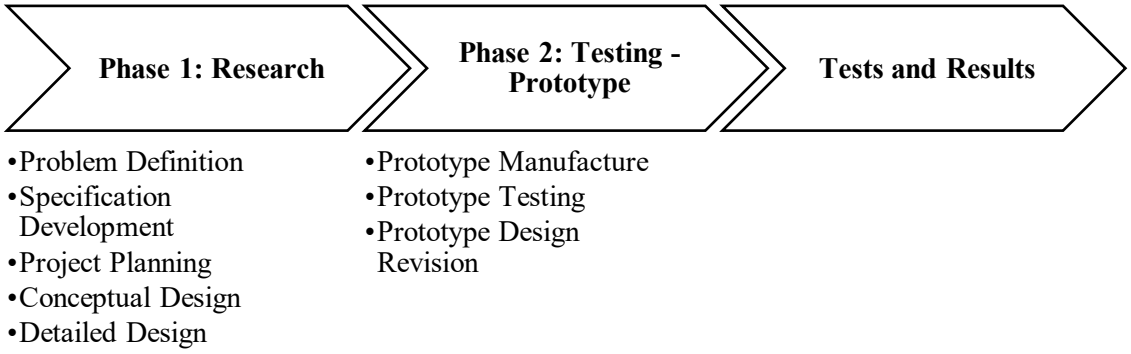

Figure 3.1: Phases of the general methodology for assessing LDSs

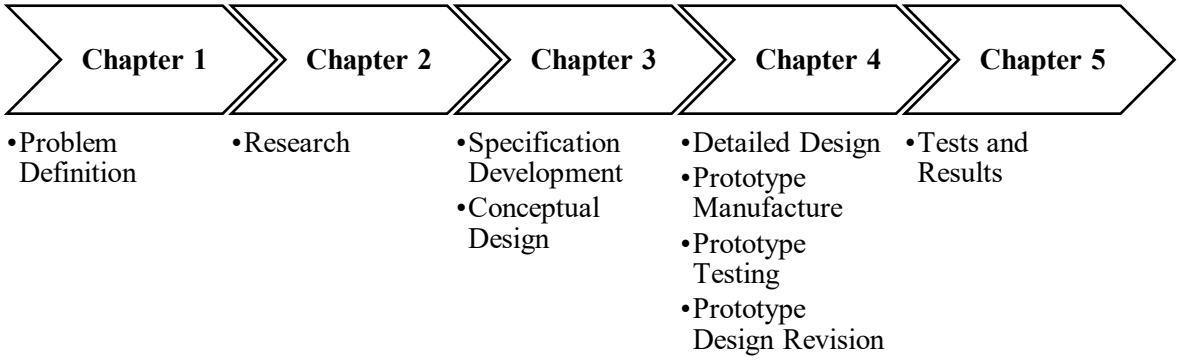

Figure 3.2: General methodology for assessing different LDSs

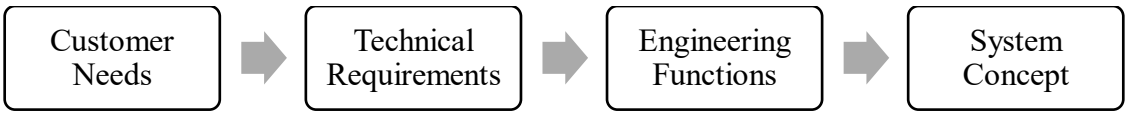

Figure 3.3: Baseline of specification development, and conceptual design

3.2.1 Specification development: customer needs

Assessing customer needs is the first step to define the technical requirements of leak detection systems, and this creates the basis of the engineering functions. Customers or stakeholders are broad; they are pipeline owners, public, and third-party landowners, but the

most important one in terms of defining the LDSs technical requirements are the government agencies or regulators. Pipeline Licenses try to decrease pipeline leaks because of its implications, i.e., public relation issues, cleaning costs, and so on. The public wants from pipelines no accidents, no leaks, and no pollution; these requirements are unrealistic due to the complexity of pipeline systems. Although expectations and requirements from stakeholders are wide, regulatory entities are at the stakeholder's requirements helm. The National Energy Board (NEB) defines the regulatory requirements for oil and gas pipelines that cross provincial or international border whereas provinces regulate the pipeline network within its border, for instance, the Alberta Energy Regulator (AER) regulates the pipeline system within Alberta.

The NEB (2017) requires that "pipeline companies to have integrity management programs in place to ensure the physical condition of the pipeline is monitored and maintained so that releases do not occur."

The NEB also on its National Energy Board Act establish liabilities:

> "48.12 (1) If an unintended or uncontrolled release from a pipeline of oil, gas or any other commodity occurs, all persons to whose fault or negligence the release is attributable … are … liable for … all actual loss or damage incurred … as a result of the release … the costs and expenses … all loss of non-use value relating to a public resource that is affected by the release …."

The NEB determines that the CSA Standard Z662 (Oil and Gas Pipeline Systems) is the standard that pipeline owners shall abide to meet the Canadian safety requirements for the Oil and Gas Pipeline Systems. This standard covers the design, construction, operation, maintenance, deactivation, and abandonment of oil and gas industry pipeline systems used for liquid hydrocarbons, including crude oil, multiphase fluids, condensate, liquid petroleum products; and, natural gas liquids and liquefied petroleum gas.

3.2.2 Specification development: technical requirements

The CSA group (2015) requires that "a leak detection system shall be implemented using one or a combination of various methodologies. An operating company shall evaluate

applicable leak detection methodologies to determine their effectiveness for the pipeline under consideration and how various methodologies can complement each other." They also recommend the API 1130 (Computational Pipeline Monitoring for Liquids) standard when designing LDSs, amongst other standards.

The API 1130 (2012) recommends many considerations to design the leak detection system; some of them are:

- Possess accurate commodity release alarming.
- Possess high sensitivity to commodity release.
- Allow for timely detection of commodity release.
- Require minimal software configuration and tuning.
- Be able to perform its CPM functions with existing sensors and instruments (or does not have special or additional requirements for instrumentation).
- Accommodate complex operating conditions and be configurable to complex pipeline networks.
- Be available during transients.
- Possess dynamic alarm thresholds.
- Provide the pipeline system's real-time hydraulic pressure profile, recognizing MAOP and elevation violations.
- Identify a release with appropriate milepost location or the nearest station.
- Minimize the number of alarms by requiring supporting and independent commodity release confirmation.
- Identify the leak rate.
- Performance of database queries should be at minimal time frames of 5 seconds.
- Validate commodity release alarms using redundant analysis within the same method as well as the redundant analysis between methods.

3.2.3 Specification development: engineering functions

A multifunctional team is assigned to design a leak detection system able to meet the CSA Standard Z662 specifications. This research proposes in further researches, a hybrid

CPM technique combining a hydraulic model with inductive machine learning that evaluates pipeline condition. The input and expertise of several field experts are required. For instance, experts in computational intelligence (fuzzy logic and neural networks), machine learning, and data mining; experts in computational hydraulics and experts in linking engineering aspects of technology, processes, and people.

The Annex 'E' of the standard Z662's establishes the normative and requirements for leak detection based upon internal and external leak detection methods:

"E.1.3: A leak detection strategy shall be implemented using a combination of methodologies…. the leak detection requirements for the pipeline…should address all modes of pipeline operations, including steady-state, transient, and shut-in operations."

Leak detection strategies shall include multiple leak detection methods; some examples of recommended LDM (leak detection method) are:

- Liquid sensing (e.g., fiber optic cables, electro-chemical, optical sensors);
- Line balance methods (Line Balance, Volume Balance, Modified Volume Balance, Compensated Mass Balance).
- Real-Time transient model, and statistical analysis.
- Pressure/Flow Monitoring, and acoustic/negative pressure wave.
- Acoustic sensing ,e.g., digital acoustic cables
- Electro-optical remote sensing; and
- Visual methods (e.g., line patrol, on-site inspections, vegetation surveys).

Leak detection systems include instruments, communication channels, data processing elements, inference engine, and alert algorithms. Pumps move commodities from the upstream sector to the midstream and downstream sectors through pipelines. The proposed testbed reproduces the complexity of a real-world pipeline system, and it includes a pump to move the fluid, a pipe loop to simulate a pipeline network, hard sensors, and a SCADA system to process the sensors' data. The current proposal focuses only on buried pipelines applications because most pipelines are buried. Therefore, the laboratory-scale apparatus includes a piece of pipe underground, which recreates the failure modes.

3.2.4 Conceptual design: technical assessment

The proposed apparatus is a model of oil pipeline networks. The testbed tries to recreate the flow of commodities and pipelines failure modes in scaled-laboratory conditions. However, general assumptions are made in order to recreate in these conditions the complexity of real-world pipeline systems:

- Either Vegetable oil or water is hydraulically similar to oil commodities.
- Soil is homogeneous all along the pipeline.
- The soil employed in experiments is similar to the soil surrounding real-life pipelines.
- Flow turbulence of both the fluid moved by real-life pipelines and in laboratory conditions are similar. The testbed only recirculates liquids; analysis for LDSs for gas-pipeline applications is out of the research scope.
- Weather variables such as winds, atmospheric conditions, hydrologic conditions (temperature, pH value, and resistivity), are considered constant in laboratory conditions, and similar to real-life pipeline system's.
- Pressure waves from leakages behave similarly in pipes of copper, PVC, and carbon steel.
- Fluid temperature is constant throughout the pipeline.
- The ratios between the depth of pipelines and their pipe-diameters are alike in laboratory conditions.
- External corrosion is neglected thus environmental parameters such as resistivity, salinity, oxygen content of the environment, bacterial activity, level of moisture, potential in-growth of tree roots, and potential soil pollution by hydrocarbons and other pollutants, are not considered.
- Topographical conditions are assumed homogeneous in real-life conditions.

3.2.5 Conceptual design: proposed testbed

The conceptual design includes producing ideas and taking into account the advantages and disadvantages of all propositions. The hypothesis is that LDSs detect the release of hydrocarbons by either monitoring internal pipeline parameters or directly detecting physical changes in the environment due to the presence of a hydrocarbon.

The purpose of the experiments is to compare alternatives and identify significant inputs. An Ishikawa diagram models the typical LDSs variables, they categorize the potential outputs of an LDS in order to identify their causes. Figure 3.5 shows all the factors and output resulting from the literature review in chapter two; and, table 3.1 categorizes them into manipulated, controlled, and responding variables.

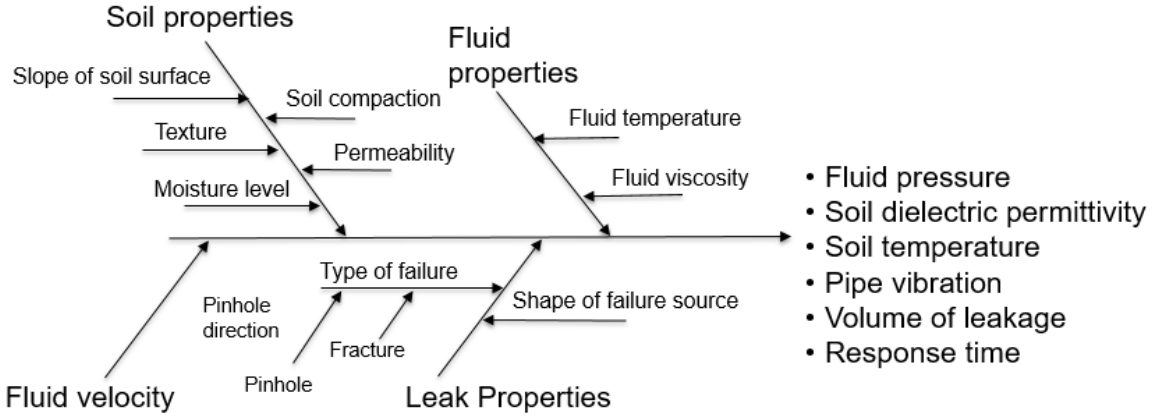

Figure 3.5: Testbed variables

Table 3.1: Pipeline LDS variables

Manipulated variables	Controlled Variables	Responding variables
Pipe diameter	Type of fluid	Fluid pressure
Pinhole size	Type of soil	Soil dielectric permittivity
Fluid temperature	Depth of pipe	Soil temperature
Fluid velocity	Direction of pinhole	Pipe vibration
	Soil moisture	Volume of leakage
		Response time

Figure 3.6 illustrates the system block diagram of the testbed to test the hypothesis by relating all the variables defined in table 3.1. Designing the testbed is an iterative process, this laboratory-scale apparatus initially includes elements such as a reservoir, centrifugal pump, heating system, variable frequency drive (VFD), sensor suite, and a SCADA system.

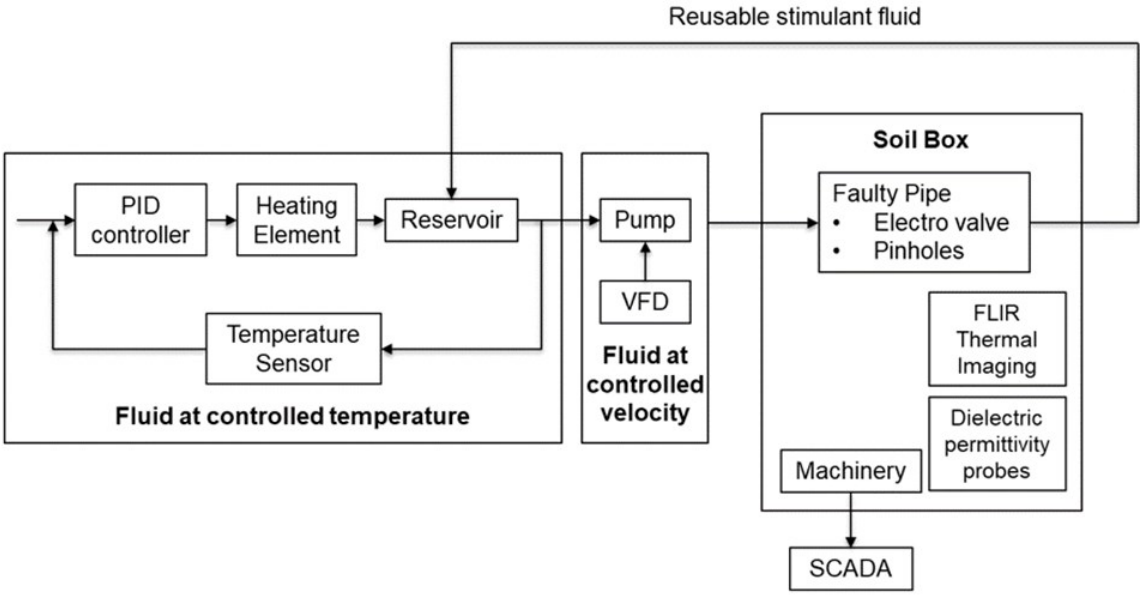

Figure 3.6: System block diagram of the testbed

Figure 3.7 shows the first testbed design, being subsequently improved to a low-cost version while including a more efficient sensor suite to test the experiment hypothesis. The design starts by selecting the pump, which defines the Reynolds number, used to predict flow patterns in different fluid flow situations. The testbed aims to replicate this number because it is a cornerstone in pipeline operations.

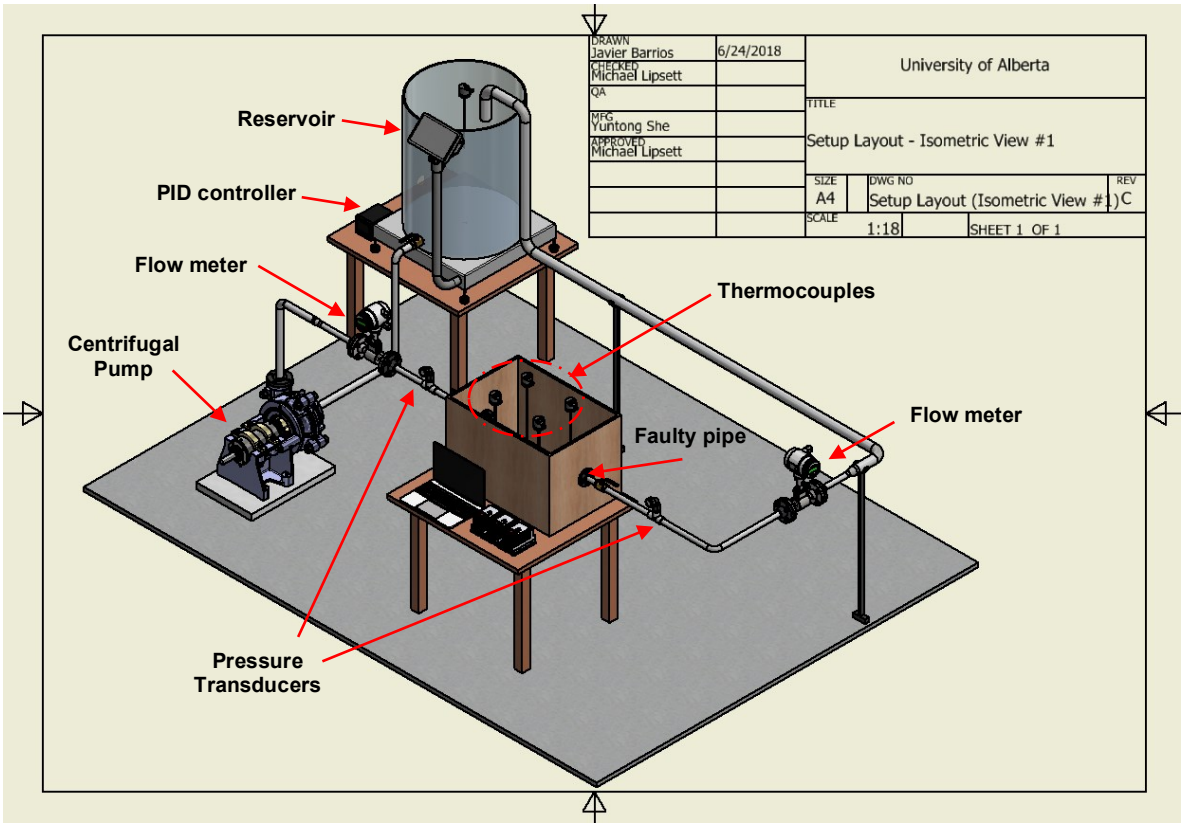

Figure 3.7: First testbed proposal

3.2.6 Conceptual design: final design of apparatus

Figure 3.9 displays the final design of the testbed; its operativity starts when the pump recirculates the simulant fluid through the pipe loop at a controlled temperature and velocity. The pipeline is segmented into three lengths, each one made with pipes of different pipe diameters, ¾”, 1” and 1 ½”. This configuration optimizes the pump horsepower while decreasing the fluid resistance around 40%. The 1 ½”-pipe length is furnished with one flow meter and one pressure transducer. The ¾”-pipe segment senses is supplied with two pressure transducers, one temperature transducer, and one accelerometer; the fluid behavior in this segment replicates the real-life conditions. Finally, the reservoir and the centrifugal pump are connected using the 1”-pipe segment.

The ¾”-pipe recreates the failure modes, a pinhole in the pipe create small leakage and an electrovalve creates pipe rupture. This segment is buried in the soil, so when the fluid

recirculates some portion leaks through the pinhole to the soil. As a result, soil's properties and the profile of fluid-pressure changes. The load cell measures the mass transferred to the soil box; two pressure sensors sense the differential pressure between the ends of the faulty pipe, two dielectric permittivity probes measure the soil impedance, and an accelerometer senses pipe vibrations. The testbed only has one accelerometer due limitations of the data acquisition instrument. On the other hand, a third pressure transducer tests the transient-model-based leak detection technique. The SCADA processes in real-time the responding variables: leak vibration, mass transferred, pressure, soil temperature, soil impedance.

The ¾"-pipe furnished with the electro-valve replicates a pipe fracture, causing a 17%-rupture of nominal flow. This arrangement can create hydraulic transients. Data is acquired by using LabView 2018®, presenting the data in an excel file. Figure 3.8 details the final proposed testbed.

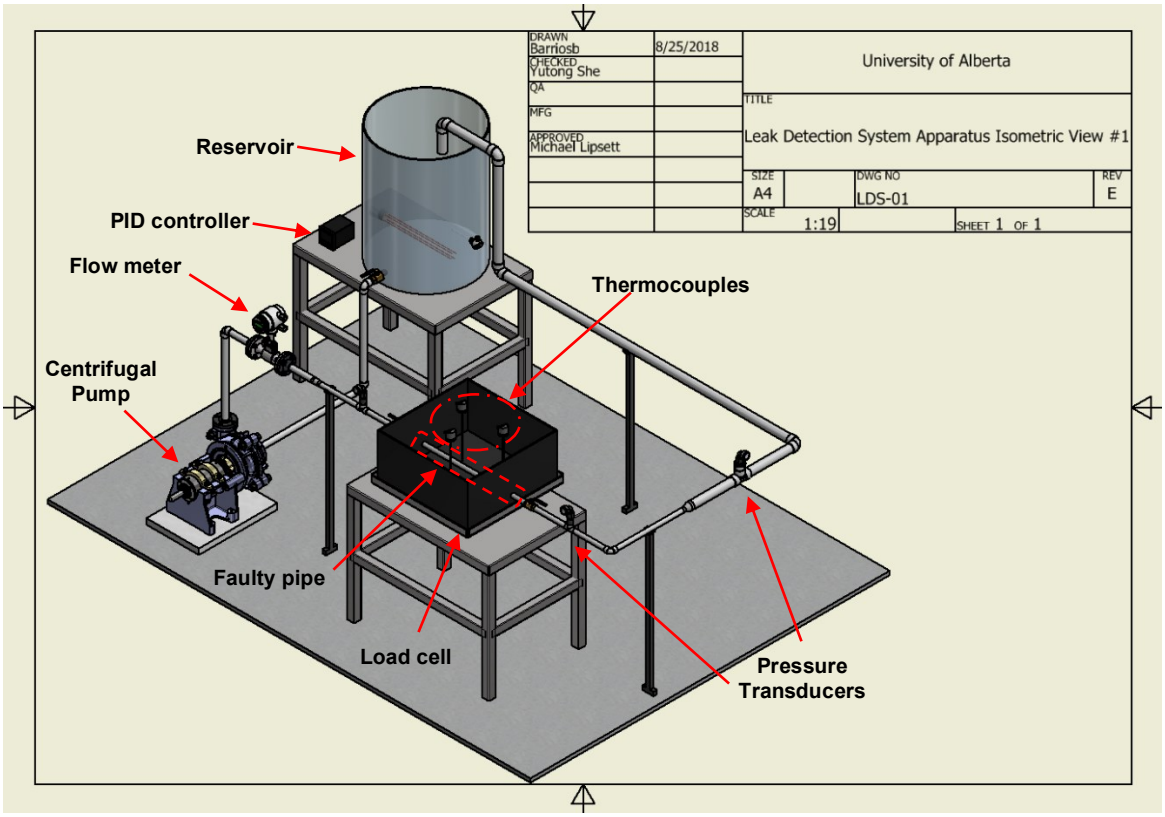

Figure 3.8: Concept design (LDS apparatus Rev E)

3.3 Testing equipment

The concept system involves several uncertainties because of general assumptions. Testing the leak detection technologies is required to mitigate some uncertainties as well as to address safety hazards. ISO 13623 defines the requirements of the hydrostatic test for pipelines.

"Hydrostatic testing equipment should include the following:

- *deadweight tester or other devices with equivalent accuracy;*
- *pressure gauges;*
- *volume measuring equipment;*
- *temperature measuring equipment;*
- *pressure and temperature recording equipment.*
- *Current certificates of calibration that identify the instrument with the calibration certification shall be provided."*

3.4 Evaluation of components in isolation

Multi-factor experiments are performed to evaluate multiple factors set at two (2) different levels. Fractional Factorial design is used to evaluate no-leaking conditions to reduce the number of runs. ANOVA is used to analyze each element in isolation. The truth of the null hypothesis is assumed; it presumes that all groups are random samples from the same population. For instance, when examining the effect of fluid velocity, moisture level, pinhole size, and type of soil, on similar test samples, the null hypothesis would be that all input variables have the same effect on the responding variables.

Chapter 4: Apparatus design and methodology for testing

This chapter details the evolution of the testbed from its conceptual design to a tested prototype. Data from the energy transportation industry defines a baseline to employ dimensional similitude to produce conditions close to that of a full-scale line under steady-flow conditions, characterizing the pipe's observability as a result. Limitations of the laboratory-scale apparatus are also outlined.

4.1 Analysis of pipeline operator data

Table 4.1 shows the operational values from a major pipeline operator, as outlined in chapter 3, Reynolds number is key to model pipeline systems because it characterizes the conditions and variables involved when conveying commodities through pipelines, i.e., commodity density and viscosity, fluid velocity and pipe diameter.

Table 4.1: Operational values in several pipelines

Line number	Fluid name	Density (kg/m^3)	Flow (m^3/s)	Hydraulic diameter of the pipe (m)	Kinematic viscosity of the fluid (cSt)	Pipe's cross-sectional area (m^2)	Reynolds number
1	NGL	548.0	0.33	0.51	[redacted]	2.507	123,387
2	UHC	814.9	0.90	0.66	3.04	0.342	572,893
3	CNS	822.5	0.80	0.86	4.15	0.586	283,092
4	LSB	838.8	1.63	1.22	5.66	1.167	300,390
5	NGL	548.0	1.01	0.76	0.30	0.456	5,600,670
6	CL	925.7	0.92	0.86	219.50	0.586	6,154
7	CL	925.7	0.47	0.76	219.50	0.456	3,595
8	UHC	814.9	0.34	0.51	3.04	0.203	277,112
9	UHC	814.9	0.17	0.51	3.04	0.203	137,411
10	FCP	735.0	0.42	0.76	0.70	0.456	994,594
11	UHC	814.9	0.16	0.51	3.04	0.203	132,831
12	FSP	735.0	0.14	0.93	0.70	0.679	275,988
14	LSB	838.8	0.63	0.61	5.03	0.292	259,354
15	CL	925.7	0.18	0.41	219.50	0.130	2,580
16	OSQ	923.0	0.58	0.76	20.40	0.456	47,893
17	PSC	837.5	0.83	0.76	5.43	0.456	256,433

Line number	Fluid name	Density (kg/m^3)	Flow (m^3/s)	Hydraulic diameter of the pipe (m)	Kinematic viscosity of the fluid (cSt)	Pipe's cross-sectional area (m^2)	Reynolds number
18	NW	822.5	0.07	0.31	4.15	0.073	67,061
19	OSA	863.5	0.07	0.30	7.51	0.073	38,627
20	OSN	719.5	0.08	0.22	1.30	0.038	372,514
21	OSN	719.5	0.11	0.22	1.30	0.038	496,686
22	OSN	719.5	0.14	0.25	0.50	0.051	1,392,432
23	PSC	837.5	0.17	0.30	5.43	0.073	128,217
24	LSB	838.8	0.39	0.61	5.66	0.292	145,462
25	LSB	838.8	0.73	1.07	5.66	0.894	154,022
26	AHS	934.2	0.25	0.59	253.00	0.272	2,125
27	AWD	851.0	1.64	0.91	4.90	0.657	464,775

The Reynolds number changes from four-significant to seven-significant-figure because of the commodities kinematic viscosity. In laboratory-conditions water simulates low viscous liquids, whereas canola oil recreates high viscous commodities. Selection of centrifugal pump is based on pressure-loss and Re number. Table 4.2 shows the pressure loss per meter (Psi) for the pipeline operator aforementioned; figure 4.1 compares these estimations.

Table 4.2: Pressure loss per meter (psi) in several pipelines

Line Number	Fluid name	Reynolds number	Ɛ_D (dimensionless)	Friction Factor (dimensionless)	Pressure Loss per meter (psi)
1	NGL	**123,387**	0.0030	0.0273	**0.000**
2	UHC	**572,893**	0.0023	0.0246	**0.015**
3	CNS	**283,092**	0.0017	0.0234	**0.003**
4	LSB	**300,390**	0.0012	0.0216	**0.002**
5	NGL	**5,600,670**	0.0020	0.0234	**0.006**
6	CL	**6,154**	0.0017	0.0379	**0.007**
7	CL	**3,595**	0.0020	0.0441	**0.004**
8	UHC	**277,112**	0.0030	0.0267	**0.009**
9	UHC	**137,411**	0.0030	0.0272	**0.002**
10	FCP	**994,594**	0.0020	0.0236	**0.001**
11	UHC	**132,831**	0.0030	0.0273	**0.002**
12	FSP	**275,988**	0.0016	0.0230	**0.000**
13	LSB	**259,354**	0.0025	0.0255	**0.012**
14	CL	**2,580**	0.0037	0.0502	**0.016**
15	OSQ	**47,893**	0.0020	0.0268	**0.004**

Line Number	Fluid name	Reynolds number	Ɛ_D (dimensionless)	Friction Factor (dimensionless)	Pressure Loss per meter (psi)
16	PSC	**256,433**	0.0020	0.0242	**0.006**
17	NW	**67,061**	0.0049	0.0319	**0.005**
18	OSA	**38,627**	0.0049	0.0329	**0.006**
19	OSN	**372,514**	0.0068	0.0338	**0.039**
20	OSN	**496,686**	0.0068	0.0337	**0.070**
21	OSN	**1,392,432**	0.0059	0.0320	**0.049**
22	PSC	**128,217**	0.0049	0.0312	**0.032**
23	LSB	**145,462**	0.0025	0.0260	**0.005**
24	LSB	**154,022**	0.0014	0.0230	**0.001**
25	AHS	**2,125**	0.0025	0.0522	**0.005**
26	AWD	**464,775**	0.0016	0.0228	**0.010**

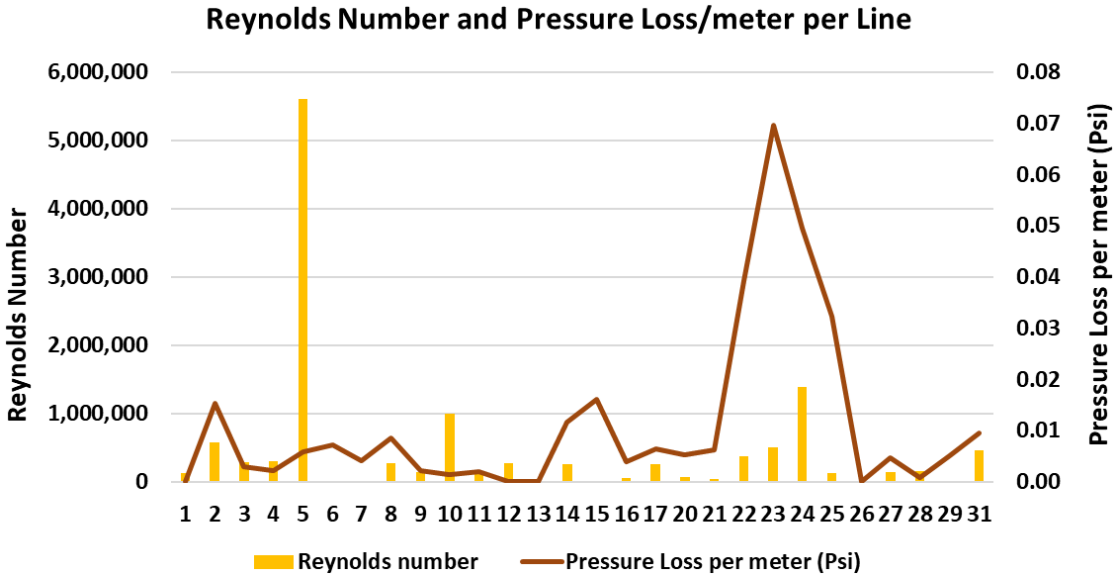

Figure 4.1: 'Re' number and pressure loss (per meter) per line in a major pipeline operator

4.2 Selection of testbed's elements

4.2.1 Centrifugal pump, reservoir, type of fluid and fluid velocity

Pump head has to significant components, static and dynamic head. The fluid is supplied to the pump by gravity because the reservoir is above the pump, so the pump's static head is:

$$TSH = Discharge\ Head - Suction\ Head \qquad (4.1)$$

Friction losses define the total dynamic head in this system; several steps are required to calculate these losses.

1) Solve Reynolds number (Defined in Appendixes)
2) Solve the Relation between Roughness Coefficient and the diameter of the pipe (Ɛ_D) (Defined in Appendixes)
3) Solve the friction factor (Defined in Appendixes)
4) Solve the Dynamic Head loss according to the Darcy–Weisbach equation (3.2):

$$h_f = F_m * \frac{L}{D_H} * \frac{V^2}{2*g} \qquad (4.2)$$

Where:

$$a)\ L\text{: } Pipe\ length\ (m) \quad b)\ V\text{: } Mean\ flow\ velocity\ \left(\frac{m}{s}\right)$$

$$g\text{: } Local\ acceleration\ due\ to\ gravity\ (m/s2)$$

From Appendix 1, the Darcy–Weisbach defines pressure loss in a pipe:

$$\Delta P = F_m * \frac{L}{D} * \frac{v^2}{2g} \qquad (4.3)$$

a) ΔP: $Pressure\ loss\ (psi)$ $\quad b)\ F_m$: $Friction\ Factor$ $\quad c)\ v$: $fluid\ velocity\ (m/s)$

c) L: $Pipe\ lenght\ (m)$ $\quad d)\ D$: $pipe\ hydraulic\ diameter\ (m)$

$f)\ g$: $local\ acceleration\ due\ to\ gravity\ (m/s^2)$

Losses at each pipe-loop segment compound total loss. The pump operational pressure must be higher than the total pressure loss due to friction loss and static head to ensure trouble-free operation. The centrifugal pump defines the hydraulic limits of the apparatus. Table 4.3 shows that recirculating water at 38 GPM is the apparatus' operational limit under no-leak conditions, which is the baseline of the apparatus in the static regime. According to table 4.4, recirculating canola using the same pump is infeasible because the resulting 'Re' is around 2000, which does not replicate real-conditions, turbulent, fluid behavior. Using bigger pumps to create turbulent patterns when moving canola oil, yet inconvenient due to space constraints. Consequently, canola oil is dismissed as a simulant fluid to run the experiments. Figure 4.2 depicts the operational points aforementioned in the IWAKI MX-251 performance curve.

Table 4.3: Total pressure loss (psi) at the apparatus operational limit (Fluid: water)

	Input Data				Calculation and Output Data (Grey cells)				
Length	Pipe Size (inches)	Pipe Material	Type of fluid	Velocity of fluid (m/s)	Reynolds number	Total pump head (ft)	Total pressure loss (psi)	Flow (GPM)	Reservoir volume (gal)
1	1	PVC and Plastic Pipes	Water	3.15	143675	12.4	5.3	35.3	38.9
2	3/4	Copper, Lead, Brass, Aluminum (new)	Water	5	180785	44.1	19.0	35.3	38.8
3	1-1/2	PVC and Plastic Pipes	Water	1.43	96843	1.5	0.6	35.4	38.9
			Total			56.5	24.3	35.3	38.9

Table 4.4: Total pressure loss (psi) at the apparatus operational limit (Fluid: canola)

	Input Data				Calculation and Output Data (Grey cells)				
Length	Pipe Size (inches)	Pipe Material	Type of fluid	Velocity of fluid (m/s)	Reynolds number	Total pump head (ft)	Total pressure loss (psi)	Flow (GPM)	Reservoir volume (gal)
1	1	PVC and Plastic Pipes	Canola	2.08	1816	11.2	4.4	23.3	25.7
2	3/4	Copper, Lead, Brass, Aluminum (new)	Canola	3.3	2284	57.3	22.4	23.3	25.6
3	1-1/2	PVC and Plastic Pipes	Canola	0.95	1232	1.9	0.7	23.5	25.9
			Total			68.6	26.8	23.4	25.7

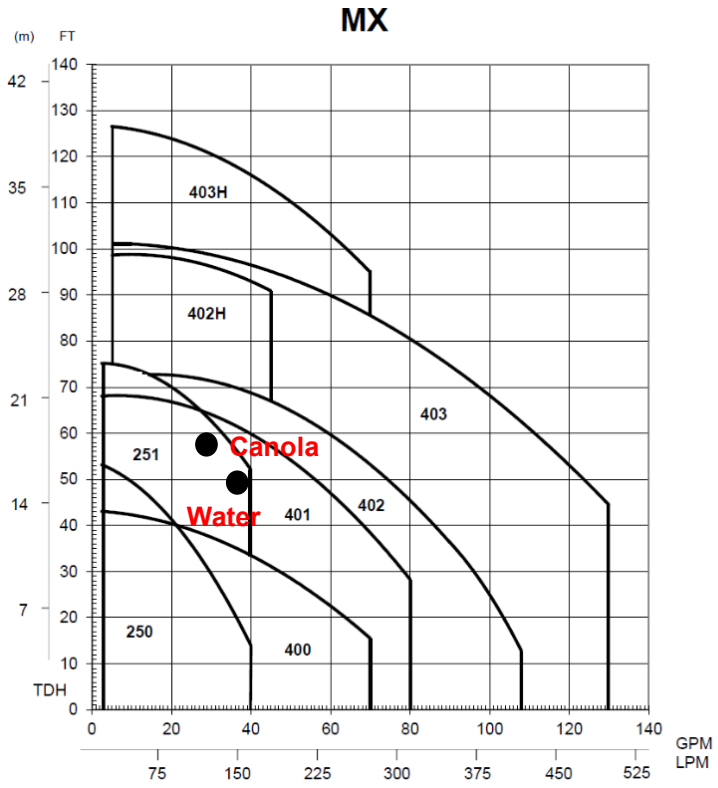

Figure 4.2: IWAKI MX-251 performance curve

Based on the pump curve, table 4.5 shows the maximum operating point at 5.5 m/s or 18 ft/s, which is lower than the sample from the energy transportation industry (20 ft/s). The testbed's Re is 198 000.

Table 4.5: Maximum apparatus fluid velocity for water

Length	Pipe Size (inches)	Fluid ID	Velocity of fluid (m/s)	Apparatus pipe length w/o fittings (m)	Reynolds number	Total Pump Head Required (ft)	Total Pressure Loss (Psi)	Flow (GPM)	Reservoir Volume (Gal)
1	3/4	Water	5.5	1.78	198864	27.2	11.7	38.8	42.7
2	1	Water	3.5	3.35	159639	9.7	4.2	39.3	43.2
3	1-1/2	Water	1.6	3.5	108355	1.2	0.5	39.6	43.5
						38.0	16.4	39.2	

Hence, the pump selected is the IWAKI MX-251 which operational pressure is 47.6 psi, and max discharge pressure is 75 feet. Fluid velocity is defined at 5 and 3.5 m/s because they are within the pump capabilities. Only water, selected as the simulant fluid, is capable of having similar Re number to real-life conditions. Reservoir size selected is 52 Gallons.

4.2.2 Apparatus R factor

According to Lu (2017), pipeline systems behave similarly in terms of scaled variables if the apparatus 'R' factor is similar to the energy industry's with identical R factor values have the same hydraulic behaviors, which allowed the reduction of a number of test scenarios and generalization of the test results. R factor is defined according to equation 4.4.

$$R = \frac{V_o}{2 * a} * \frac{L * F}{D_H} \qquad (4.4)$$

V_o: *Initial velocity of the fluid*

L: *Pipe length* F: *Friction factor*

a: *Wave speed of fluid*

D_H : *Hydraulic diameter of the pipe*

Table 4.6 reflects the 'R' factor of a major pipeline operator assuming a pipe length of 50 kilometers.

Table 4.6: 'R' factor in several pipelines

Line number	Fluid name	R factor		Line number	Fluid name	R factor
1	NGL	**0.1387**		14	CL	**3.3434**
2	UHC	**1.9078**		15	OSQ	**0.8740**
3	CNS	**0.7140**		16	PSC	**1.1237**
4	LSB	**0.4799**		17	NW	**1.8496**
5	NGL	**1.3105**		18	OSA	**1.9922**
6	CL	**1.3284**		19	OSN	**6.6040**
7	CL	**1.1602**		20	OSN	**8.7865**
8	UHC	**1.6882**		21	OSN	**6.7026**
9	UHC	**0.8542**		22	PSC	**4.5279**
10	FCP	**0.5478**		23	LSB	**1.1150**
11	UHC	**0.8268**		24	LSB	**0.3409**
12	FSP	**0.0997**		25	AHS	**1.5700**
13	LSB	**1.7333**		26	AWD	**1.2034**

R factor of laboratory-scale apparatus:

$$V_o = 2.5\ (m/s); L = 10\ (m)$$

$$F = 0.033;\ a = 1{,}406\ (m/s) D_H\ = 0.030\ (m)$$

$$R = \frac{V_o}{2 * a} * \frac{L * F}{D_H} = \left(\frac{2.5}{2 * 1{,}406}\right) * \left(\frac{10 * 0.033}{0.030}\right) = 0.00978$$

Industry R-factor ranges from 0.0997 to 8.7865, while the testbed 'R' factor is 0.00978. The industry data ten-folds the testbed data in the best-case scenario. Although the apparatus produces conditions close to that of a full-scale pipeline, i.e., the velocity of the fluid, friction factor, and wave speed; the difference between the pipe lengths yields the difference between their hydraulic behaviors.

4.2.3 Pressure transducer and thermocouples

Range of pressure transducers is 50 (psi) since the pump's operational pressure is 47.6 (psi). The soil temperature during experiments ranges from 20 to 40°C because energy pipeline moves up to 38°C-liquids, so the thermocouple selected is RTD (PT100) since its range is from -50 to 250°C.

4.2.4 Heater

The power calculation to heat the fluid (equation 4.5) (Watlow, 2018) is compounded by two factors, the energy required to heat the fluid itself (equation 4.6) and the energy lost due to heat convection from the tank to the environment (equation 4.7). Convection from the pipe loop to the environment is considered negligible.

$$P = P_{Heat\ Up} + P_{Lost\ Conducted} \quad (4.5)$$

$$P_{Heat\ Up} = \frac{M * C_p * \Delta T}{t * 3.412} \qquad (4.6)$$

$$P_{Heat\ Up} = Absorbed\ watts - raising\ temperature\ (KW)$$

$$a)\ M = weight\ of\ fluid\ (Pounds)\ b)\ Cp\ =\ specific\ heat\ of\ material\ (BTU/lb\ x\ °F)$$

$$c)\ \Delta T =\ temperature\ rise\ (°F) \quad d)\ t\ = Startup\ or\ cycle\ time\ (hrs)$$

$$P_{Lost\ Conducted} = \frac{K * A * \Delta T}{t_m * 3.412} \qquad (4.7)$$

$a)\ K =$ thermal conductivity $\left(\frac{\text{BTU}}{\text{lb}} \text{x °F}\right)$ b) A = Surface Area (ft^2)

c) $\Delta T =$ temperature differential to ambient (°F) $d)$ t = thickness of material (in)

Assuming heating 125 liters of water in two hours and 15 minutes, the energy required to heat it from 20 °C to 38 °C, including energy lost due to heat convection from the tank to the environment, is:

$$P_{(water)} = 1{,}154 + 282 = 1{,}436\ (W)$$

Thereby a 1,500-watt heater can heat the simulant liquid; the PID controller compensates any heat conduction energy loss.

4.2.5 Type of soil

Pipelines are buried under several types of soil since the Canadian landmass is diversified. According to Canadian Soil Information Service (2018) Alberta clusters nine types of soil whereas Saskatchewan eleven, so if the research includes eleven types of soil (levels), it would be required 132 tests and 13,200 Kg of soil. Only black loam and sand are

used because they are the primary type of soil where the oil pipeline is deployed in Alberta. As a result, using only two types of soil narrows down the number of tests from 132 to 24. Appendix 3 maps the soil group of Alberta and Saskatchewan.

4.2.6 Flowmeter

A magnetic flowmeter with a flow range between 0.05 to 5 m/s (0.15 to 16.4 ft/s) is selected. This meter is installed in the $1^{1/2}$" where the flow ranges up to 1.6 m/s.

4.2.7 Scale

The scale measures the mass transferred to the soil under leak conditions, so the weighing platform bears all the weight of liquid transferred, platform, soil, and soil box. Equation 4.5 defines the maximum mass to be measured by the scale. A 45-min test, soil box filled up to 6 $^{1/2}$" height, and four ft^2 mild steel platform (1/4 inch thickness) is considered to calculate the total weight. Appendix 3 shows the platform stress analysis done in inventor 2018®.

$$Total_{mass} = Soil_{mass} + Fluid_{mass} + Platform_{mass} + Soil\ box_{mass} \qquad (4.5)$$

Platform weight, 30 (kg), is estimated using inventor 2018®; the weight of the plastic box is 10 (kg) according to its manufacturer; the weight of soil, 100 (kg), is determined based on soil density and volume.

A pinhole in the pipe loop simulates the liquids pipeline under leak conditions, to produce dimensional similitudes data and equations below solve the leak flow and total volume leaked per test.

$$Discharge\ coefficient: C_d = 0.61$$

$$Area\ of\ 2\ and\ 3-mm\ Pinhole: A_o = 0.3183\ and\ 0.7162mm^2$$

$$Density\ of\ the\ fluid: \rho - S: Specific\ Gravity = 0.9922$$

$$Pressure\ Drop: \Delta P = Pump\ Pressure - Atmosphere\ Pressure$$

$$Q = C_d * A_o \sqrt{\frac{2 * \Delta P}{S * \rho}} \qquad (4.6)$$

Table 4.7 calculates pinhole leak rates through a pipe under pressure.

Table 4.7: Small leak estimation delivered by apparatus

INPUT DATA	
Pump Pressure (kPa abs)	172.37
Secondary Pressure (kPa abs)	99.90
Discharge coefficient	0.61
Orifice diameter (mm)	2.00
Liquid specific gravity	0.9922

→

Q (m3/h)	0.0833

→

Q (l/min)	1.39
Q (gal/min)	0.37
Q (l/h)	83.28
Leak Size (%)	1.04%

INPUT DATA	
Pump Pressure (kPa abs)	172.37
Secondary Pressure (kPa abs)	99.90
Discharge coefficient	0.61
Orifice diameter (mm)	3.00
Liquid specific gravity	0.9922

→

Q (m3/h)	0.1874

→

Q (l/min)	3.12
Q (gal/min)	0.82
Q (l/h)	187.38
Leak Size (%)	2.33%

The mass leaked to the soil when running 30-long experiments is around 90 (kg), so the total mass estimated is:

$$Total_{mass} = 100 + 90 + 30 + 10 = \ 230\ kg$$

$\therefore$ Selected load cell bears up to 300 kg.

4.2.8 Pinhole size

Small leakage is one of the failure modes, according to table 4.7 pinholes of two and three millimeters create leak rates (based on the percentage of nominal flow) of 1.04% and 2.33%.

4.2.9 Dielectric permittivity probe and accelerometer

Selected dielectric permittivity probes are one ECH2O EC-5 and one ECH2O 10HS. These probes measure moisture indirectly by measuring dielectric permittivity, or conductivity. The accelerometer selected is a miniature triaxial piezoelectric CCLD accelerometer, sensitivity: 100 mV/g, and maximum operational level: 70 g.

Figure 4.3 details the testbed key elements.

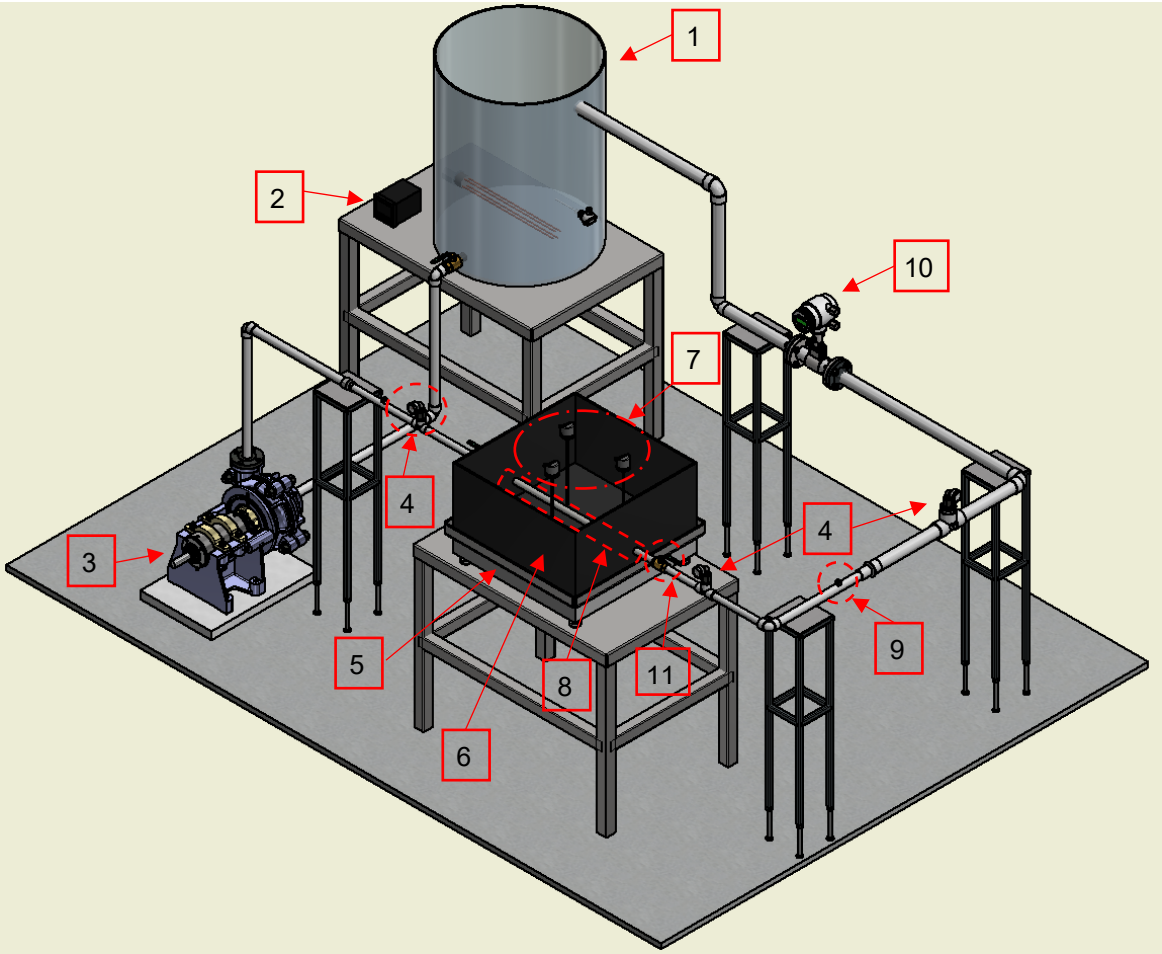

N°	Equipment	Specifications
1	Vessel	Vessel from zeebest (Code: OTC45 - 45 gallons)
2	PID Controller	Universal Temperature Process Controller
3	Pump	Manufacturer: IWAKI / Code: MX-251CV6-2
4	Pressure Transducers	Code: PX359-050AI / Span Limit: 50 psi / Output: 4-20 mA
5	Weighing platform	Meter Toledo, Model: PBA220-QD300 / Capacity: 300 (Kg)
6	Sand Box	Tote box from zeebest (Code: T162426T - 36 gallons)
7	• Temperature sensors • DP Probes	• RTD (Pt100) Probe • One ECH_2O EC-5, and one ECH_2O 10HS
8	Faulty Pipe	Copper pipe with(out) electrovalve
9	Accelerometer	Manufacturer: Bruel and Kjaer; Model: Type 4506
10	Flow Meter	Code: FMG3002-PP, 1 1/2" pipe size, 4 to 20 mA output
11	Mainstream valve	3/4" Ball Valve, Push to Connect

Figure 4.3: Apparatus layout

4.3 Apparatus range variables

Estimations made in point 4.2 define the variables range:

Table 4.8: Apparatus variables range

Type of variable	Variable name	Range	Unit
Manipulated	Fluid temperature	(37 , 40)	°C
Manipulated	Fluid Velocity	(3.5 , 5.0)	m/s
Manipulated	Pipe diameter	(3/4 , 1 1/2)	Inch
Manipulated	Pinhole size (diameter)	(0, 2 , 3)	mm
Controlled	Type of fluid	Water	dimensionless
Controlled	Type of soil	Black loam or sand	dimensionless
Controlled	Depth of pipe	3	Inch
Controlled	Soil moisture	(2 , 47)	%
Controlled	Depth of soil	(5, 6)	Inch
Controlled	Reynolds number	(100000, 190000)	dimensionless
Responding	Fluid pressure	<3.3	psi
Responding	Soil temperature	(20 , 40)	°C
Responding	Soil dielectric permittivity	(4 , 80)	F/m
Responding	Pipe Vibration	<0.04	g
Responding	Volume of leakage	(0.489 , 2.138)	lt/min
Responding	Response time	(1, 20)	

4.4 Experimental Matrix

4.4.1 Steady State under no and small leak conditions

The steady-state simulates a liquids pipeline under no-leak conditions to evaluate the sensors' sensitivity. The pipe loop has no orifice, so the experiments have three factors while delivering eight experimental conditions; table 4.9 displays its design matrix. The apparatus generates the flow conditions by pumping through the ¾"-pipe simulant liquids at either 3.5 or 5.0 m/s. Soil moisture content has two levels, dry and saturated. Small-leaking-condition

experiments have four experimental factors: fluid velocity, moisture content, orifice size and type of soil, resulting in sixteen experimental conditions. Table 4.10 depicts the design matrix for the experiments under small leaks.

Table 4.9: Design matrix for the experiment under no leaks

Experiment Number	Type of Soil	Moisture Content (%)	Orifice Size (mm)	Fluid Velocity @ 3/4" Pipe (m/s)
Experiment 1	Black chernozemic soil	17	0	3.5
Experiment 2	Black chernozemic soil	17	0	5.3
Experiment 3	Black chernozemic soil	45	0	3.5
Experiment 4	Black chernozemic soil	45	0	5.3
Experiment 5	Sand	2	0	3.5
Experiment 6	Sand	2	0	5.3
Experiment 7	Sand	25	0	3.5
Experiment 8	Sand	25	0	5.3

Table 4.10: Design matrix for experiments under small leaks

Experiment Number	Type of Soil	Moisture Content (%)	Orifice Size (mm)	Fluid Velocity @ 3/4" Pipe (m/s)
Experiment 1	Black chernozemic soil	17	2	3.5
Experiment 2	Black chernozemic soil	17	2	5.3
Experiment 3	Black chernozemic soil	17	3	3.5
Experiment 4	Black chernozemic soil	17	3	5.3
Experiment 5	Black chernozemic soil	45	2	3.5
Experiment 6	Black chernozemic soil	45	2	5.3
Experiment 7	Black chernozemic soil	45	3	3.5
Experiment 8	Black chernozemic soil	45	3	5.3
Experiment 9	Sand	17	2	3.5
Experiment 10	Sand	17	2	5.3
Experiment 11	Sand	17	3	3.5
Experiment 12	Sand	17	3	5.3
Experiment 13	Sand	45	2	3.5
Experiment 14	Sand	45	2	5.3
Experiment 15	Sand	45	3	3.5
Experiment 16	Sand	45	3	5.3

Experiments levels under rupture conditions are the combinations of following conditions: pump (ON/OFF), electrovalve (ON/OFF), and mainstream valve (ON/OFF). These combinations create conditions to evaluate the LD pressure-transient method.

Table 4.11: Design matrix for experiments under rupture conditions

N°	Experimental condition		Downstream valve status
Experiment 1	Steady-state (full speed)	No leak imposed	Fully open (always)
Experiment 17	Steady-state (full speed)	No leak imposed	90% closed (always)
Experiment 25	Steady-state (full speed)	No leak imposed	Fully open and 90% closed (Cycle)
Experiment 2	Steady-state (full speed)	Leak imposed	Fully open (always)
Experiment 3	Steady-state (full speed)	Leak imposed	90% closed (always)
Experiment 4	Steady-state (full speed)	Leak imposed	90% closed when imposing the leak fully open when sealing the leak
Experiment 16	Steady-state (full speed)	Leak imposed	Fully open when imposing the leak and 90% closed when sealing the leak
Experiment 5	Leak imposed when stopping the pump (1 time)		Fully open (always)
Experiment 8	Leak imposed when stopping the pump (several times)		Fully open (always)
Experiment 13	Leak imposed when stopping the pump (several times)		90% closed (always)
Experiment 9	Leak imposed when stopping the pump (several times)		90% closed when imposing the leak and fully open when sealing the leak
Experiment 20	Leak imposed when stopping the pump (several times)		Fully open when imposing the leak and 90% closed when sealing the leak
Experiment 6	Leak imposed when starting the pump (several times)		90% closed (always)
Experiment 18	Leak imposed when starting the pump (several times)		Fully open (always)
Experiment 7	Leak imposed when starting the pump (several times)		90% closed when imposing the leak and fully open when sealing the leak

N°	Experimental condition	Downstream valve status
Experiment 19	Leak imposed when starting the pump (several times)	Fully open when imposing the leak and 90% closed when sealing the leak
Experiment 10	Leak imposed when increasing flow (45 to 60 Hz)(several times)	Fully open (always)
Experiment 14	Leak imposed when increasing flow (45 to 60 Hz)(several times)	90% closed (always)
Experiment 11	Leak imposed when increasing flow (45 to 60 Hz)(several times)	90% closed when increasing flow and fully open when decreasing the flow
Experiment 15	Leak imposed when increasing flow (45 to 60 Hz)(several times)	90% closed when decreasing flow and fully open when increasing the flow
Experiment 21	Leak imposed when decreasing flow (60 to 45 Hz)(several times)	Fully open (always)
Experiment 22	Leak imposed when decreasing flow (60 to 45 Hz)(several times)	90% closed (always)
Experiment 23	Leak imposed when decreasing flow (60 to 45 Hz)(several times)	90% closed when increasing flow and fully open when decreasing the flow
Experiment 12	Leak imposed when decreasing flow (60 to 45 Hz)(several times)	90% closed when decreasing flow and fully open when increasing the flow

4.5 Procedure to minimize systematic error

Systematic errors in experiments come from measuring instruments. Two types of systematic error occur with instruments having a linear response. The offset or zero-setting error the instrument does not read zero when the measured variable is zero. The multiplier or scale factor error the instrument reads changes in the measured quantity greater or less than the actual changes, so to minimize systematic errors follow next steps for each experiment:

a) Fill the reservoir with room temperature tap water. Turn on both the PID controller and National Instruments CompactDAQ 9178 chassis, read from the LabVIEW code the readings from accelerometers, flow meter, load cell, and thermocouples. Compare this data against table 4.12:

Table 4.12: Reference numbers to check systematic error

Sensor	Reference number
Accelerometer (mV/g)	0
Flow meter (m/s)	0
Load Cell (kg)	40
Soil Thermocouples*	Temperature from a handheld thermometer
Pipe Thermocouple**	Temperature from PID controller

*To check the soil thermocouples fill a bucket with room temperature tap water and record its temperature with the handheld thermometer as well as the thermocouples.

** To check the pipe thermocouple record the reading after having one minute the pump off. Turn off the pump after sampling the temperature.

b) Fill up the soil box using a bucket, record the weight of the filled bucket every time before pouring the soil into the box. Repeat the process up to set 5 inches of soil. Sum all these values, including the soil box and its plate; compare the sum with the weight read by the SCADA.
c) Compare the reservoir fluid temperature, when reaching 38 °C, with the reading from the handheld thermometer.
d) Turn on the centrifugal pump and set the VFD at 20 Hz, place the bucket at the pipe loop return –or drain-, fill the bucket and measure the filling time using a stopwatch. Solve the fluid flow (m/s) indirectly by solving its GPM and dividing it by 24.737 (this ratio comes from the velocity and flow rate equation). Repeat the process with VFD at both 40 and 60 Hz.

4.6 Data Acquisition

A system NI cDAQ-9178 acquires, analyzes, presents, and manages the measurement data from the process sensors. Both pressure sensors and load cell signals are converted into 4-20 mA, at this point acquired by the NI 9203 module. The NI 9230 and 9217 modules

acquired the signals directly from the thermistors and accelerometers. LabView deliveries the data in excel format. Figure 4.4 diagrams of the data acquisition system.

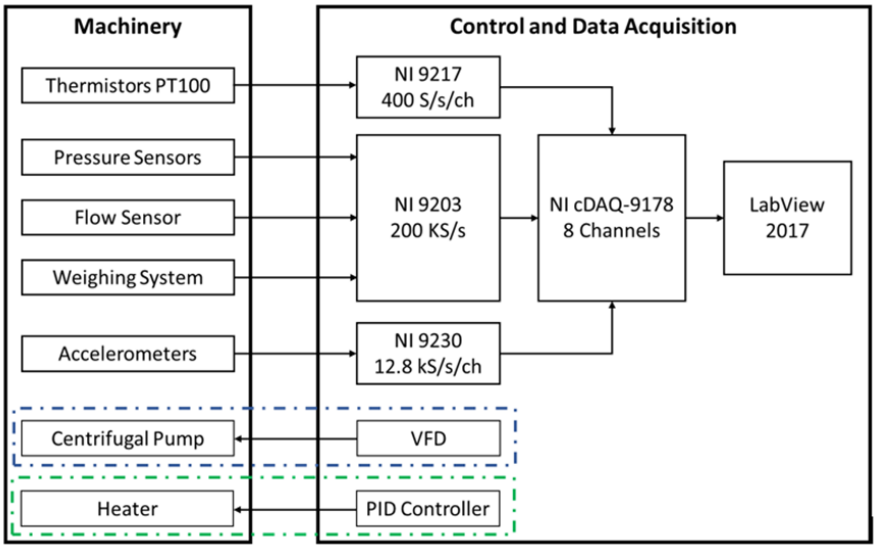

Figure 4.4: Data acquisition system diagram

Two ECH$_2$O 10HS probes measure the soil conductivity, and the Em50 manual-download logger records the streaming data through a USB port to the laboratory PC. The processed data is saved in an excel file. Figure 4.5 shows the logger application when downloading the streaming data.

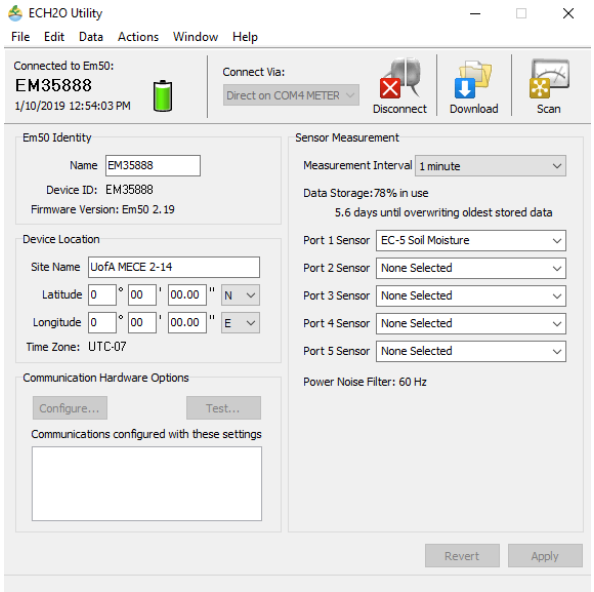

Figure 4.5: Application to download the dielectric permittivity data

Figures 4.6 and 4.8 show the LabVIEW graphical code to stream data from process sensors for small leak and transient state experiments, whereas figure 4.7 and 4.9 show their data in real-time.

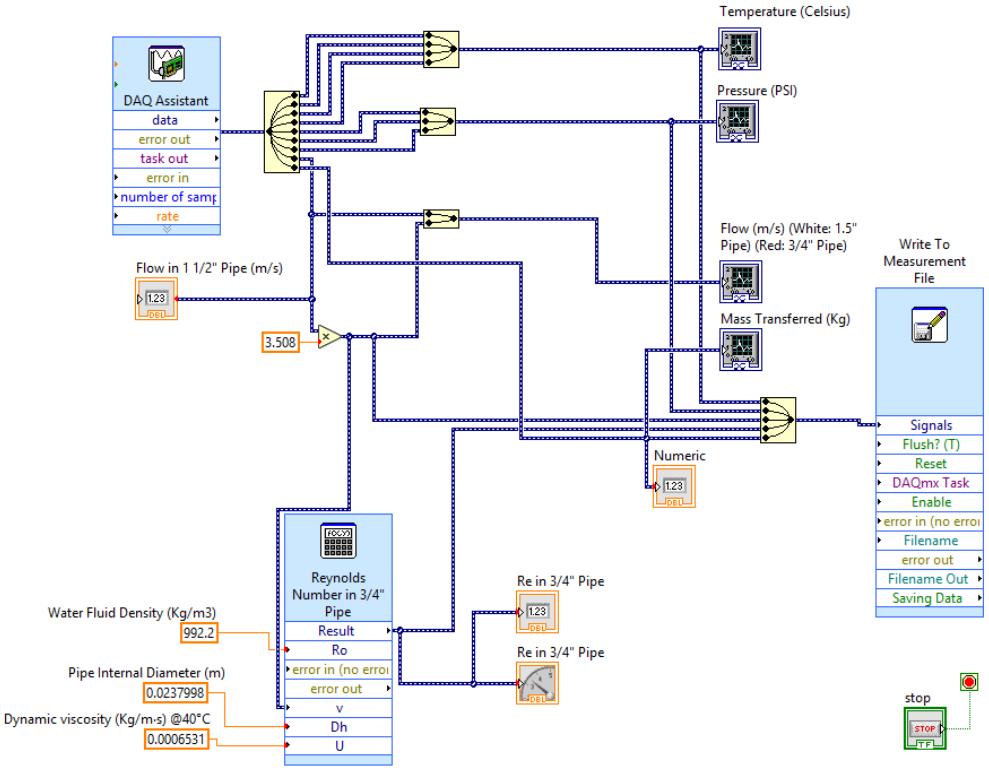

Figure 4.6: LabVIEW graphical code to stream data for small leak experiments

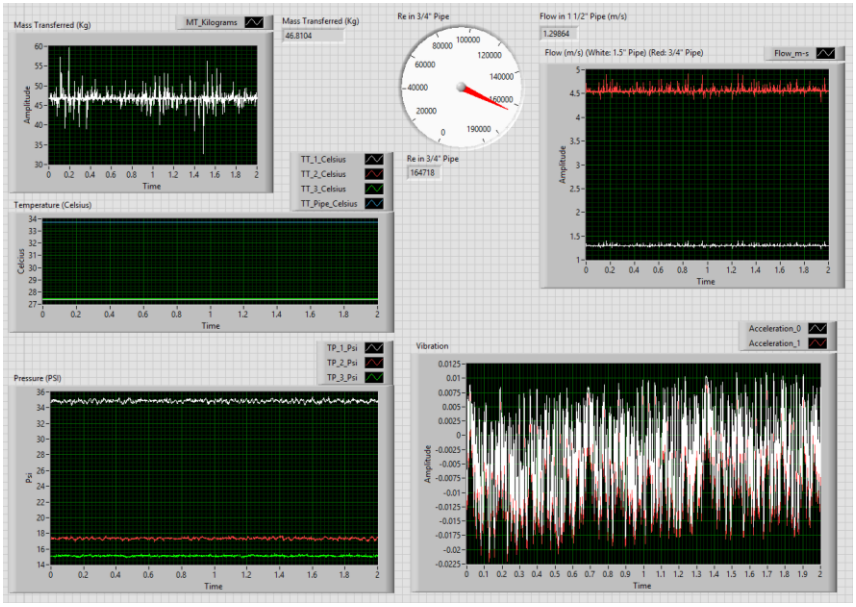

Figure 4.7: Sensors data in real-time of leak experiment

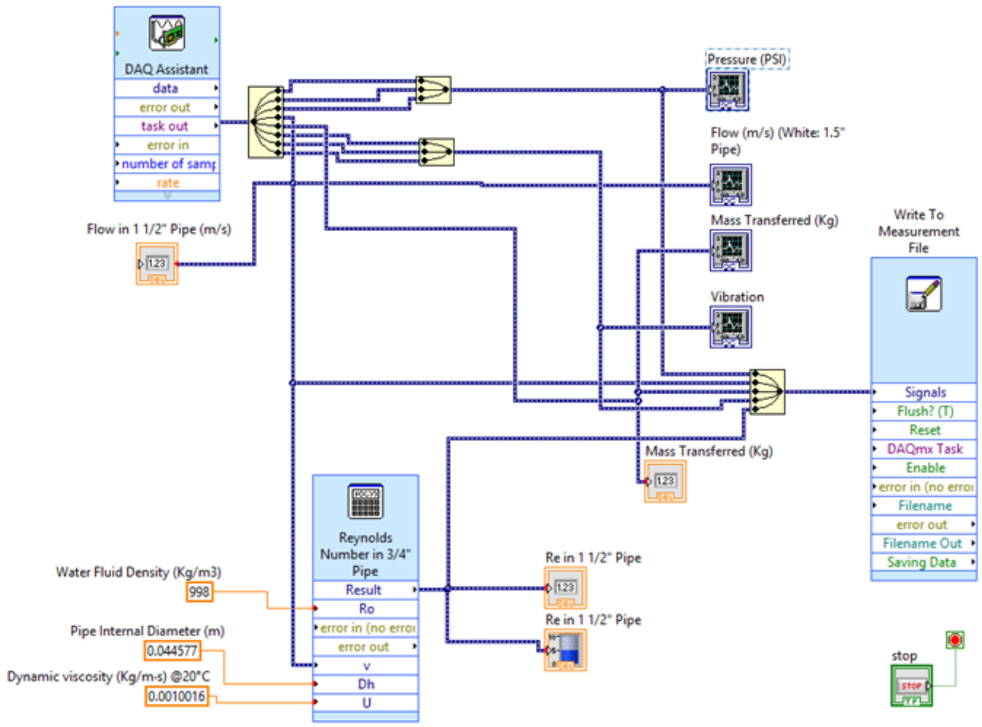

Figure 4.8: LabVIEW graphical code to stream data for transient state experiments

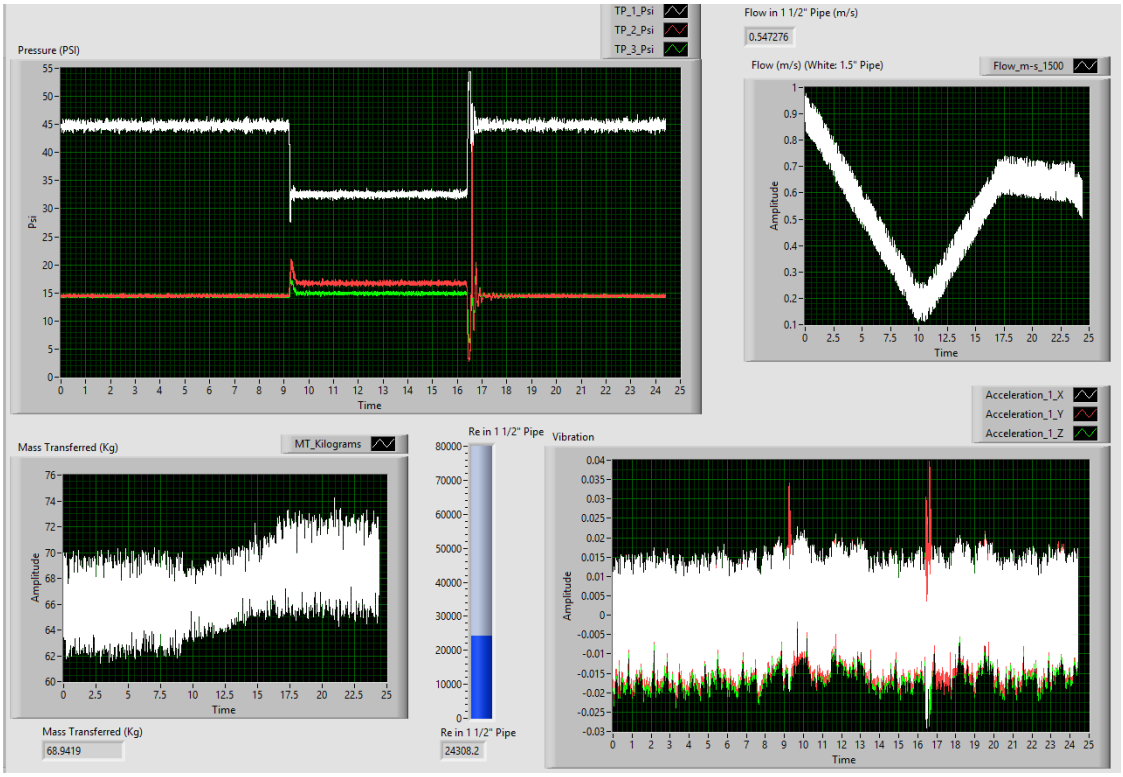

Figure 4.9: Transient state experiment in real-time

4.7 Apparatus set up

Next pictures details the apparatus elements and experimental setups:

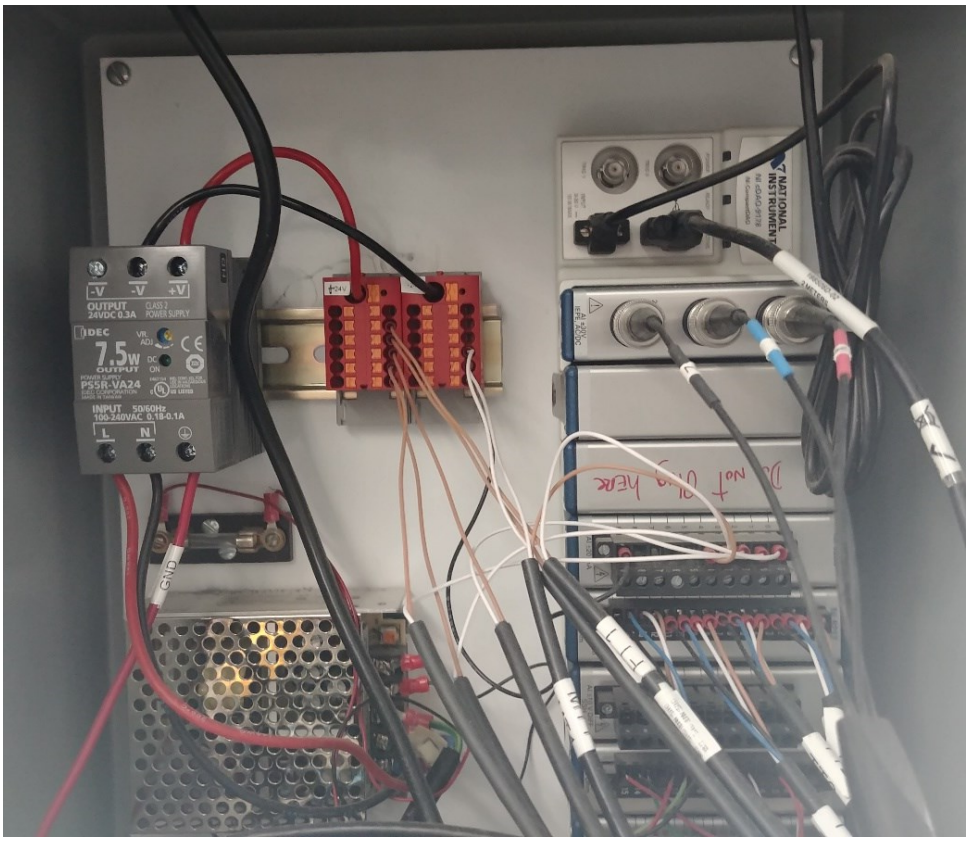

Figure 4.10: Connections from sensors to the NI cDAQ-9178 (SCADA)

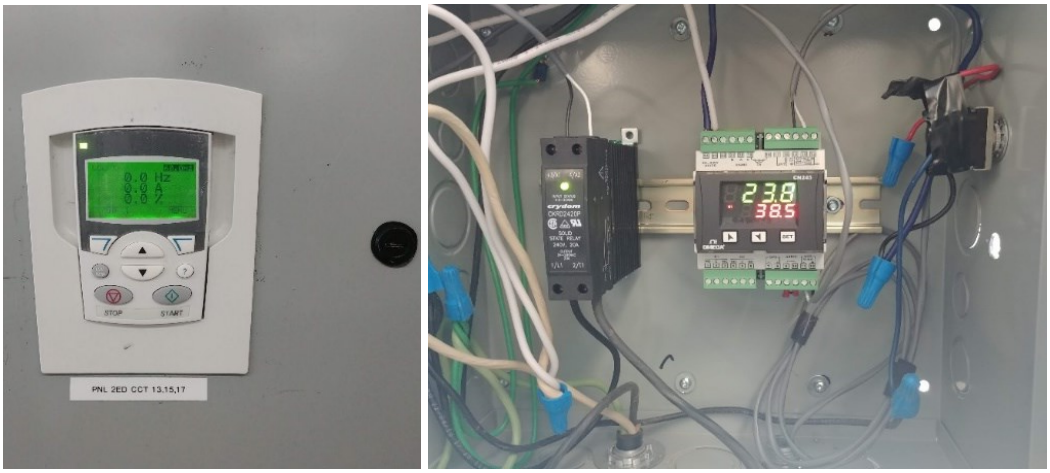

Figure 4.11: VFD and temperature controller power boxes

Figure 4.12: Centrifugal pump and reservoir

Figure 4.13: Isometric view of apparatus

Figure 4.14: Dry black loam and at saturation point

Figure 4.15: Dry and saturated sand

4.7.1 Transient-model-based method experimental set up

The transient state requires creating an abrupt alteration of the flow condition such as closing a valve to generate transient pressure waves; figure 4.16 depicts ball -downstream and upstream- valves to create the abrupt alteration of the flow. Turning off the pump through the variable frequency drive (figure 4.11) also creates a sudden alteration of the flow. If the wave finds a physical discontinuity such as a leak then it generates a reflective wave to the signal source, figure 4.17 shows pinholes in the pipe who produces a small leak (around 2% of nominal flow) whereas figure 4.18 depicts the electrically-actuated valve which creates the rupture -about 17% of nominal flow- conditions. Pressure sensors and accelerometers displayed in figures 4.20 and 4.21 measure the wave reflection as pressure variation and vibration. Figure 4.22 and 4.23 depict variables behavior under no-leak conditions and small-leak conditions. Figure 4.9 plots the hydraulic behavior under rupture conditions.

Figure 4.16: On-off valves to create an abrupt alteration of the flow

Figure 4.17: Small leak source (Pinholes)

Figure 4.18: Large leak source (electrically-actuated valve)

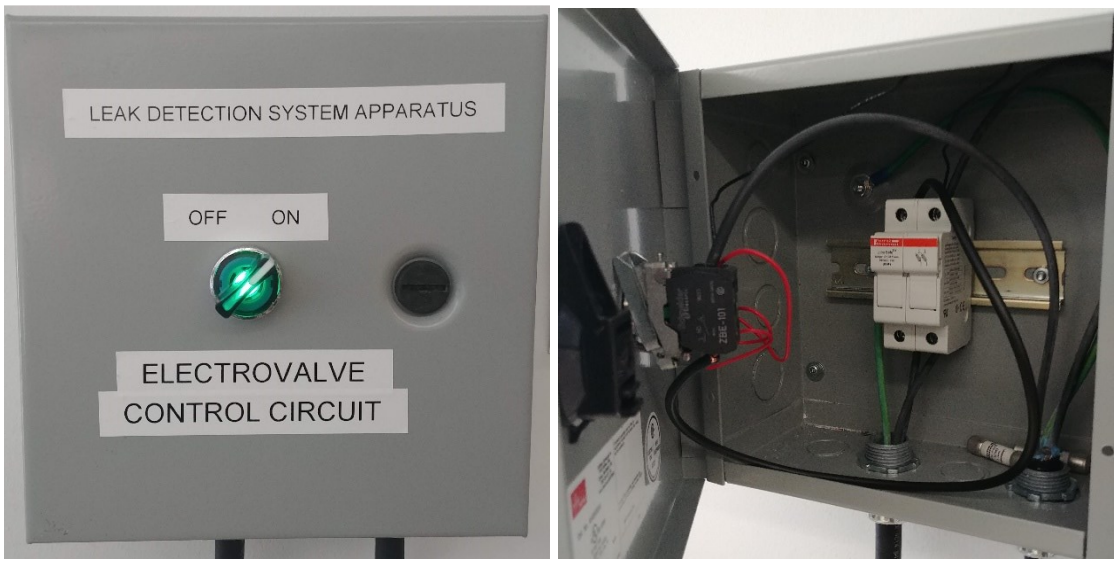

Figure 4.19: Control circuit for the electrically-actuated valve

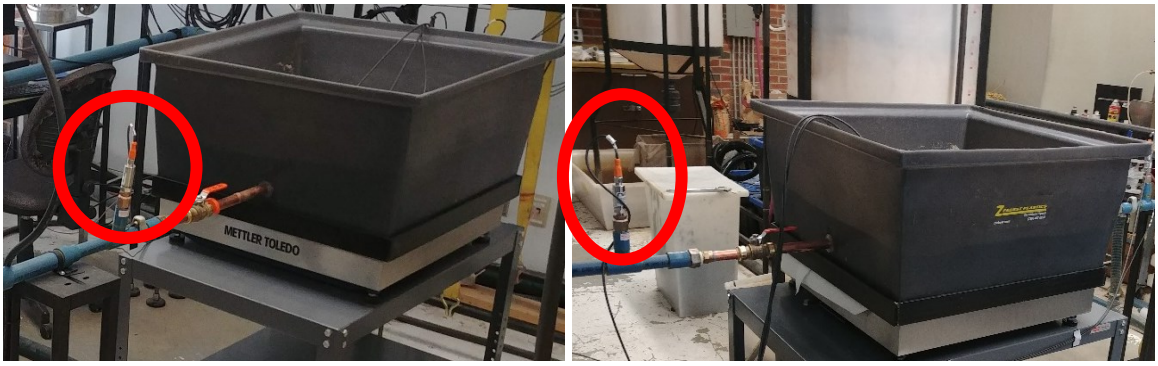

Figure 4.20: Pressure transducers

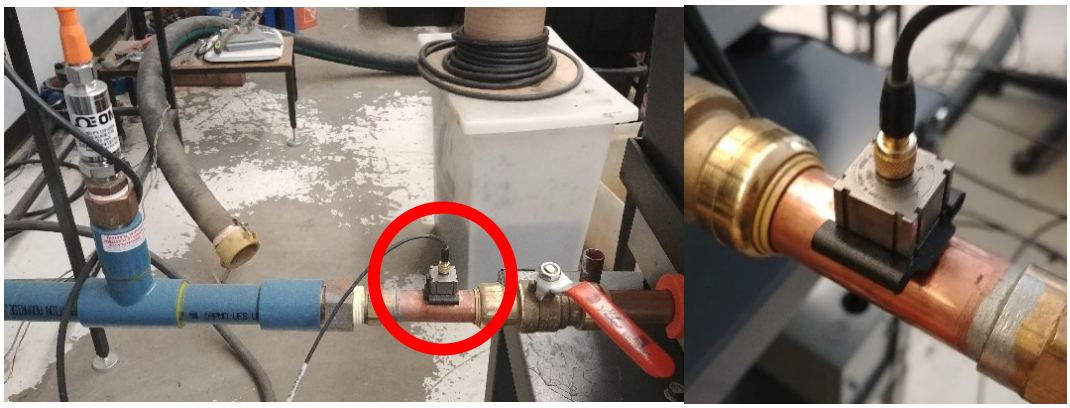

Figure 4.21: Triaxial accelerometer

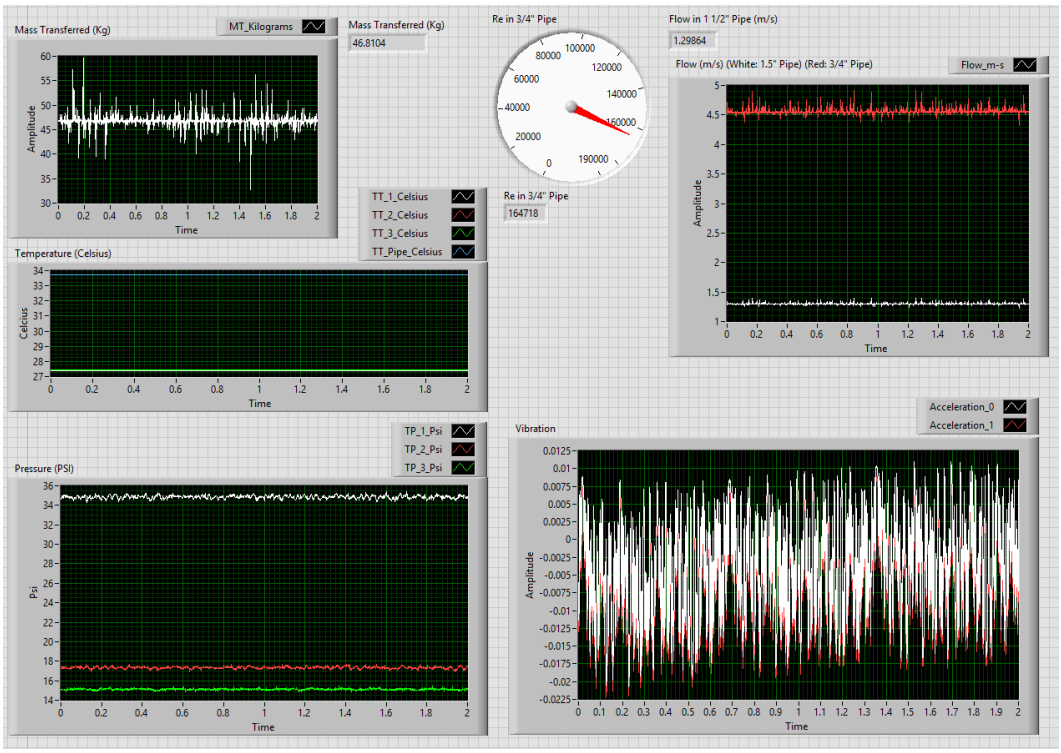

Figure 4.22: Stream sensor data under no-leak conditions

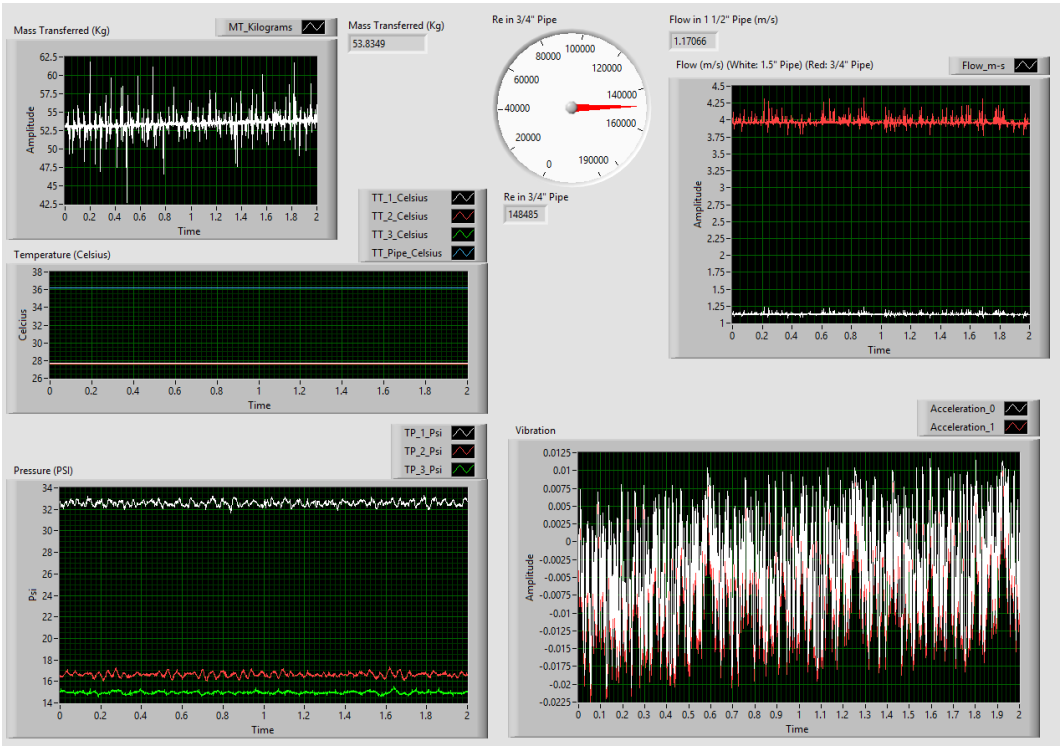

Figure 4.23: Stream sensor data under small-leak conditions

4.8 Denoising sensors stream data

The apparatus' sensor suite consists of one accelerometer, one flow meter, three pressure transmitters, three thermistors, and one scale. PT100 are active transducers, so the DAQ hardware acquires high-quality data out of them, thus turning denoising this variable unnecessary. Conversely, denoising is required for accelerometers' -type 4506B003- signals because they are IEPE transducers which produce a minimal signal, susceptible to electrical noise. Pressure transducers -PX309- also require signal conditioning because their piezoelectric elements are susceptible to vibrations. The flow and weight signals are denoised because a non-ideal 24-VDC power supply energizes these transducers.

The MATLAB Wavelet Toolbox™ analyzes and denoises the signals mentioned above. Wavelet families have different features, so the signal's characteristics define the best fit to denoise them. Therefore, denoising these signals is an iterative process where the raw signal is denoised iteratively using different Wavelets parameters. For example, several iterations were done to denoise pressure transducers' data because these transducers are sensitive to pump vibrations. Conversely, denoising temperature's signal was straightforward because of its resilience to white noise and pump vibration. Appendix 8 and Appendix 16 shows the Wavelet algorithms and the denoising parameters used for the variables plotted in the present research.

Table 4.13: Denoising parameters of variables (Figures 4.24 to 4.28)

Test	Variable	Type of Wavelet	Level	Denoising Method	Thres. Rule	Noise	Additional denoising
Test7 (Round 2): FV: 5 m/s - Saturated black soil- 0% Leakage	TT_1_Celsius	sym4	16	Bayes	Mean	Level Independent	Not Applicable
Test7 (Round 2): FV: 5 m/s - Saturated black soil- 0% Leakage	TP_1_Psi	db5	13	Bayes	Soft	Level Dependent	Not Applicable
Test7 (Round 2): FV: 5 m/s - Saturated black soil- 0% Leakage	TP_2_Psi	db5	13	Bayes	Soft	Level Dependent	Not Applicable
Test7 (Round 2): FV: 5 m/s - Saturated black soil- 0% Leakage	Flow_ms_750	db10	12	Bayes	Soft	Level Dependent	Gaussian smoothing method

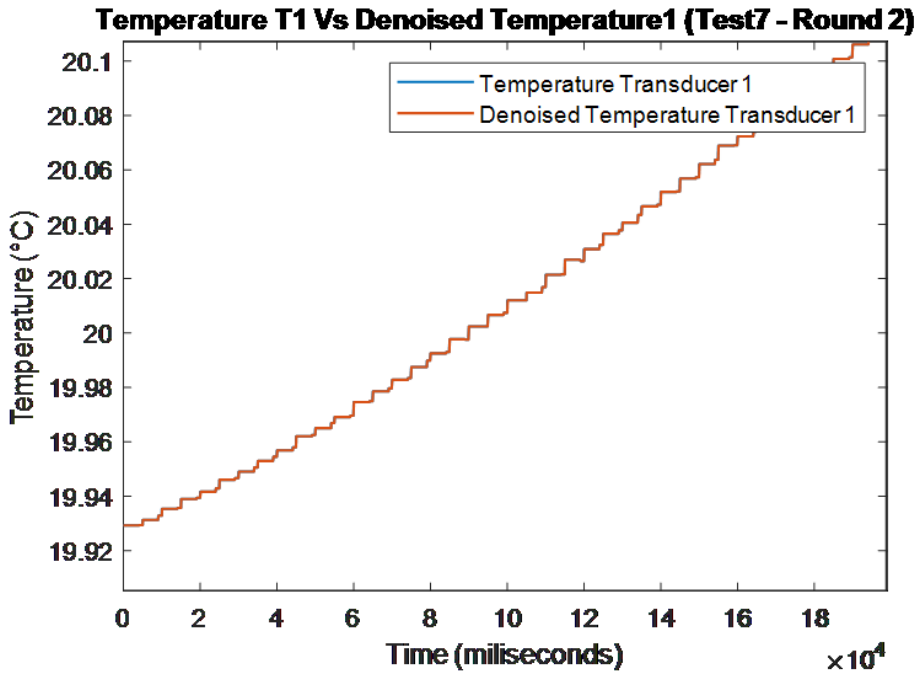

Figure 4.24: Temperature T1 and its denoised version (Test7 –Round 2)

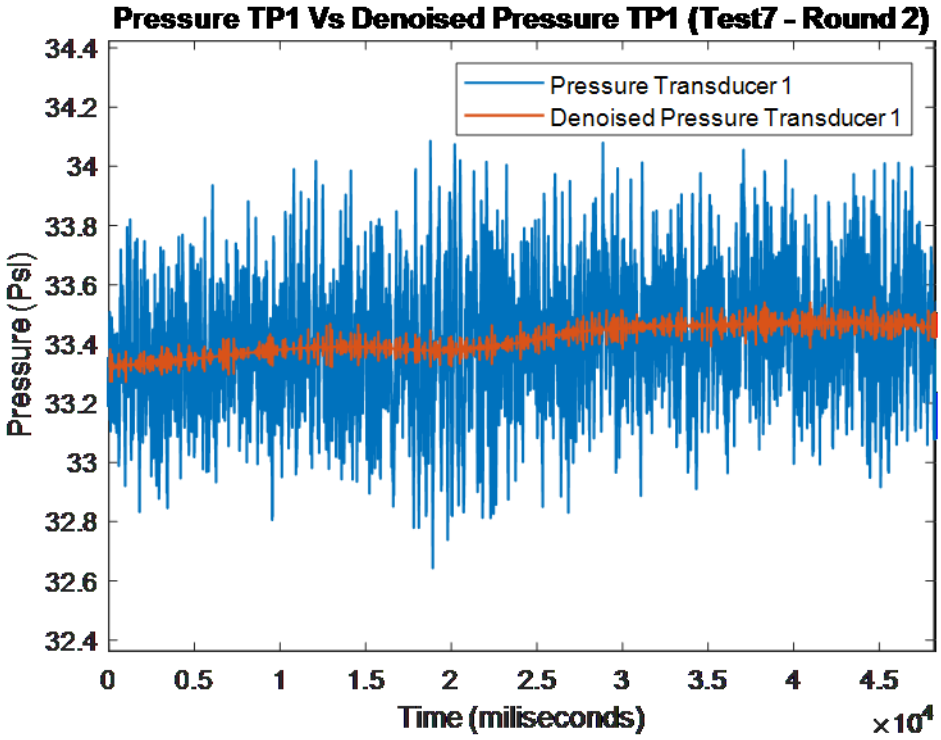

Figure 4.25: Pressure TP1 and its denoised version (Test7 –Round 2)

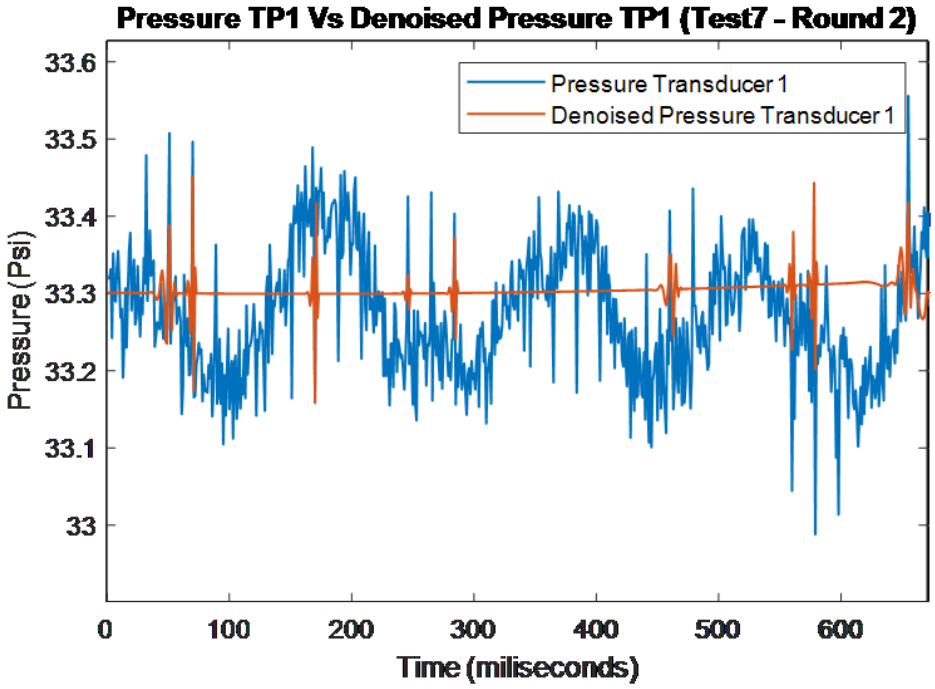

Figure 4.26: Pressure TP1 and its denoised version (Test7 –Round 2)

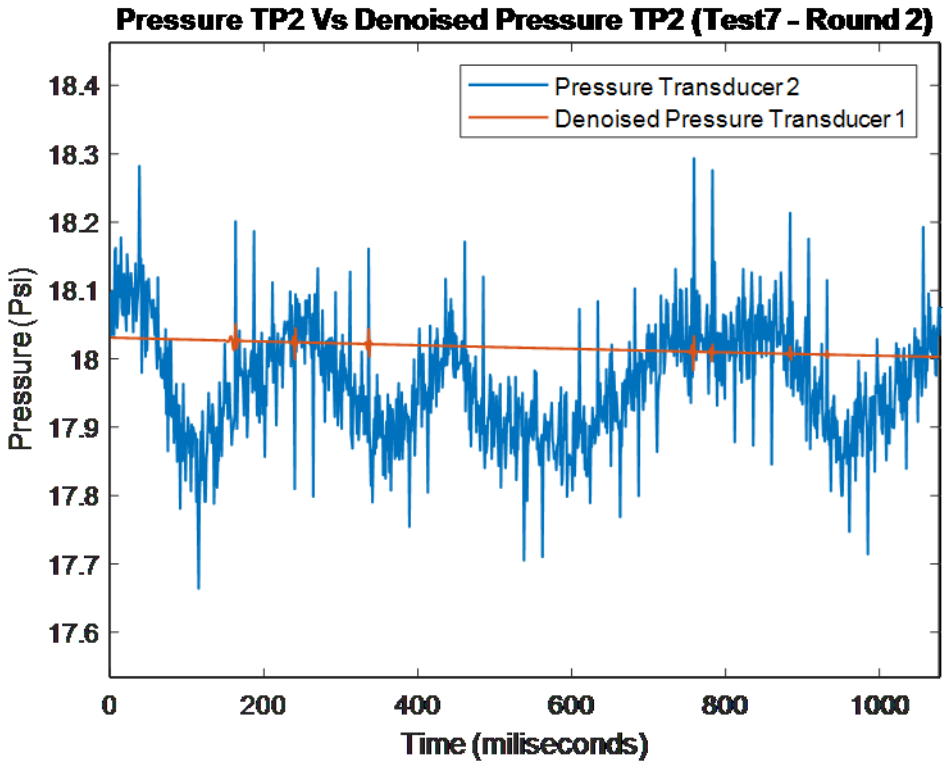

Figure 4.27: Pressure TP2 and its denoised version (Test7 –Round 2)

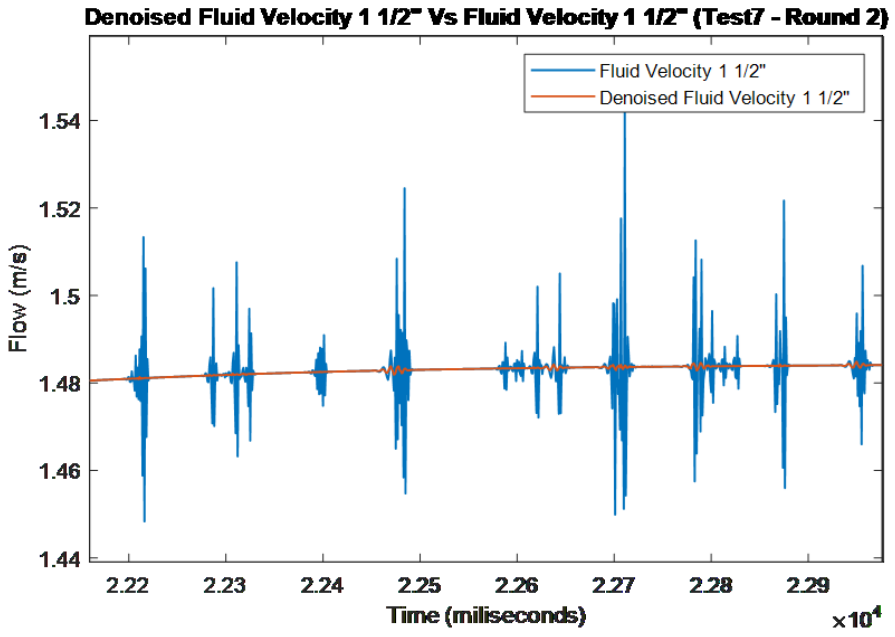

Figure 4.28: Fluid velocity and its denoised version (Test7 –Round 2)

4.9 Limitations of the experimental design

- Apparatus cannot replicate the industry operational Reynold number using canola oil because it is highly viscous and behaves in the laminar regime. Water is the best simulant liquid for research purposes.
- Subsidence cannot be simulated because the soil-box has not a drain.
- Pump vibration conceals the signals of the pressure transducer and accelerometer set beside the upstream valve. Even though the centrifugal pump is bolted to the ground and a sphere union is attached to the pump to damp pump-vibrations, resulting signals still present unwanted features. The MATLAB Wavelet Toolbox™ addresses these features at a signal distortion cost.
- Alberta Agriculture compounds the Albertan soil group by eight types of soil. The experimental conditions only include the most common type of soil across Alberta and Saskatchewan, black chernozemic soil.
- Although sensing volatile organic compounds is currently an important LDM, it is not tested because hydrocarbons are hazardous when stored in confined spaces.

- Water is the only simulant liquid used in the experiments because of its safety, low viscosity, and turbulent properties.
- The fluid velocity of crude oil usually tops 20 ft/s -6.1 m/s- in pipelines (according to a Canada-based energy transportation company). Maximum fluid velocity reproduced in laboratory conditions is 5.0 m/s.
- Pinhole sizes are two and three millimeters, resulting in estimated leak rates between 1.04 and 2.33 % (percentage of Nominal flow). Time-span of tests varies depending on experimental conditions.
- An electrically actuated valve creates the rupture, leak about 17% of nominal flow-, needed to evaluate the transient-model-based method. More significant ruptures require a bigger electrically actuated valve.
- The pipeline system used as a reference is deployed across Alberta and Saskatchewan, where soil moisture ranges from less than 5% to 35%. Soil moisture in experiments ranges from 2% to 26% for sand, and 15% to 45% for black soil. Upper limits are the saturation point where leaks happen adjacent to or under rivers. Experiments using dryer black soil requires an unavailable large drying oven (vented, thermostatically controlled, and capable of maintaining a uniform temperature of 110 °C).

Chapter 5: Results

The following chapter presents results obtained from the experimental trials under different conditions: fluid velocity, leak size, soil moisture level, type of soil. It also presents the results of transient conditions. These results validate the hypothesis of that LDSs detect the release of hydrocarbons by either monitoring internal pipeline parameters or directly detecting physical changes in the environment due to the presence of hydrocarbons.

5.1 Dimensional scale limitations

The fluid velocity of crude oil usually tops 20 ft/s -6.1 m/s- in pipelines whereas the LDS apparatus runs liquids up to 16.4 ft/s -5.0 m/s-. The fluid viscosity, fluid velocity, and pipe size define the fluids hydraulic behavior, represented by the Reynolds number. In energy transportation, the fluid usually behaves turbulently because diameters of average pipelines are 10" or more while 'Re' can be 1,000,000 or more. Laboratory-scale apparatus using 10"-pipe is prohibitively expensive. Therefore the pipe diameter is ¾", and 1" and 1 ½". The DAQ device cannot store continuous data if experiments last at least four minutes since the DAQ's memory overflows. Configurating the signal acquisition to 'N sample' addresses this problem because the sample rate depends on the hardware clock, which is faster than a software loop. This configuration is designed to acquire finite high-frequency signals, such as an audio signal.

Pinholes of 2 and 3 millimeters drilled in copper pipes yield average leaks of 0.66 and 1.84 % of nominal flow, whereas an electrovalve creates a controlled rupture of 17%. The electrovalve paired up with both the downstream valve and the variable frequency drive, create the failure conditions –pipeline startup and shutdown, and pump and valve operations- to evaluate the transient-model-based method. Soil porosity and field capacity define moisture level at saturation point, black soil and sand have a saturation point of 45 % and 26 % respectively. Experiments are run twice to ensure repeatability; table 5.1 shows the experimental conditions for the first round of experiments, designed to test small leaks while Table 5.2 depicts the configurations of the second round of experiments. Table 5.3 compares

leakage rate for both rounds of experiments. Moisture and small leakage rate were not controlled but measured. Fluid rate is calculated by measuring the liquid's mass transferred to the soil box during each experiment. The sequence of experiments is different between round #1 and round #2.

Table 5.1: Experimental conditions for small leak tests – First round

N°	Type of Soil	Moisture Content (%)	Soil condition	Fluid Velocity (m/s)	Fluid velocity (liters / second)	Liters Leaked / second	% Leak respect fluid velocity
1	Sand	2	Dry	5.00	2.22	0.000	0%
2	Sand	2	Dry	3.50	1.56	0.000	0%
3	Black Soil	15	Dry	3.50	1.56	0.000	0.0%
4	Black Soil	15	Dry	5.00	2.22	0.000	0.0%
5	Black Soil	15	Dry	5.01	2.23	0.020	0.88%
6	Black Soil	45	Saturated	5.05	2.25	0.021	0.95%
7	Black Soil	45	Saturated	3.57	1.59	0.013	0.82%
8	Sand	2	Dry	5.05	2.25	0.015	0.66%
9	Sand	26	Saturated	5.06	2.25	0.018	0.82%
10	Sand	26	Saturated	3.58	1.59	0.015	0.96%
11	Sand	26	Saturated	5.00	2.22	0.000	0.0%
12	Sand	26	Saturated	3.50	1.56	0.000	0.0%
13	Sand	2	Dry	3.56	1.58	0.011	0.67%
14	Sand	26	Saturated	5.03	2.24	0.030	1.33%
15	Sand	26	Saturated	3.54	1.57	0.034	2.15%
16	Black Soil	15	Dry	5.03	2.24	0.044	1.97%
17	Black Soil	45	Saturated	5.03	2.24	0.038	1.69%
18	Black Soil	15	Dry	3.54	1.58	0.034	2.14%
19	Black Soil	45	Saturated	3.52	1.57	0.034	2.14%
20	Black Soil	15	Dry	3.55	1.58	0.011	0.67%
21	Black Soil	45	Saturated	5.00	2.22	0.000	0.0%
22	Black Soil	45	Saturated	3.50	1.56	0.000	0.0%
23	Sand	2	Dry	5.05	2.25	0.027	1.19%
24	Sand	2	Dry	3.56	1.58	0.019	1.21%

Table 5.2: Experimental conditions for small leak tests – Second Round

N°	Type of Soil	Moisture Content (%)	Soil condition	Fluid Velocity (m/s)	Fluid velocity (liters / second)	Liters Leaked / second	% Leak respect fluid velocity
1	Black Soil	15	Dry	5.01	2.23	0.042	1.90%
2	Black Soil	45	Saturated	5.02	2.23	0.043	1.93%
3	Black Soil	15	Dry	5.00	2.22	0.000	0.00%
4	Black Soil	15	Dry	3.50	1.56	0.000	0.00%
5	Black Soil	15	Dry	3.51	1.56	0.032	2.08%
6	Black Soil	45	Saturated	3.52	1.57	0.033	2.11%
7	Black Soil	45	Saturated	5.00	2.22	0.000	0.00%
8	Black Soil	45	Saturated	3.50	1.56	0.000	0.00%
9	Black Soil	15	Dry	5.08	2.26	0.018	0.79%
10	Black Soil	45	Saturated	5.04	2.24	0.019	0.87%
11	Black Soil	15	Dry	3.56	1.58	0.014	0.90%
12	Black Soil	45	Saturated	3.55	1.58	0.014	0.90%
13	Sand	2	Dry	5.00	2.22	0.000	0%
14	Sand	2	Dry	3.50	1.56	0.000	0%
15	Sand	2	Dry	5.02	2.23	0.042	1.90%
16	Sand	26	Saturated	4.99	2.22	0.044	1.98%
17	Sand	2	Dry	3.52	1.57	0.025	1.60%
18	Sand	26	Saturated	3.49	1.55	0.033	2.14%
19	Sand	26	Saturated	5.00	2.22	0.000	0.00%
20	Sand	26	Saturated	3.50	1.56	0.000	0.00%
21	Sand	2	Dry	5.03	2.24	0.020	0.87%
22	Sand	26	Saturated	5.04	2.24	0.020	0.90%
23	Sand	2	Dry	3.55	1.58	0.014	0.89%
24	Sand	26	Saturated	3.57	1.59	0.015	0.95%

Table 5.3: Leak rate comparison between the first and second round

Round #1 Tests	Round #2 Tests	Type of Soil	Soil condition	Fluid Velocity #1 (m/s)	Fluid Velocity #2 (m/s)	% Leak rate #1	% Leak rate #2
1	13	Sand	Dry	5.00	5.00	0.00%	0.00%
2	14	Sand	Dry	3.50	3.50	0.00%	0.00%
3	4	Black Soil	Dry	3.50	3.50	0.00%	0.00%
4	3	Black Soil	Dry	5.00	5.00	0.00%	0.00%
5	9	Black Soil	Dry	5.01	5.08	0.88%	0.79%
6	10	Black Soil	Saturated	5.05	5.04	0.95%	0.87%
7	12	Black Soil	Saturated	3.57	3.55	0.82%	0.90%
8	21	Sand	Dry	5.05	5.03	0.66%	0.87%
9	22	Sand	Saturated	5.06	5.04	0.82%	0.90%
10	24	Sand	Saturated	3.58	3.57	0.96%	0.95%
11	19	Sand	Saturated	5.00	5.00	0.00%	0.00%
12	20	Sand	Saturated	3.50	3.50	0.00%	0.00%
13	23	Sand	Dry	3.56	3.55	0.67%	0.89%
14	16	Sand	Saturated	5.03	4.99	1.33%	1.98%
15	18	Sand	Saturated	3.54	3.49	2.15%	2.14%
16	1	Black Soil	Dry	5.03	5.01	1.97%	1.90%
17	2	Black Soil	Saturated	5.03	5.02	1.69%	1.93%
18	5	Black Soil	Dry	3.54	3.51	2.14%	2.08%
19	6	Black Soil	Saturated	3.52	3.52	2.14%	2.11%
20	11	Black Soil	Dry	3.55	3.56	0.67%	0.90%
21	7	Black Soil	Saturated	5.00	5.00	0.00%	0.00%
22	8	Black Soil	Saturated	3.50	3.50	0.00%	0.00%
23	15	Sand	Dry	5.05	5.02	1.19%	1.90%
24	17	Sand	Dry	3.56	3.52	1.21%	1.60%

Controlled variables are fluid velocity and pinhole size; leak rates are indirectly calculated by measuring the mass of the liquid transferred to the soil box during each experiment. Leak rates are not controlled but measured, they are similar as expected, yet

three experiments (dry and saturated sand conditions) shows different leakages between repetitions due to non-controlled variables. On the other hand, leakages when using black soil are in general higher than sand's because of their permeability; this will be explained in 5.2.1.

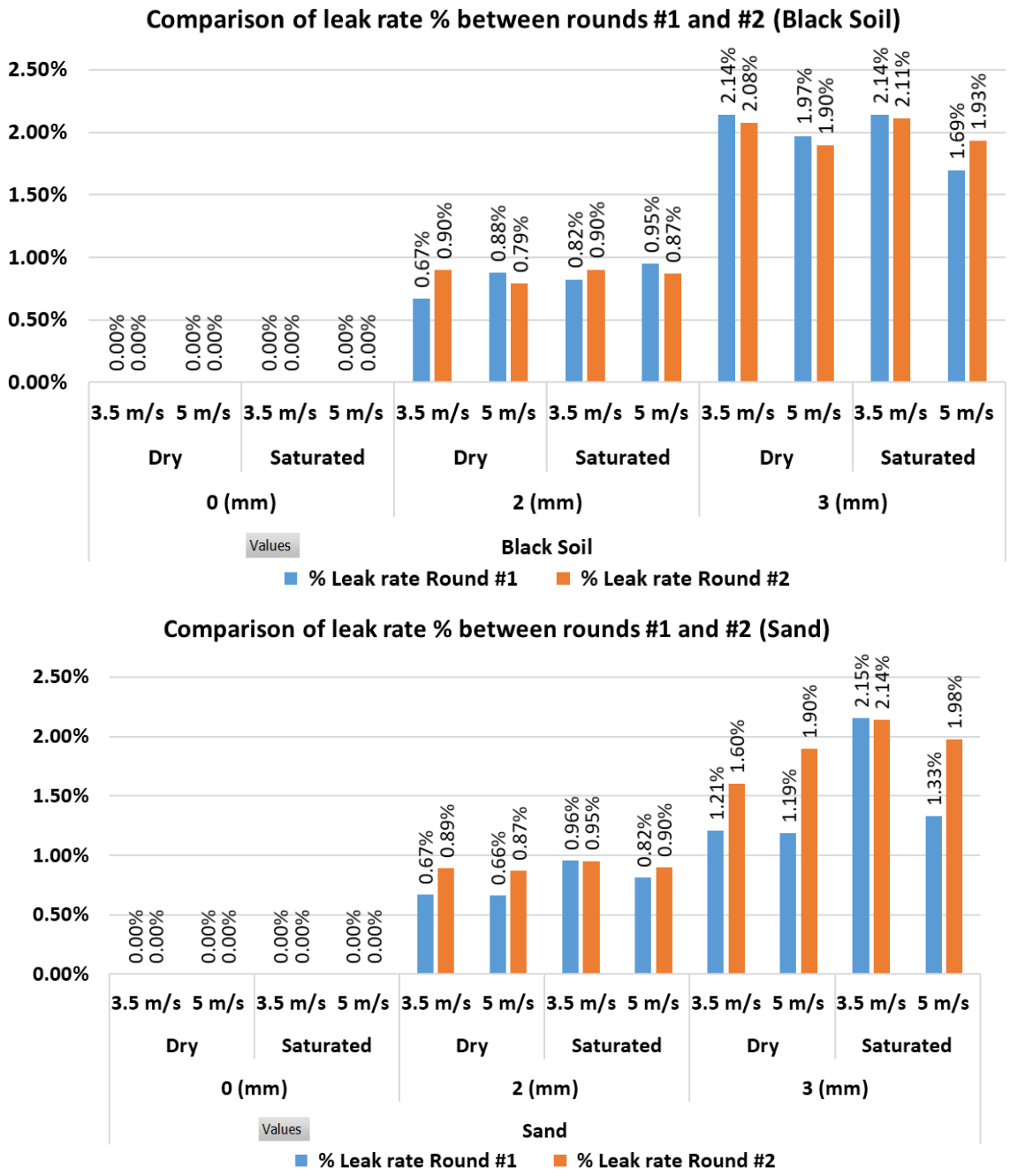

Figure 5.1: Comparison of leak rates between repetitions / Top: Black Soil - Bottom: Sand

5.2 Results

Appendix A.11 shows all the thermal images of steady-state and small leak experiments from round #1. Manipulated variables broadly influence responding variables, from negligible impact under no-leak conditions to substantial effect under leak conditions. Responding variables remain stable throughout experiments under no-leak conditions, delta temperature is one-Celsius degree as shown in FLIR images, as expected, due convection from the pipe to the soil.

‖--------16”---------‖ ‖------------------------16”--------------------------‖

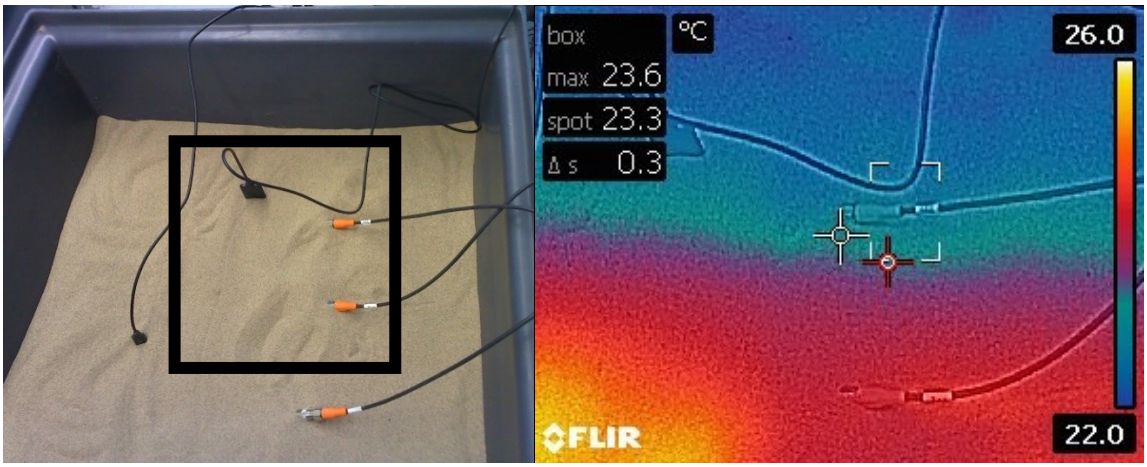

Figure 5.2 (a): Experimental setup #2 at the minute zero

‖---------- 24”----------‖

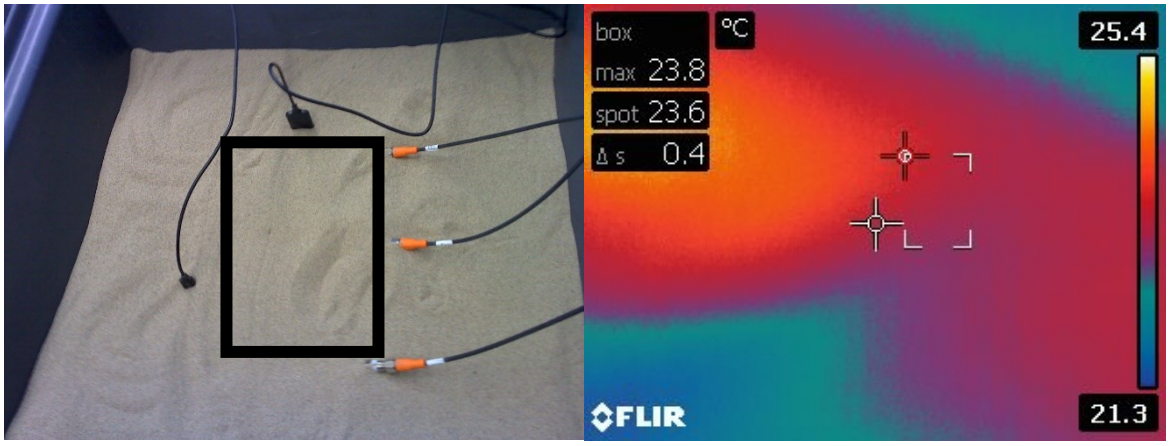

Figure 5.2 (b): Experimental setup #2 at the minute 35

‖---------- 16”----------‖

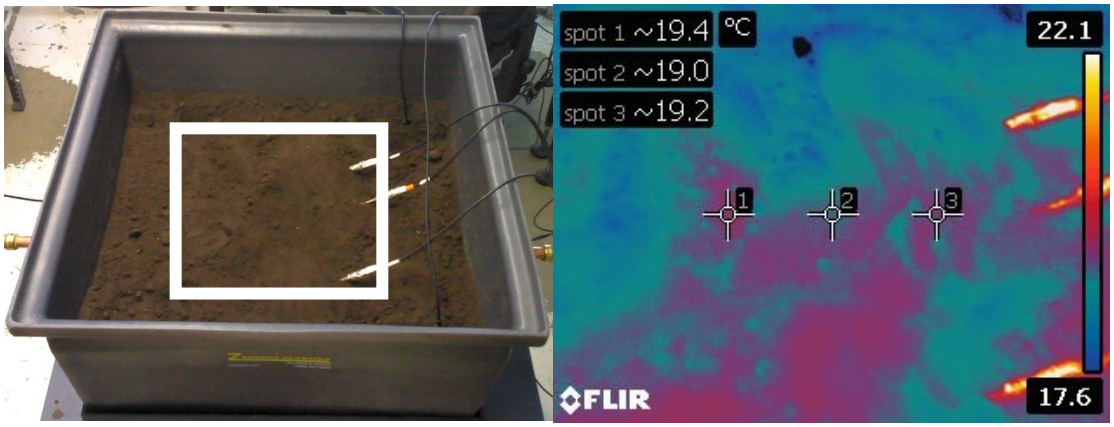

Figure 5.3 (a): Experimental setup #3 at the minute zero

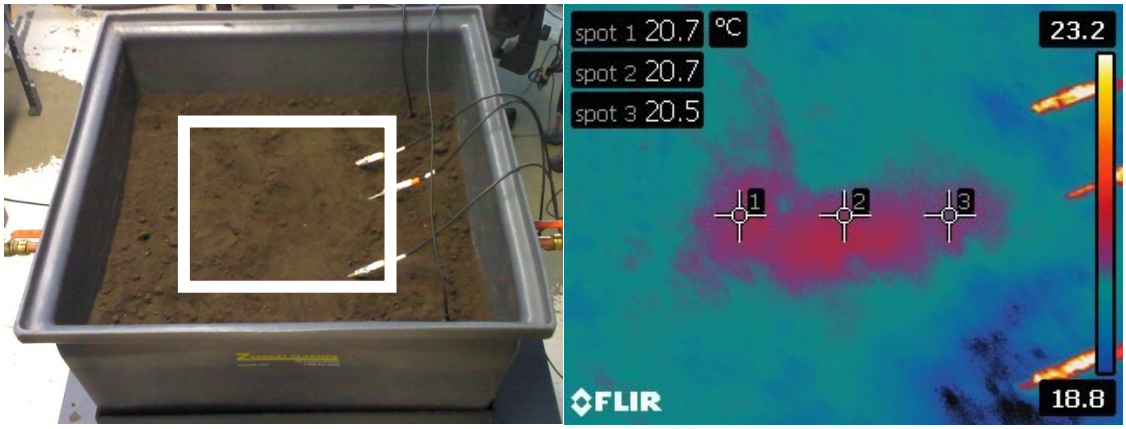

Figure 5.3 (b): Experimental setup #3 at the minute 30

Signals are denoised using the MATLAB Wavelet Toolbox™, yet its efficacy depends on the parameters configuration -type of wavelet, level, denoising method, threshold rule- and the type of noise in signal processing, so the configuration is cautiously defined considering its denoising efficiency and signal distortion level. Appendix A-15 incorporates the parameter configurations for each experiment. The most effective configuration for steady-state experiments are, as portrayed in figure 5.4, ‘Wavelet: db3 / Level: 13 / Denoising Method: Bayes / Threshold Rule: soft / Noise: Level-Dependent’ because their output has the least level of noise with no critical information removed. Hence, distortion level in these particular case is minimal since pressure and vibrations are regular and steady, yet this configuration performs poorly with transient state data because it has

critical features such as oscillation or peaks that are removed under this wavelet arrangement. The accelerometer streams data of vibration on axial, longitudinal, and transverse direction; its data set is denoised using different parameters configuration because they might have sharp features. Figure 5.4 depicts the denoised pressure before the leak in experiment #2 – round 1-; noise distortion is significant in pressure and vibration measures because shock and vibration measuring systems are susceptible to noise generated by ground loops and by pickup from electrostatic and electromagnetic fields.

Results for no-leak experiments are consistent amongst all technologies, as shown in figures 5.4 to 5.8. Responding variables such as dielectric permittivity, flow, mass transferred, pressure, vibration, and temperature, are steady throughout experiments.

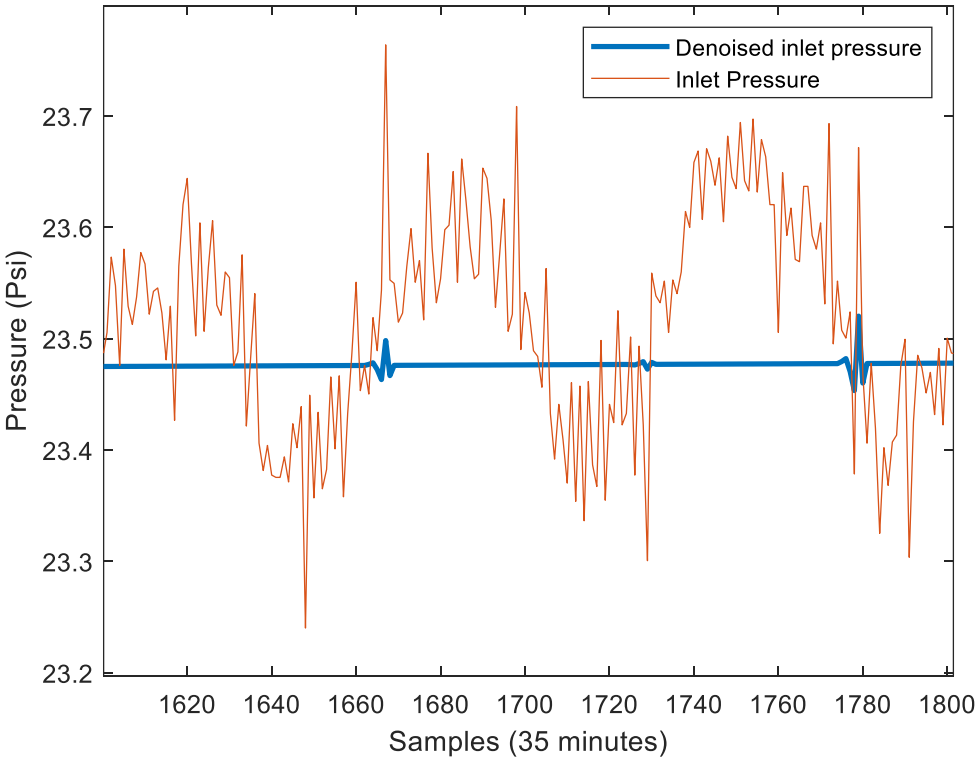

Figure 5.4: Denoised and raw inlet pressure (Experiment #2 – Round #1)

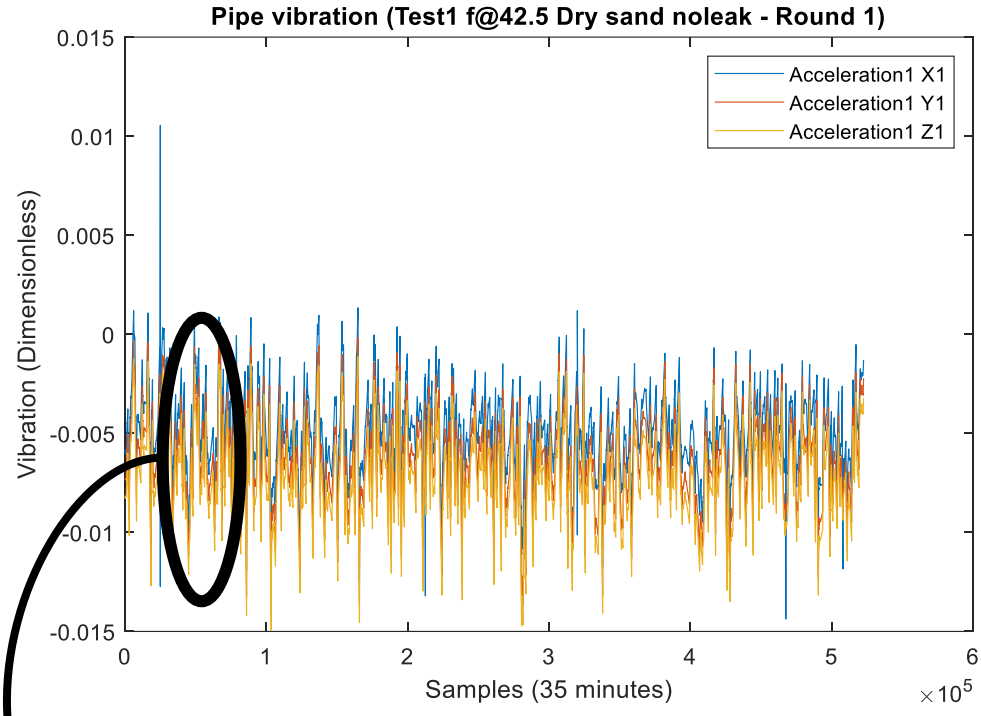

Figure 5.5: Pipe vibration (Experiment #2 – Round #1)

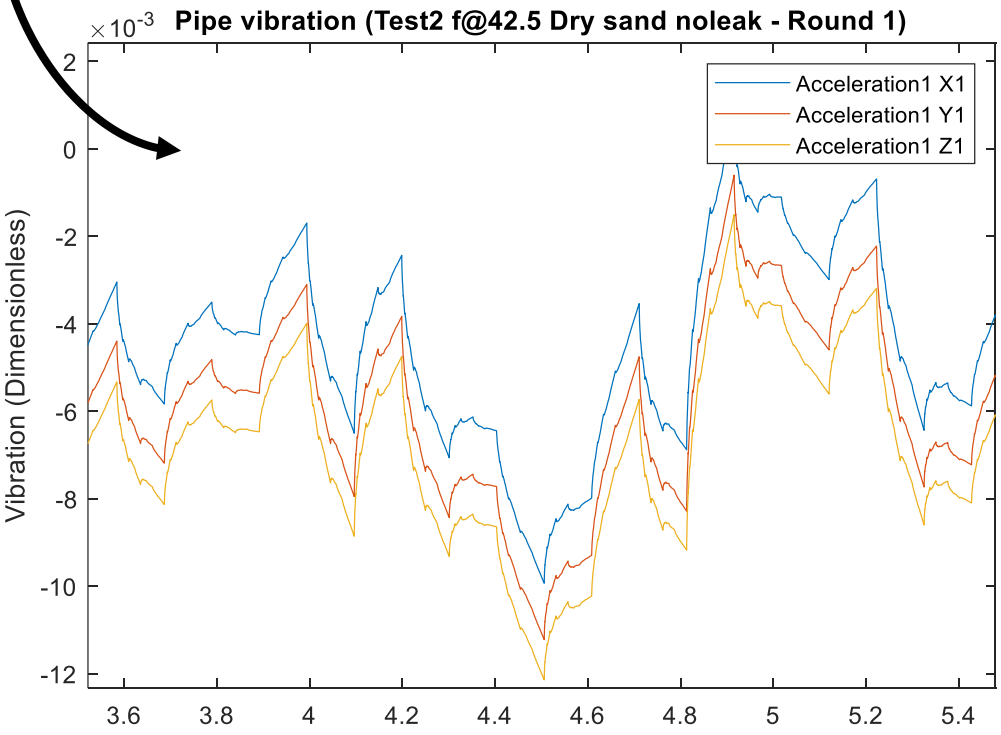

Figure 5.6: Zoom in pipe vibration (Experiment #2 – Round #1)

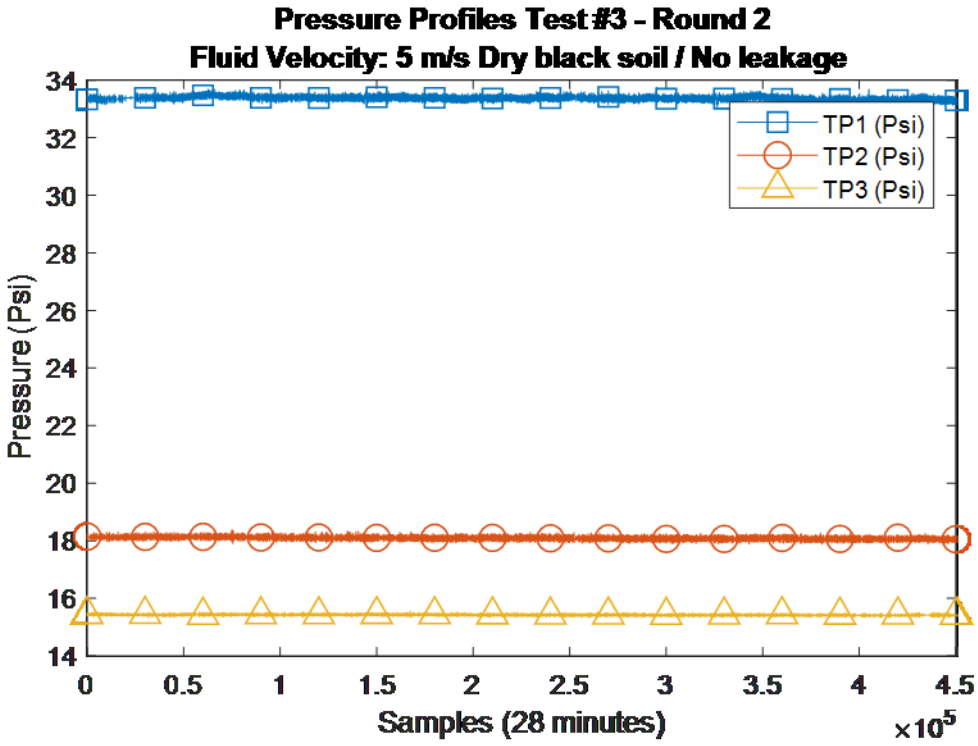

Figure 5.7: Pressure profiles (Experiment #3 – Round #2)

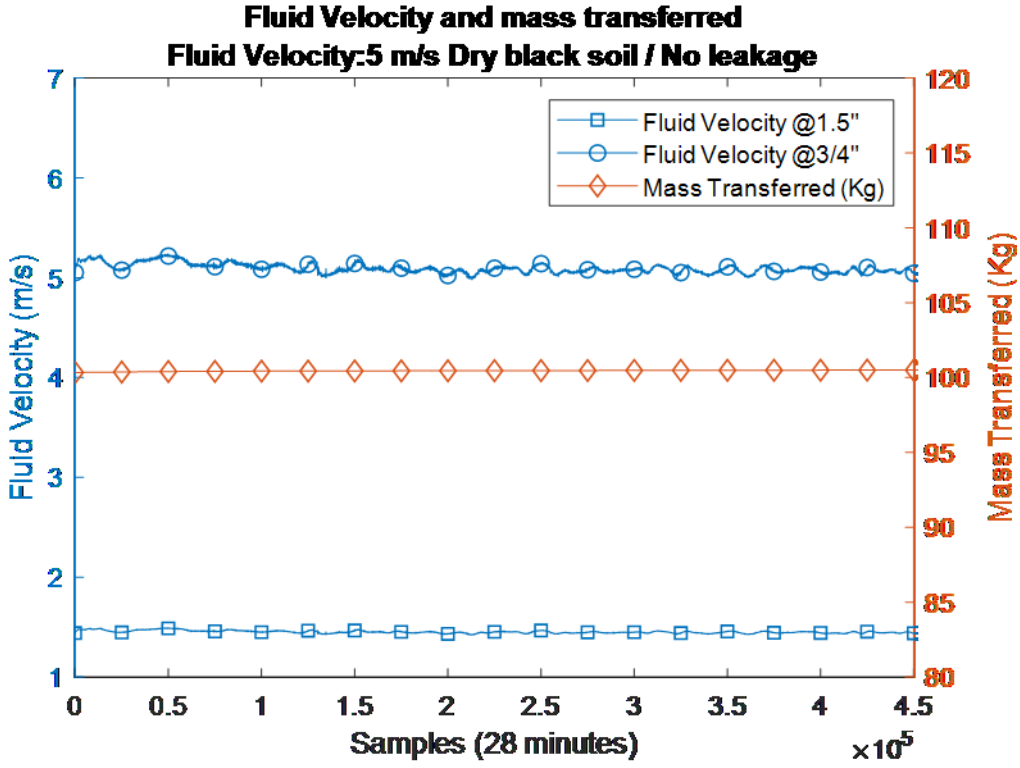

Figure 5.8: Fluid flow and mass transferred (Experiment #3 – Round #2)

5.2.1 Dielectric permittivity Results

Dielectric permittivity –soil conductance/impedance- is a variable who responds linearly to water content up to reaching the saturation point where soil cannot absorb more water. Two volumetric water content sensors, ECH$_2$O 10HS and EC-5, determine the volumetric water content (VWC) by measuring the dielectric constant of the media using capacitance and frequency domain technology (Meter Group, 2019). Their 70-MHz frequency minimizes salinity and textural effects, yet readings between them present a systematic error because their probe lengths are 16 and 8.9 cm, so the sensor 10HS has three times the volume of influence compared to the EC-5's, Figure 5.9(a) details the error mentioned above. All results detailed below are from second-round experiments.

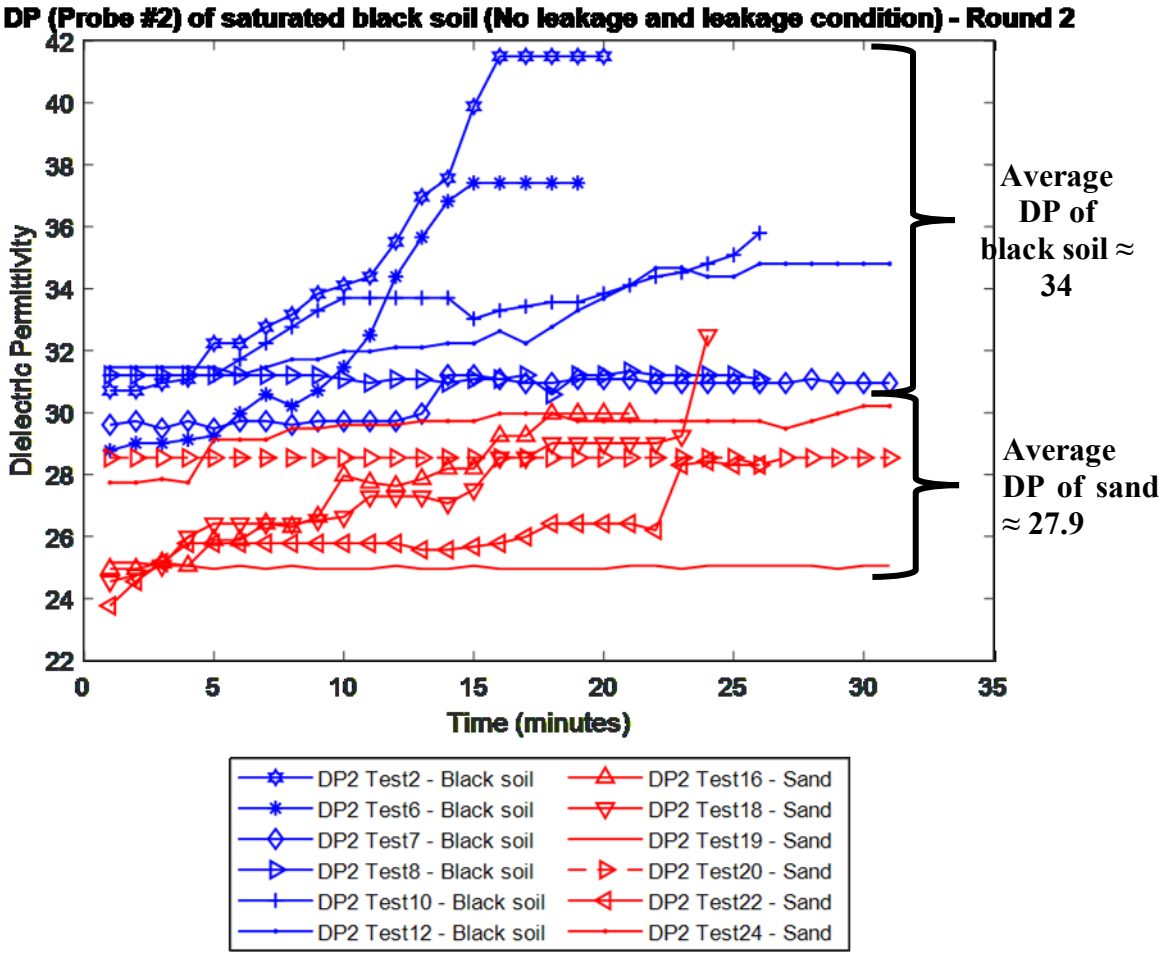

5.9 (a): Dielectric permittivity of saturated black soil and sand under leak conditions

Figure 5.9(a) plots the dielectric permittivity of saturated soils under both leak and no-leak conditions; they range between 25 and 40 as expected per Kargas and George (2019). In general, dielectric permittivity increases with increasing the clay or inorganic content of the soil (Schön, 2015); results plotted in figure 5.9(b) confirm this because the average DP for dry black soil is 5.22 while 3.56 for dry sand.

DPs plotted in figure 5.9(a) yield 34 for black soil 27.9 for sand at saturation point as anticipated by Mohamed and Paleologos (2018). Soil medium characteristics define the dielectric permittivity plateau. Figure 2.9 (chapter 2) shows the volumetric soil moisture Vs. the dielectric constant for different types of soil.

DP probes are imperceptive to leaks under saturation conditions because the leak flow has the next characteristics: (a) it takes place in the direction of decreasing potential, (b) the rate of flow is proportional to the potential gradient, and (c) it is affected by the geometric properties of the pore channels through which the flow takes place. In other words, since the ground surface is the water table in experiments and the pressure head of the leak is higher than the atmospheric pressure, the liquids built up at the ground surface and they cannot infiltrate the soil because the potential energy (gravity) is insufficient to break the already established water-soil bond. Therefore, saturated soil will neither change its hydraulic conductivity, nor change its dielectric permittivity, nor replace its moisture by new liquids. This explanation also backs up the performance of thermocouple probes as detailed in further analysis.

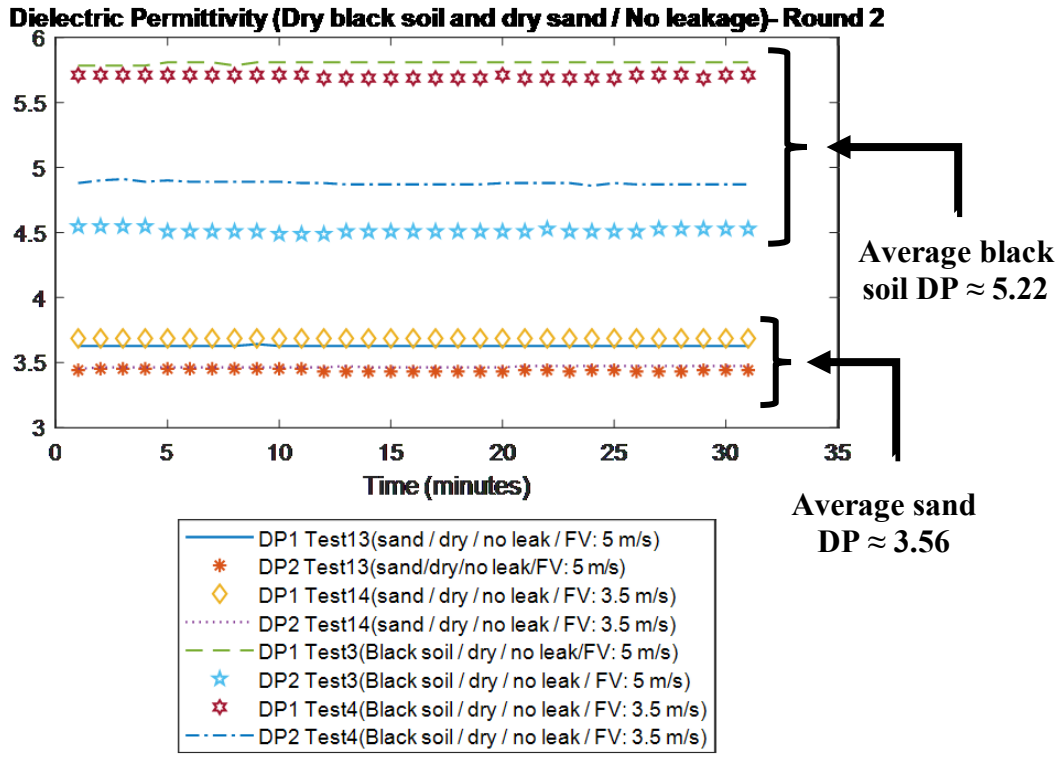

5.9 (b): Dielectric permittivity of dry black soil and sand under no-leak conditions

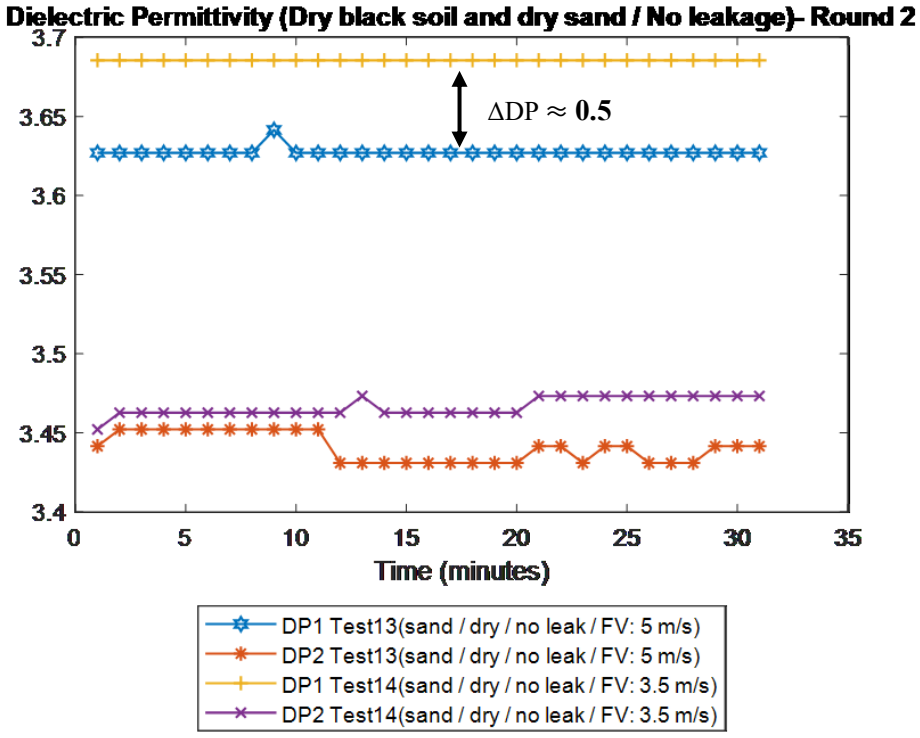

5.10 (a): Dielectric permittivity of dry sand (No leak)

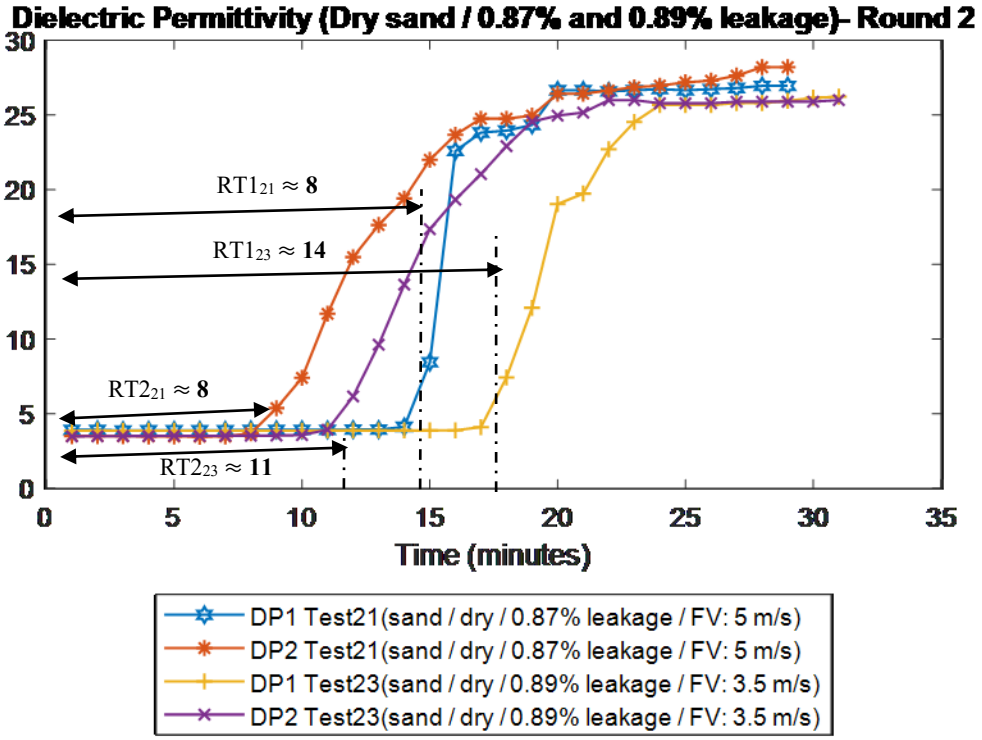

5.10 (b): Dielectric permittivity of dry sand (0.87% and 0.89% Leakage)

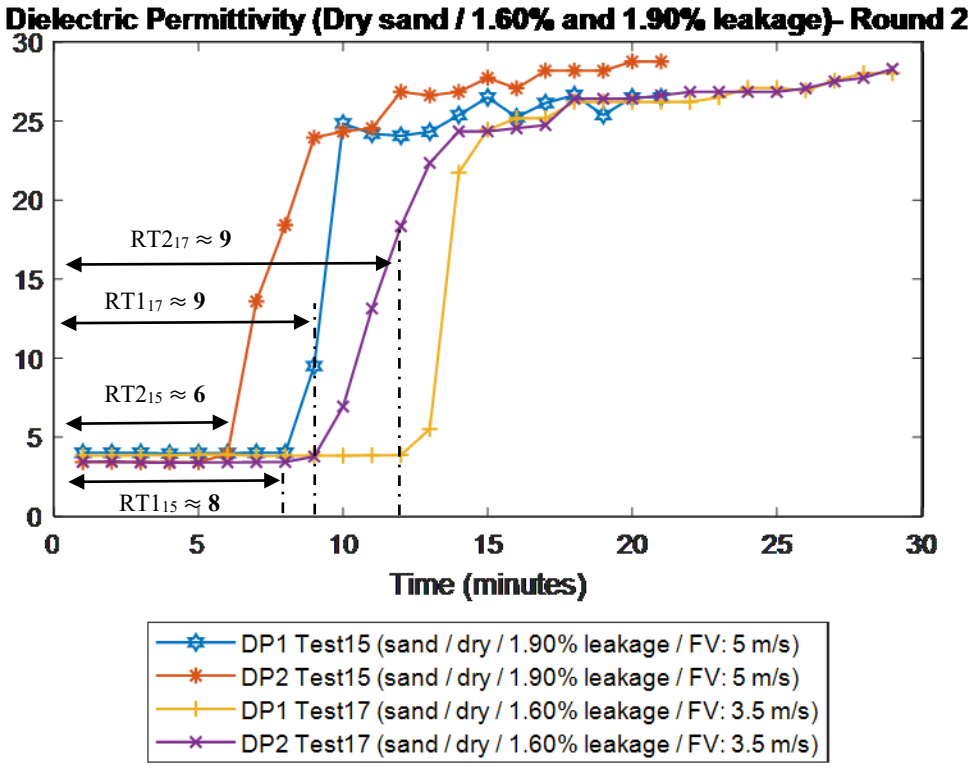

5.10 (c): Dielectric permittivity of dry sand (Leakage of 1.60% and 1.90%)

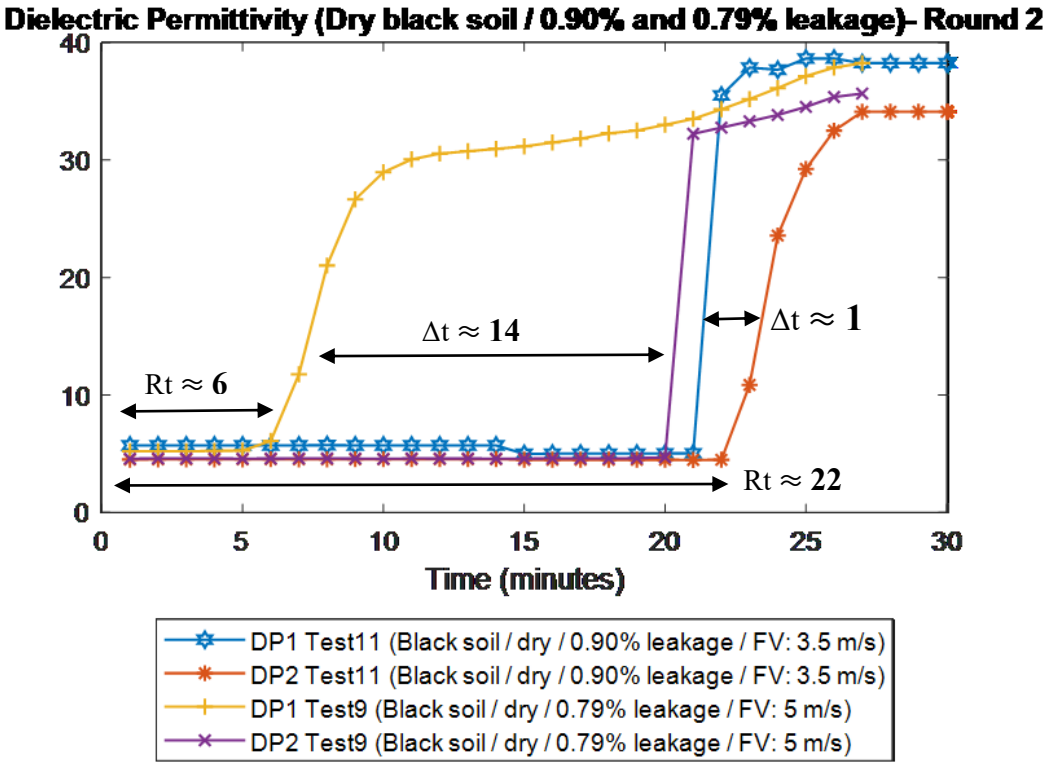

5.11 (a): Dielectric permittivity of dry black soil (Leak of 0.90% and 0.79%)

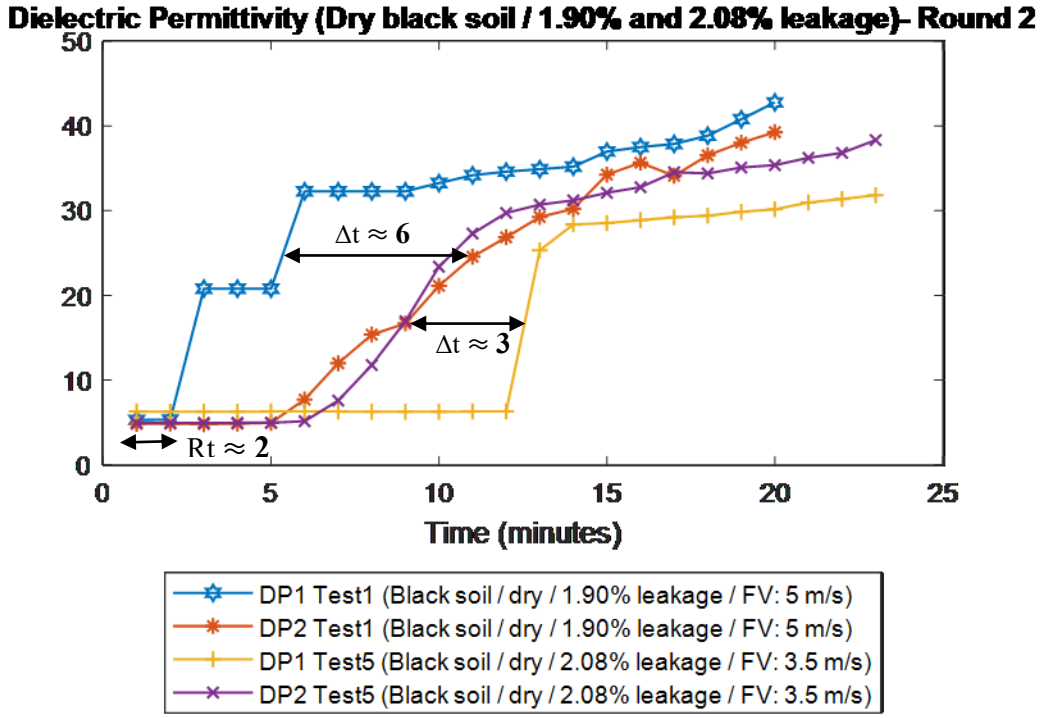

5.11 (b): Dielectric permittivity of dry black soil (Leak of 1.90% and 2.08%)

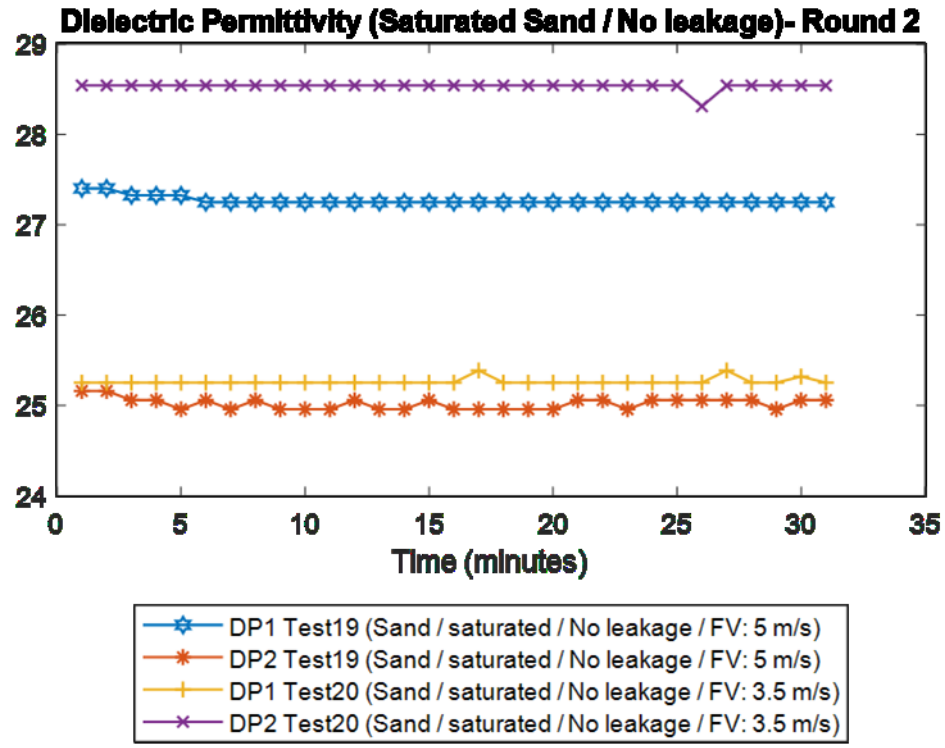

5.12 (a): Dielectric permittivity of saturated sand (No leak)

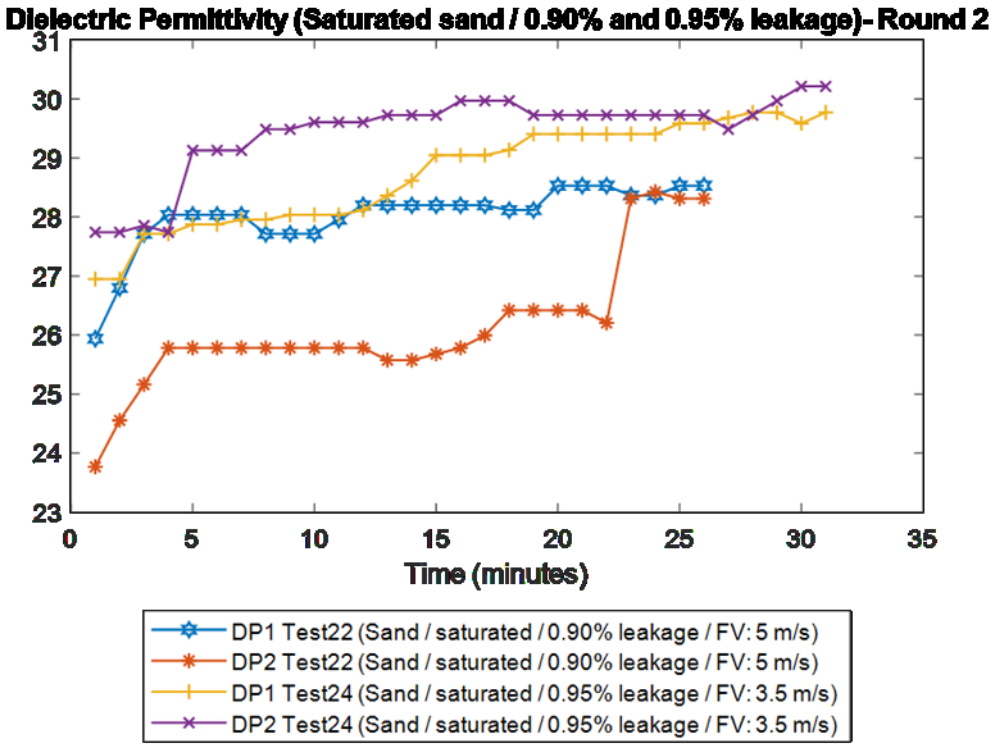

5.12 (b): Dielectric permittivity of saturated sand (Leakage 0.90% and 0.95%)

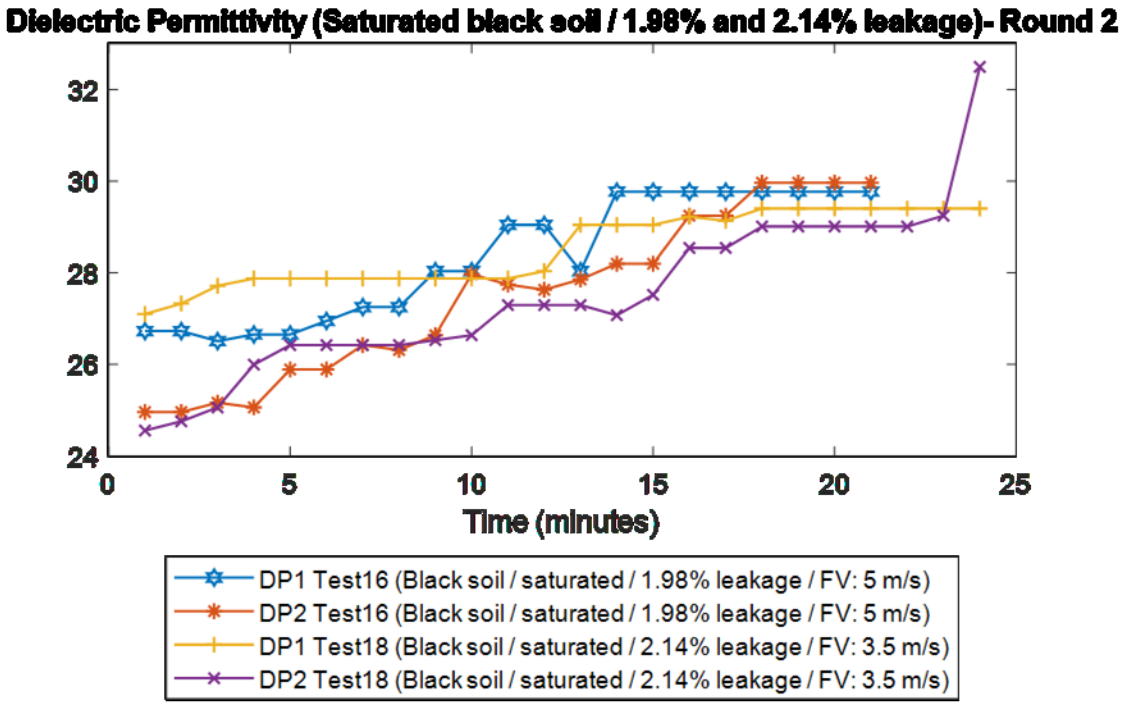

5.12 (c): Dielectric permittivity of saturated sand (Leakage of 1.98% and 2.14%)

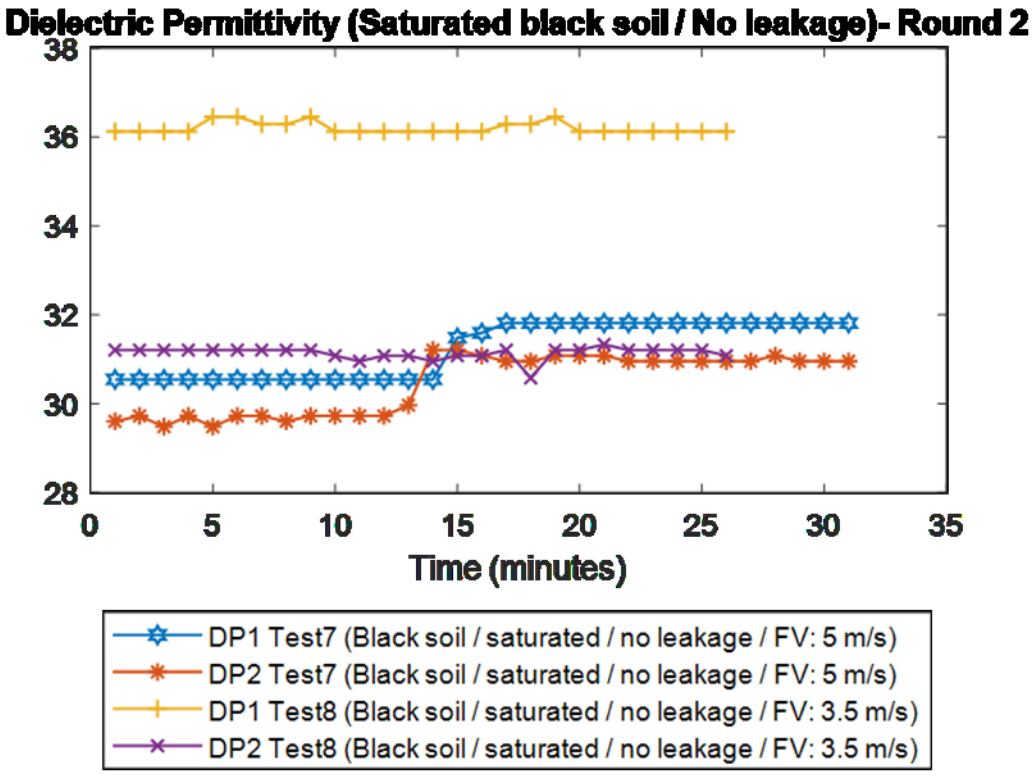

5.13 (a): Dielectric permittivity of saturated black soil (No leak)

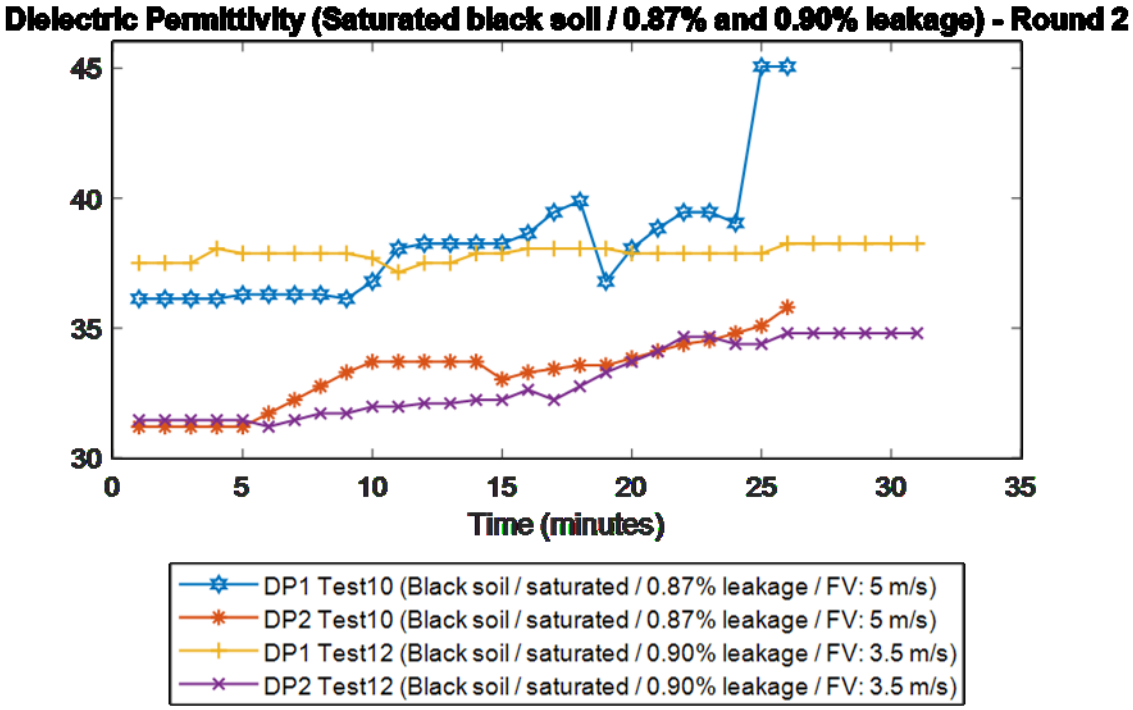

5.13 (b): Dielectric permittivity of saturated black soil (Leakage of 0.87% and 0.90%)

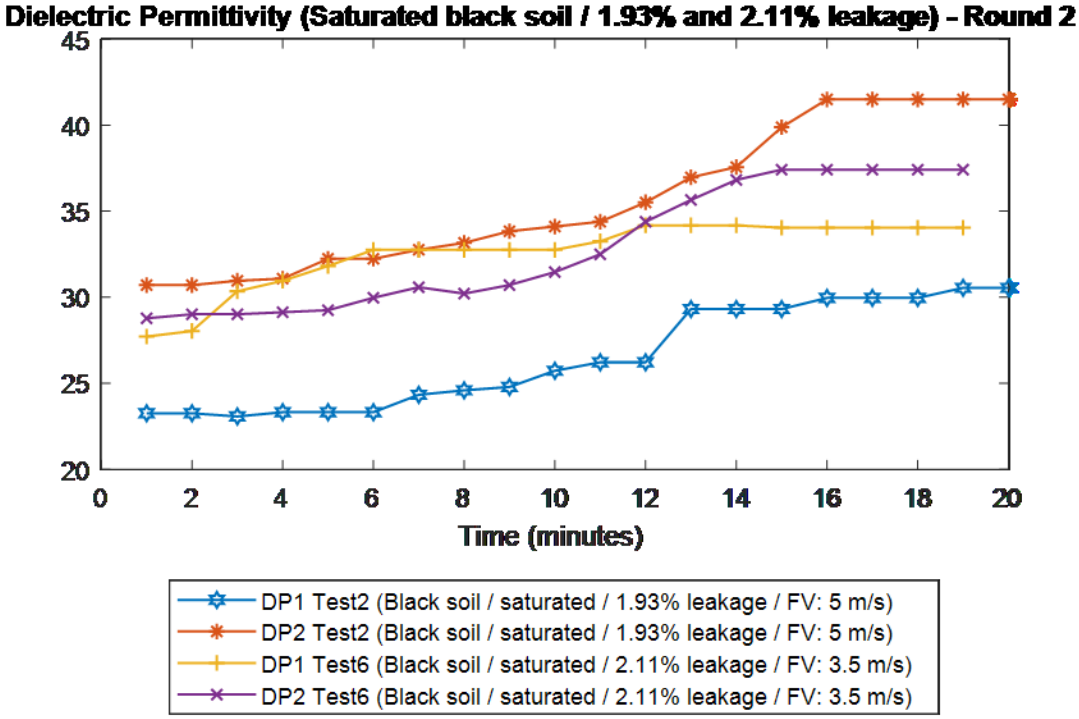

5.13 (c): Dielectric permittivity of saturated black soil (3-mm pinhole)

Soil permeability determines soils' ability of liquids draining. For instance, sand particles and their pore spaces are more significant, allowing water to drain quickly and air to enter the sand as opposed to clay whose particles are smaller. Clay soils drain poorly liquids and hold on to them in their pore spaces for much longer. Mohamed and Paleologos contend (2018) that sand's permeability is up to 100 times higher than silts and clays. The slope of dielectric permittivity –DP- in figures 5.10(b) and 5.10(c) validate this for sand because of the straight relation between leak rates and curves slopes; the average values of slopes are 2.62 and 10 for leaks of 0.97% and 2.2%. Moreover, response time of DP probes are coherent with Mohamed and Paleologos (2018) since probe #2 reacts faster than probe #1 due (a) probe #2 is longer than probe #1 and water builds up from bottom to top then it reaches probe #2 sooner, and (b) leak points towards probe #2. Average response time for both the 0.97% and 2.2% leaks are 10.25 and 8 minutes respectively.

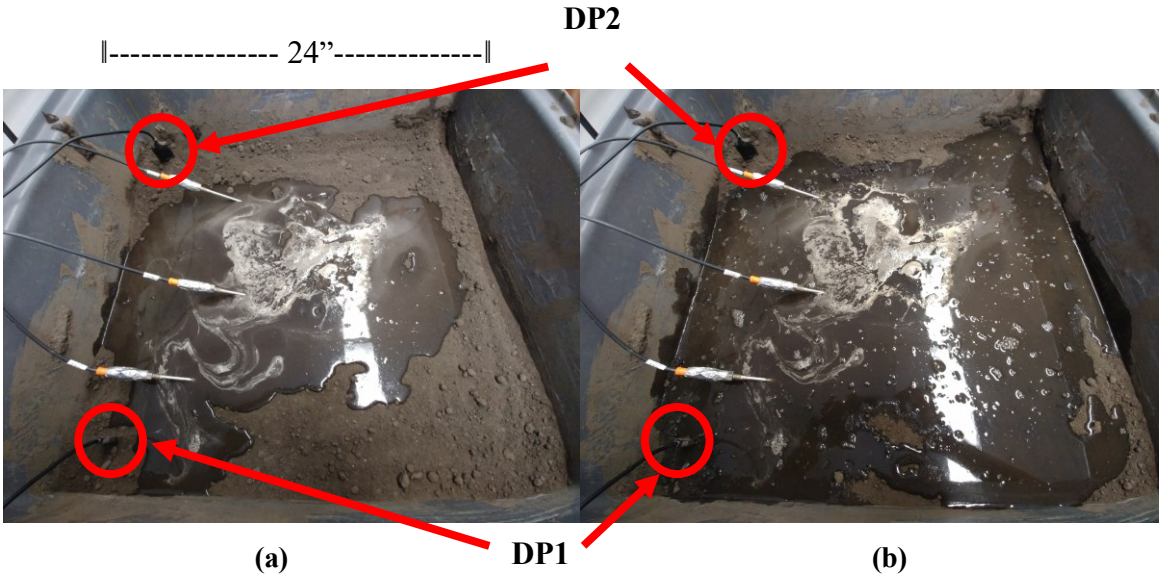

Figure 5.14: Water Soil for the experiment #9 (second round) at (a) 2:39 pm and (b) 2:55 pm

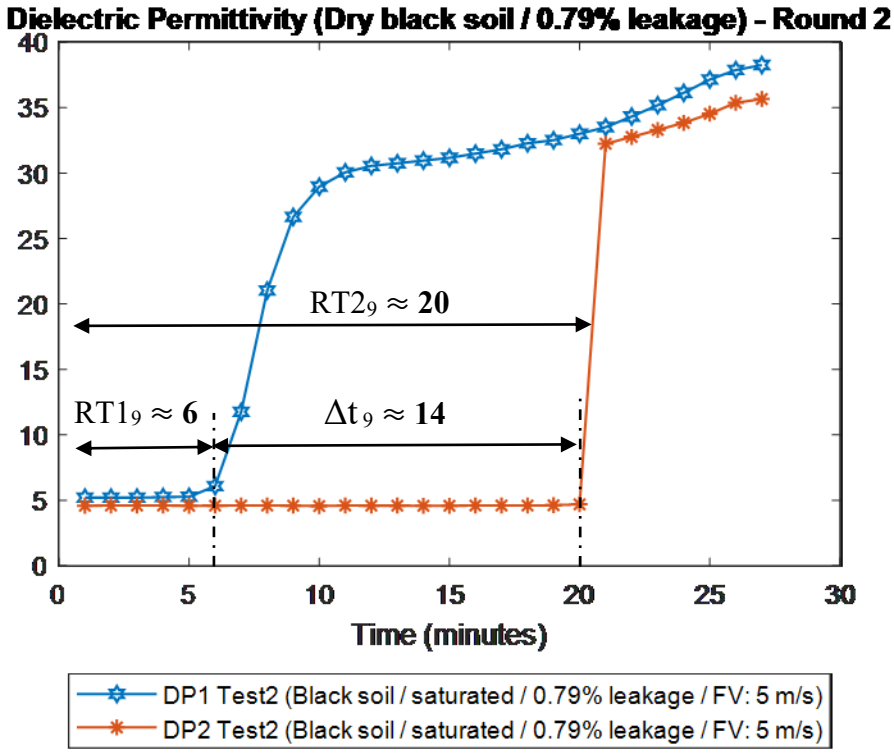

Figure 5.15: DP of Water Soil for experiment #9 (second round)

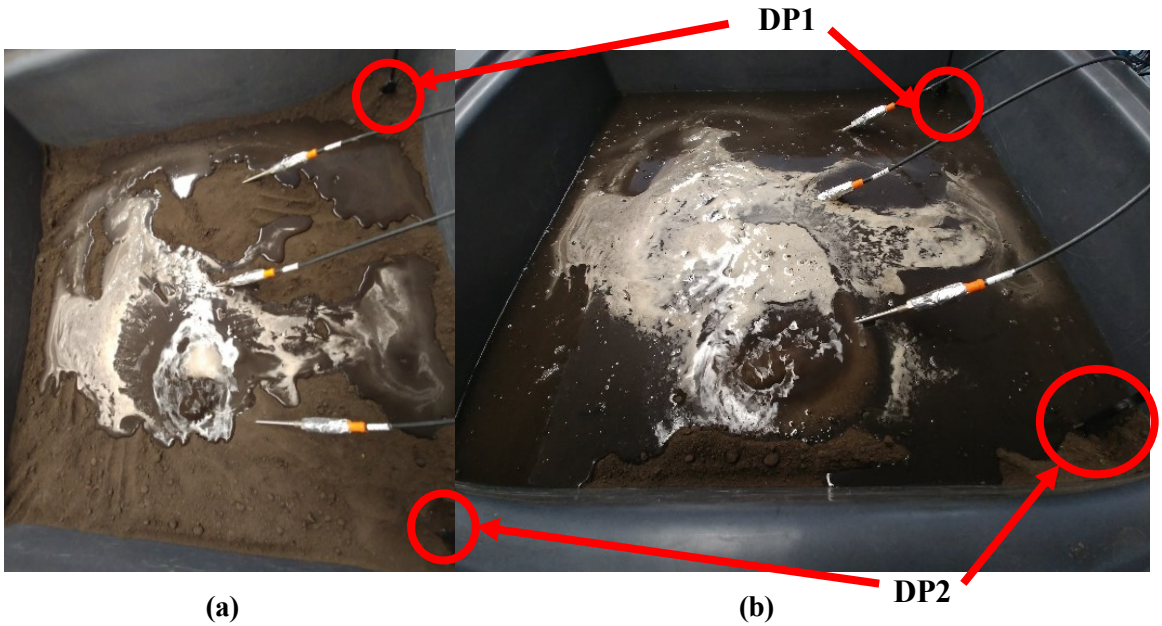

(a) **(b)**

Figure 5.16: Water Soil for experiment #9 (first round) at (a) 2:50 pm and (b) 2:55 pm

Figure 5.17: Water Soil for experiment #16 (first round) at 3:05 pm

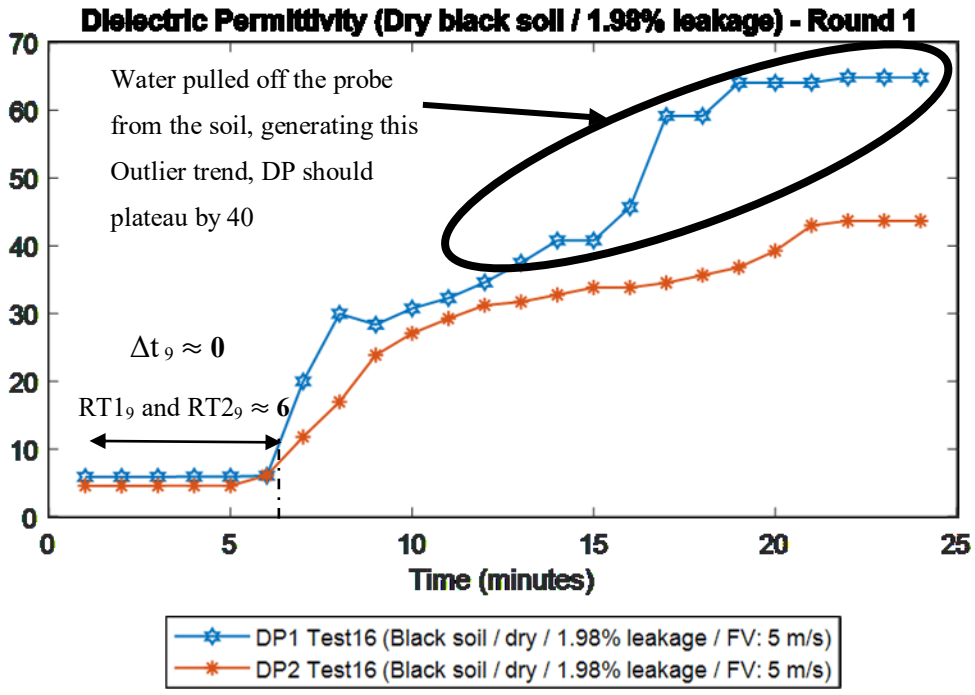

Figure 5.18: DP of Water Soil for experiment #16 (first round)

Dielectric permittivity plotted in figures 5.11(a), 5.11(b) and 5.15 show different slopes for black soils, dielectric permittivity increases slowly for a 2.08% leak-rate while spikes at 0.79 %. Response time in three out four readings is 6 minutes, and 20 minutes the fourth one, although they manifest similarly, their relation is nonlinear because black soil is an anisotropic porous media. It drains liquids poorly because of its low permeability, so under leak-conditions, the liquids built up at the ground surface, then they slowly infiltrate the ground. As a result, the probes are very sensitive to a variety of factors: soil compaction, ground surface slope, drag or shear forces at the interface of water-solid surfaces. The driving force resulting from the effective potential gradient was homogenous amongst experiments. The Meter Group (2019) (moisture sensor manufacturer) acknowledges in the EC-5 manual,

> Soil adjacent to the sensor surface has the strongest influence on the sensor reading and that the sensor measures the volumetric water content of the soil. Therefore any air gaps or excessive soil compaction around the sensor and in between the sensor prongs can profoundly influence the readings.

Black soil employed is susceptible to compaction due to the factors mentioned above. Figure 5.17 depicts another example of anisotropy flow direction in black soil as well as the air bubbles highlighted in figures 5.17 and 5.20; bubbles appear in black soil because its unequal conductivities in the three directions, air escapes the soil only at the highlighted points. Conversely, bubbles do not materialize in sand experiments because water infiltrates equally across all surface.

Figure 5.19: Experiment #5 (first round), 14 minutes after starting

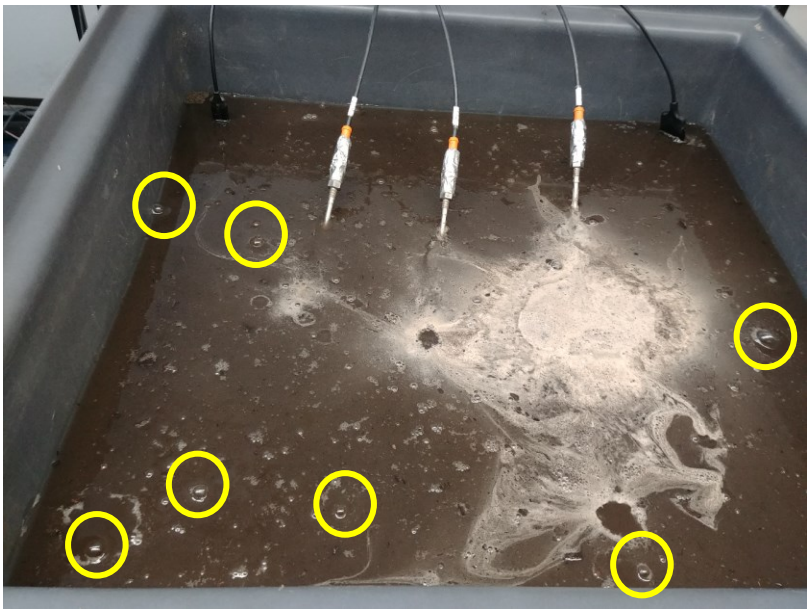

Figure 5.20: Air bubbles 21 minutes after starting experiment #18 (first round)

5.2.2 FLIR images results

FLIR images - 5.21(a) to 5.21(d)- also demonstrates that the liquid's flow is homogeneous in isotropic soils (sand) and heterogeneous in anisotropic porous media (black soil) as shown in figures 5.21(a) to 5.21(d) where liquids spread out irregularly onto the ground surface.

‖----- 12"------‖ ‖---------- ≈12"----------‖

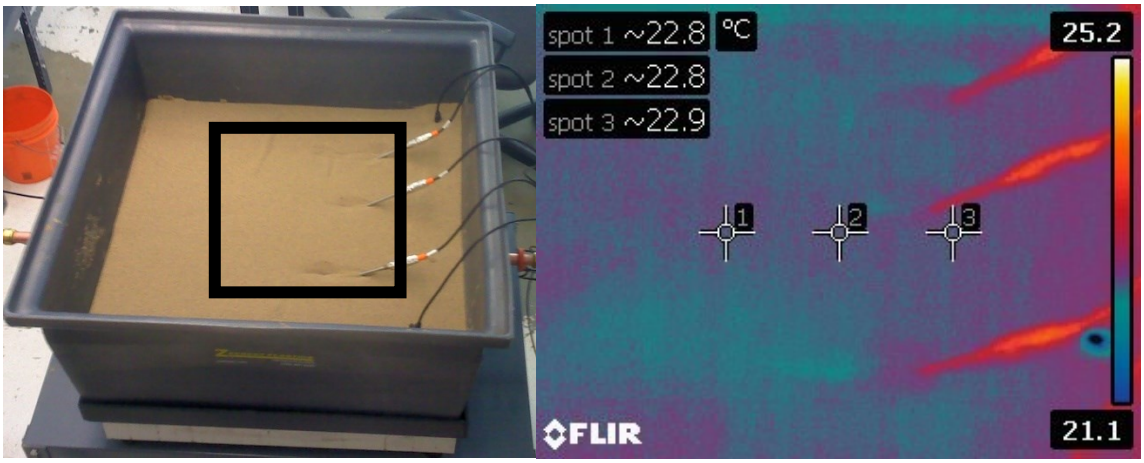

Figure 5.21 (a): Experiment #21 (2nd Round) before starting leaking (12:36 pm)

‖-- ≈6”--‖ ‖---------- ≈6”----------‖

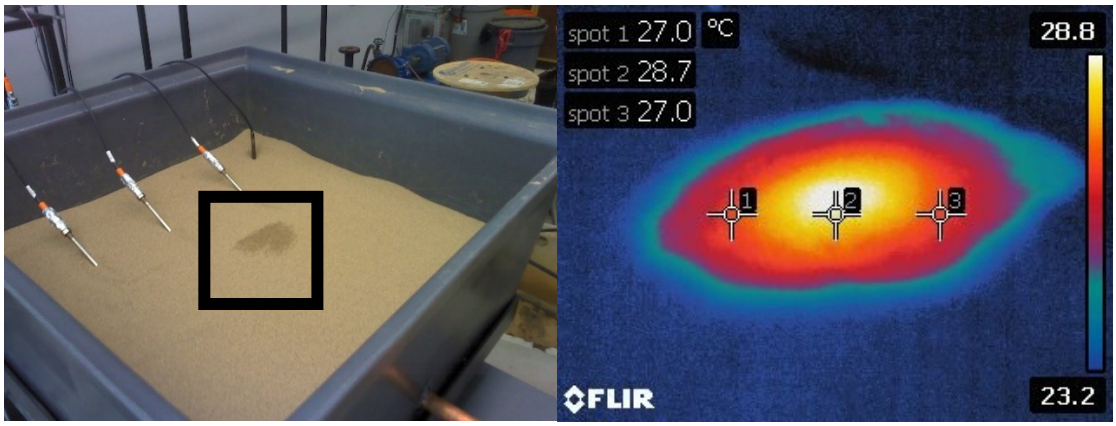

Figure 5.21 (b): Experiment #23 (2nd Round) after 1 minute of leaking (12:44 pm)

‖------ ≈16”---------‖ ‖---------- ≈16”----------‖

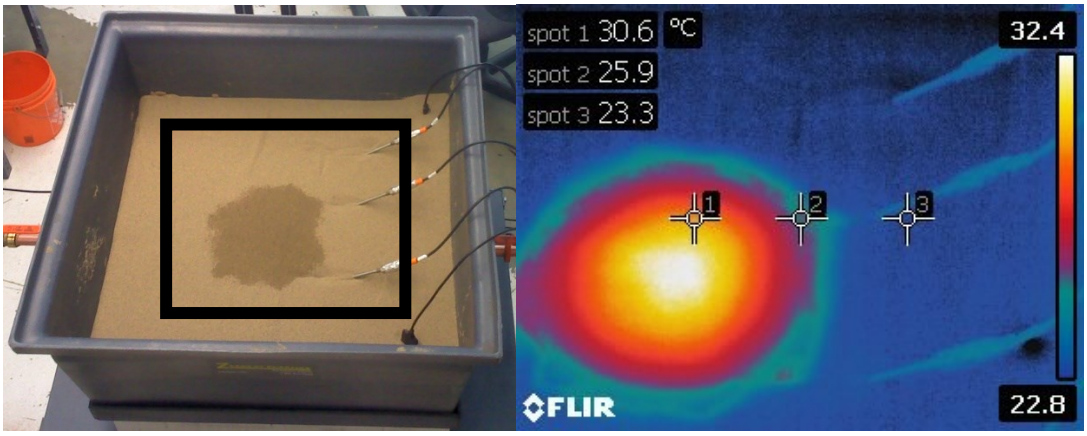

Figure 5.21 (c): Experiment #23 (2nd Round) after 5 minutes of leaking (12:48 pm)

‖---- ≈12”-----‖ ‖---------- ≈12”----------‖

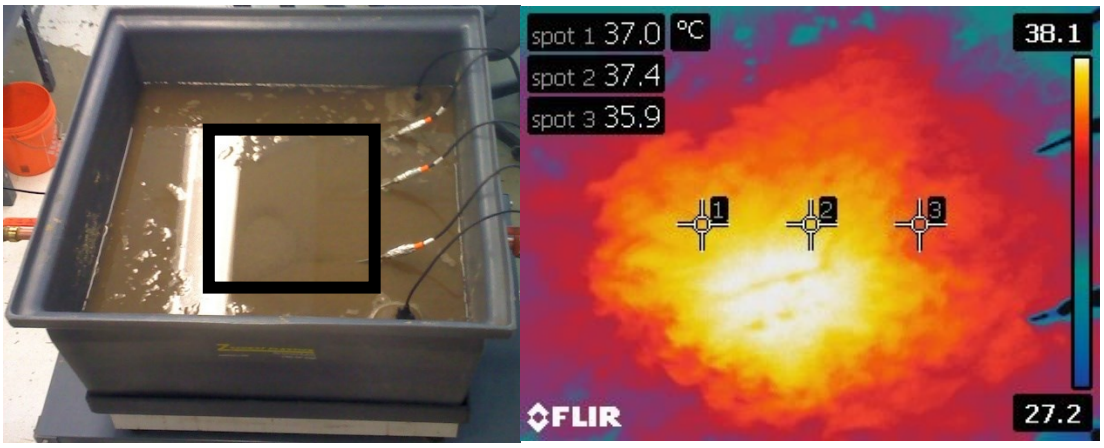

Figure 5.21 (d): Experiment #23 (2nd Round) when ending after 19 minutes (1:02 pm)

‖------ ≈12”------‖ ‖---------- ≈12”----------‖

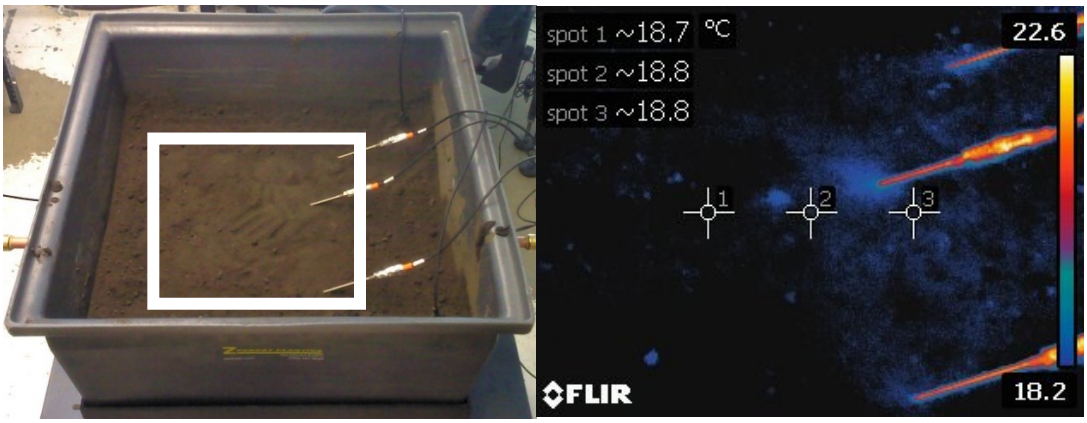

5.22 (a): Experiment #9 (2nd round) before starting leaking (2:28 pm)

‖------ ≈12”------‖ ‖---------- ≈12”----------‖

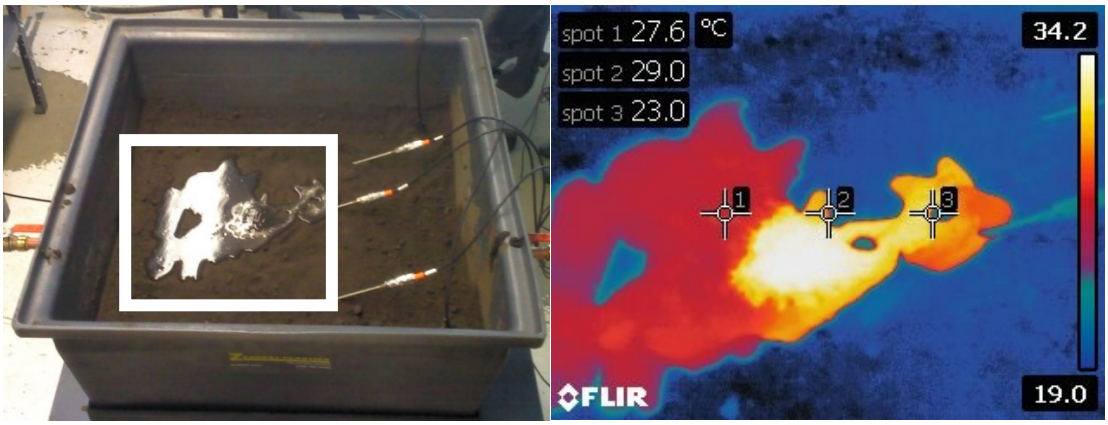

5.22 (b): Experiment #9 (2nd Round) when starting leaking (2:36 pm)

‖------ ≈12”------‖ ‖---------- ≈12”----------‖

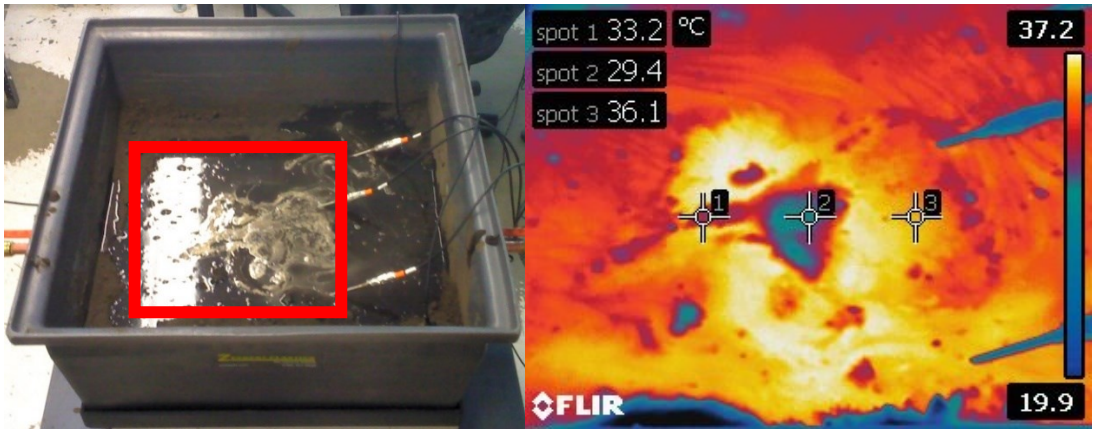

5.22 (c): Experiment #9 (2nd Round) after 5 min of leaking (2:41 pm)

‖------ ≈12”------‖ ‖------------------ ≈12”------------------------‖

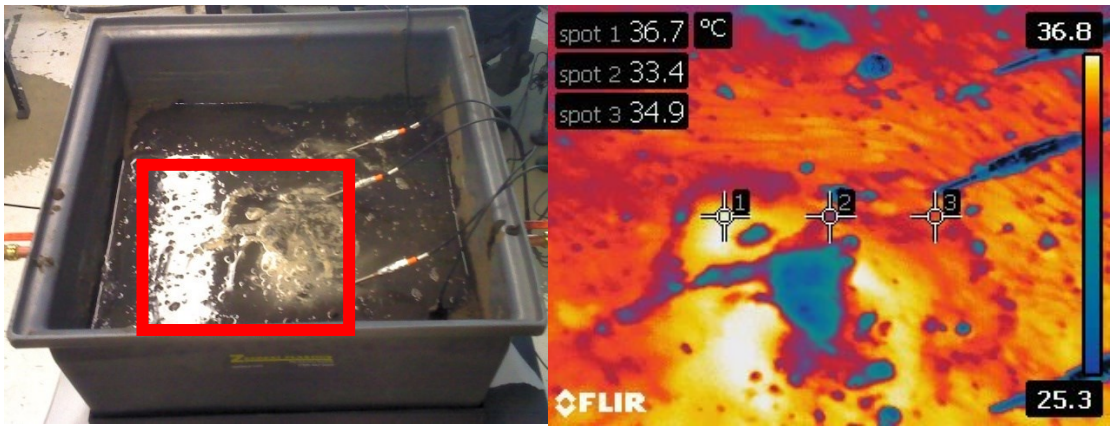

5.22 (d): Experiment #9 (2nd Round) after 18 min of leaking (2:54 pm)

‖-------- ≈13”--------‖ ‖---------------------- ≈13”-------------------------‖

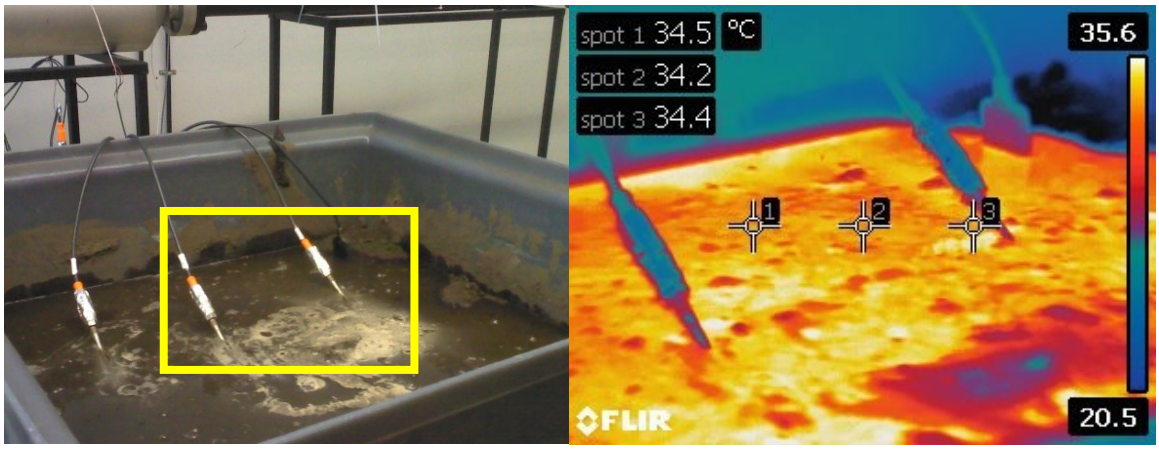

5.22 (e): Experiment #9 (2nd Round) when ending leaking (3:02 pm)

Thermal energy detection technology is very instrumental in detecting leaks regardless the soil medium because thermal imaging devices do not need to be in touch with liquids to sense temperature changes, so this technology is less sensitive to soil permeability, soil compaction and ground surface slope as dielectric permittivity and thermocouples probes are. Response time is almost instantaneous, the E50 FLIR camera detects temperature changes for both sand and black soil within one minute of starting leaking in experiments 1, 5, 9, and 11, whereas the dielectric permittivity technique responds between 2 and 22 minutes in same experiments according to figures 5.11(a) and 5.11(b). Moreover, DP response time increases if the probe is deployed farther from the leak source.

‖---------- ≈16”----------‖

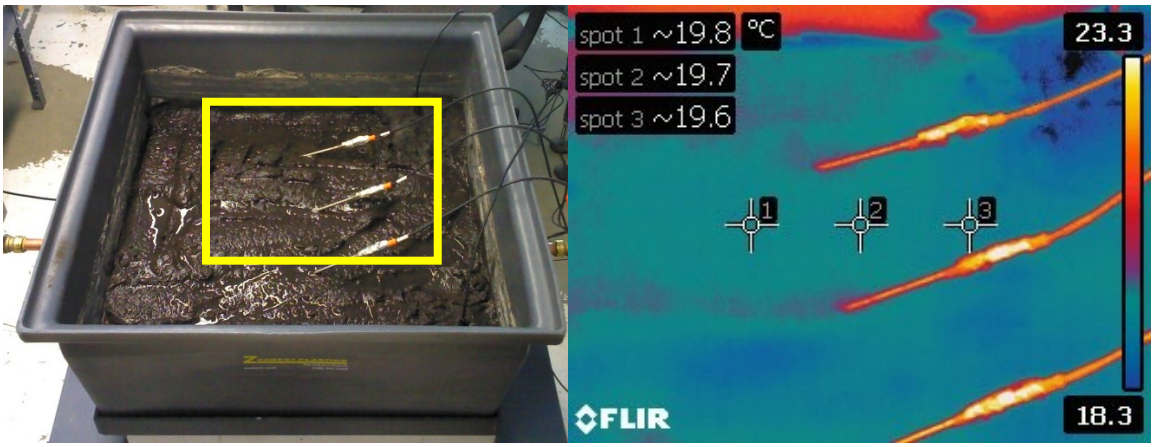

Figure 5.23 (a): Experiment #2 (2nd Round) before starting leak (3:24 pm)

‖---------- ≈12”----------‖

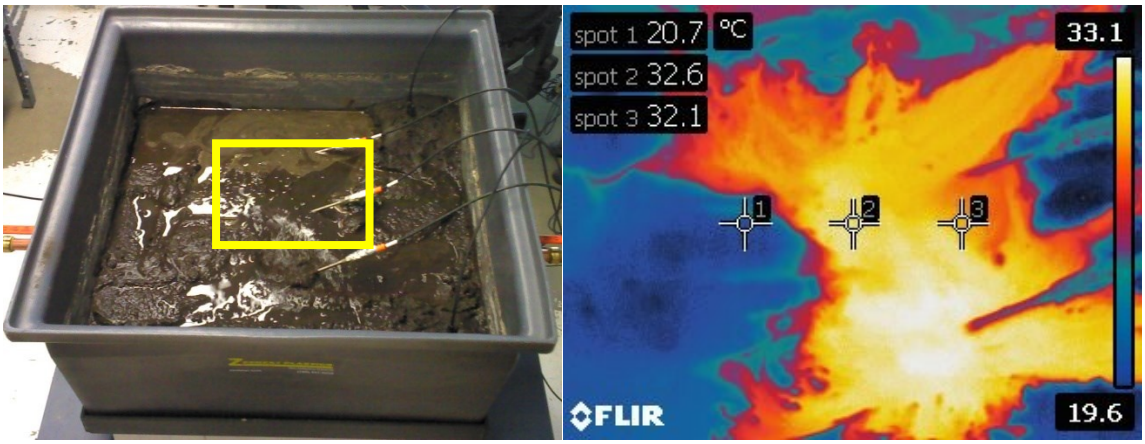

5.23 (b): Experiment #2 (2nd Round) within 1 minute of starting leaking (3:31 pm)

‖---------- ≈12”----------‖

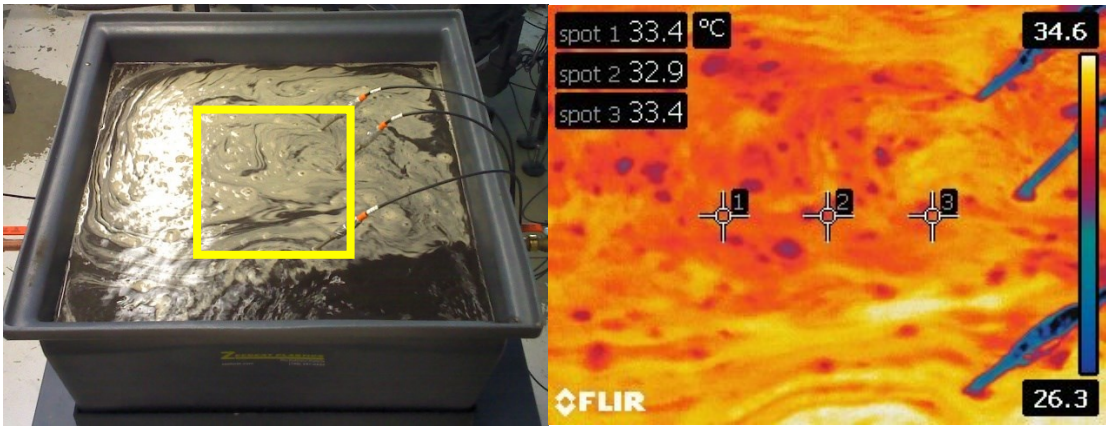

5.23 (c): Experiment #2 (2nd Round) when ending leaking (3:45 pm)

‖---------- ≈12”----------‖

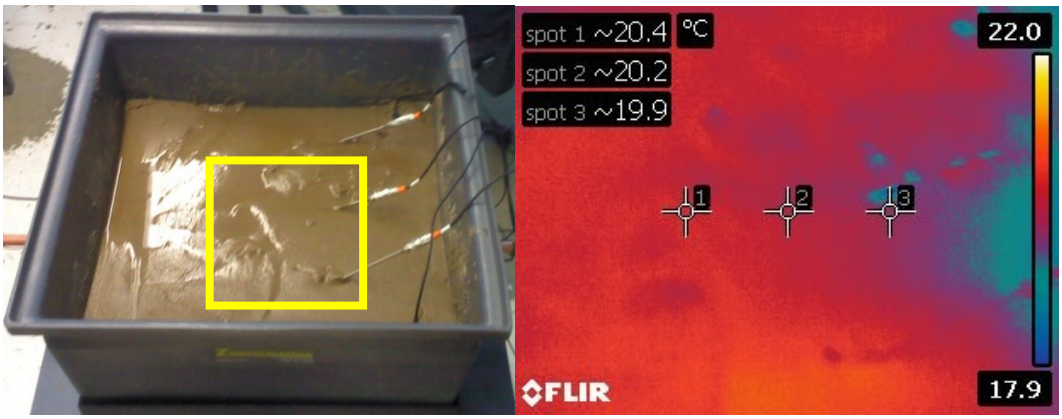

Figure 5.24 (a): Experiment #16 (2nd Round) when starting leak (4:13 pm)

‖---------- ≈14”----------‖

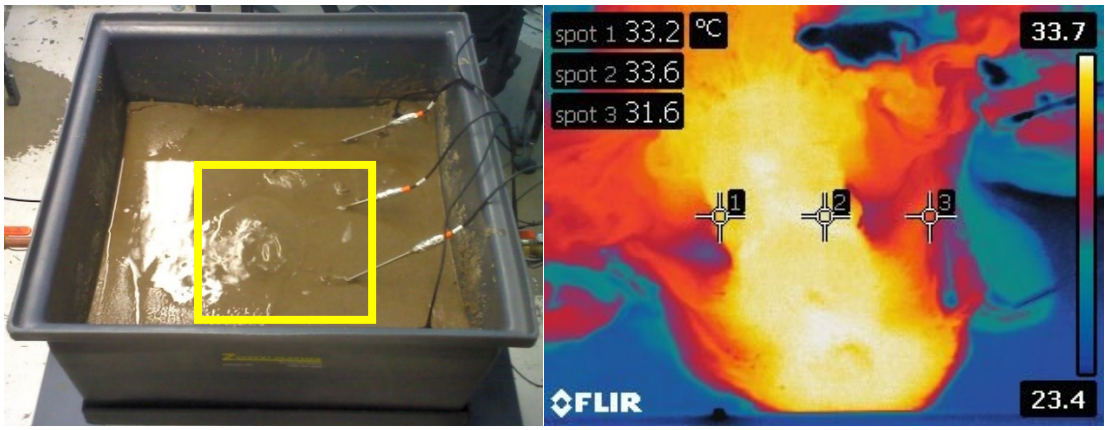

5.24 (b): Experiment #16 (2nd Round) within 2 minutes of starting leaking (4:15 pm)

‖---------- ≈14”----------‖

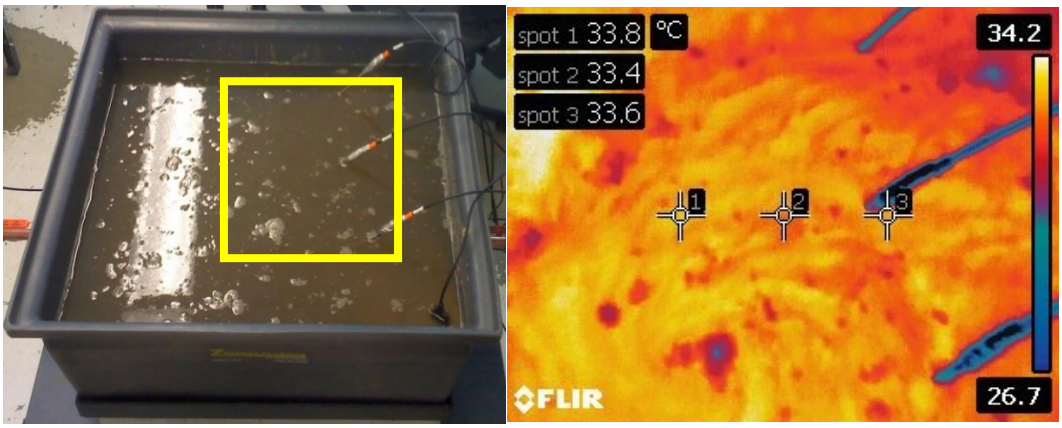

5.24 (c): Experiment #16 (2nd Round) after 14 minutes of leaking (4:29 pm)

This technique detects leaks effectively under both dry and saturated soil. Figures 5.23(a) and 5.24(b) exhibits response time within 2 minutes in both cases. The radiation emitted by an object increases with temperature according to the black body radiation law, so the E50 produce images of radiation detected as well as variations in temperature (sensitivity 0.05 °C). This technique senses changes in temperature because the simulant liquids –water- emits more thermal energy than soil's, the "heat signature" between them are different, materializing their differences when sitting next to one another. Thermal imaging can turn inefficient if liquids temperature equals soil's, this condition happens due to free convection; this depends on the heat transfer coefficient of the medium and the difference between the fluid and surface temperature. Further research is recommended to assess the cooling time against external factors such as the type of fluids, meteorological elements, heat capacity, and thermal conductivity of the soil.

5.2.3 Thermocouple probes results

Thermocouples probes consist of two different types of metals, joined together at one end. When the junction experiences a change in temperature, a voltage is created that is correlated back to the temperature by the CompactDAQ 9178 chassis. Change of temperature happens if the released substances come into contact with the probe. Figure 5.25 shows the thermocouples deployment as well as both the leak direction and leak position. TT1 -Temperature Transmitter- and TT3 are 10" apart and mirrored themselves using the pipe as their mirror axis, TT2 adjoins the leak source. Leak points towards TT1. The variable 'TT Pipe' is the fluid temperature, which is 38 °C, and it ranges between 37 and 40 °C throughout experiments. Figures from 5.25 to 5.37 display the temperature changes due to liquids release as well as their water flow patterns in different experimental conditions.

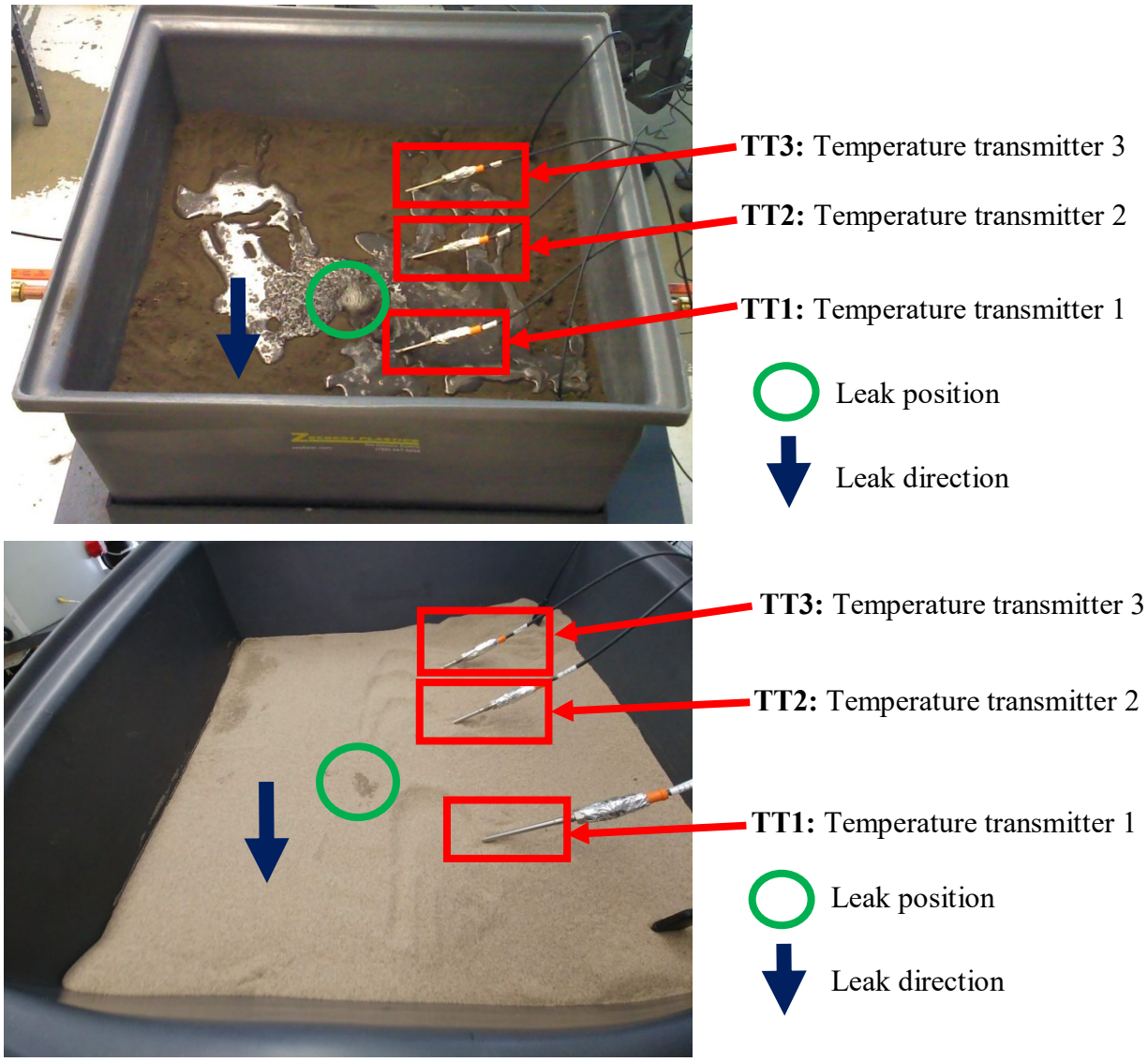

Figure 5.25: Deployment of temperature transmitters

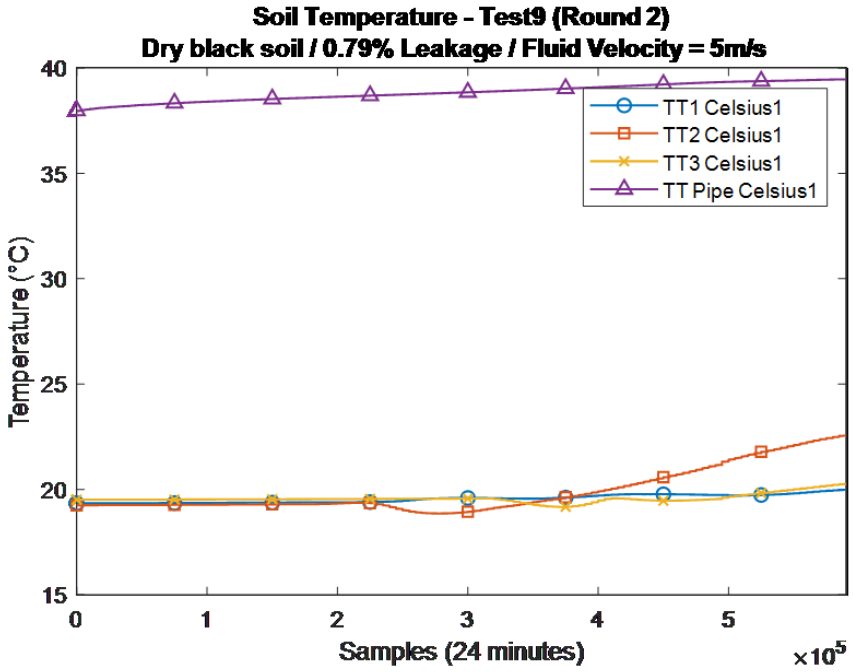

Figure 5.26: Temperature of dry black soil / 0.79% leak / Fluid Velocity: 5 m/s (Test #9)

(a) Minute 1 **(b) Minute 3**

(a) Minute 9 **(b) Minute 21**

Figure 5.27: A sequence of liquids flow in Test #9 (Round 2)

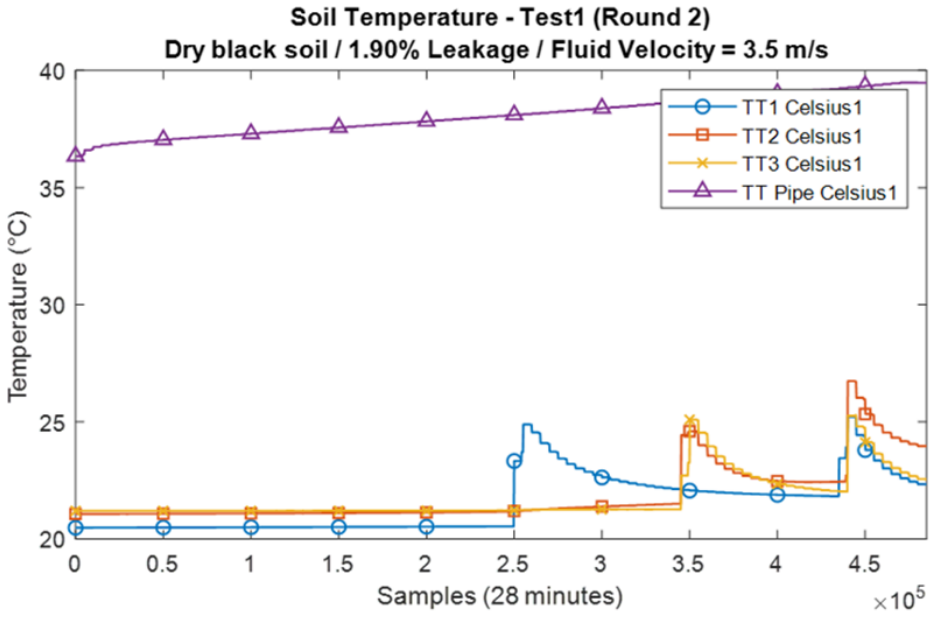

Figure 5.28: Temperature of dry black soil / 1.90% leak / Fluid Velocity: 5 m/s (Test #1)

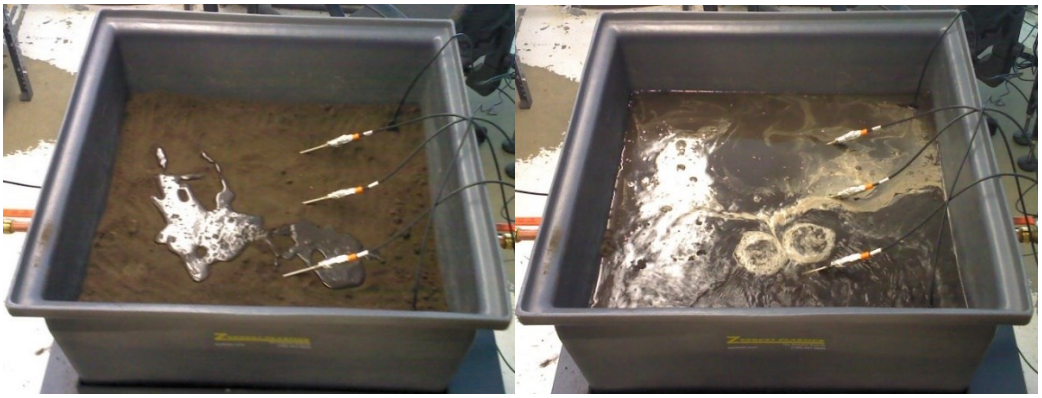

(a) Minute 0 **(b) Minute 4**

(a) Minute 9 **(b) Minute 18**

Figure 5.29: A sequence of liquids flow in Test #1 (Round 2)

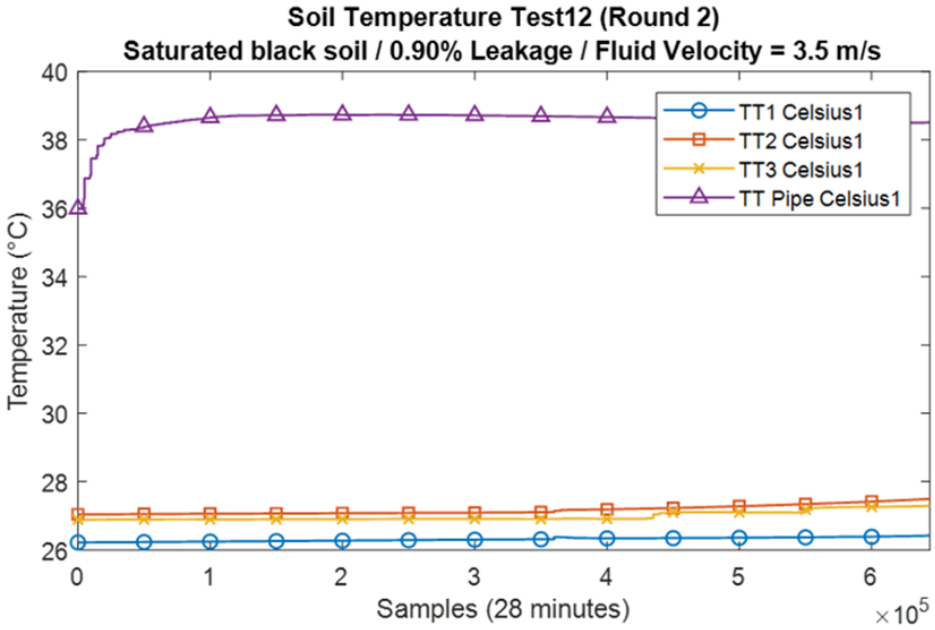

Figure 5.30: Temp. of saturated black soil / 0.90% leak / Fluid Velocity: 3.5 m/s (Test #12)

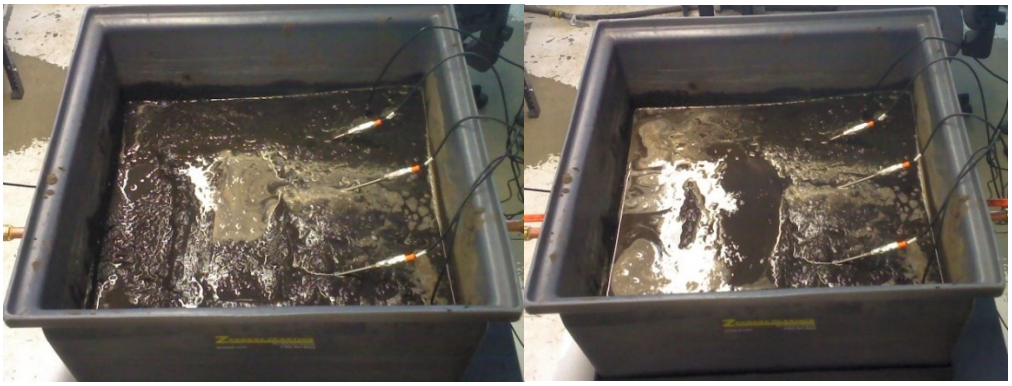

(a) Minute 0 **(b) Minute 3**

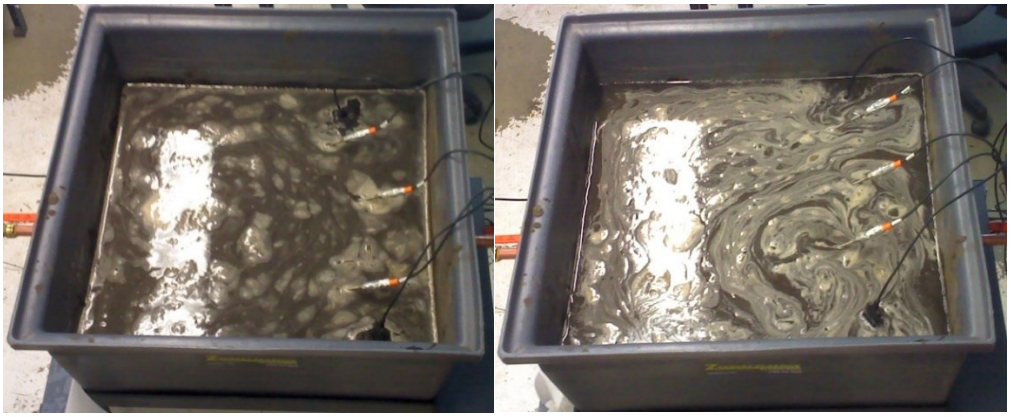

(a) Minute 10 **(b) Minute 28**

Figure 5.31: A sequence of liquids flow in Test #12 (Round 2)

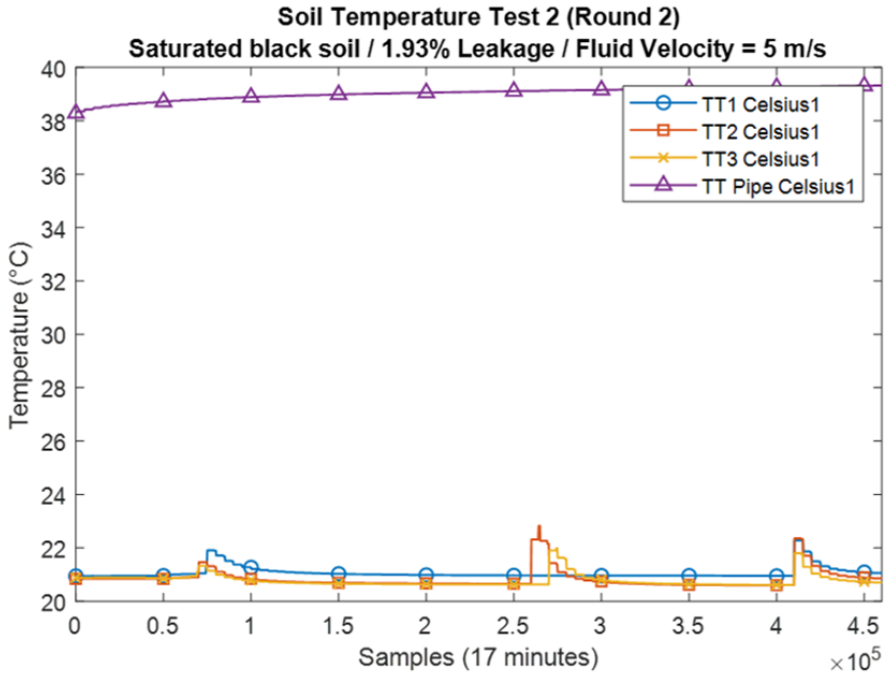

Figure 5.32: Temperature of saturated black soil / 1.93% leak / Fluid Velocity: 5 m/s (Test #2)

(a) Minute 0 **(b) Minute 2**

(a) Minute 10 **(b) Minute 15**

Figure 5.33: A sequence of liquids flow in Test #2 (Round 2)

Permeability of soils determines its ability to suction liquids. In other words, soil's permeability influences the efficacy and response time of thermocouples. According to the Food and Agriculture Organization of the United Nations (2012), sand and loam's permeability coefficients are around 5 and 0.8 cm/hour. Figures 5.26 to 5.33 display the temperature changes due to liquids release in black soil. Thermocouples are more inefficient than both DP probes and thermal imaging to detect changes of temperature in low permeable soils because liquids take longer to reach the probes. Liquids flow is multifactorial and depends not only on soil compaction and ground surface slope, as dielectric permittivity probes do, but external and internal elements such meteorological elements, vegetation, volumetric heat capacity, latent heat and thermal conductivity of the soil.

The concept is that thermocouples detect changes in temperature as soon as leaked liquids come in touch with them. Results reveal that thermocouples perform poorly in low permeable mediums, according to figure 5.26 TT1 and TT3 measure a negligible temperature change in 24 minutes –Test 9 period- while ΔT detected by TT2 is 3 °C; while ΔT in thermal imaging is 10 °C within one minute. Even though liquids touch the probes ΔT is minimal, as demonstrated in figure 5.27, water reaches all the probes by the third minute from start to leak. Liquids have to touch a significant portion of the thermocouple to yield more accurate results. Figure 5.28 shows similar results regardless of the higher leak rate, although water touches all three probes within 2 minutes, their readings remain stable up to minutes 15 and 20. To maintain the integrity of the SCADA system the probes are lined up with the increasing water level; as a result, temperature steps 5 °C because a significant portion of the probe is now in contact with the simulant fluid. In real-life conditions, the temperature should keep stable until water permeates the soil as probes are buried and fixated into the soil. Temperature decreases exponentially after increasing because of convection; this is consistent in all experiments using black soil. Further research is recommended to assess the heat convection from leaked liquids to the environment to estimate how long the temperature of the leaked liquids lasts warmer than the environment's; Therefore, a better understanding of thermal techniques' capabilities for leak detection.

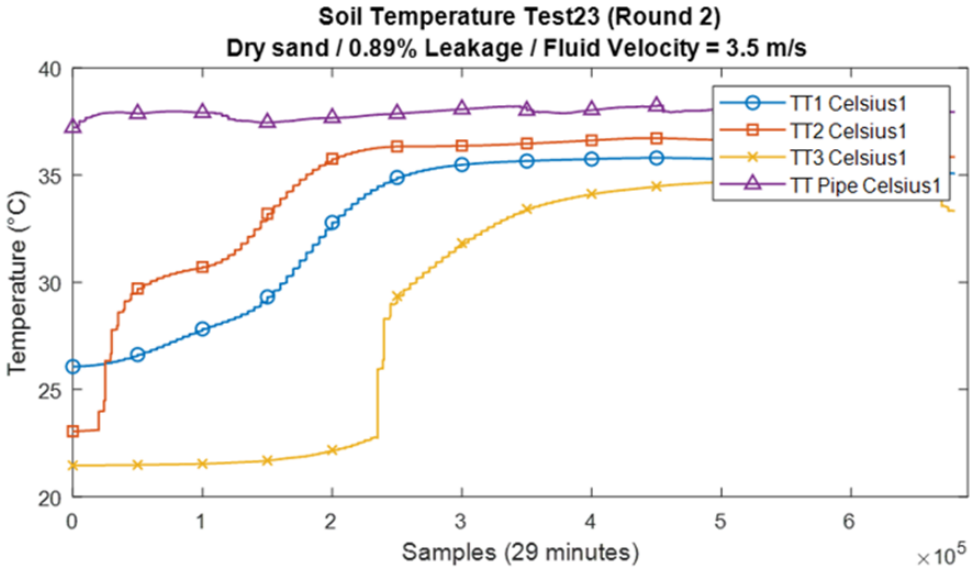

Figure 5.34: Temperature of dry sand / 0.89% leakage / Fluid Velocity: 3.5 m/s (Test #23)

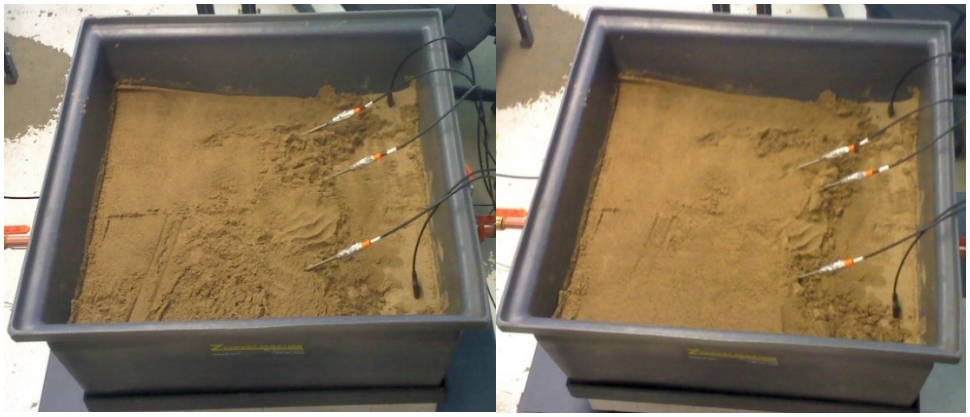

(a) Minute 0 **(b) Minute 8**

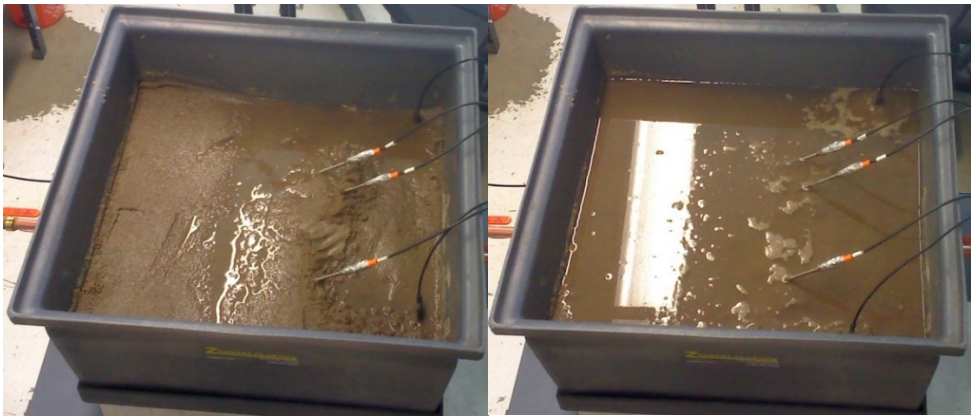

(a) Minute 20 **(b) Minute 29**

Figure 5.35: A sequence of liquids flow in Test #23 (Round 2)

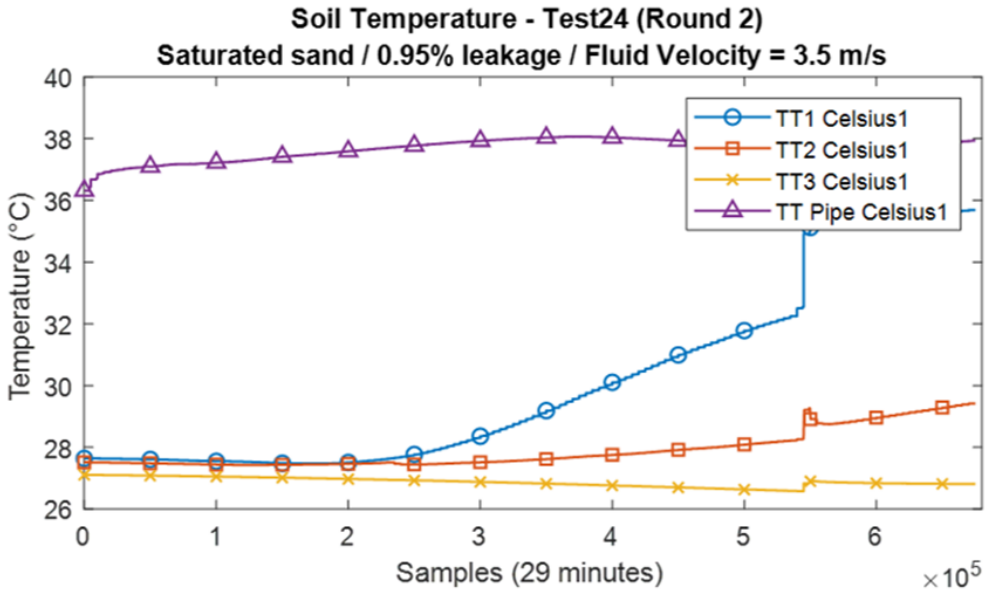

Figure 5.36: Temperature of saturated sand / 0.95% Leak / Fluid Velocity: 3.5 m/s (Test #24)

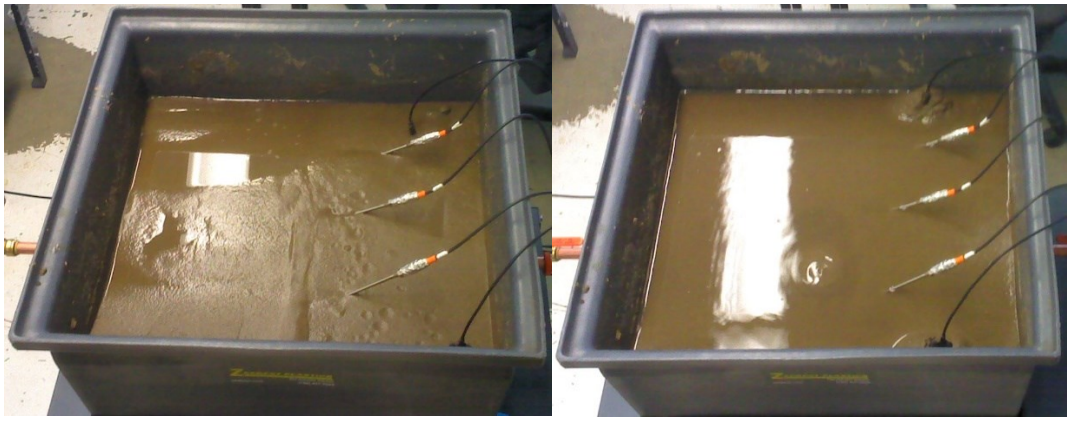

(a) Minute 0 **(b) Minute 8**

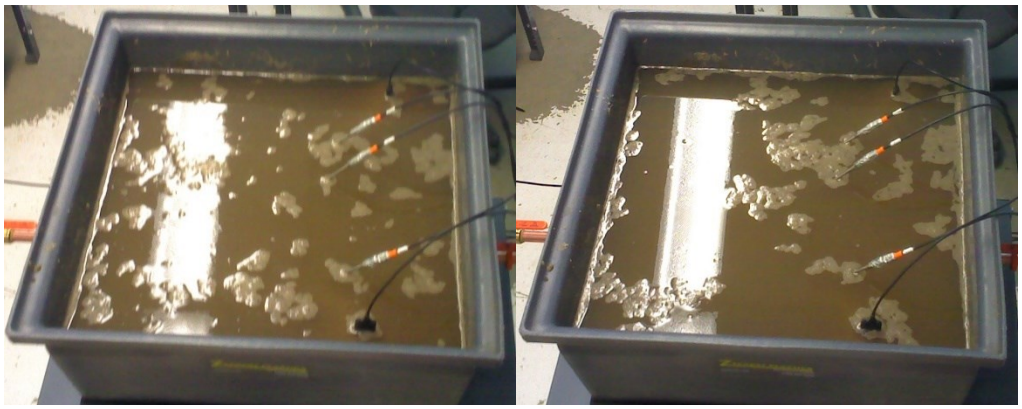

(a) Minute 22 **(b) Minute 30**

Figure 5.37: A sequence of liquids flow in Test #24 (Round 2)

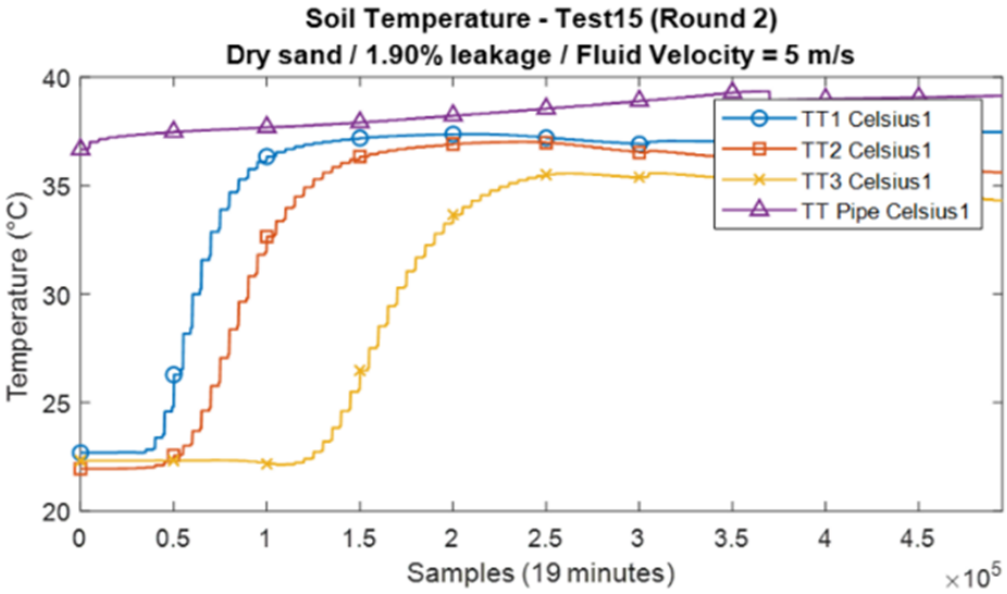

Figure 5.38: The temperature of dry sand under 1.90% leak (Experiment #15 – Round 2)

‖------ ≈16”------‖ ‖---------- ≈16”----------‖

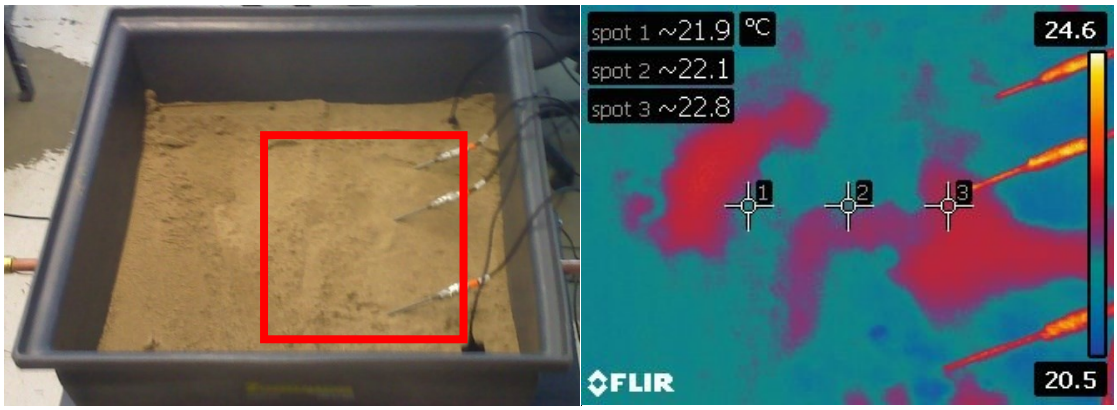

(a) Minute 0

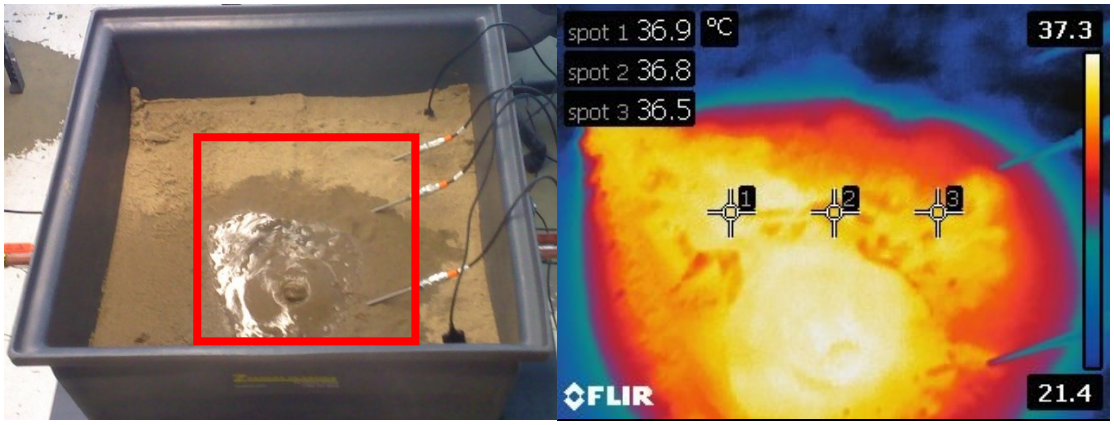

(b) Minute 4

‖------ ≈16”------‖ ‖---------- ≈16”----------‖

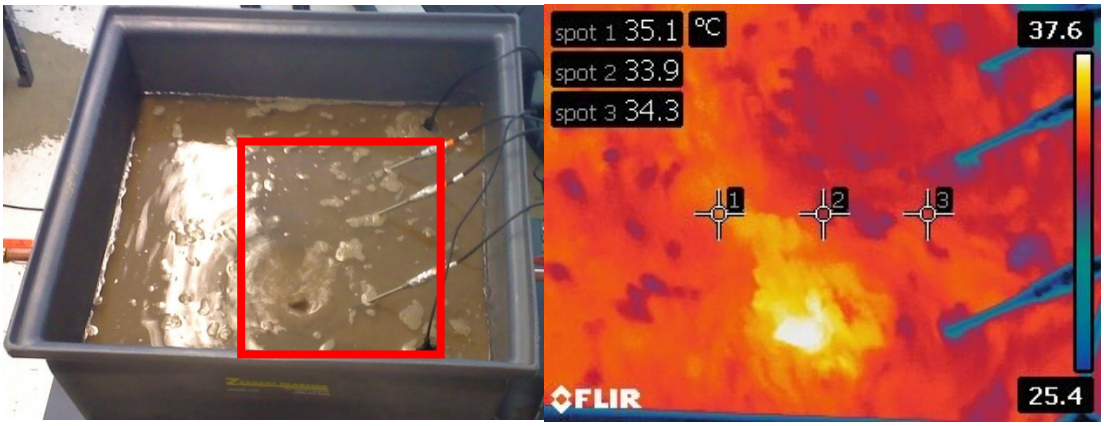

(c) Minute 10

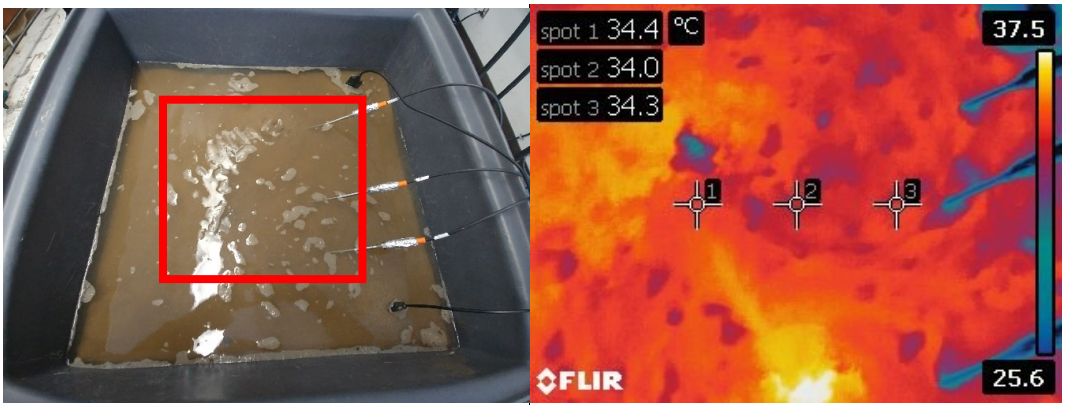

(d) Minute 14

Figure 5.39: Temperature of dry sand / 2.2% leak / Fluid Velocity: 5 m/s (Test #15)

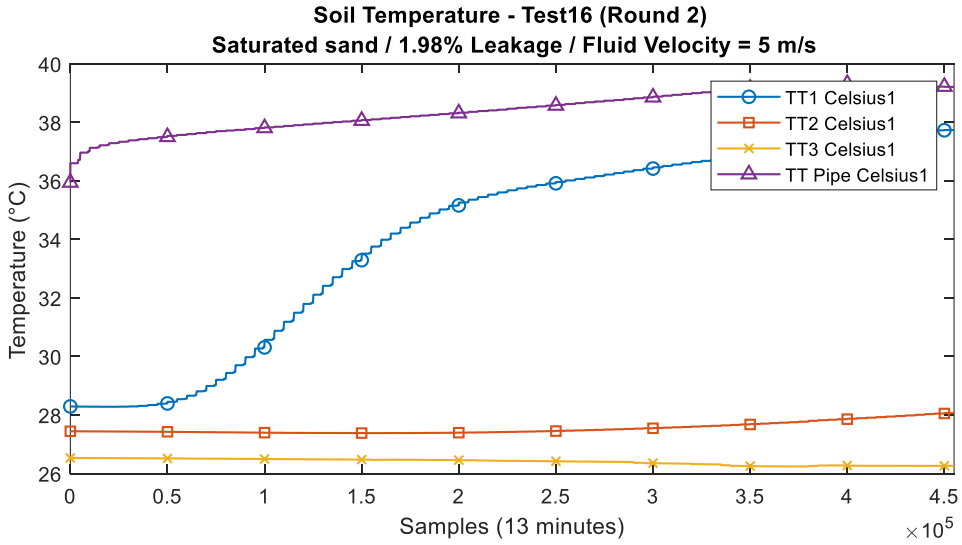

Figure 5.40: Temperature of saturated sand / 1.98% leak / Fluid Velocity: 5 m/s (Test #16)

(a) Minute 0 **(b) Minute 4**

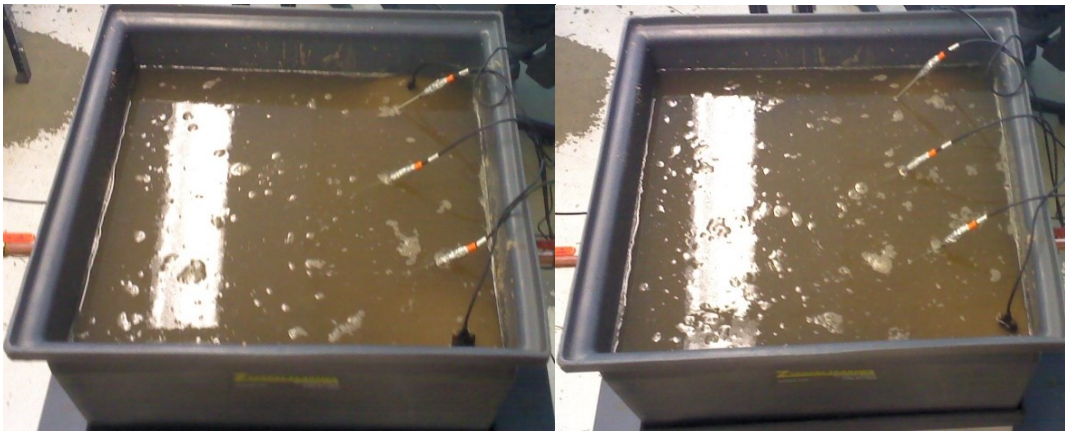

(a) Minute 10 **(b) Minute 14**

Figure 5.41: A sequence of liquids flow in Test #16 (Round 2)

TT1, TT2, and TT3's results plotted in figures 5.34 and 5.38 coincides with the outcome of dielectric permittivity and thermal imaging techniques. Temperature curves show a straight relation between leak rates and ΔTs. The average ΔT is 1.49 °C/min and 4.3 °C/min for leaks of 0.89% and 1.90%. Moreover, the response time of thermocouples is coherent with the effect of permeability described by Mohamed and Paleologos (2018) since TT1 and TT2 react within two minutes whereas TT3 by minute five; pinhole points towards TT1 and TT2. FLIR images in figure 5.21 also support the results above described for sand, as isotropic soil. Results for saturated sand are similar to black soil's, any substantial increase of temperature is due to the probes lining up with the increasing water level to maintain the integrity of the SCADA system.

Thermocouples generally perform inadequately because the relation between the soil temperature and the leak is multifactorial as mentioned above. Another critical factor when using this technology is their location respect the leak source. In experiment #8 (first round), experimental conditions are: dry sand, 0.82% leakage, fluid velocity 5 m/s. The soil temperature was measured aside using a temperature meter, and results vary drastically from 24.9 to 38.8 °C depending on the meter position, the time span for the sequence of the pictures shown in figure 5.42 is 10 minutes.

(a) 12:17 PM **(b) 12:18 PM**

(b) 12:19 PM **(d) 12:27 PM**

Figure 5.42: Sequence of soil temperature in test 9 – Round 1

5.2.4 Performance of temperature probes Vs. dielectric permittivity probes

Following figures compare the performance of temperature probes against dielectric permittivity probes under different mediums –black soil and sand- and moisture level.

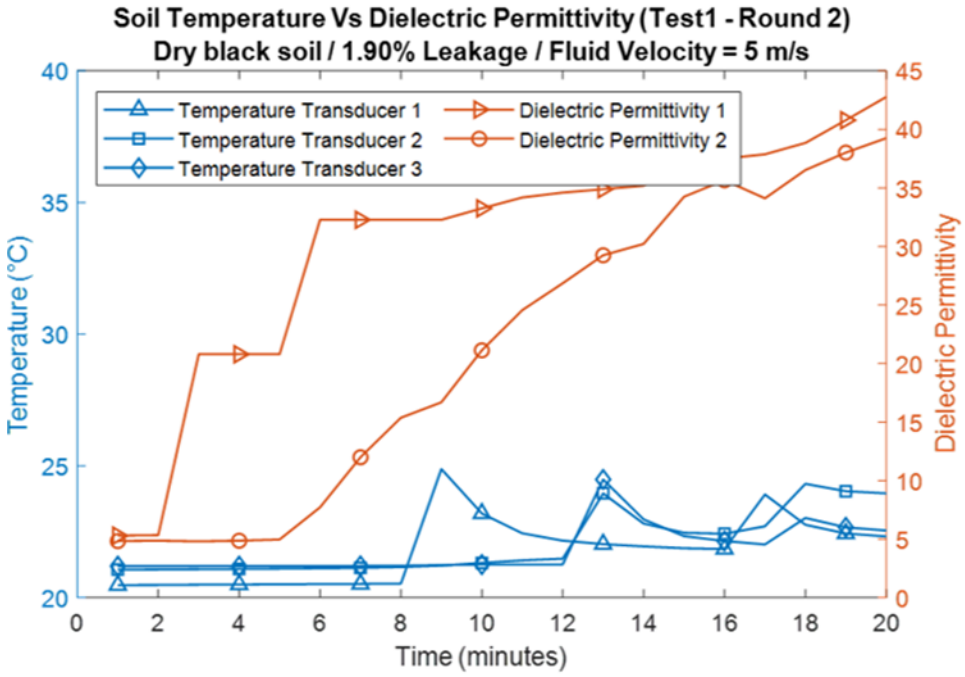

Figure 5.43: Soil Temperature Vs. Dielectric Permittivity (Test1 – Round 2)

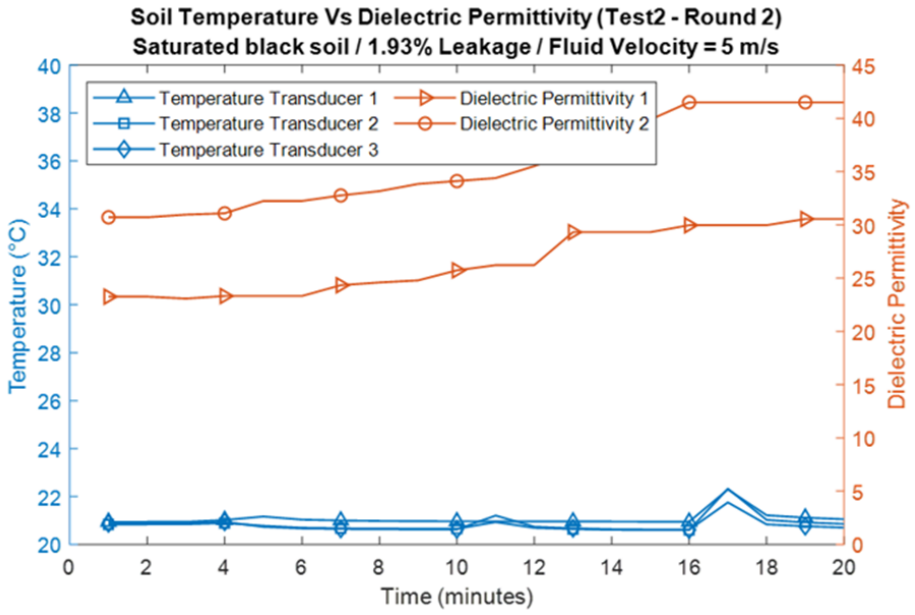

Figure 5.44: Soil Temperature Vs. Dielectric Permittivity (Test2 – Round 2)

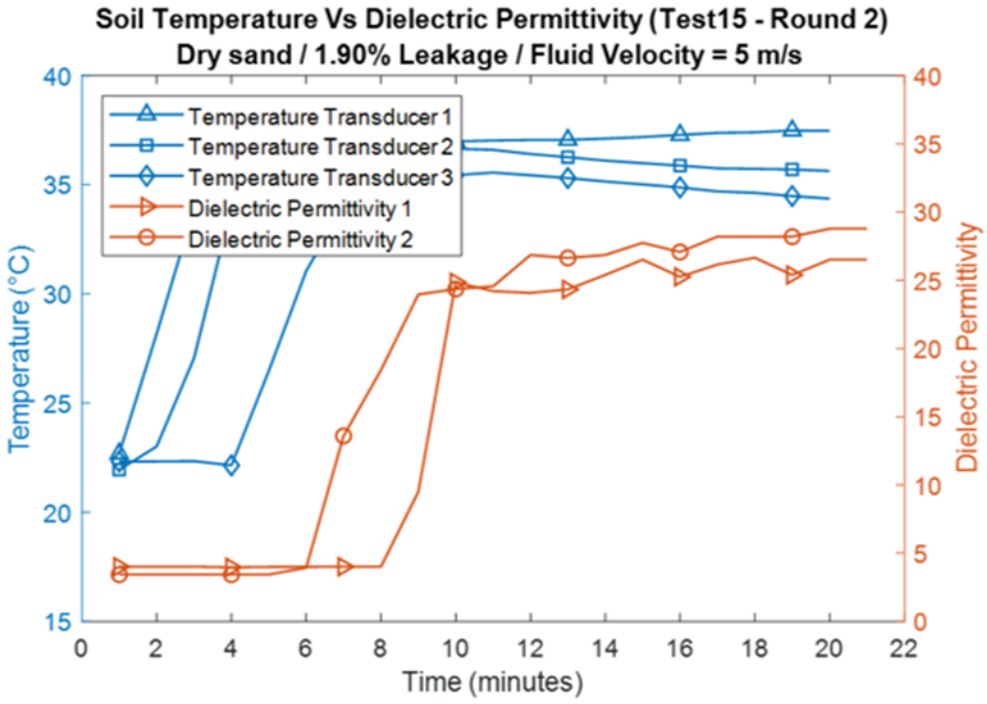

Figure 5.45: Soil Temperature Vs. Dielectric Permittivity (Test15 – Round 2)

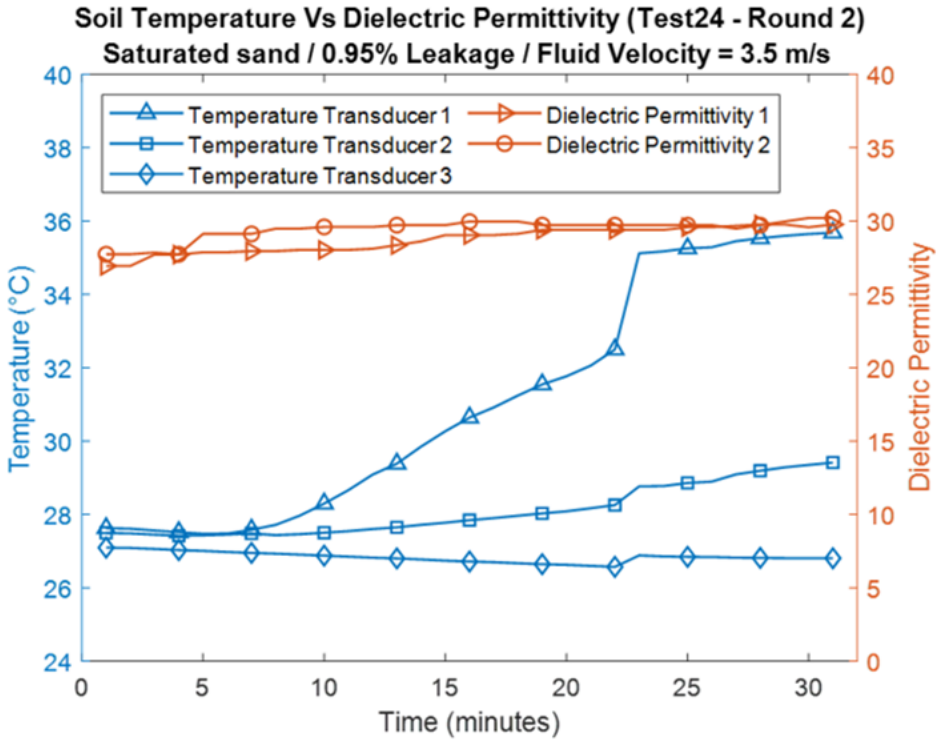

Figure 5.46: Soil Temperature Vs. Dielectric Permittivity (Test24 – Round 2)

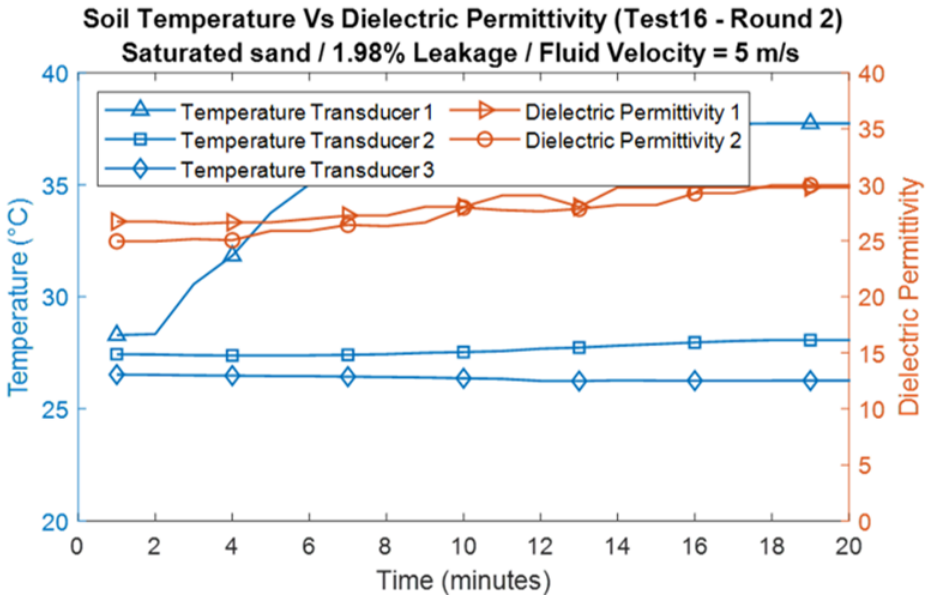

Figure 5.47: Soil Temperature Vs. Dielectric Permittivity (Test16 – Round 2)

Both thermocouples probes and dielectric probes perform better in dry sand than dry black soil due to medium permeability. Dielectric probes do not measure changes when the medium is saturated because the medium's pores are already fulfilled with water, yet if a pipe leaks hydrocarbons, it is expected that the probes measure a change of dielectric permittivity because the dielectric constant of hydrocarbons is between 2.1 and 2.4 as opposed as water's which is 80. The dielectric permittivity of mediums saturated with water -e.g., the soil beneath rivers- is around 30 as shown in experiments, so when the hydrocarbons reach the probes, then the DP will decrease triggering the LDS's threshold.

Further research is needed to assess the liquids flow in saturated mediums. This research concludes that the flow of liquids in saturated soil is irregular because its matric suction and gradient is zero. Hence the water-soil acting forces are gravity and the pressure of the leak, so the water-flow is anisotropically, resulting in lower chances to the liquids to reach the probes.

In low permeable mediums such as black loam under dry conditions, the DP probes are more efficient than thermocouples, as shown in figures 5.48 to 5.51. DPs measures a delta as soon the water reaches them, DP1 at minute 6 whereas DP2 by the minute 20 of starting the leak. However, the thermocouples do not measure any noticeable change in

temperature. Figure 5.49 shows the thermal image at minute 25 of starting leak (3:00 pm) where it exhibits that the liquids at 34 °C touch the thermocouple probes whereas figure 5.48 shows their reading, proving the poor performance under these conditions.

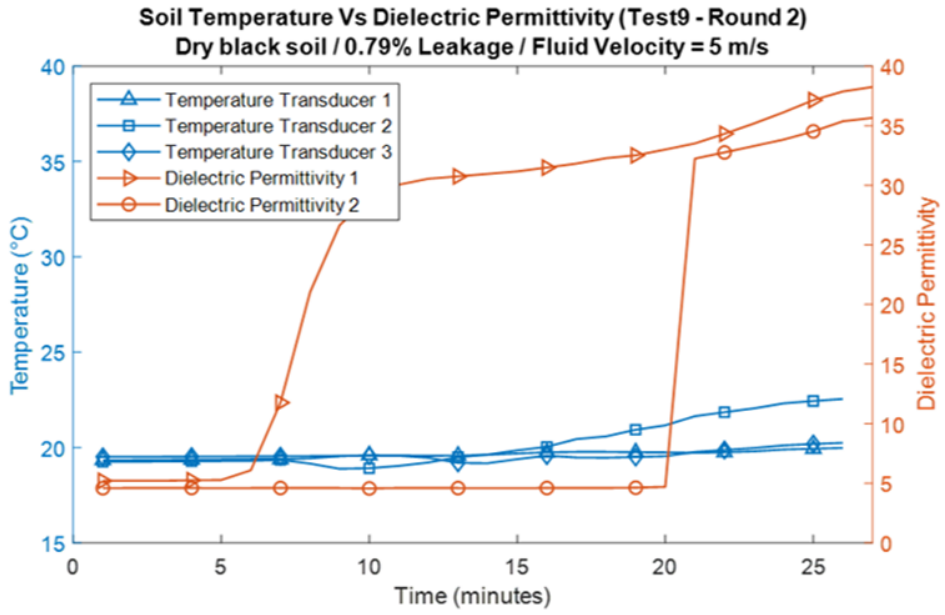

Figure 5.48: Soil Temperature Vs. Dielectric Permittivity (Test9 – Round 2)

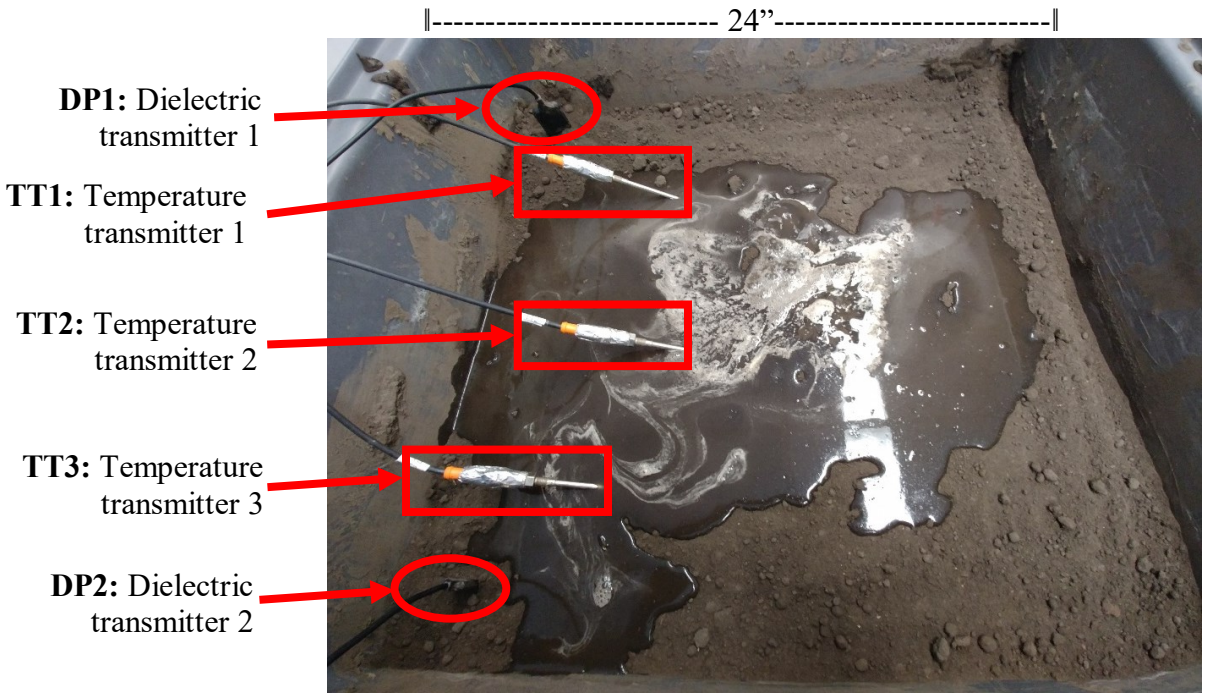

Figure 5.49: Water-soil flow at minute 4 of starting leak (2:39 pm) (Test9 – Round 2)

Figure 5.50: Water-soil flow at minute 20 of starting leak (2:55 pm) (Test9 – Round 2)

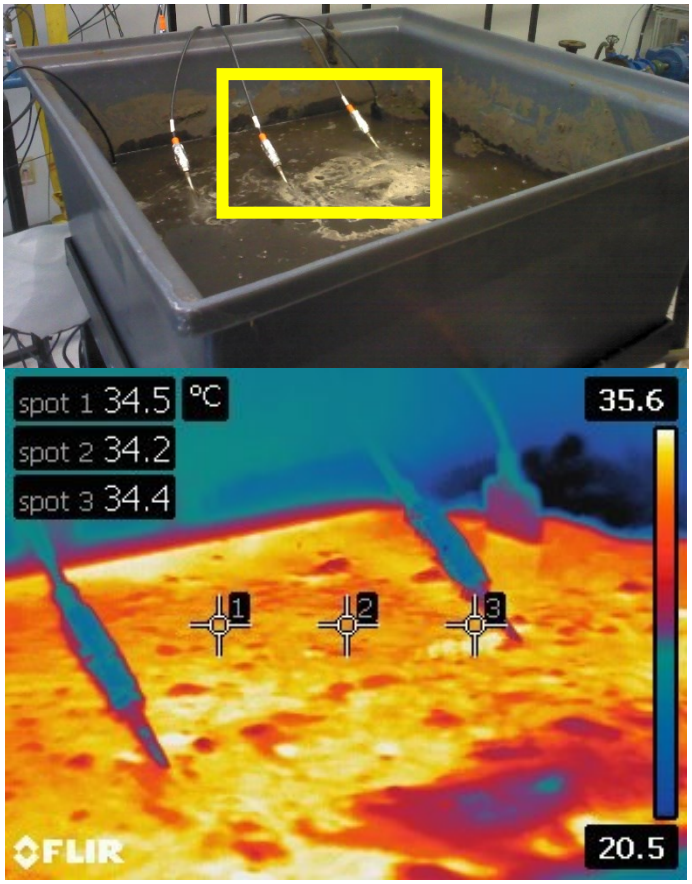

Figure 5.51: Water-soil flow at minute 25 of starting leak (3:00 pm) (Test9 – Round 2)

5.2.5 Pressure profiles results

The Bernoulli equation describes the flow of an inviscid fluid flowing from inside the pipe, '*i,*' to outside of it, '*o,*' as written in 5.1. According to Darcy-Weisbach, the pressure drop in a circular pipe is related to velocity '*v*' as described in 5.2:

$$p_i + \frac{1}{2}\rho {v_i}^2 + \rho g y_i = p_o + \frac{1}{2}\rho {v_o}^2 + \rho g y_o \qquad (5.1)$$

$$\mathrm{Q} = CA\sqrt{\frac{2\Delta p}{S{*}\rho_{w,std}}} \qquad (5.2)$$

The laboratory apparatus includes three pressure transducers (TP1, TP2, and TP3) to measure the fluid pressure. TP1 is deployed one meter upstream the leak while TP2 and TP3 are one and two meters downstream the leak source. According to Gao (2018) when a pipe leaks it generates waves along both the pipe and its surroundings. Figures 5.52 to 5.59 show raw and denoised signals from TP1, TP2 and TP3 under Leak rates of 0%, 0.79%, and 1.90%.

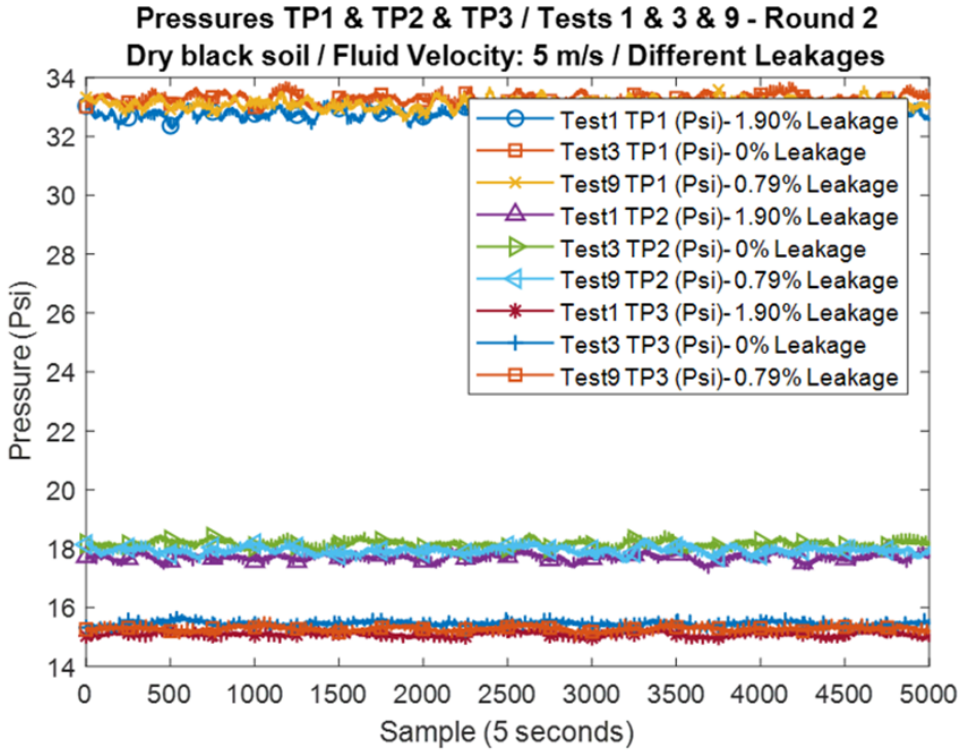

Figure 5.52: Pressures TP1/TP2/TP3 under 0% / 0.79% / 1.90% Leakage

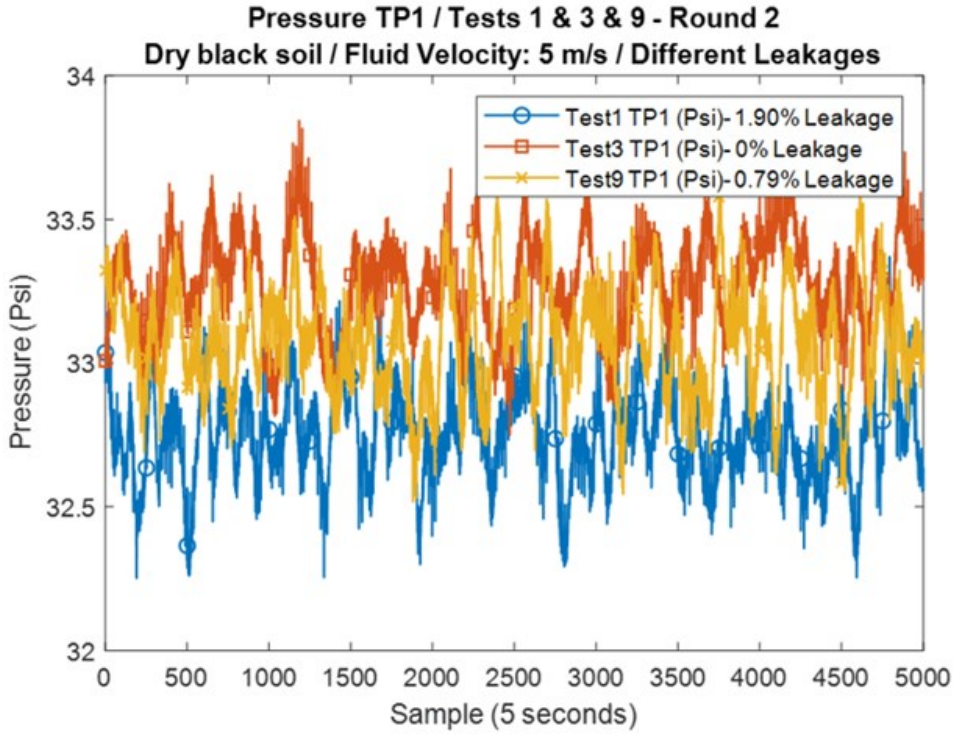

Figure 5.53: Pressure TP1 under 0% / 0.79% / 1.90% Leakage

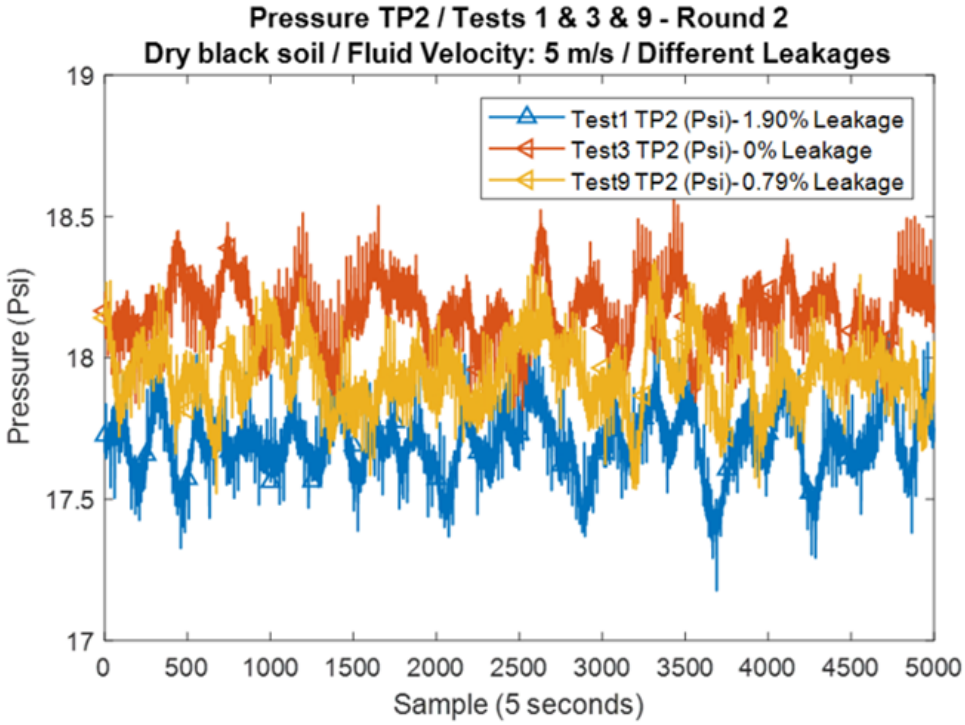

Figure 5.54: Pressure TP2 under 0% / 0.79% / 1.90% Leakage

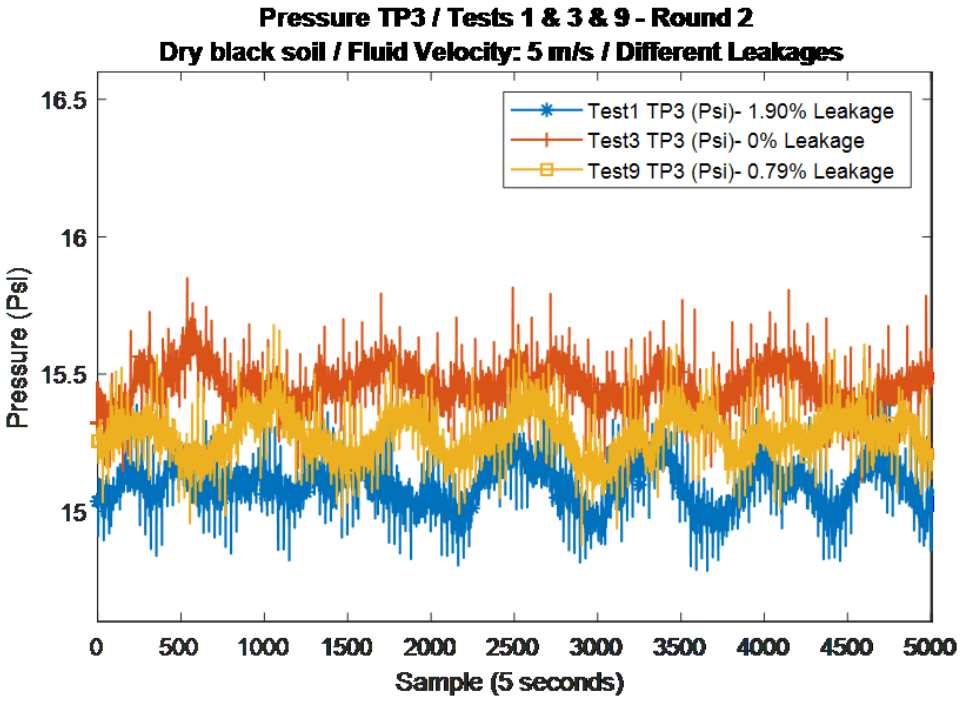

Figure 5.55: Pressure TP3 under 0% / 0.79% / 1.90% Leakage

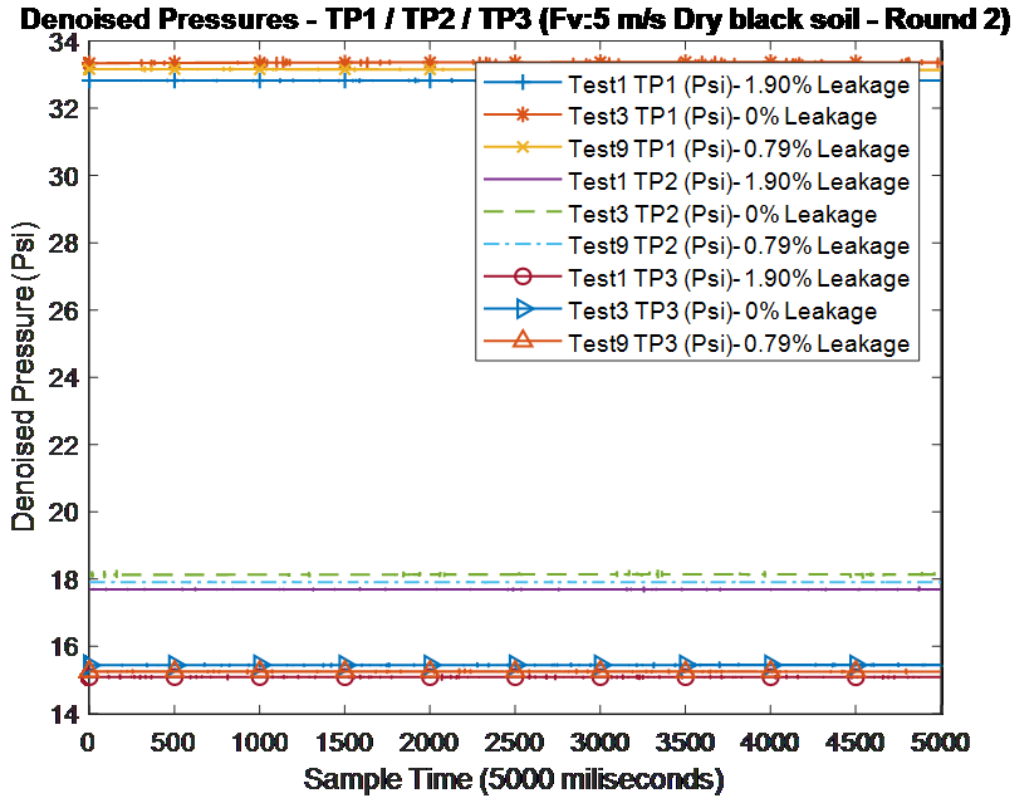

Figure 5.56: Denoised Pressures TP1/TP2/TP3 under 0% / 0.79% / 1.90% Leakage

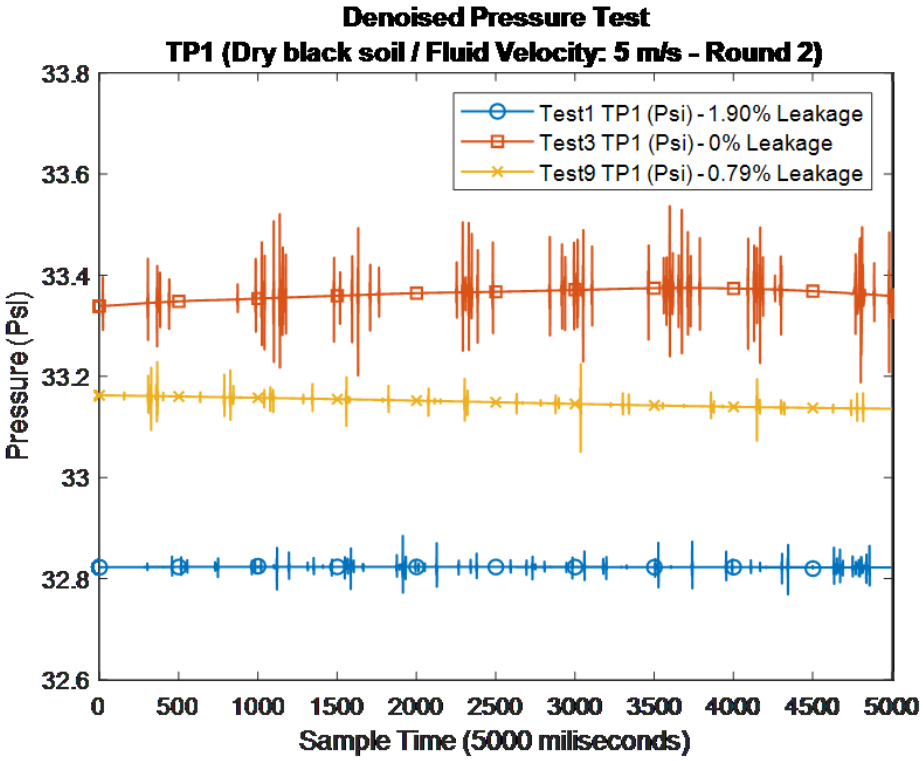

Figure 5.57: Denoised Pressure TP1 under 0% / 0.79% / 1.90% Leakage

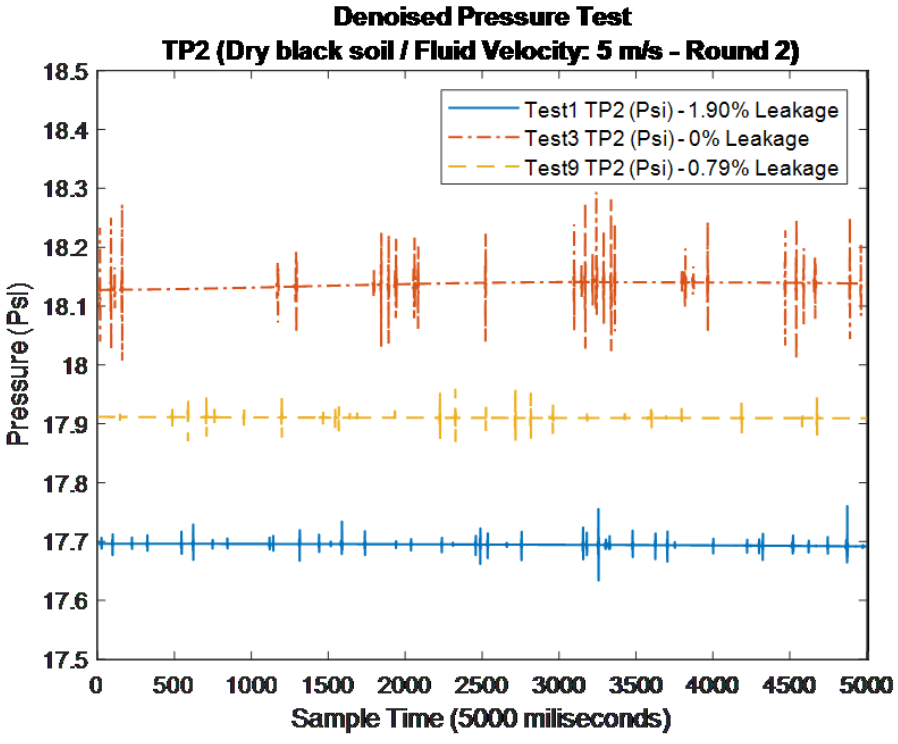

Figure 5.58: Denoised Pressure TP2 under 0% / 0.79% / 1.90% Leakage

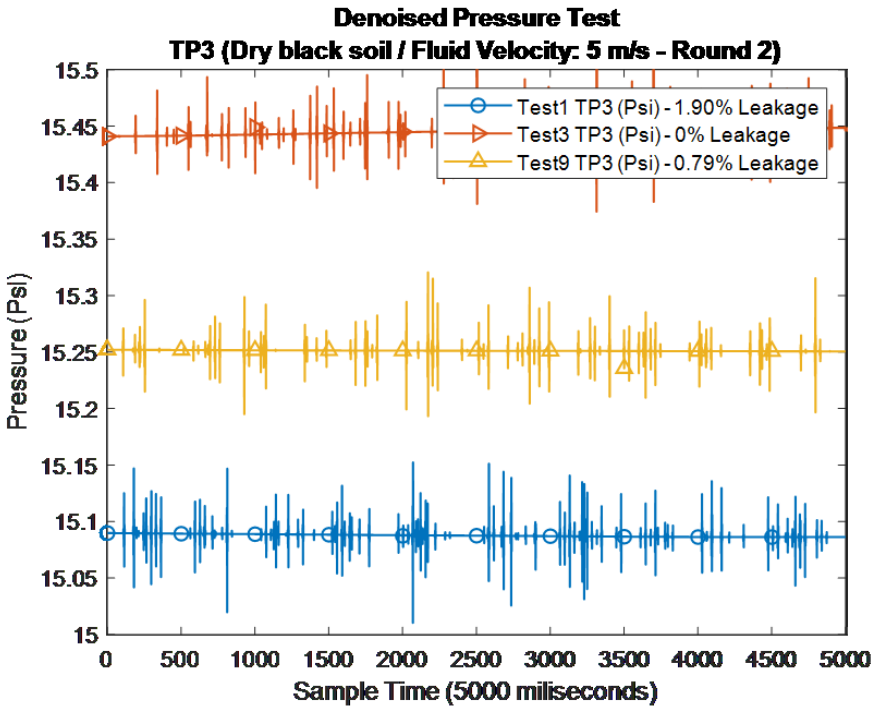

Figure 5.59: Denoised Pressure TP3 under 0% / 0.79% / 1.90% Leakage

Pressure drop increases linearly with orifice size, the pressure within the pipe are 25.25 and 25.53 (psi) when the orifice diameters are three and two millimeters respectively; atmospheric pressure is 14.7 (psi). Using the data from the pressure transducers in the Darcy-Weisbach equation (equation 5.2), the estimated Water Flow Rate through 3mm and 2 mm orifices in a circular pipe is detailed in table 5.4. Discharge coefficient is 0.61 and the water specific gravity at 38^{0}C equals to 0.9922. The dimensionless pressure drop under 1.90% and 0.79% leak rates shows the straight relation between the rate size and the pressure drop, as portrayed in results below.

Table 5.4: Estimation of water Flow Rate through 2 mm and 3mm Orifices

INPUT DATA			
Pump Pressure (kPa abs)	174.09	Pump Pressure (kPa abs)	176.02
Secondary Pressure (kPa abs)	101.35	Secondary Pressure (kPa abs)	101.35
Discharge coefficient	0.61	Discharge coefficient	0.61
Orifice diameter (mm)	3.00	Orifice diameter (mm)	2.00
Liquid specific gravity@38^{0}C	0.9922	Liquid specific gravity@38^{0}C	0.9922
ESTIMATED LEAK RATE			
Q (l/min)	3.129	**Q (l/min)**	1.409
Q (gal/min)	0.827	**Q (gal/min)**	0.372

$$TP1\ Vs\ TP2\colon \Delta_{pD(0.79\,\%\,leakage)} = \frac{33.104\ (\text{psi}) - 17.883\ (\text{psi})}{33.320\ (\text{psi}) - 18.064\ (\text{psi})} = 0.9977 \text{ or } 99.77\%$$

$$TP1\ Vs\ TP2\colon \Delta_{pD(1.90\,\%\,leakage)} = \frac{32.741\ (\text{psi}) - 17.654\ (\text{psi})}{33.320\ (\text{psi}) - 18.064\ (\text{psi})} = 0.9888 \text{ or } 98.88\%$$

$$TP1\ Vs\ TP3\colon \Delta_{pD(0.79\,\%\,leakage)} = \frac{33.104\ (\text{psi}) - 15.243\ (\text{psi})}{33.320\ (\text{psi}) - 15.414\ (\text{psi})} = 0.9975 \text{ or } 99.75\%$$

$$TP1\ Vs\ TP3\colon \Delta_{pD(0.79\,\%\,leakage)} = \frac{32.742\ (\text{psi}) - 15.072\ (\text{psi})}{33.320\ (\text{psi}) - 15.414\ (\text{psi})} = 0.9868 \text{ or } 98.68\%$$

Table 5.5: Water Flow Rate results through orifices of two and three millimeters

Test 1 - Dry Black Soil - 3 mm - Fv: 5 m/s		**Mass (Kg)**	**Test 9 - Dry Black Soil - 2 mm - Fv: 5 m/s**	**Mass (Kg)**
Intial Test Time	2/28/2019 13:50:51.000	99.376	3/5/2019 14:36:39.000	98.122
Ending Test Time	2/28/2019 14:08:40.000	144.246	3/5/2019 15:00:45.000	123.713
Test Time Span (min)	17.817		24.100	
Mass Leaked (kg)		44.870		25.591
	Leak flow (liters/minute)	**2.499**	Leak flow (liters/minute)	**1.054**

Test 2 - Saturated Black Soil - 3 mm - Fv: 5 m/s		**Mass (Kg)**	**Test 10 - Saturated Black Soil - 2 mm - Fv: 5 m/s**	**Mass (Kg)**
Intial Test Time	3/1/2019 15:32:53.000	120.921	3/5/2019 16:32:08.000	113.918
Ending Test Time	3/1/2019 15:49:50.000	164.498	3/5/2019 16:56:02.000	141.457
Test Time Span (min)	16.95		23.900	
Mass Leaked (kg)		43.577		27.538
	Leak flow (liters/minute)	**2.551**	Leak flow (liters/minute)	**1.143**

Test 15 - Dry Sand - 3 mm - Fv: 5 m/s		**Mass (Kg)**	**Test 21 - Dry Sand - 2 mm - Fv: 5 m/s**	**Mass (Kg)**
Intial Test Time	3/8/2019 12:57:44.000	119.753	3/11/2019 12:40:29.000	124.978
Ending Test Time	3/8/2019 13:16:41.000	167.543	3/11/2019 13:09:37.000	158.710
Test Time Span (min)	18.950		29.133	
Mass Leaked (kg)		47.790		33.732
	Leak flow (liters/minute)	**2.502**	Leak flow (liters/minute)	**1.149**

Test 16 - Saturated Sand - 3 mm - Fv: 5 m/s		**Mass (Kg)**	**Test 22 - Saturated Sand - 2 mm - Fv: 5 m/s**	**Mass (Kg)**
Intial Test Time	3/8/2019 16:17:32.000	138.368	3/11/2019 14:40:00.000	146.242
Ending Test Time	3/8/2019 16:33:39.000	180.502	3/11/2019 15:03:56.000	174.961
Test Time Span (min)	16.117		23.933	
Mass Leaked (kg)		42.134		28.719
	Leak flow (liters/minute)	**2.594**	Leak flow (liters/minute)	**1.191**

Avergage Leak flow (liters/minute) - Sand	**2.536**	Avergage Leak flow (liters/minute) - Black Soil	**1.134**

The estimated flow rate of liquids leaked through both the orifices of two and three millimeters are 1.409 and 3.129 liters/minute. The scale measures the mass leaked, so this is used to validate the estimation, table 5.5 shows the average leak rate for several experimental conditions, including the type of soil and moisture level. The experimental results show leak rates of 1.134 and 2.536 liters/minute through the pinholes. Error is 24% amongst them, yet next systematic errors influence this difference: the orifice diameters are not precisely two and three millimeters; the pressure of the fluid is assumed as the mean of TP1 and TP2 because the transducers are considered equally separated at one meter from the leak source, upstream and downstream; the discharged coefficient is assumed 0.61. Nevertheless, the pressure curves work to feed the machine-learning algorithm because the signals have noticeable differences that can be captured by the algorithm to make a variety of relationships between them.

According to Gao et al. (2018), the leak generates waves along both the pipe and its surroundings. The current apparatus includes three pressure transducers deployed (TP1, TP2, and TP3) through pipe fittings, and one triaxial accelerometer cemented to the pipe. TP1 is one meter upstream the leak whereas TP2 and TP3 are one and two meters downstream. The continuous leak signals are used in the correlation analysis to calculate the time difference between their arrivals at where the pressure and vibration sensors are; this involves the problem of time delay estimation (TDE) of sensor signals in the presence of background noise.

Figures from 5.60 to 5.63 picture the pipe vibration under 0%, 0.79%, and 1.90% leak conditions. Although steps were taken to minimize the signal background noise, for example, set a spherical joint to damper pump vibration; fasten the pump to the floor; power up the NI cDAQ-9178 using a battery to discard power supply noise –this step was dismissed because the noise remains stable regardless the power supplies-. The noise still diminishes the cross-correlation effectiveness because the vibrations are alike in all conditions as portrayed in below figures. The signals neither show a distinctive peak to create a baseline “acoustic map” of the pipeline. Peaks appear in the transient experiments

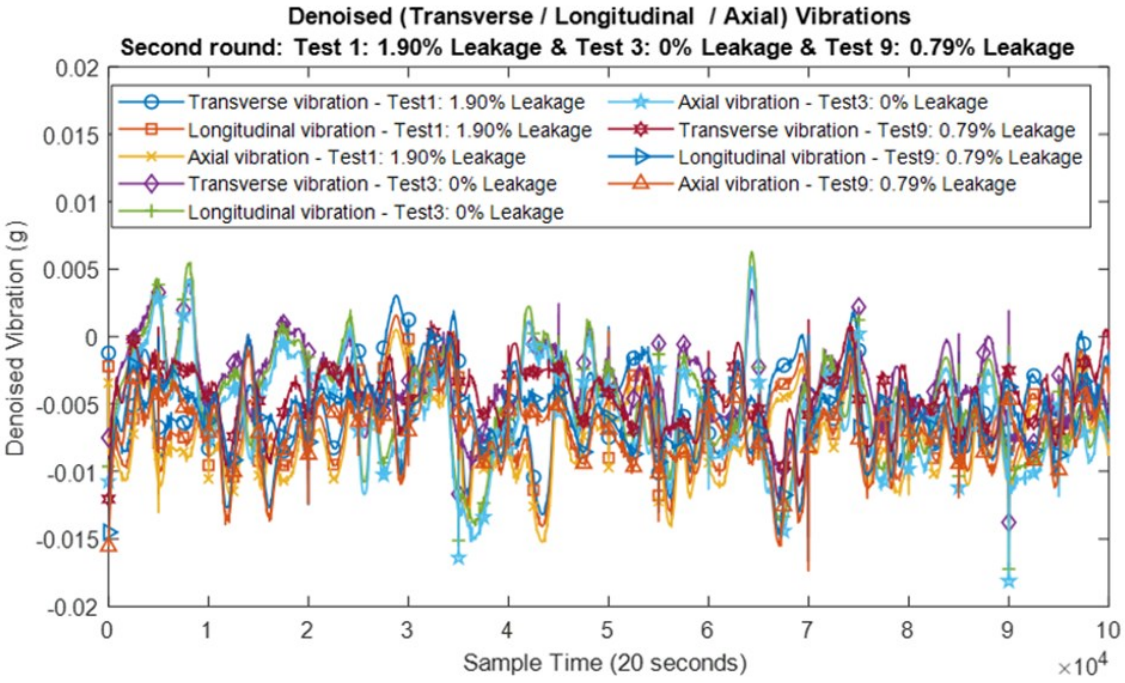

Figure 5.60: Pipe vibration in three axes – 1.90% / 0% / 0.79% leakage

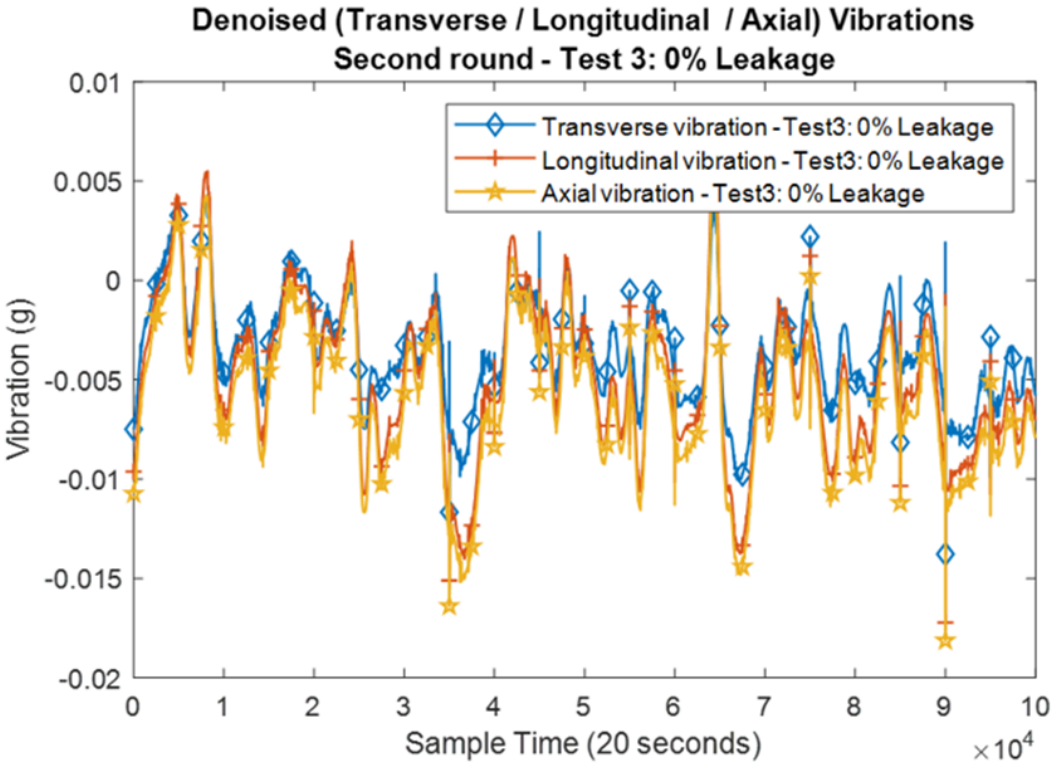

Figure 5.61: Pipe vibration in three axes – No leak

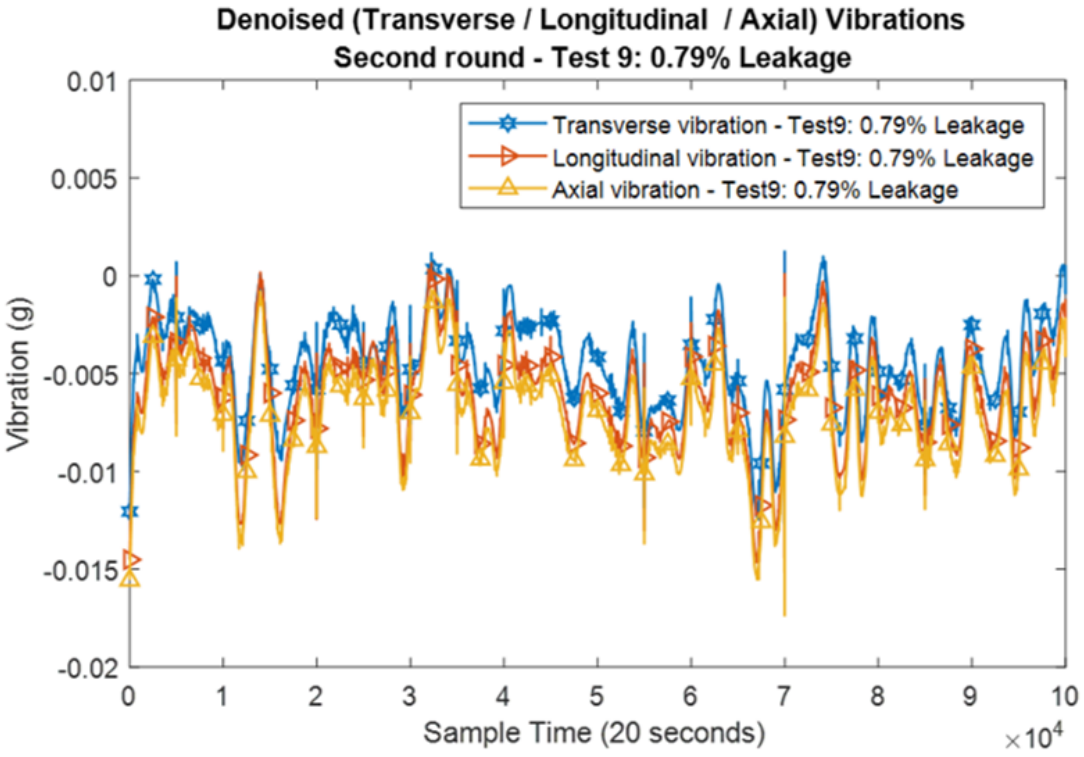

Figure 5.62: Pipe vibration in three axes – 0.79% leakage

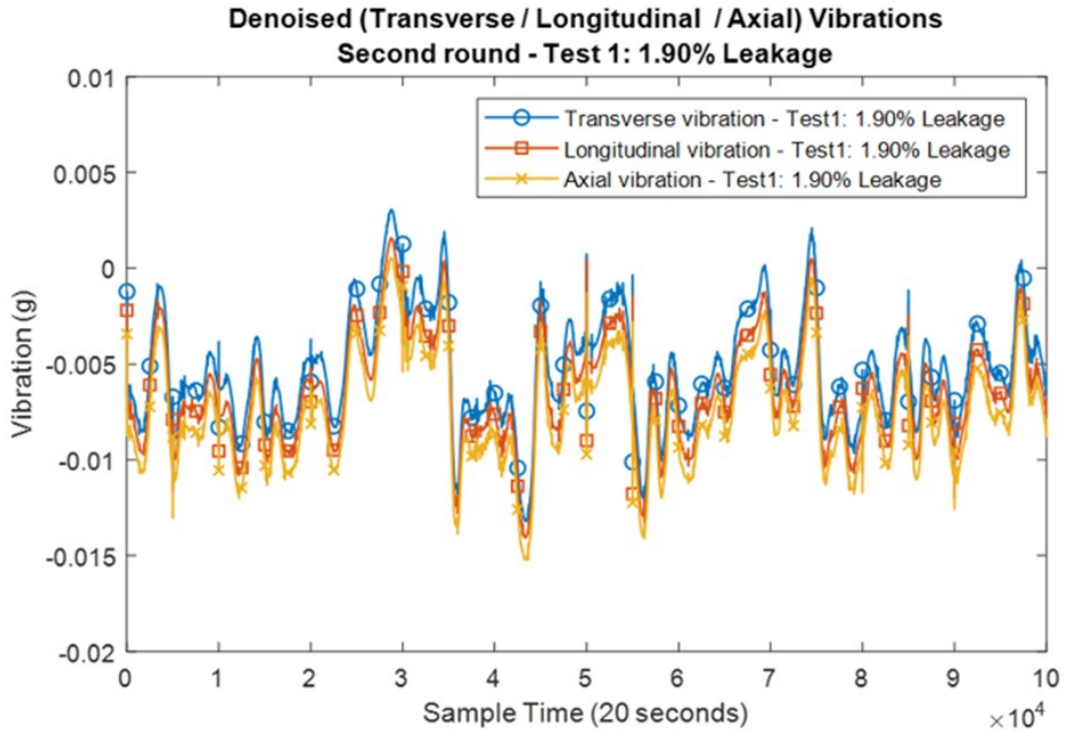

Figure 5.63: Pipe vibration in three axes – 1.90% leakage

5.2.6 Transient-state results

Transients are generated by all the operational combinations between the pump, electro-valve (to create a rupture of 17%) and check valve; for instance, by simultaneously stopping the pump, shutting down 90% the check valve, and turning on the electrovalve. Experiments are performed twice, and transients are created several times during each experiment, to ensure repeatability. Results from repetitions are compared to each other to validate that the responses match the parameters defined by Jonsson (1994). Table 5.6 shows all the experimental conditions under rupture and transient state.

Table 5.6: Experimental conditions for transient state tests

N°	Experimental condition		Downstream valve status
1	Steady state (full speed)	No leak imposed	Fully open (always)
17	Steady state (full speed)	No leak imposed	90% closed (always)
25	Steady state (full speed)	No leak imposed	Fully open and 90% closed (Cycle)
2	Steady state (full speed)	Leak imposed	Fully open (always)
3	Steady state (full speed)	Leak imposed	90% closed (always)
24	Steady state (full speed)	Leak imposed	Fully open and 90% closed (Cycle)
4	Steady state (full speed)	Leak imposed (Cycle)	90% closed when imposing the leak fully open when sealing the leak
16	Steady state (full speed)	Leak imposed (Cycle)	Fully open when imposing the leak and 90% closed when sealing the leak
28	Pump is turned on and off (Cycle)	No leak imposed	90% closed when turning off the pump and fully open when turning on the pump
5	Leak imposed when stopping the pump (1 time)		Fully open (always)
8	Leak imposed when stopping the pump (several times)		Fully open (always)
13	Leak imposed when stopping the pump (several times)		90% closed (always)
9	Leak imposed when stopping the pump (several times)		90% closed when imposing the leak and fully open when sealing the leak
20	Leak imposed when stopping the pump (several times)		Fully open when imposing the leak and 90% closed when sealing the leak
6	Leak imposed when starting the pump (several times)		90% closed (always)
18	Leak imposed when starting the pump (several times)		Fully open (always)

N°	Experimental condition	Downstream valve status
7	Leak imposed when starting the pump (several times)	90% closed when imposing the leak and fully open when sealing the leak
19	Leak imposed when starting the pump (several times)	Fully open when imposing the leak and 90% closed when sealing the leak
10	Leak imposed when increasing flow (45 to 60 Hz)(several times)	Fully open (always)
14	Leak imposed when increasing flow (45 to 60 Hz)(several times)	90% closed (always)
11	Leak imposed when increasing flow (45 to 60 Hz)(several times)	90% closed when increasing flow and fully open when decreasing the flow
15	Leak imposed when increasing flow (45 to 60 Hz)(several times)	90% closed when decreasing flow and fully open when increasing the flow
21	Leak imposed when decreasing flow (60 to 45 Hz)(several times)	Fully open (always)
22	Leak imposed when decreasing flow (60 to 45 Hz)(several times)	90% closed (always)
23	Leak imposed when decreasing flow (60 to 45 Hz)(several times)	90% closed when increasing flow and fully open when decreasing the flow
12	Leak imposed when decreasing flow (60 to 45 Hz)(several times)	90% closed when decreasing flow and fully open when increasing the flow

Detecting a leak by analyzing a pressure transient is based on the assumption that a leak will cause extra reflexions which will modify the fundamental transient propagating back and forth in the pipeline. TP1 is three feet upstream the leak, TP2 and TP3 are 3 and 6.5 feet downstream the leak. Transients are generated by shutting down 90% the mainstream valve; pump is always on (cases 24A Vs. 25A). Figures 5.64 and 5.65 shows the transients under these conditions. All transient experiments are run twice for repeatability purposes, also on each trial, the transients were created several times to ensure repeatability.

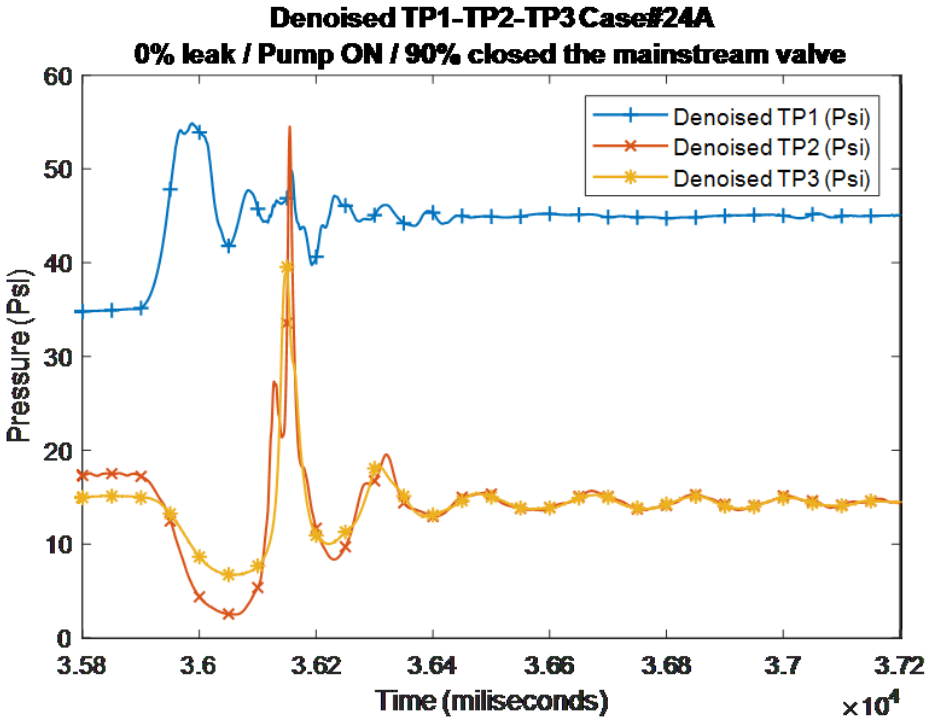

Figure 5.64: Denoised TP1-TP2-TP3 / Case #24A (Pump always ON - 0% Leak rate)

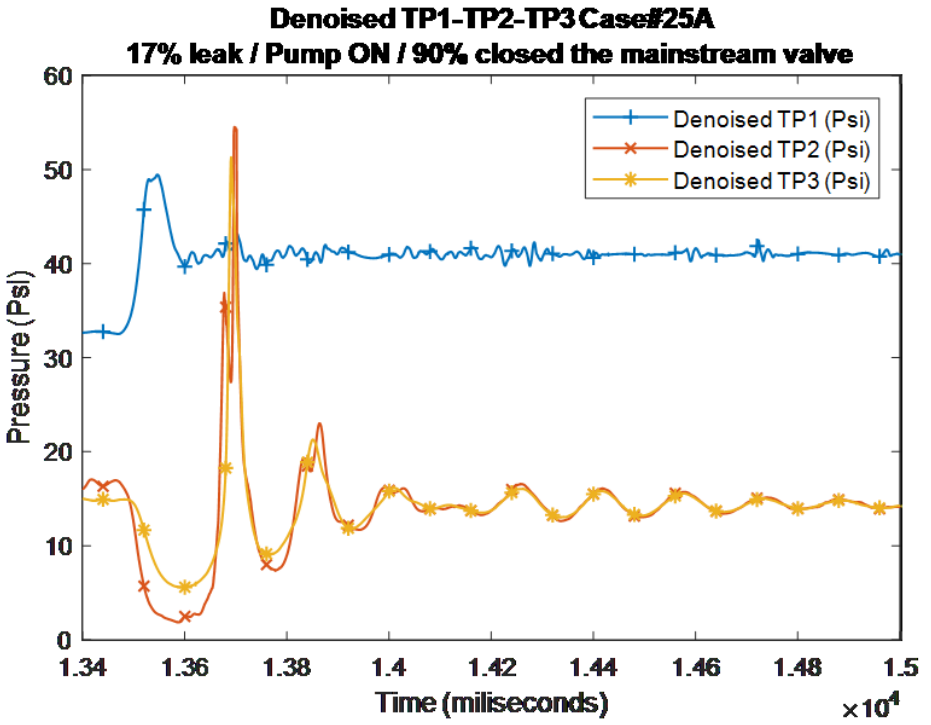

Figure 5.65: Denoised TP1-TP2-TP3 / Case #25A (Pump always ON - 17% Leak rate)

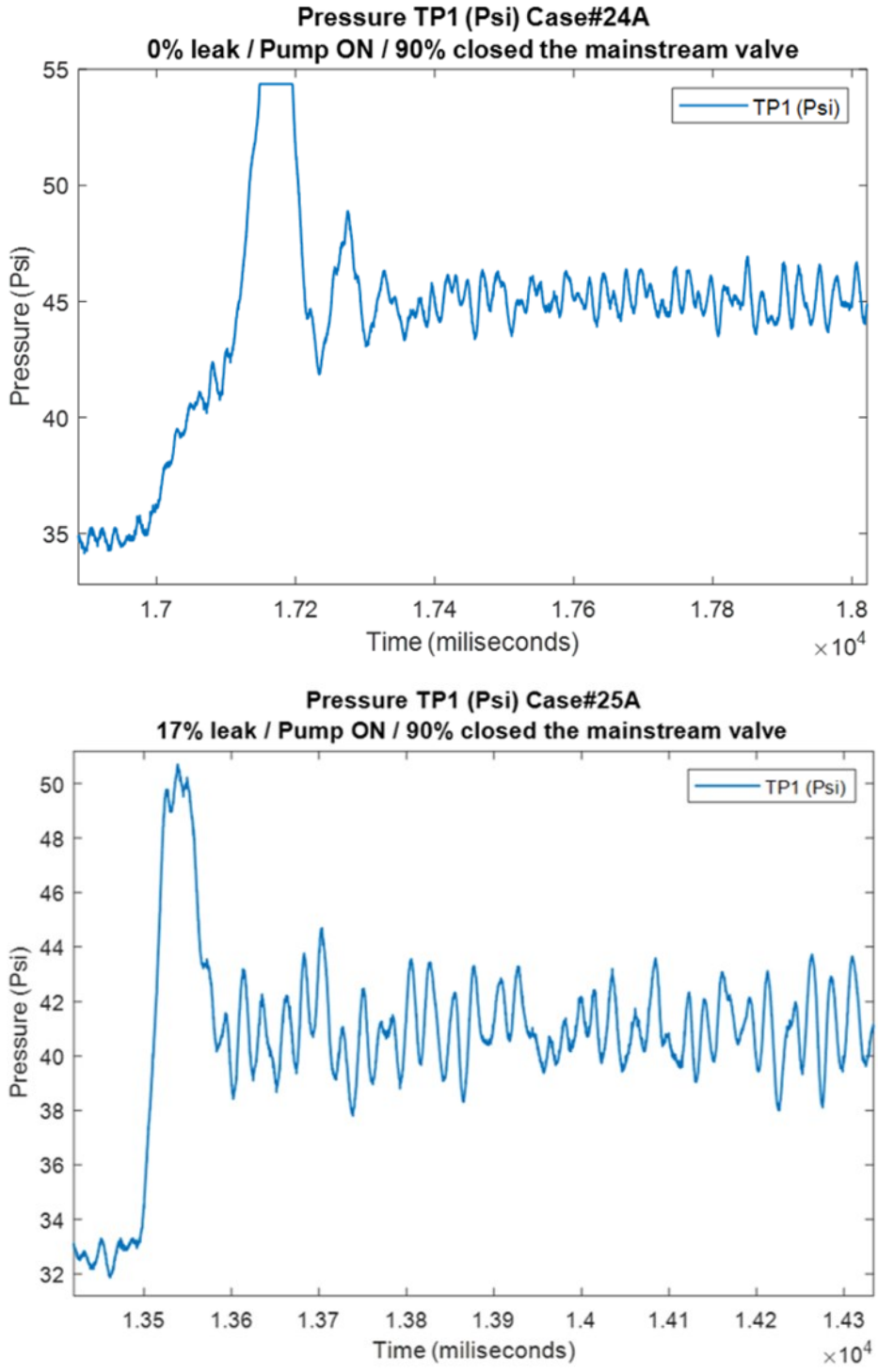

Figure 5.66: Pressure TP1 / Top: TP1 Case #24A (0% Leakage)
Bottom: TP1 Case #25A (17% Leakage)

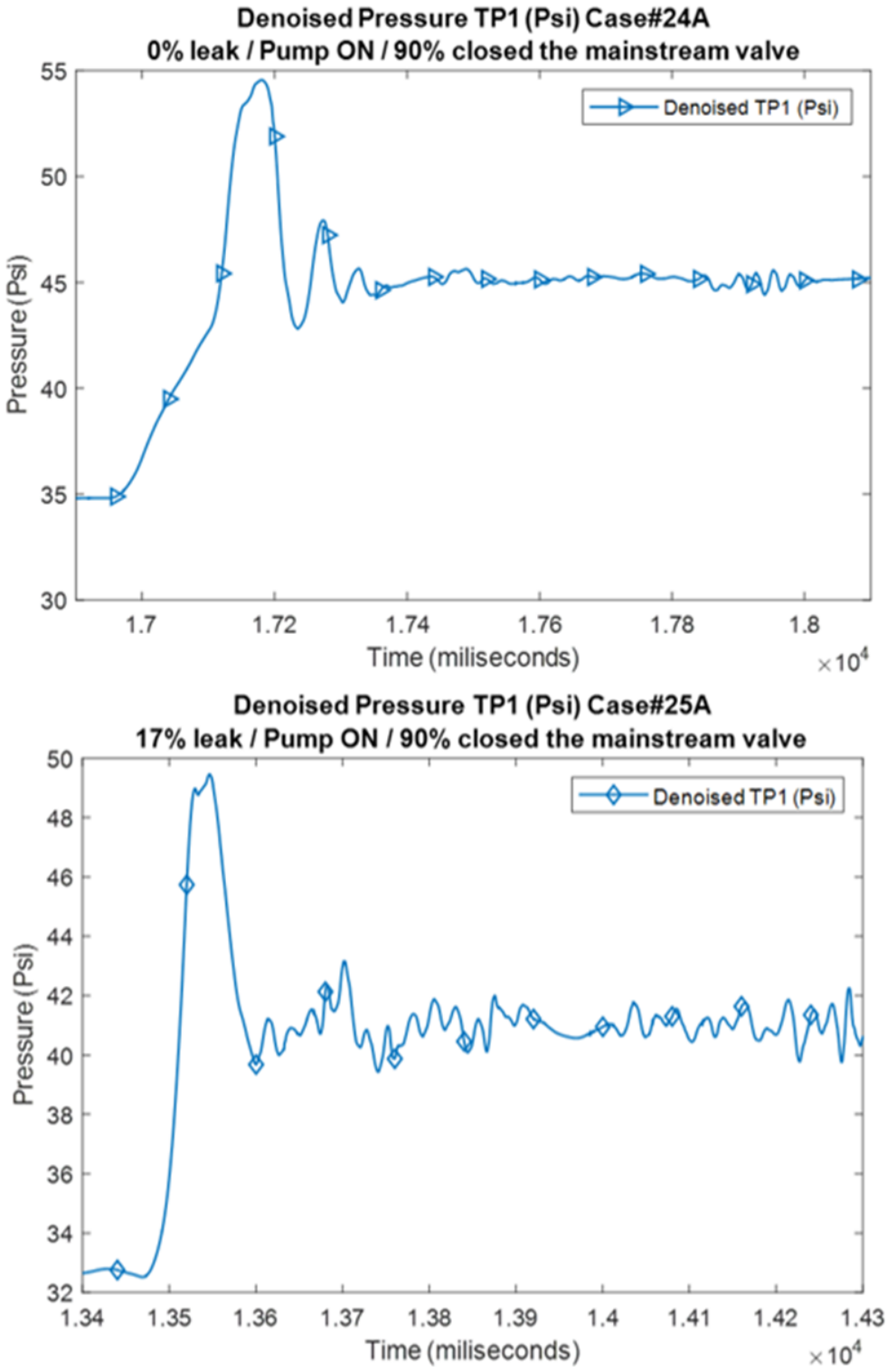

Figure 5.67: Top: Denoised TP1 Case #24A (0% Leakage)

Bottom: Denoised TP1 Case #25A (17% Leakage)

Experiments 24A (0% Leakage) and 25A (17% Leakage) create transients by closing the mainstream valve 90% while the pump is always 'On.' The leak will cause extra reflexions in the pressure signal (Jonsson, 1994), so pressure transient in case #24A should have negligible reflexions as opposed as case #25A. Figure 5.66 plots the raw transient at TP1, and figure 5.67 draws the denoised version. Transients under no leakage show no reflexion while the 17%-leak does, as expected. Pump noise challenges the analysis because it masks the leak reflexions in the transient, yet the denoised transient at TP1 shows under rupture conditions a larger order of the oscillation period than no leakage conditions', as expected by Jonsson. The pressure transient analysis also yields that the transient attenuates faster under leak conditions than no leakage conditions, but the machine learning algorithm finds difficult to recognize the leak reflexions from the pump vibration. Another limitation of generating transients with pump always 'On' is the transient overpressure surpasses the pressure transducer operational range, so the measured transient might miss key information since its first peak is incomplete. Figures from 5.68 to 5.72 show transients at TP2 and TP3, which are installed after the mainstream valve and the soil box, so pump vibrations do not distort the transients here as they do at TP1. Figures 5.73 to 5.79 depict transients created by closing the mainstream valve 90% while turning off the pump.

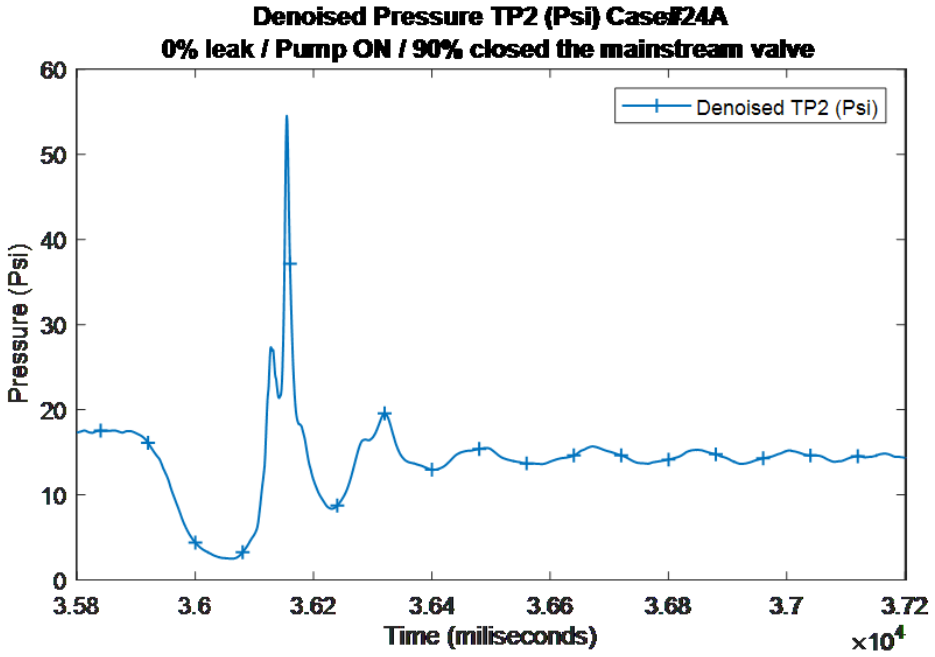

Figure 5.68: Denoised TP2 Case #24 (0% Leak rate)

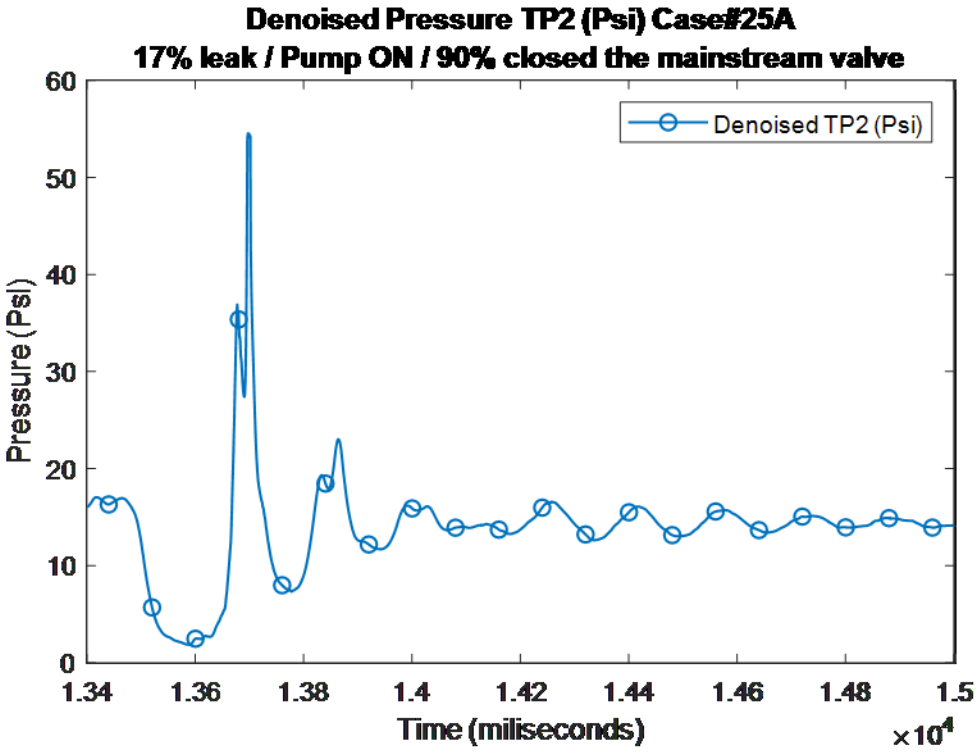

Figure 5.69: Denoised TP2 Case #25A (17% Leak rate)

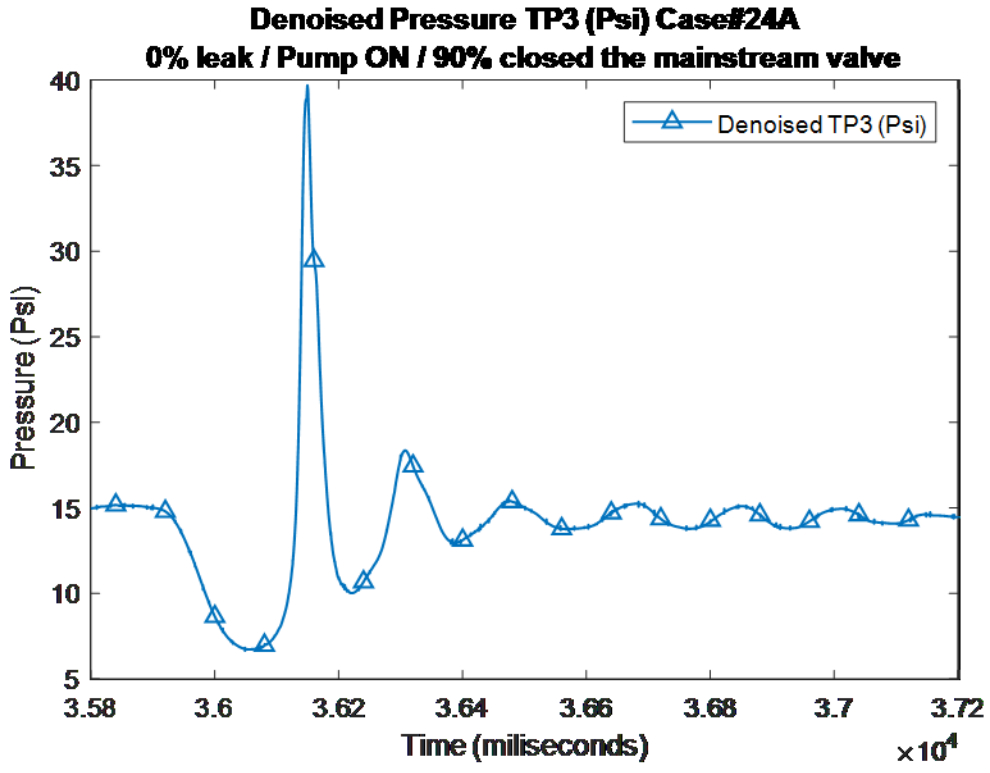

Figure 5.70: Denoised TP3 Case #24A (0% Leak rate)

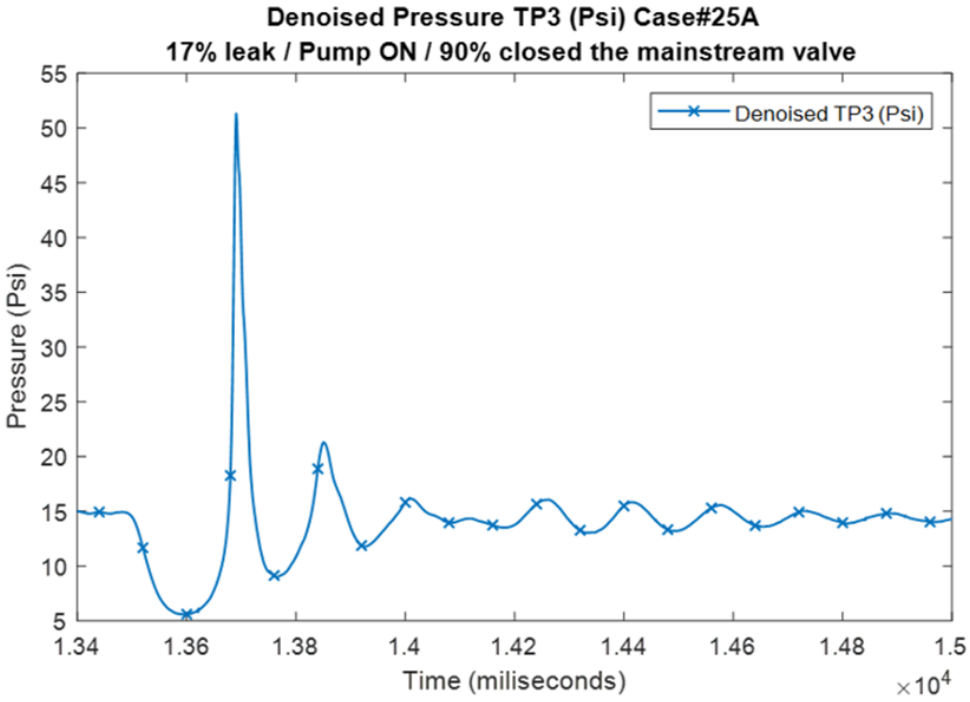

Figure 5.71: Denoised TP3 Case #25A (17% Leak rate)

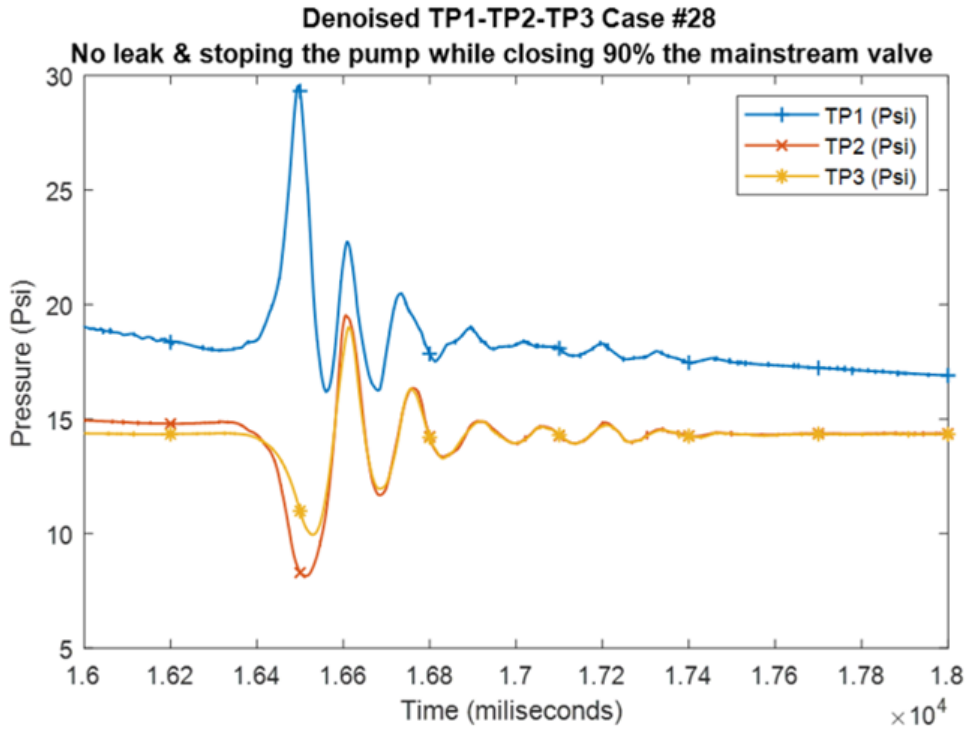

Figure 5.72: TP1-TP2-TP3 – Case #28A: 0% Leak rate & stopping the pump when closing 90% the mainstream valve

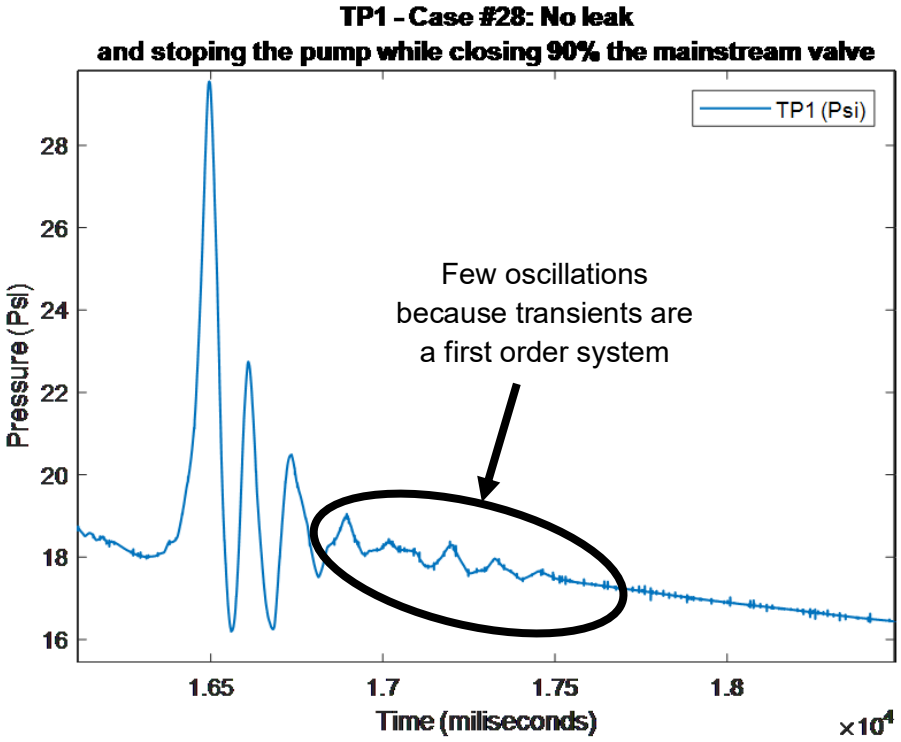

Figure 5.73: TP1 – Case #28A: 0% Leak rate & stopping the pump when closing 90% the mainstream valve

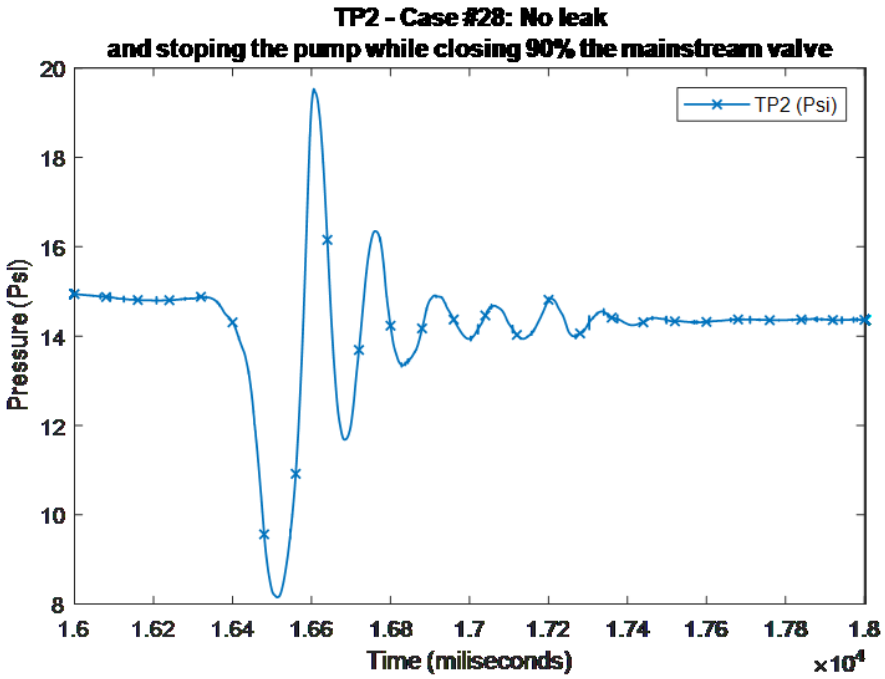

Figure 5.74: TP2 – Case #28A: 0% Leak rate & stopping the pump when closing 90% the mainstream valve

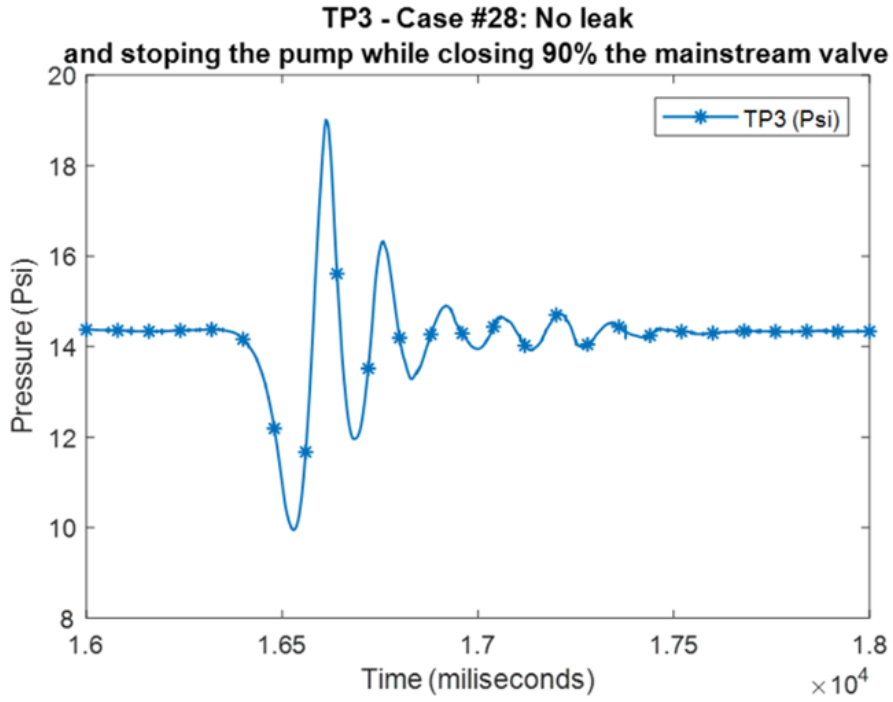

Figure 5.75: TP3 – Case #28A: 0% Leak rate & stopping the pump when closing 90% the mainstream valve

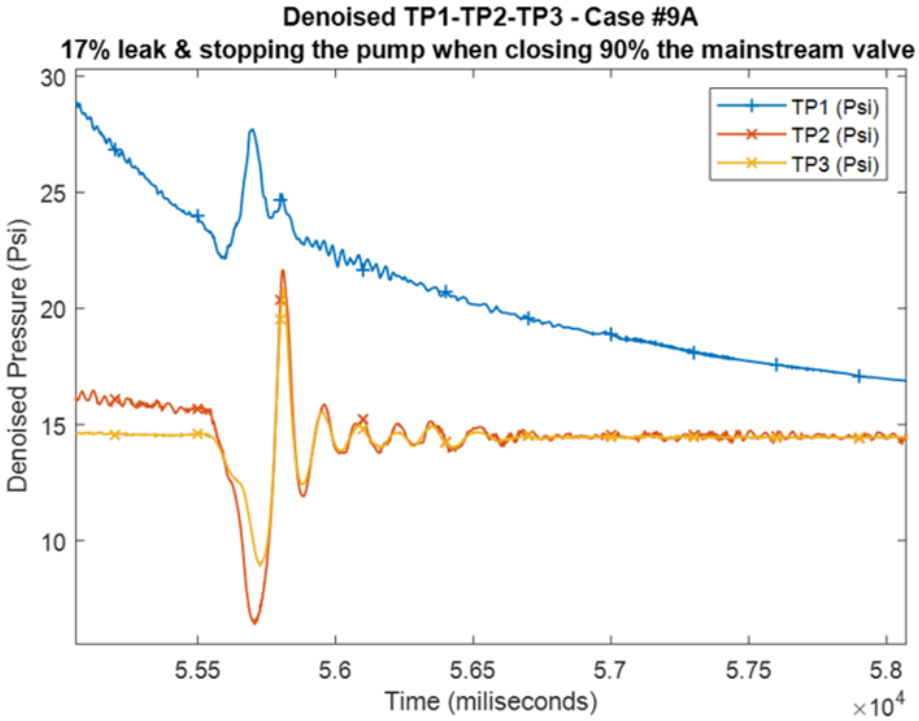

Figure 5.76: Pressure TP1-TP2-TP3 – Case #9A: 17% Leak rate &stopping the pump when closing 90% the mainstream valve

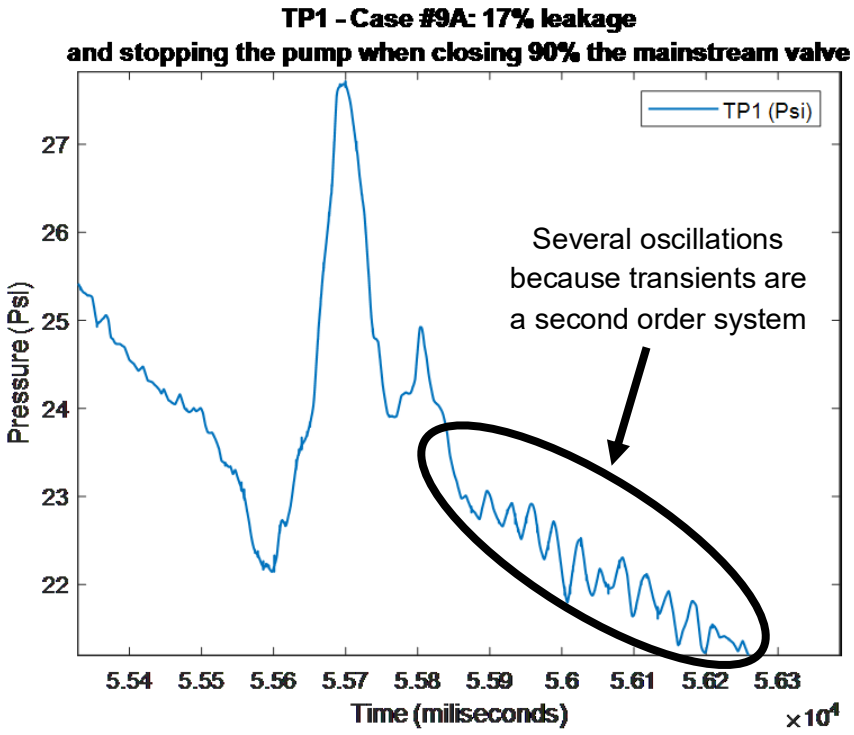

Figure 5.77: TP1 – Case #9A: 17% Leak rate & stopping the pump when closing 90% the mainstream valve

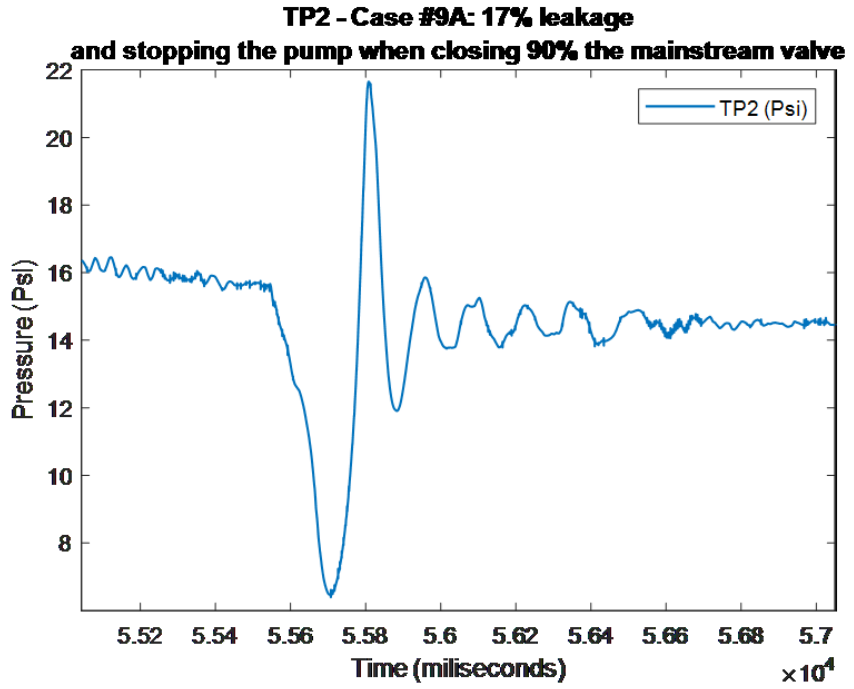

Figure 5.78: TP2 – Case #9A: 17% Leak rate & stopping the pump when closing 90% the mainstream valve

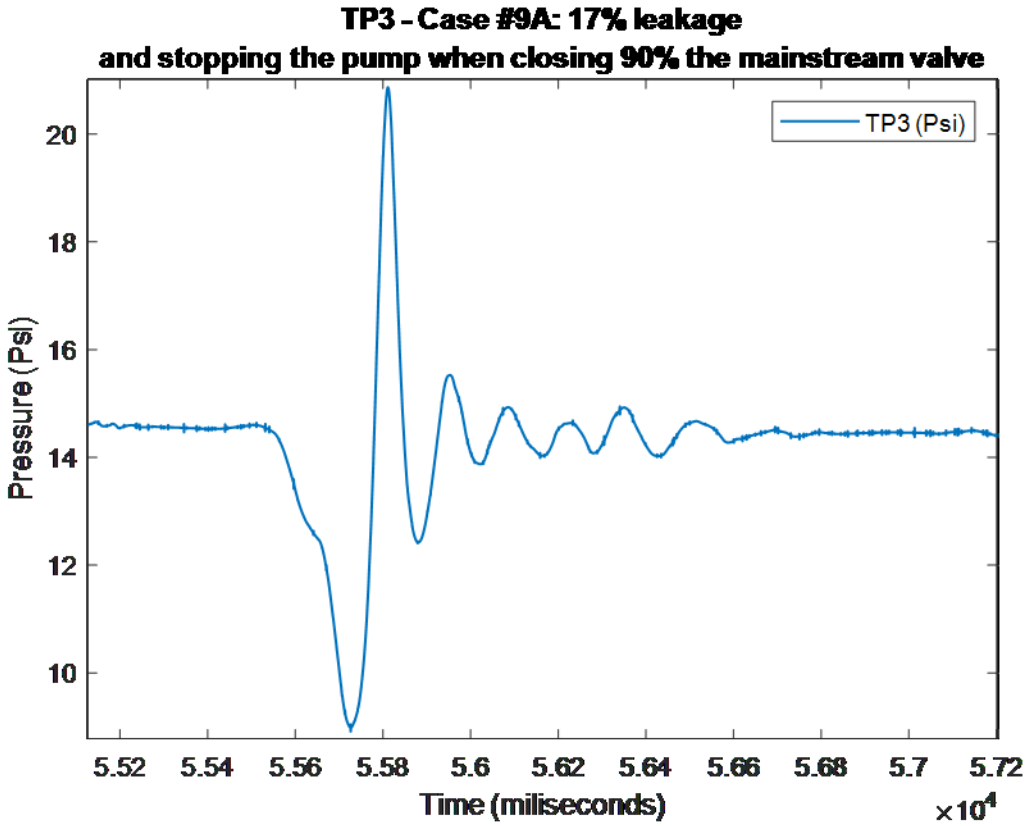

Figure 5.79: TP3 – Case #9A: 17% Leak rate & stopping the pump when closing 90% the mainstream valve

The effect of leakage is to attenuate the transient pressure oscillations significantly. The leakage rate is correlated with the attenuation of the transient. Moreover, the attenuation effect is more pronounced as more significant the order of the oscillation period is (Jonsson, 1994). Figures 5.80 and 5.81 confirm this conclusion; Figure 5.80 shows the pressure transient at TP1 when the pump is stopped under no leakage, while figure 5.81 does the same with a 17% leakage. Pressure transient with no leakage oscillates seven times before damping completely, with a period of 115 milliseconds (16,610 – 16,495 = 115). Conversely, pressure transient under 17%-leakage damped entirely after two oscillations with a period of 252 milliseconds (55,816.4 – 55,664.4 = 252). On the other hand, figure 5.77 shows the initial transient behavior (TP1) under rupture conditions which gives way to several resonant oscillations while figure 5.73 does similarly under no leakage conditions which results in few resonant oscillations.

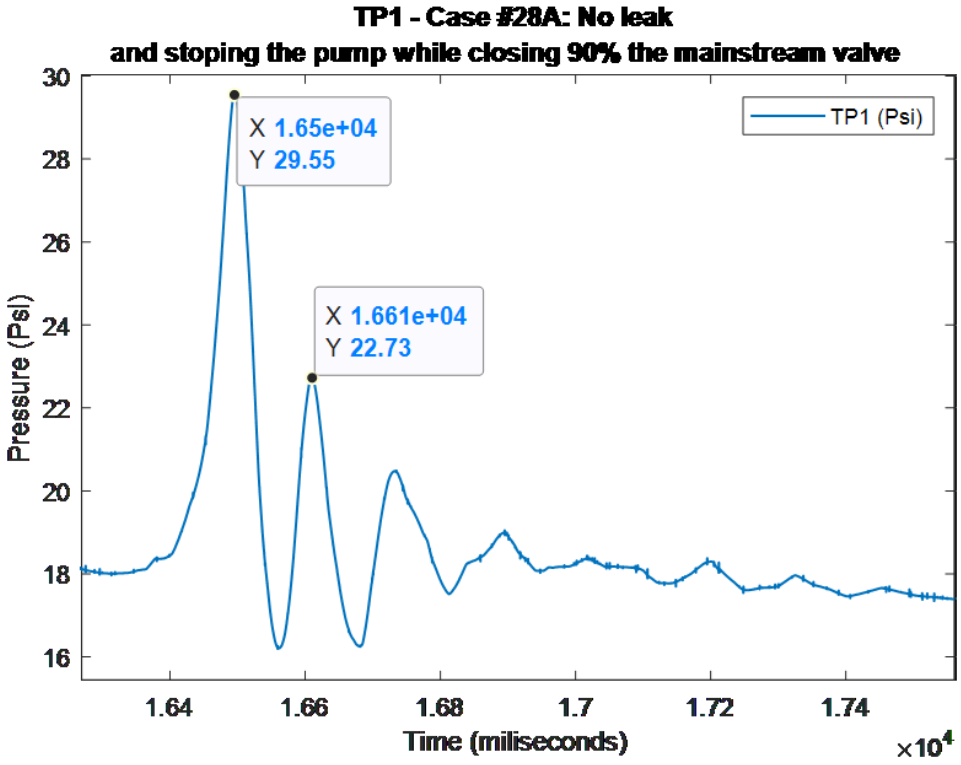

Figure 5.80: Pressure transient at TP1 when the pump is stopped / No leakage

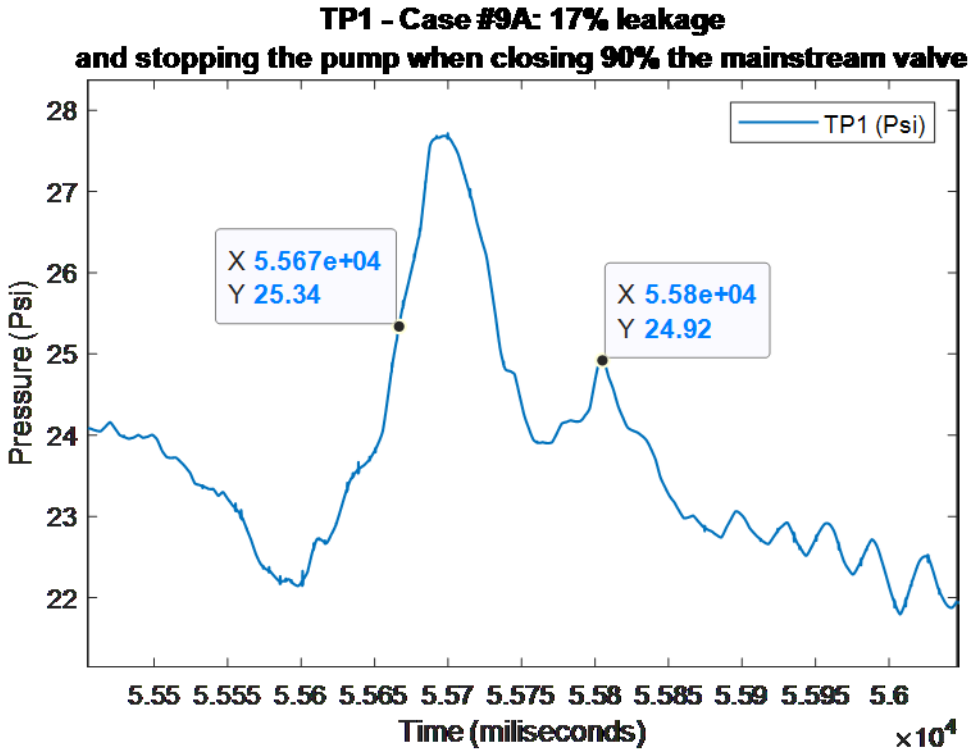

Figure 5.81: Pressure transient at TP1 when the pump is stopped / 17 % Leakage

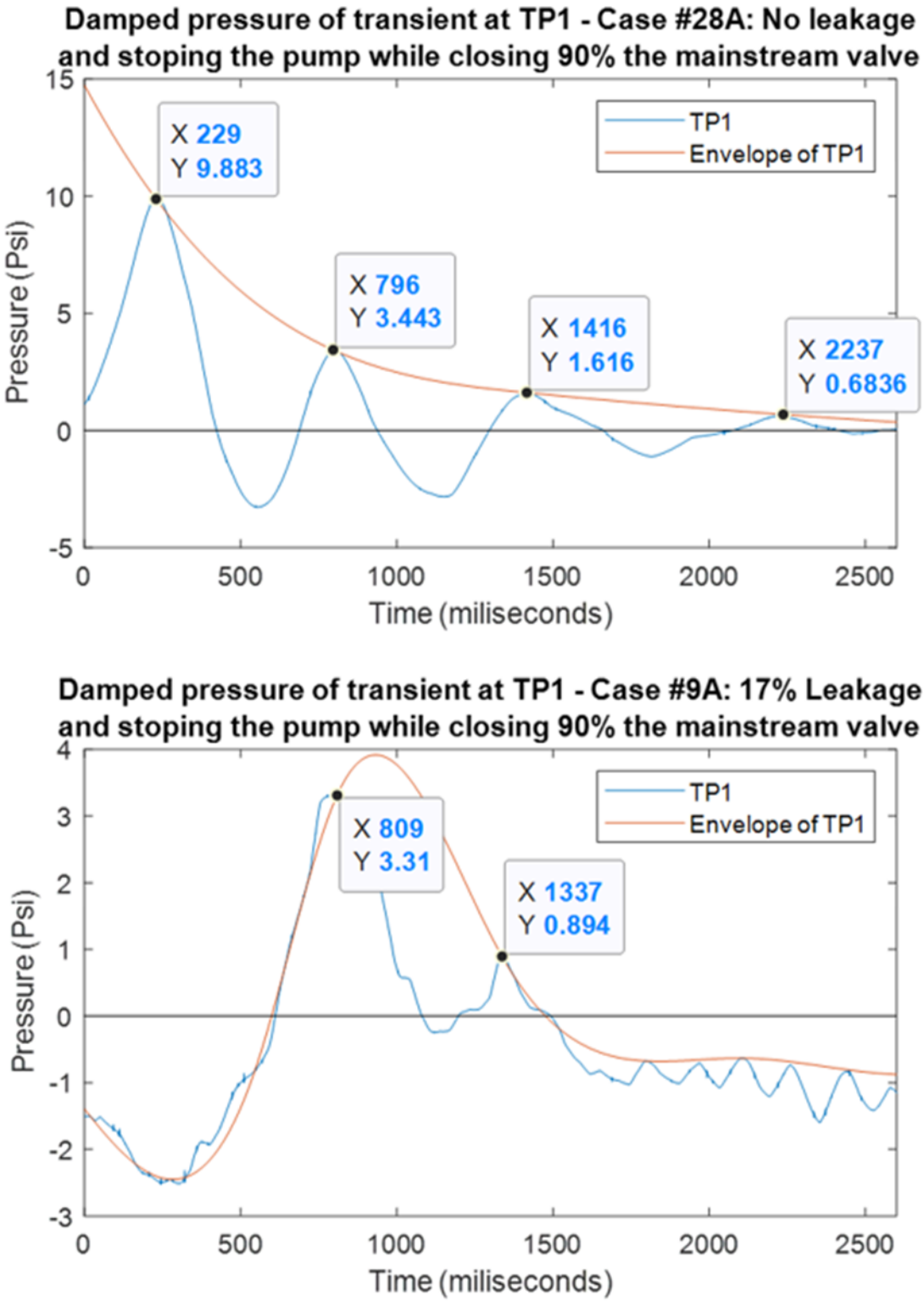

Figure 5.82: Envelope of pressure transients for cases 9A and 28A

Figure 5.82 shows the envelope of transients for cases 9A (17 % leakage) and 28A (No leakage), this data needs to be preprocessed to avoid systematic errors; damping ratio is calculated by relating two peaks of the oscillating signal who should oscillate about pressure equals zero. To calculate the damping coefficient using the graphical method requires the excitation signal to be a step. Transient happens when the pump is turned off, so the pressure falls steadily from 35 to 14.5 (psi), so to compensate this the data is narrowed down to 2.5 seconds, it is also calculated the pressure offset and pressure slope of the pump to trade off these differences, results are plotted in figure 5.82. The rate at which the amplitude of vibrations decays over time provides an advantageous method of identifying the degree of damping. The damping ratio ζ can be expressed in terms of the logarithmic decrement δ. Equations 5.1 and 5.2 defines the damping coefficient:

$$logarithmic\ decrement: \delta = ln\left(\frac{X_n}{X_{n+1}}\right) \qquad (5.1)$$

$$Damping\ coefficient: \xi = \frac{\delta}{\sqrt{(2\pi)^2 + \delta^2}} \qquad (5.2)$$

$$\delta_{no\ leakage} = ln\left(\frac{X_n}{X_{n+1}}\right) = ln\left(\frac{9.983}{3.443}\right) = 1.0545$$

$$\xi_{no\ leakage} = \frac{\delta}{\sqrt{(2\pi)^2 + \delta^2}} = \frac{1.0545}{\sqrt{(2\pi)^2 + 1.0545^2}} = 0.1655$$

$$\delta_{17\%\ leakage} = ln\left(\frac{3.31}{0.894}\right) = 1.309$$

$$\xi_{17\%\ leakage} = \frac{1.309}{\sqrt{(2\pi)^2 + 1.309^2}} = 0.2040$$

Coefficients concord with the leakage rate correlations, the coefficient for the no-leakage scenario is smaller than the resulting one in rupture conditions. The transient with the no-leakage condition is very clean as opposed to the transient under rupture conditions, which is distorted due to the pressure peaks out of the leak disturbance. As a result, the damping coefficient for the ruptured case includes both an instrumental and theoretical error because the data could not be leaned to oscillate about zero -psi- as for the no-leakage case;

on the other hand, the signal –for rupture- is not purely sinusoidal, hence the distortion on their peaks yields the aforementioned theoretical error.

The second way of studying the effect of a leak on the transient is related to the behavior of the pressure oscillations after valve closure. A leak will cause a growing disturbance of the pressure peaks making even small leaks visible provided that a large enough number of oscillations occur (Jonsson, 1994). Figure 5.83 zooms in the transient of case #9 at TP1, and results show the disturbance of the visible pressure peaks in the oscillations. Jonsson also claimed that a large enough number of oscillations occur, as portrayed in figure 2.10 (chapter 2), yet for the present research oscillations are lower because the pump's inertia is low. Thus the research-pump entirely stops in five seconds whereas Jonsson's stops by 3 minutes or so.

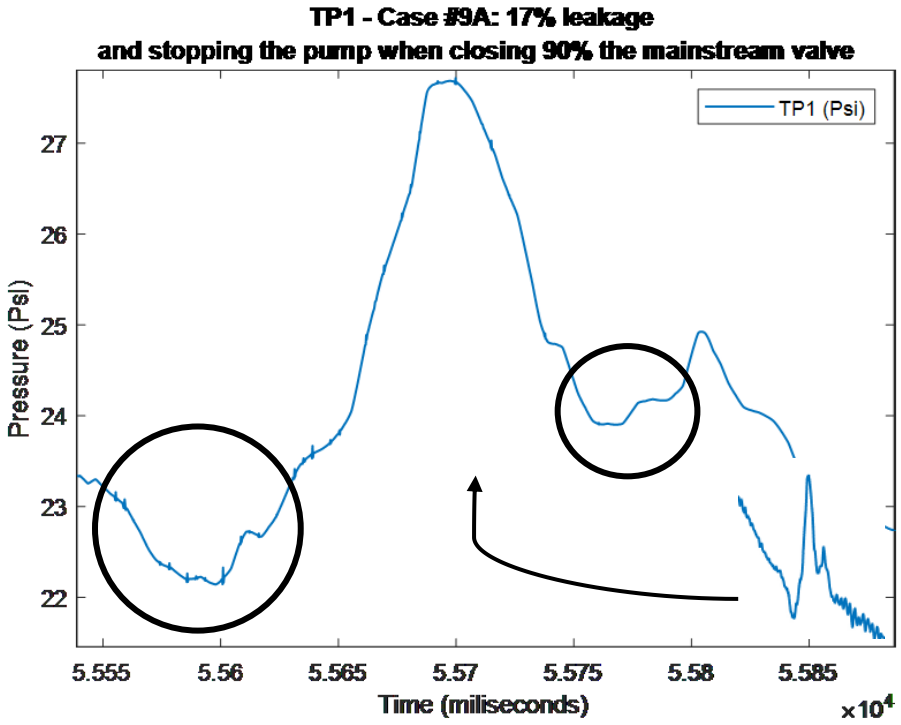

Case #9: 17% Leakage/closing valve when the pump is stopped

Figure 5.83: Zoom in of Transient at TP1

As Jonsson said, "the combination of pump stop and small inertia gives rise to a very steep negative wave part of it being reflected at the leak situated at an unknown distance from the pump." The return of the reflected wave is visible as a small, abrupt pressure change

in the computed pressure transient at the pump. Figure 5.84 shows this effect in experiment #9A, the denoising technique is Wavelet: bior2.4 / Level: 7 / Denoising Method: Universal Threshold / Threshold Rule: Soft / Noise: Level Dependent. This technique removes the pump-noise efficiently at a high signal distortion cost. However, for analysis purposes, the signal shows the steep negative wave part of it being reflected at the leak, as stated by Jonsson. Appendix 11 details all the denoising parameters for the signals denoised.

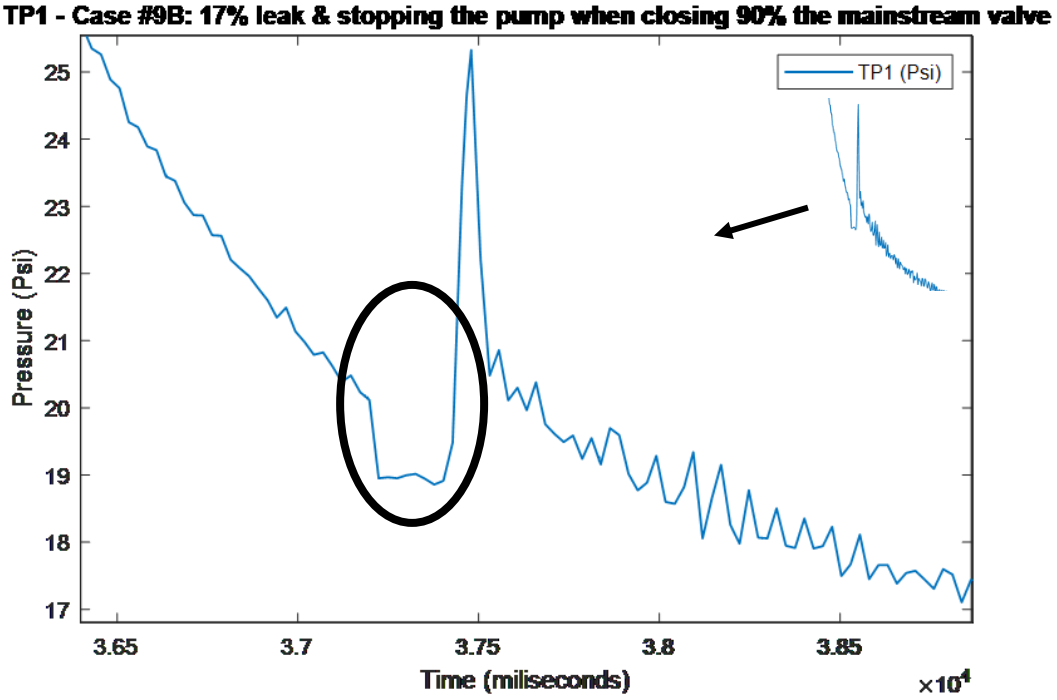

Case #9B: 17% Leakage/closing valve when the pump is stopped

Figure 5.84: Zoom in of Transient at TP1

5.2.6.1 Transient-state (vibration) results

Figures from 5.85 to 5.88 shows the pipe vibration under no-leakage and rupture conditions. Pressure transient is also reflected as pipe vibration, under no-leakage, the accelerometers show no vibrations, whereas transients under rupture conditions show vibration peaks. Throughout the current experiments, the vibration results do not show unique features as the pressure transducers do because of the accelerometer' specifications, their resolution is very low for this application, according to the manufacturer its applications are automotive-body and power-train measurements.

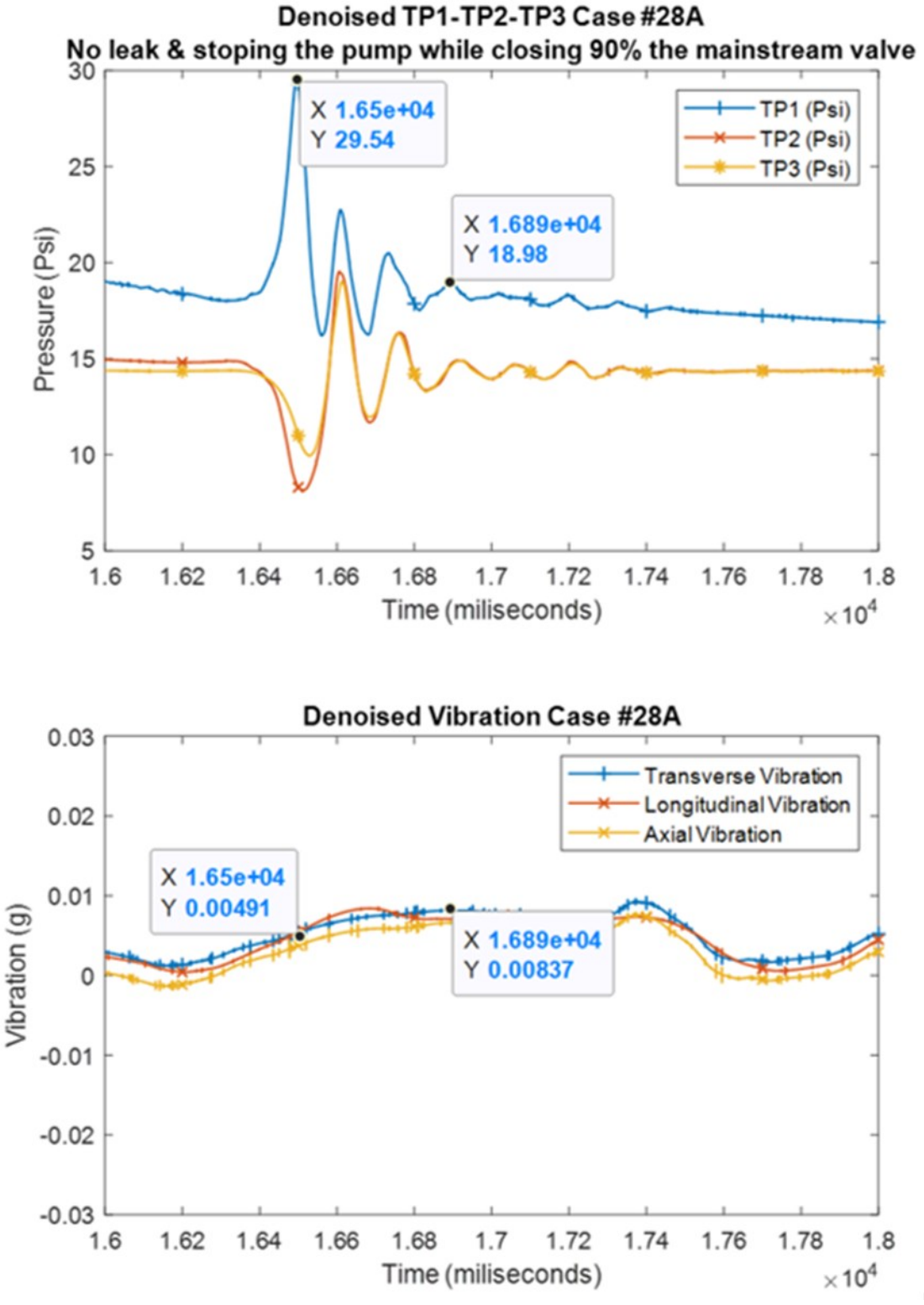

Case #28A: Closing 90% mainstream valve when the pump is stopped / Leakage 0 %

Figure 5.85: Pipe vibration when pressure transient (First trial)

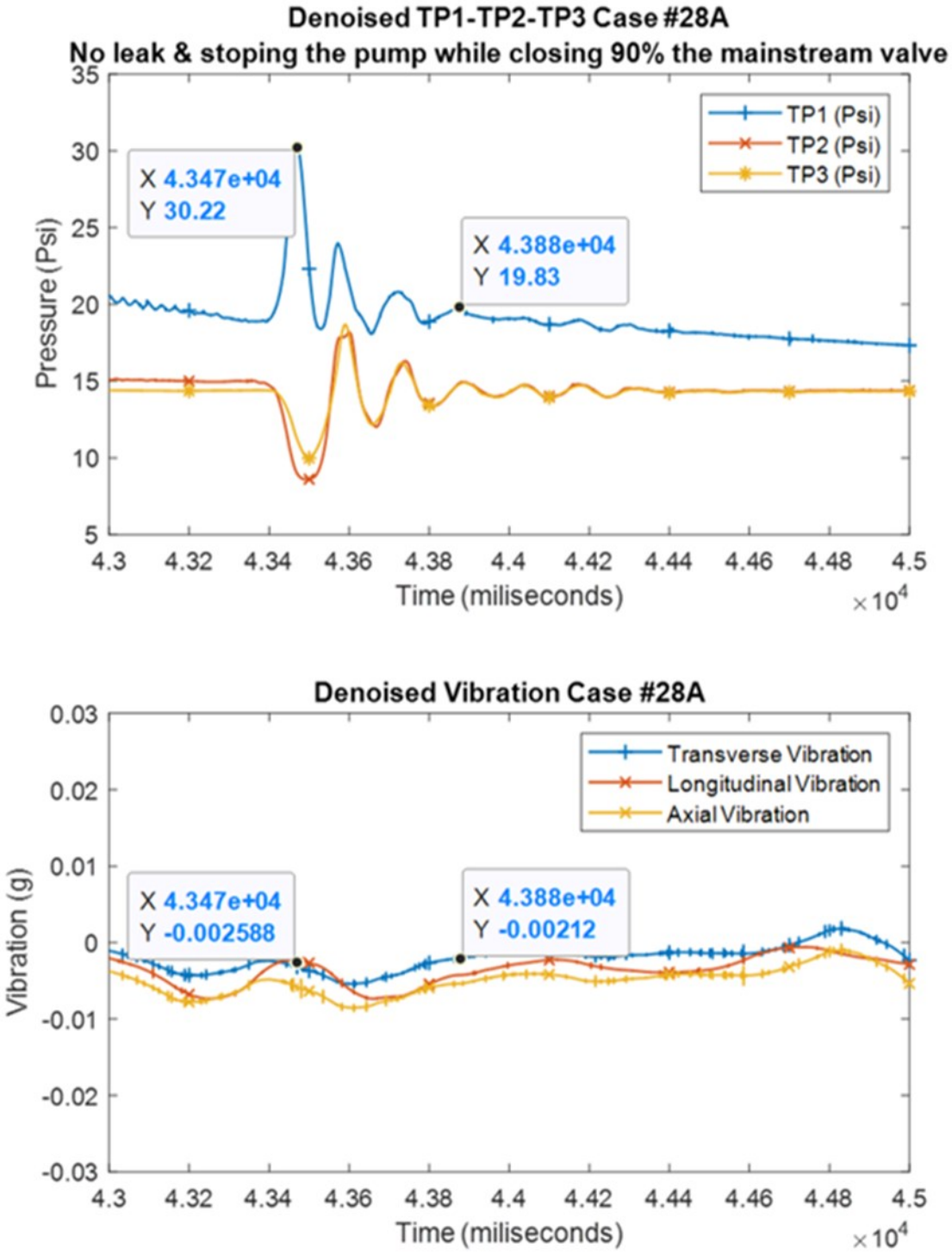

Case #28A: Closing 90% mainstream valve when the pump is stopped / Leakage 0 %

Figure 5.86: Pipe vibration when pressure transient (Second trial)

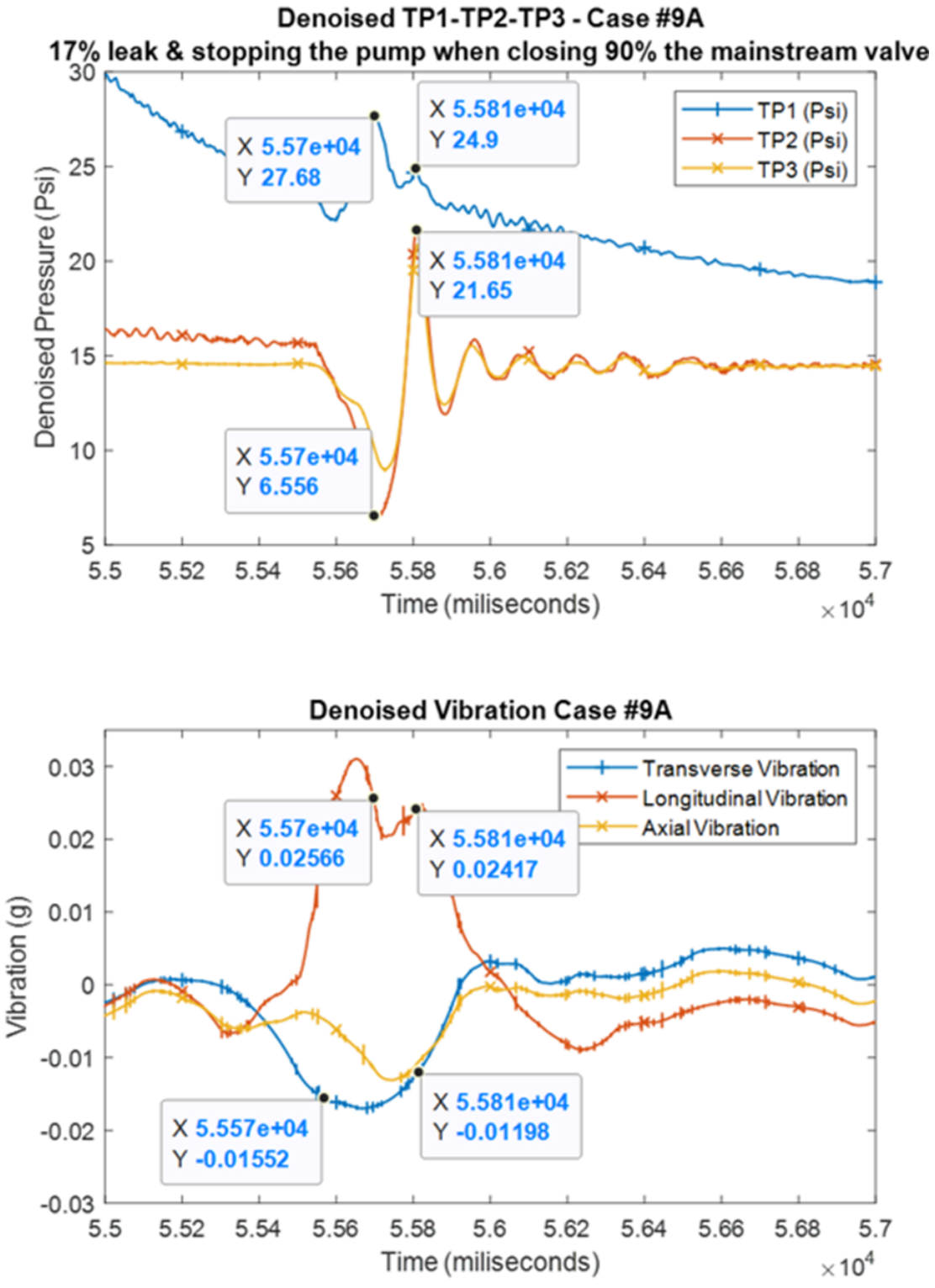

Case #9A: Closing 90% mainstream valve when the pump is stopped / Leakage 17 %

Figure 5.87: Pipe vibration when pressure transient (First trial)

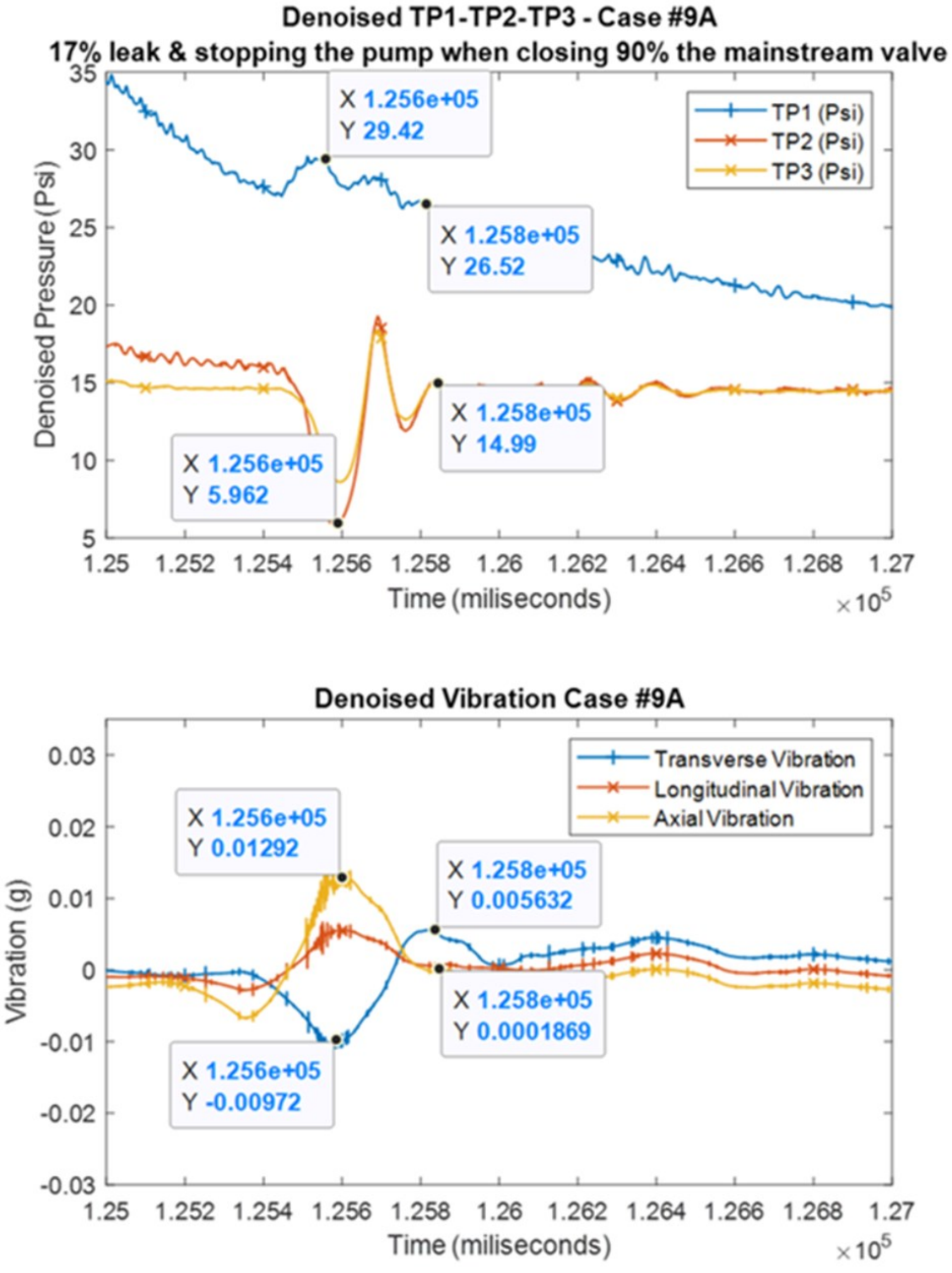

Case #9A: Closing 90% mainstream valve when the pump is stopped / Leakage 17 %

Figure 5.88: Pipe vibration when pressure transient (Second trial)

5.2.7 ANOVA analysis

5.2.7.1 ANOVA analysis of dielectric permittivity

ANOVA is used to analyze the testbed's experimental data. Assuming the truth of the null hypothesis, the rejection of this hypothesis is justified, if the probability (p-value) is less than 0.05 (significance level). The null hypothesis assumes that all groups are random samples from the same population. For instance, when examining the effect of different factors (such as fluid velocity, moisture level, pinhole size, type of soil) on similar test samples, the null hypothesis would be that all input variables have the same effect on the responding variables. Rejecting the null hypothesis means that the differences in observed effects are unlikely to be due to random chance. On the other hand, an F-ratio higher than one means that the variation amongst group means is more than expected to see by chance. ANOVA is performed to Dielectric Permittivity under leaking conditions, figures 5.89 to 5.94, and no-leaking conditions, figures 5.96 to 5.99; Figure 5.95 shows the ANOVAN analysis of DP under leaking conditions.

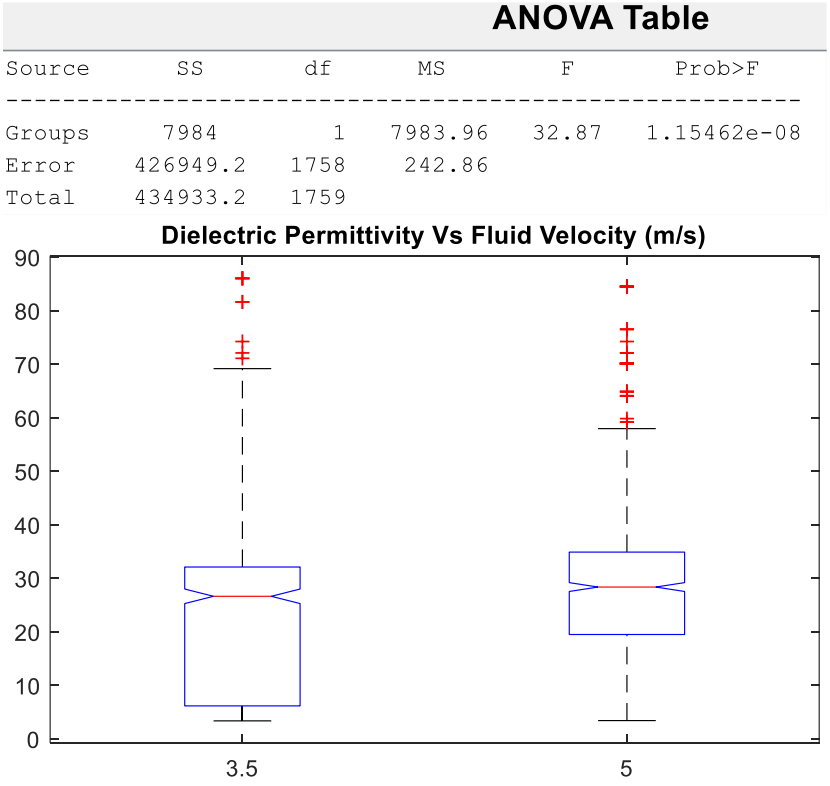

Figure 5.89: Fluid velocity effect on DP under leakage conditions

ANOVA Table

Source	SS	df	MS	F	Prob>F
Groups	25894.7	1	25894.7	111.29	2.85413e-25
Error	409038.5	1758	232.7		
Total	434933.2	1759			

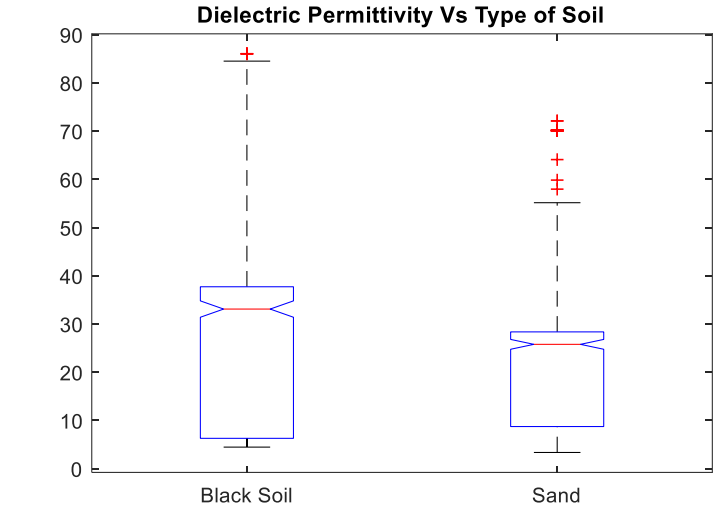

Figure 5.90: Type of soil effect on DP under leakage conditions

ANOVA Table

Source	SS	df	MS	F	Prob>F
Groups	162233.5	22	7374.25	46.97	3.18475e-158
Error	272699.7	1737	156.99		
Total	434933.2	1759			

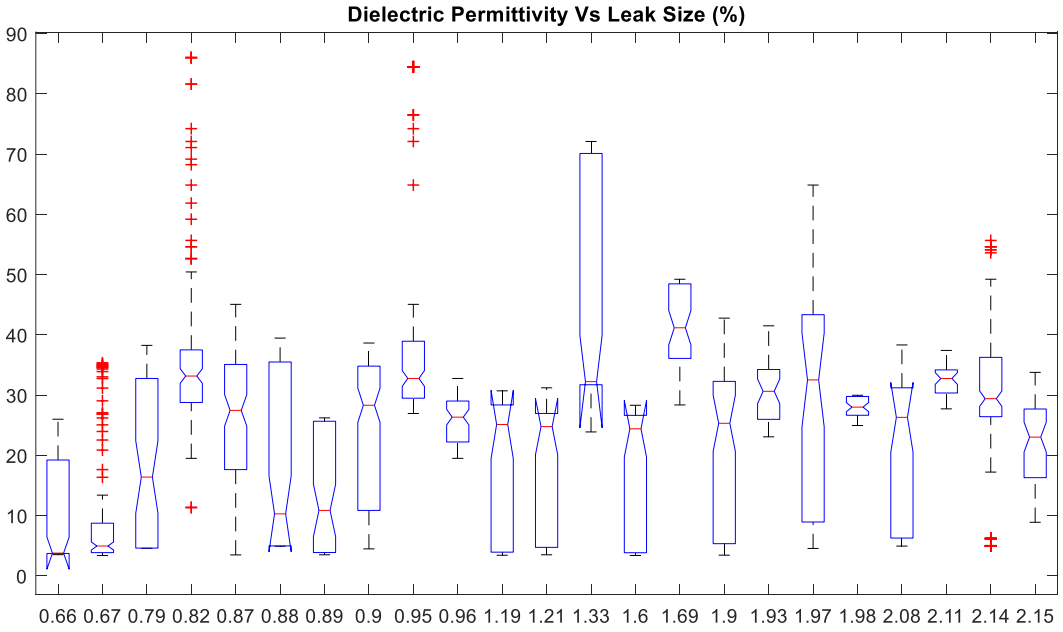

Figure 5.91: Leak size effect on DP under leakage conditions

ANOVA Table

Source	SS	df	MS	F	Prob>F
Groups	137808	1	137808	815.37	1.1715e-147
Error	297125.1	1758	169		
Total	434933.2	1759			

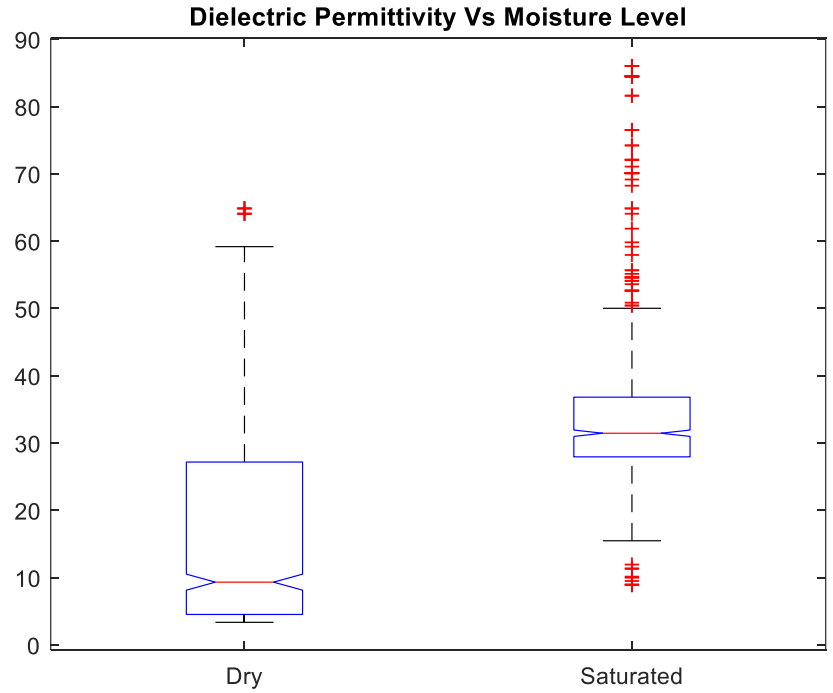

Figure 5.92: Moisture level effect on DP under leakage conditions

The dielectric permittivity probes were reallocated when increasing the water level to ensure their integrity, resulting in the outliers shown in figure 5.92; this happened mainly in saturation conditions. Figure 5.89 shows no incidence of fluid velocity on the mean of dielectric permittivity because this variable depends primarily on the amount of commodity released. Soil's permeability impacts DP as plotted in figure 5.90. Figure 5.91 shows the substantial influence of leak size as expected. F-values calculated among groups are higher than one (1) as expected, proving that the variation amongst groups is due to the factors' influences on the soil's dielectric permittivity rather than random error. Results in figure 5.94 assess how the probe location influences the results; leak points towards DP2 whereas DP1 is deployed in the opposite direction.

ANOVA Table

Source	SS	df	MS	F	Prob>F
Groups	4537.6	1	4537.6	18.53	1.76067e-05
Error	430395.6	1758	244.82		
Total	434933.2	1759			

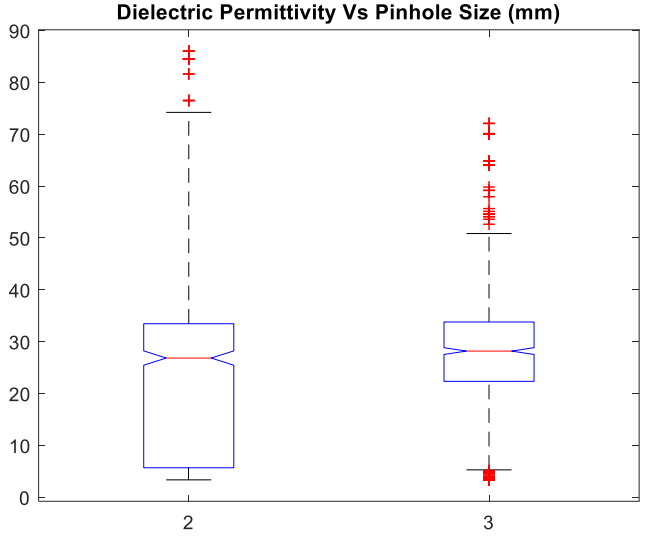

Figure 5.93: Pinhole size effect on DP under leakage conditions

ANOVA Table

Source	SS	df	MS	F	Prob>F
Groups	6656.1	1	6656.12	27.32	1.92768e-07
Error	428277.1	1758	243.62		
Total	434933.2	1759			

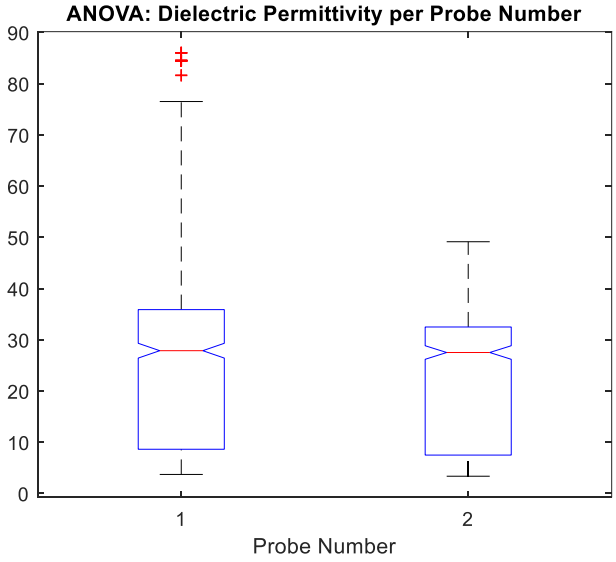

Figure 5.94: Probe number effect on DP under leakage conditions

Analysis of Variance

	Source	Sum Sq.	d.f.	Mean Sq.	F	Prob>F
	FVelocity	9800	1	9800	69.62	0
	Pinholesize	5070.8	1	5070.8	36.02	0
#	SoilCondition	124776.3	1	124776.3	886.42	0
#	TypeofSoil	22167.2	1	22167.2	157.48	0
	FVelocity*Pinholesize	595.9	1	595.9	4.23	0.0398
#	FVelocity*SoilCondition	75.5	1	75.5	0.54	0.4641
#	FVelocity*TypeofSoil	348	1	348	2.47	0.116
#	Pinholesize*SoilCondition	7614.8	1	7614.8	54.1	0
#	Pinholesize*TypeofSoil	1552.9	1	1552.9	11.03	0.0009
#	SoilCondition*TypeofSoil	2810.6	1	2810.6	19.97	0
	Error	246197.8	1749	140.8		
	Total	434933.2	1759			

Figure 5.95: ANOVAN analysis of DP under leakage conditions

P-results from the N-way analysis of variance (ANOVAN) indicates how significant are the interactions between factors. High p-values indicate that the corresponding interactions are not significant, whereas low p-values indicate otherwise. As a result, pinhole size, and type of soil are significant because the soil is either isotropically or anisotropically, thus defining how the liquids permeate the medium, and pinhole size defines the amount of liquids released, so the interaction of both variables impacts the soil's dielectric permittivity significantly. On the other hand, the interaction between fluid velocity and soil condition have a negligible impact on DP because fluid velocity does not affect the soil moisture in saturation point, for instance.

All 'F-values' from ANOVA are higher than one (1) whereas 'P-values' are less than 0.05. As a result, the null hypothesis is rejected, meaning, that factors have different effects on the responding variables under leaking conditions. Moreover, observed differences are unlikely to be due to random sampling.

Figures 5.96 to 5.99 shows ANOVA results of DP under no-leaking conditions, the only 'P-value' higher than 0.05 is when analyzing the effect of the probes themselves. Hence, even though the probes are different, their systematic error negligibly influences the soil's dielectric permittivity.

ANOVA Table

Source	SS	df	MS	F	Prob>F
Groups	1010	1	1009.99	7.42	0.0066
Error	154645.7	1136	136.13		
Total	155655.6	1137			

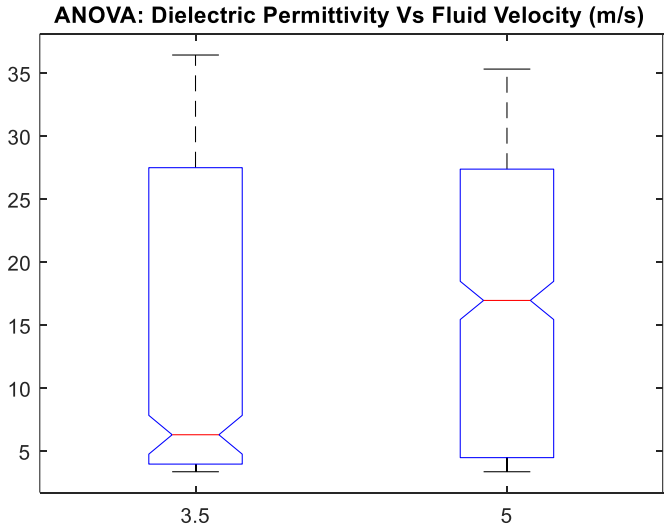

Figure 5.96: Fluid velocity effect on DP under no-leakage conditions

ANOVA Table

Source	SS	df	MS	F	Prob>F
Groups	8116	1	8116.02	62.49	6.30036e-15
Error	147539.6	1136	129.88		
Total	155655.6	1137			

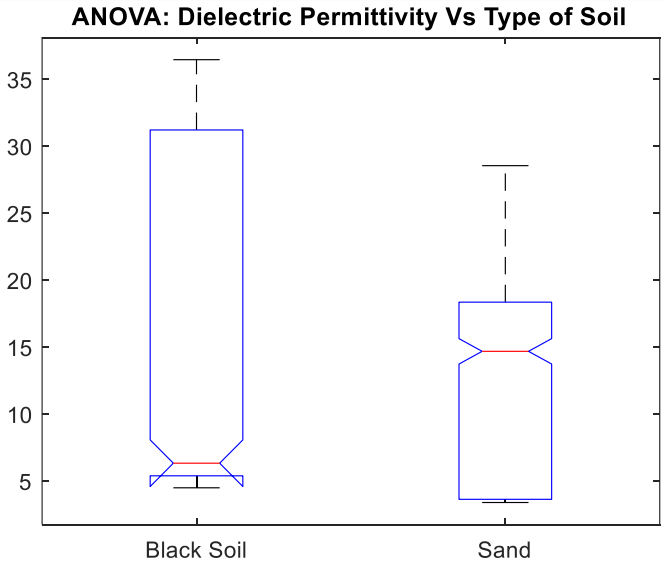

Figure 5.97: Type of soil effect on DP under no-leakage conditions

ANOVA Table

Source	SS	df	MS	F	Prob>F
Groups	129265.7	1	129265.7	5564.46	0
Error	26389.9	1136	23.2		

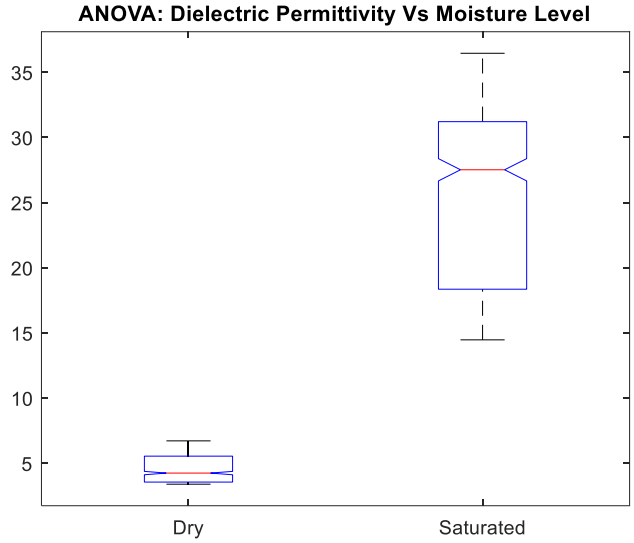

Figure 5.98: Moisture level effect on DP under no-leakage conditions

ANOVA Table

Source	SS	df	MS	F	Prob>F
Groups	51.7	1	51.679	0.38	0.5392
Error	155604	1136	136.975		
Total	155655.6	1137			

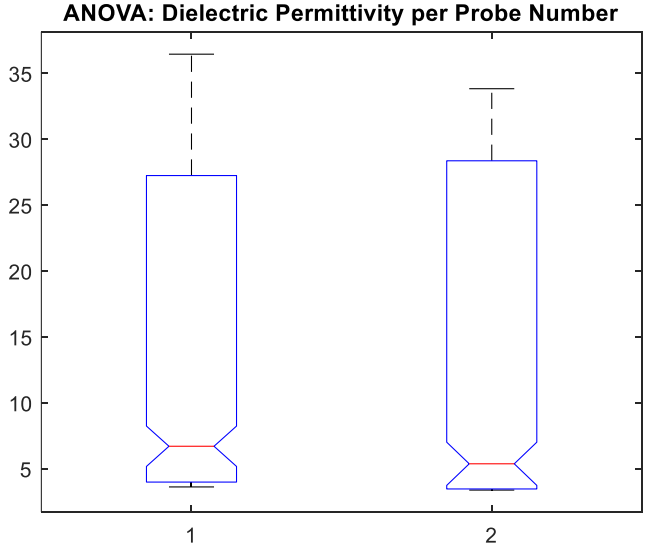

Figure 5.99: Probe number effect on DP under no-leakage conditions

5.2.7.2 ANOVA analysis of soil temperature

ANOVA is performed to test the null hypothesis, which examines the effect of different factors (such as fluid velocity, moisture level, pinhole size, type of soil) on similar test samples. The factors have a different effect on the soil's temperature if the null hypothesis is rejected. Figures 5.100 to 5.114 shows ANOVA results per thermocouple.

ANOVA Table

Source	SS	df	MS	F	Prob>F
Groups	3921.6	1	3921.59	83.82	6.58064e-20
Error	428219.4	9153	46.78		
Total	432141	9154			

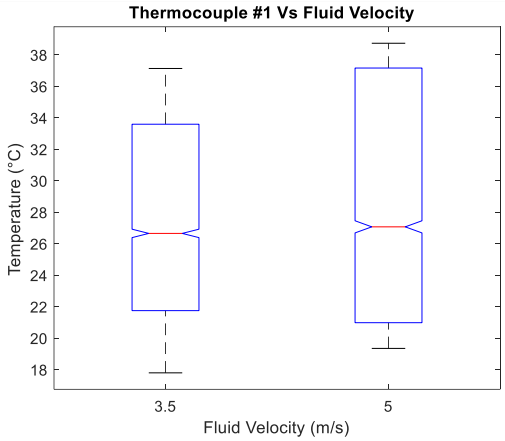

Figure 5.100: Fluid velocity effect on TT1 under leakage conditions

ANOVA Table

Source	SS	df	MS	F	Prob>F
Groups	130.5	1	130.509	3.34	0.0676
Error	357582	9153	39.067		
Total	357712.6	9154			

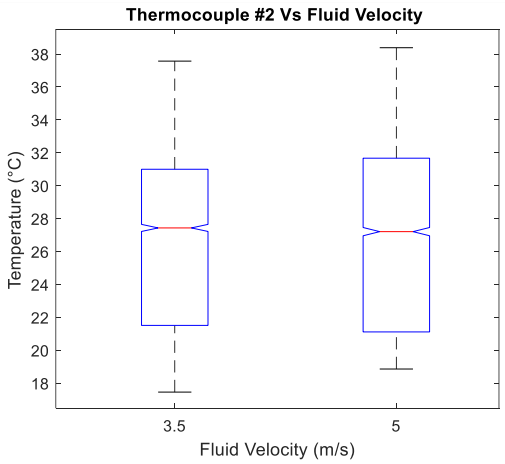

Figure 5.101: Fluid velocity effect on TT2 under leakage conditions

ANOVA Table

Source	SS	df	MS	F	Prob>F
Groups	893.8	1	893.769	31.25	2.33598e-08
Error	261798	9153	28.602		
Total	262691.8	9154			

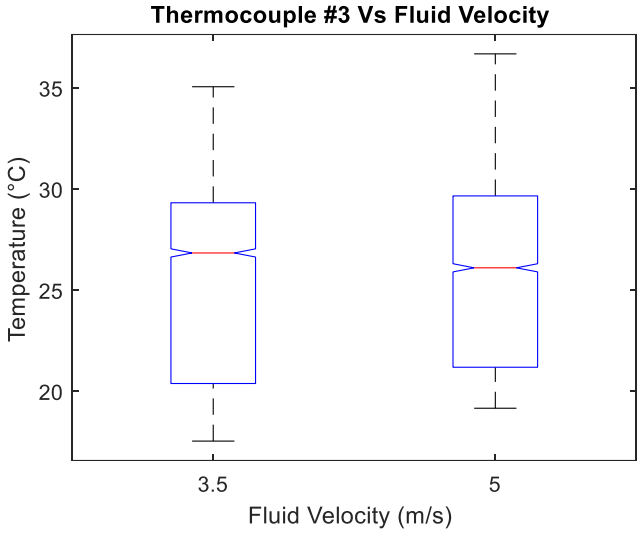

Figure 5.102: Fluid velocity effect on TT3 under leakage conditions

ANOVA Table

Source	SS	df	MS	F	Prob>F
Groups	302783.8	1	302783.8	21424.25	0
Error	129357.2	9153	14.1		
Total	432141	9154			

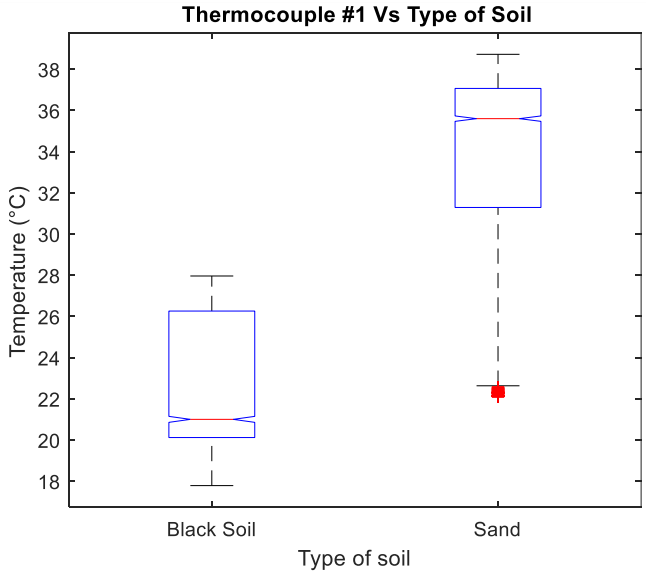

Figure 5.103: Type of soil effect on TT1 under leakage conditions

ANOVA Table

Source	SS	df	MS	F	Prob>F
Groups	217194.3	1	217194.3	14147.48	0
Error	140518.3	9153	15.4		
Total	357712.6	9154			

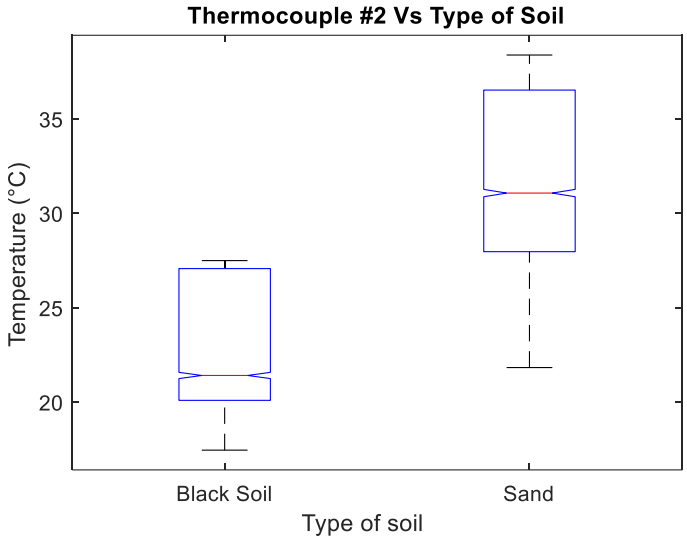

Figure 5.104: Type of soil effect on TT2 under leakage conditions

ANOVA Table

Source	SS	df	MS	F	Prob>F
Groups	124065.2	1	124065.2	8191.57	0
Error	138626.5	9153	15.1		
Total	262691.8	9154			

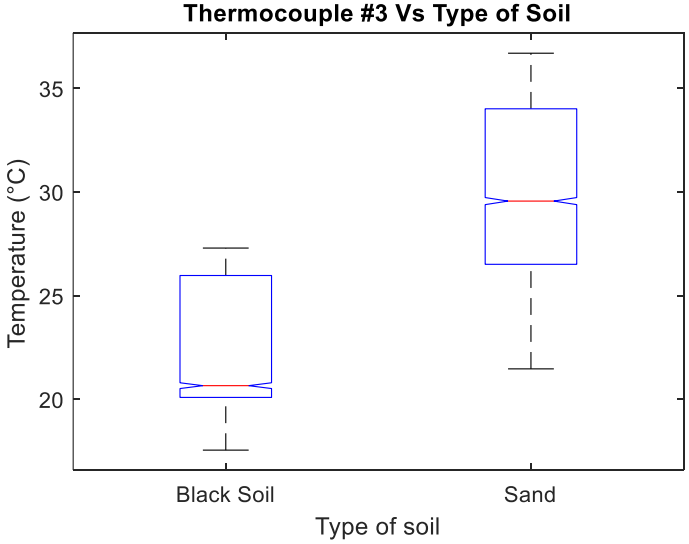

Figure 5.105: Type of soil effect on TT3 under leakage conditions

All ‘F-values’ from ANOVA are higher than one (1) whereas ‘P-values’ are less than 0.05, so both fluid velocity and type of soil affect differently the thermocouple’s readings because (a) the thermocouples are deployed at different places, and (b) fluid velocity depends linearly on fluid pressure. On the other hand, the soil’s permeability defines how the liquids permeate the medium, substantially affecting the soil temperature when a leak happens. The thermocouples were reallocated when increasing the water level to ensure their integrity, resulting in the outliers plotted in figures 5.106 to 5.108.

ANOVA Table

Source	SS	df	MS	F	Prob>F
Groups	231584.5	11	21053.1	959.77	0
Error	200556.5	9143	21.9		
Total	432141	9154			

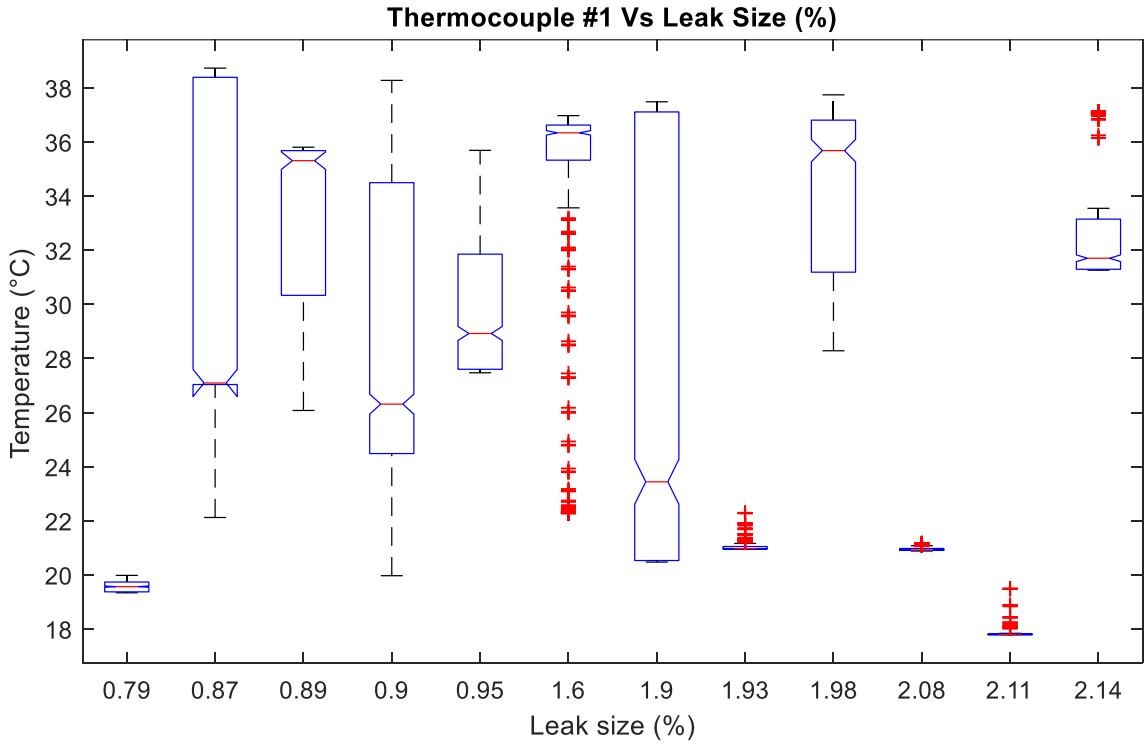

Figure 5.106: Leak size effect on TT1 under leakage conditions

ANOVA Table

Source	SS	df	MS	F	Prob>F
Groups	213212.7	11	19382.98	1226.43	0
Error	144499.8	9143	15.8		
Total	357712.6	9154			

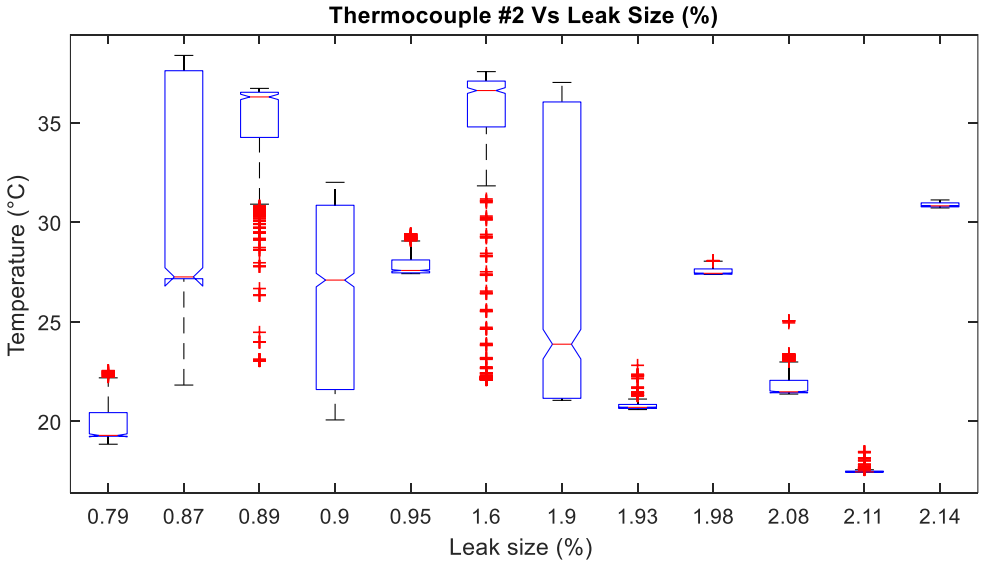

Figure 5.107: Leak size effect on TT2 under leakage conditions

ANOVA Table

Source	SS	df	MS	F	Prob>F
Groups	121508	11	11046.2	715.35	0
Error	141183.8	9143	15.4		
Total	262691.8	9154			

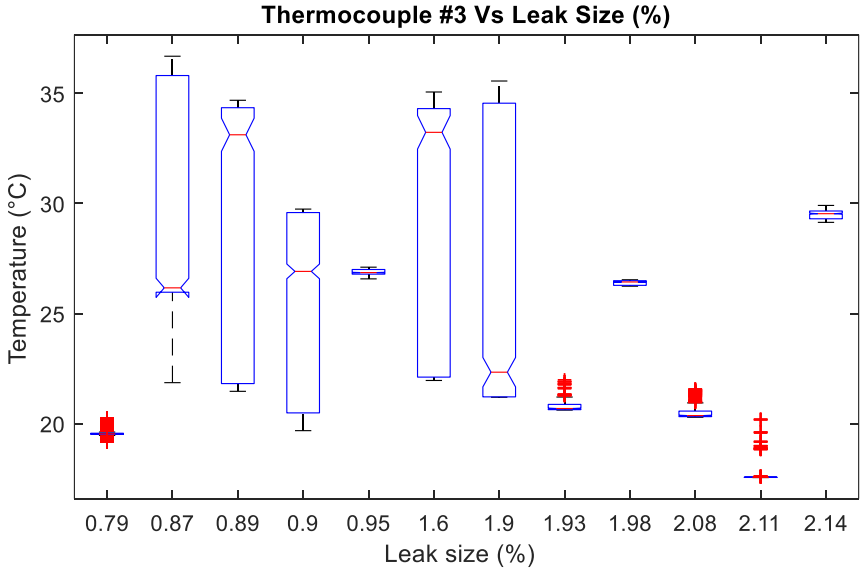

Figure 5.108: Leak size effect on TT3 under leakage conditions

ANOVA Table

Source	SS	df	MS	F	Prob>F
Groups	219.4	1	219.422	4.65	0.0311
Error	431921.5	9153	47.189		
Total	432141	9154			

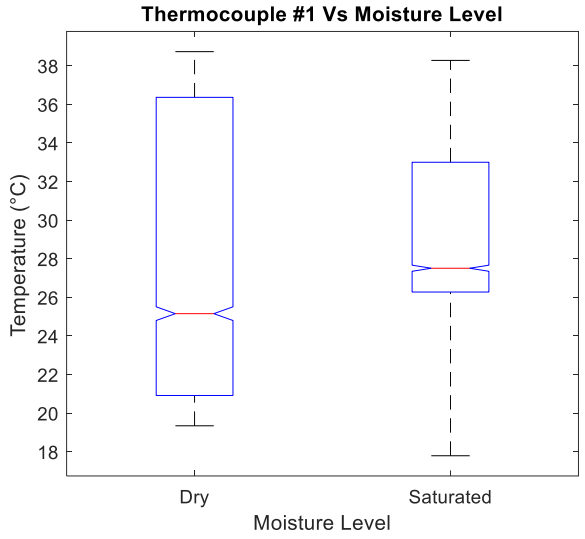

Figure 5.109: Moisture effect on TT1 under leakage conditions

ANOVA Table

Source	SS	df	MS	F	Prob>F
Groups	5880.5	1	5880.51	152.98	7.33085e-35
Error	351832	9153	38.44		
Total	357712.6	9154			

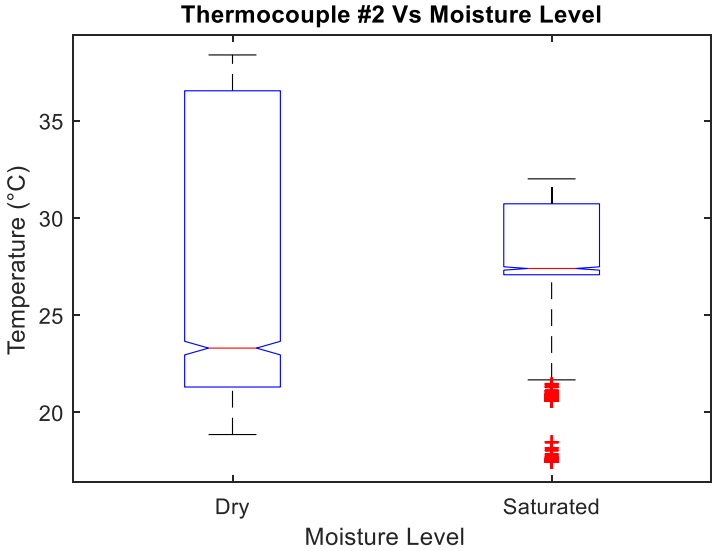

Figure 5.110: Moisture effect on TT2 under leakage conditions

ANOVA Table

Source	SS	df	MS	F	Prob>F
Groups	38.5	1	38.5024	1.34	0.2468
Error	262653.3	9153	28.6959		
Total	262691.8	9154			

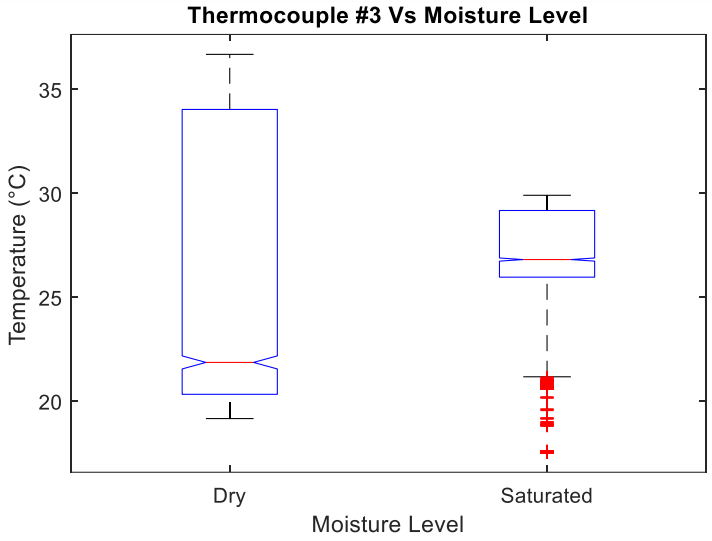

Figure 5.111: Moisture effect on TT3 under leakage conditions

ANOVA Table

Source	SS	df	MS	F	Prob>F
Groups	5432.2	1	5432.2	116.52	5.30998e-27
Error	426708.8	9153	46.62		
Total	432141	9154			

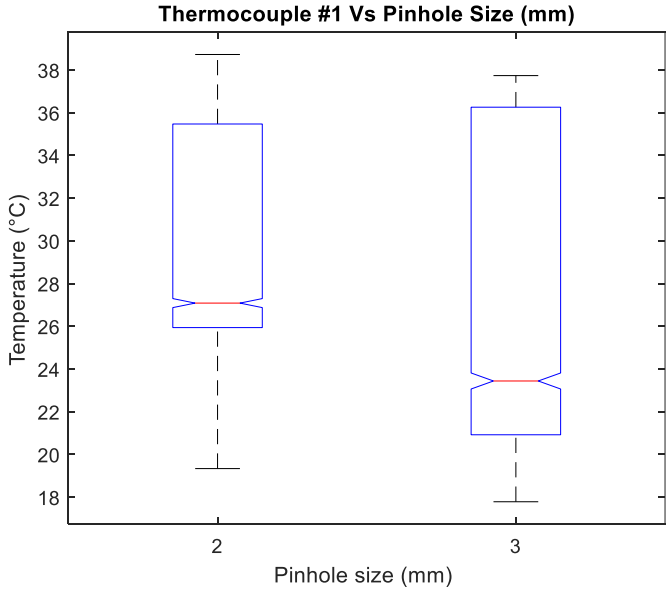

Figure 5.112: Pinhole size on TT1 under leakage conditions

ANOVA Table

Source	SS	df	MS	F	Prob>F
Groups	8170.1	1	8170.05	213.94	6.58149e-48
Error	349542.5	9153	38.19		
Total	357712.6	9154			

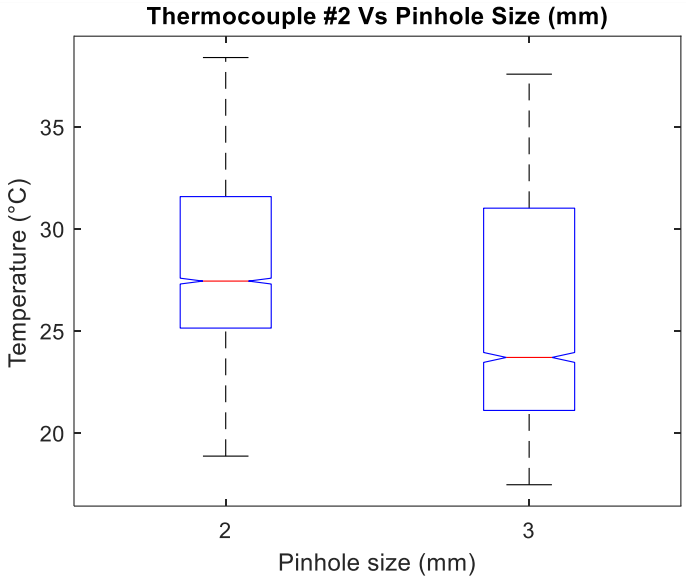

Figure 5.113: Pinhole size on TT2 under leakage conditions

ANOVA Table

Source	SS	df	MS	F	Prob>F
Groups	6267.2	1	6267.19	223.71	5.46387e-50
Error	256424.6	9153	28.02		
Total	262691.8	9154			

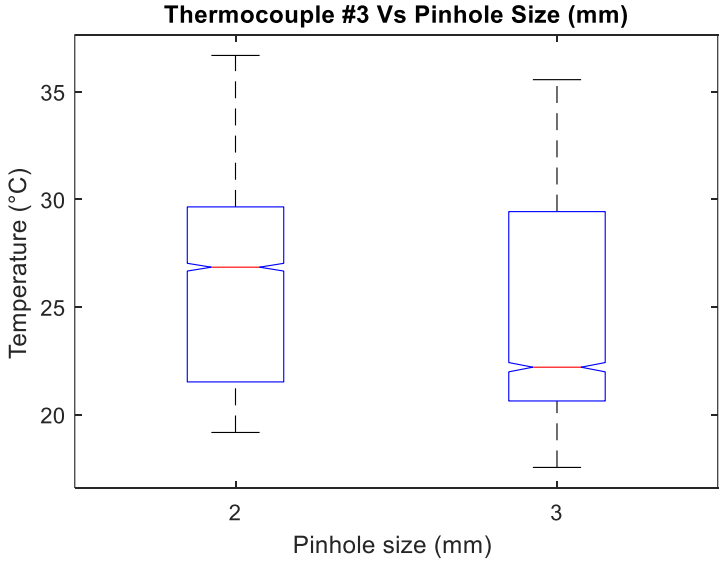

Figure 5.114: Pinhole size effect on TT3 under leakage conditions

Analysis of Variance

Source	Sum Sq.	d.f.	Mean Sq.	F	Prob>F
FVelocity	3168.4	1	3168.4	30.03	0
Pinholesize	74465.2	1	74465.2	705.83	0
SoilCondition	723229.9	1	723229.9	6855.28	0
TypeofSoil	1551933.9	1	1551933.9	14710.32	0
FVelocity*Pinholesize	163.2	1	163.2	1.55	0.2136
FVelocity*SoilCondition	3.5	1	3.5	0.03	0.8545
FVelocity*TypeofSoil	2572.3	1	2572.3	24.38	0
Pinholesize*SoilCondition	2.3	1	2.3	0.02	0.8818
Pinholesize*TypeofSoil	148260.5	1	148260.5	1405.32	0
SoilCondition*TypeofSoil	22.6	1	22.6	0.21	0.6432
Error	964689	9144	105.5		
Total	3538157.6	9154			

Analysis of Variance

Source	Sum Sq.	d.f.	Mean Sq.	F	Prob>F
FVelocity	329	1	329	38.41	0
Pinholesize	9094.7	1	9094.7	1061.64	0
SoilCondition	5245.1	1	5245.1	612.27	0
TypeofSoil	215468.7	1	215468.7	25152.01	0
FVelocity*Pinholesize	653.2	1	653.2	76.25	0
FVelocity*SoilCondition	356.5	1	356.5	41.62	0
FVelocity*TypeofSoil	4.3	1	4.3	0.51	0.4767
Pinholesize*SoilCondition	8965	1	8965	1046.5	0
Pinholesize*TypeofSoil	3288.1	1	3288.1	383.82	0
SoilCondition*TypeofSoil	34349.4	1	34349.4	4009.67	0
Error	78333.5	9144	8.6		
Total	357712.6	9154			

Analysis of Variance

Source	Sum Sq.	d.f.	Mean Sq.	F	Prob>F
FVelocity	1263.3	1	1263.3	111.93	0
Pinholesize	6557.9	1	6557.9	581.05	0
SoilCondition	16.3	1	16.3	1.44	0.2295
TypeofSoil	126608	1	126608	11217.79	0
FVelocity*Pinholesize	70.2	1	70.2	6.22	0.0126
FVelocity*SoilCondition	236.7	1	236.7	20.97	0
FVelocity*TypeofSoil	258.7	1	258.7	22.92	0
Pinholesize*SoilCondition	8522	1	8522	755.07	0
Pinholesize*TypeofSoil	4023.6	1	4023.6	356.5	0
SoilCondition*TypeofSoil	14296.2	1	14296.2	1266.68	0
Error	103202.5	9144	11.3		
Total	262691.8	9154			

Figure 5.115: ANOVAN analysis of thermocouples under leaking conditions (upper) TT1 (medium) TT2 (lower) TT3

Interaction between factors affects more -as expected- readings of thermocouple TT1 than both TT2 and TT3's, under leaking conditions. TT1 is more sensitive to these interactions because the leak points towards to the thermocouple n°1, so TT1's response time is faster than the others. Hence, the maximum temperature detected by TT1 is also higher since the liquids cool down due to heat convection. Figures from 5.116 to 5.120 show the ANOVA results to the thermocouples all together.

ANOVA Table

Source	SS	df	MS	F	Prob>F
Groups	2023.4	1	2023.43	1637.53	0
Error	21116.2	17089	1.24		
Total	23139.6	17090			

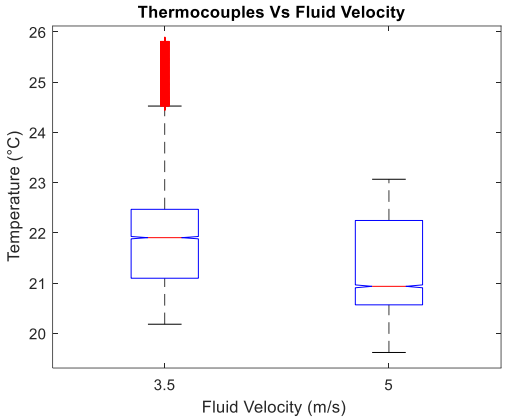

Figure 5.116: Fluid velocity effect on TT1/TT2/TT3 under no-leakage conditions

ANOVA Table

Source	SS	df	MS	F	Prob>F
Groups	3951.8	1	3951.79	3519.53	0
Error	19187.8	17089	1.12		
Total	23139.6	17090			

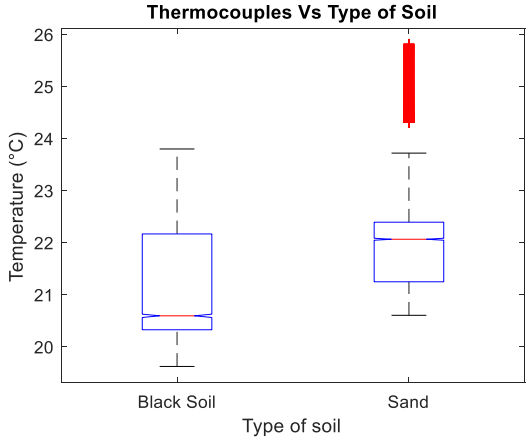

Figure 5.117: Type of soil effect on TT1/TT2/TT3 under no-leakage conditions

ANOVA Table

Source	SS	df	MS	F	Prob>F
Groups	57.6	1	57.6278	42.67	6.67852e-11
Error	23082	17089	1.3507		
Total	23139.6	17090			

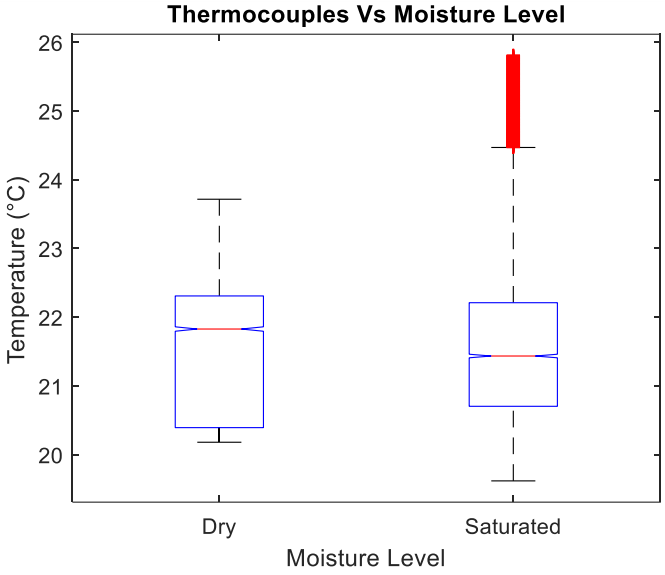

Figure 5.118: Moisture effect on TT1/TT2/TT3 under no-leakage conditions

ANOVA Table

Source	SS	df	MS	F	Prob>F
Groups	31323.2	2	15661.6	408.63	1.33324e-175
Error	1052545.3	27462	38.3		
Total	1083868.5	27464			

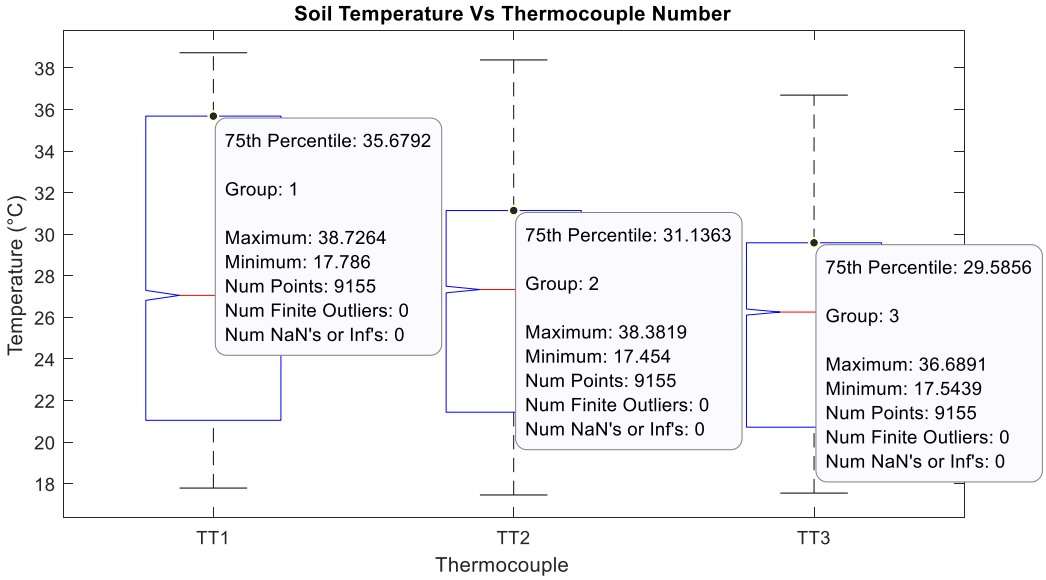

Figure 5.119: Variance of TT1/TT2/TT3 under leakage conditions

Analysis of Variance

Source	Sum Sq.	d.f.	Mean Sq.	F	Prob>F
FVelocity	5408	1	5408	439.76	0
Pinholesize	21276.7	1	21276.7	1730.13	0
SoilCondition	803	1	803	65.3	0
TypeofSoil	634657.8	1	634657.8	51607.76	0
FVelocity*Pinholesize	406.4	1	406.4	33.05	0
FVelocity*SoilCondition	1548.3	1	1548.3	125.9	0
FVelocity*TypeofSoil	2315.3	1	2315.3	188.27	0
Pinholesize*SoilCondition	24489.9	1	24489.9	1991.42	0
Pinholesize*TypeofSoil	15102	1	15102	1228.03	0
SoilCondition*TypeofSoil	50086.4	1	50086.4	4072.82	0
Error	337621.6	27454	12.3		
Total	1083868.5	27464			

Figure 5.120: ANOVAN analysis of TT1/TT2/TT3 under leakage conditions

Figure 5.120 proves that TT1 is more sensitive to leaks than TT2 and TT3. TT1's upper confidence limit is 35.67 °C, whereas TT2's equals 31.13 °C and TT3's is 29.58 °C. Given these points, the null hypothesis is rejected, meaning, that factors do affect the soil temperature. Observed differences are unlikely to be due to random sampling.

5.2.7.3 ANOVA analysis of pressure

ANOVA Table

Source	SS	df	MS	F	Prob>F
Groups	91077.6	1	91077.6	2441.33	0
Error	1024551.6	27463	37.3		
Total	1115629.2	27464			

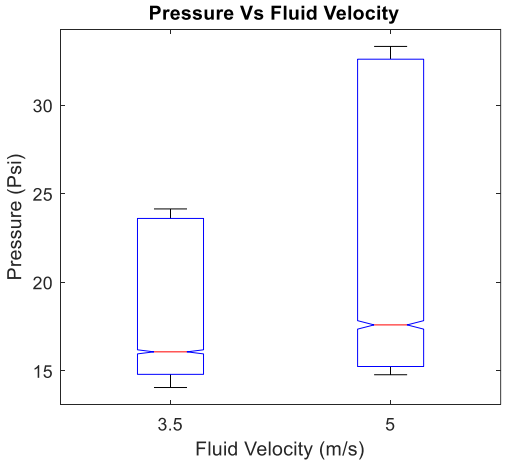

Figure 5.121: Effect of fluid velocity on pressure under leakage conditions

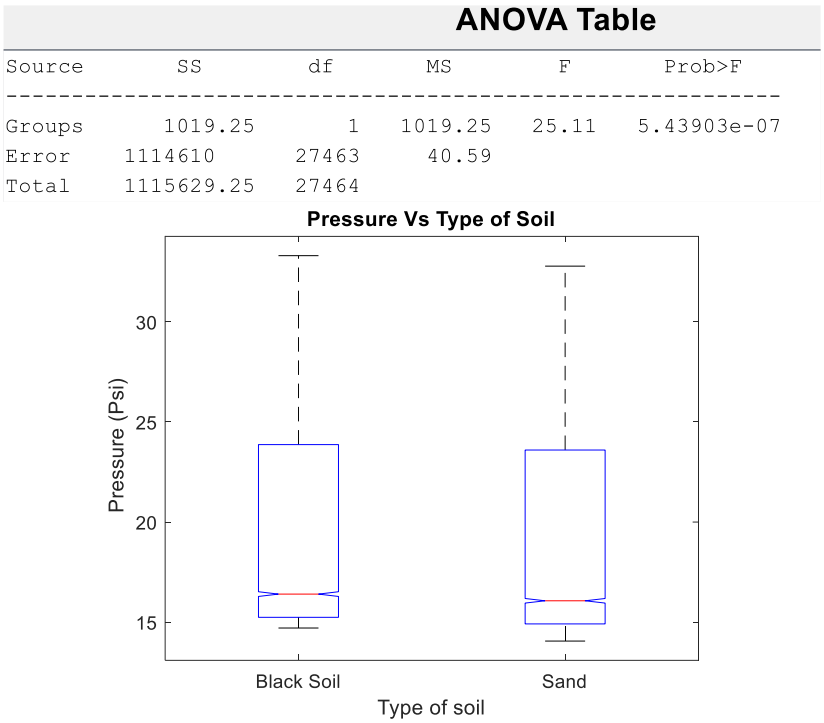

Figure 5.122: Effect of fluid velocity on pressure under leakage conditions

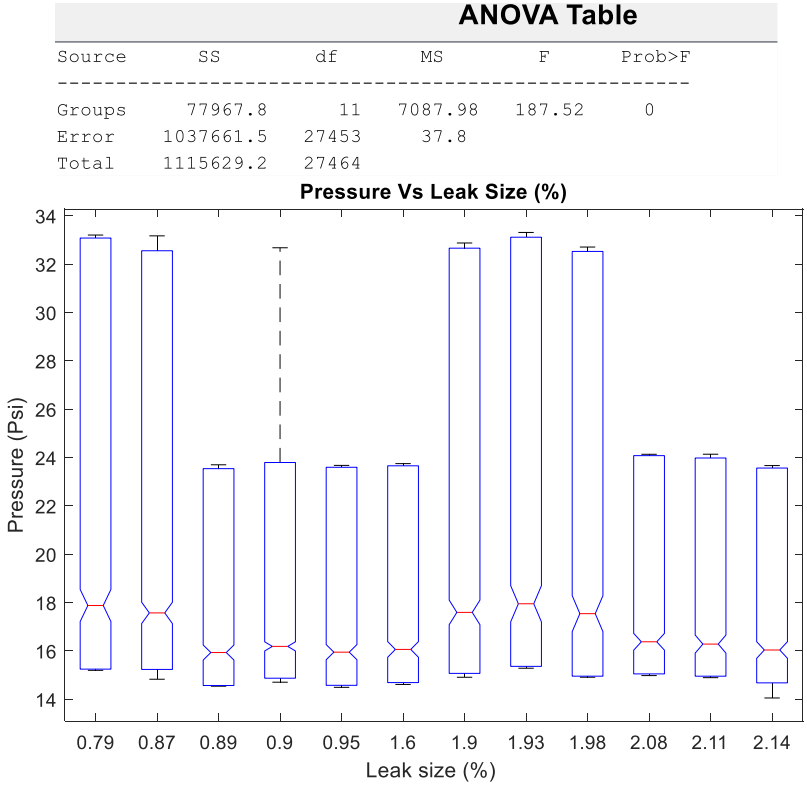

Figure 5.123: Effect of leak size on pressure under leakage conditions

ANOVA Table

Source	SS	df	MS	F	Prob>F
Groups	0.35469	1	0.3547	0.01	0.9256
Error	1115628.89354	27463	40.623		
Total	1115629.24823	27464			

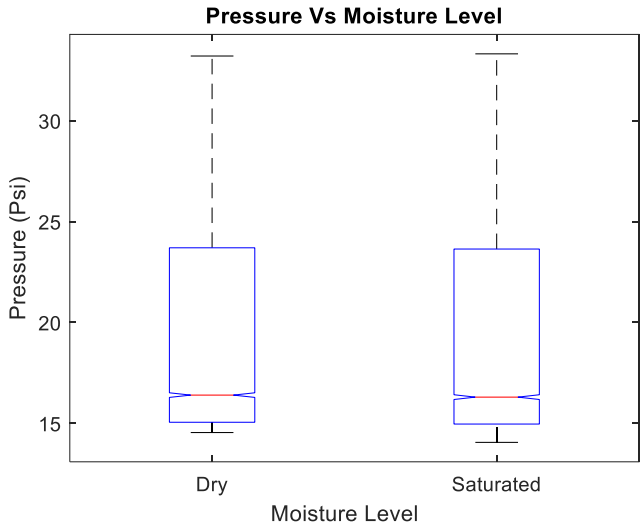

Figure 5.124: Effect of Moisture on pressure under leakage conditions

ANOVA Table

Source	SS	df	MS	F	Prob>F
Groups	1.46409	1	1.4641	0.04	0.8494
Error	1115627.78413	27463	40.6229		
Total	1115629.24823	27464			

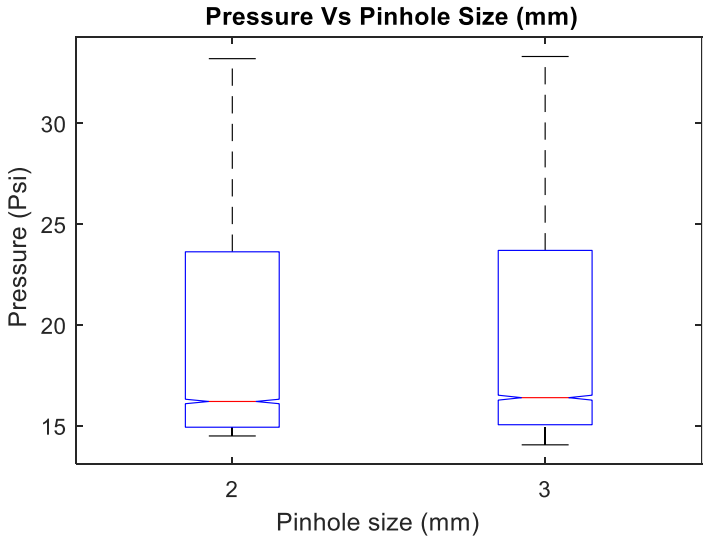

Figure 5.125: Effect of pinhole size on pressure under leakage conditions

Analysis of Variance

	Source	Sum Sq.	d.f.	Mean Sq.	F	Prob>F
	FVelocity	89251.1	1	89251.1	2393.37	0
	Pinholesize	32.5	1	32.5	0.87	0.3502
#	SoilCondition	1.4	1	1.4	0.04	0.8466
#	TypeofSoil	661.9	1	661.9	17.75	0
	FVelocity*Pinholesize	38.8	1	38.8	1.04	0.308
#	FVelocity*SoilCondition	13.6	1	13.6	0.37	0.5456
#	FVelocity*TypeofSoil	7.1	1	7.1	0.19	0.6633
#	Pinholesize*SoilCondition	4.3	1	4.3	0.12	0.7345
#	Pinholesize*TypeofSoil	0	1	0	0	0.993
#	SoilCondition*TypeofSoil	2.4	1	2.4	0.06	0.7998
	Error	1023787.7	27454	37.3		
	Total	1115629.2	27464			

Figure 5.126: ANOVAN analysis of pressure under leakage conditions

Fluid velocity is by far the primary driver of the pressure profiles. Interaction between factors is no significant because pressure depends on the fluid properties and the pump horsepower, yet amongst these factors (except fluid velocity), pinhole size influences the most pressure, these results are consistent with the pressure-profile technique -5.2.5-.

5.2.7.4 ANOVA analysis of vibration

ANOVA Table

Source	SS	df	MS	F	Prob>F
Groups	0.00007	1	7.3282e-05	9.27	0.0023
Error	0.07232	9153	7.90133e-06		
Total	0.07239	9154			

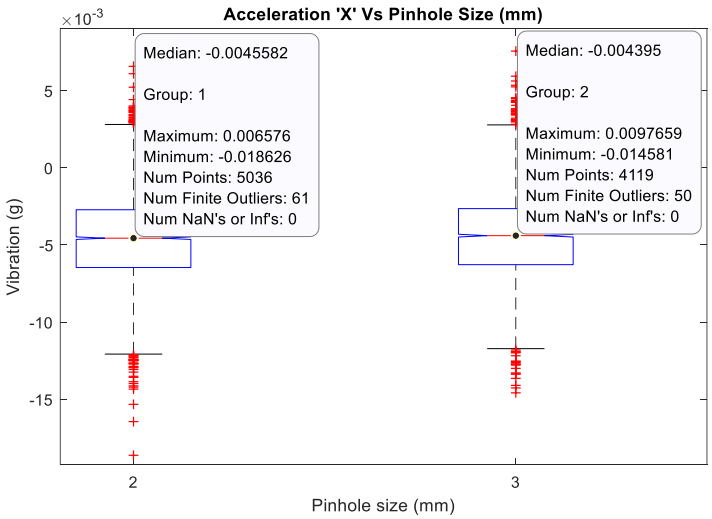

Figure 5.127: Effect of pinhole size on vibration 'X' under leakage conditions

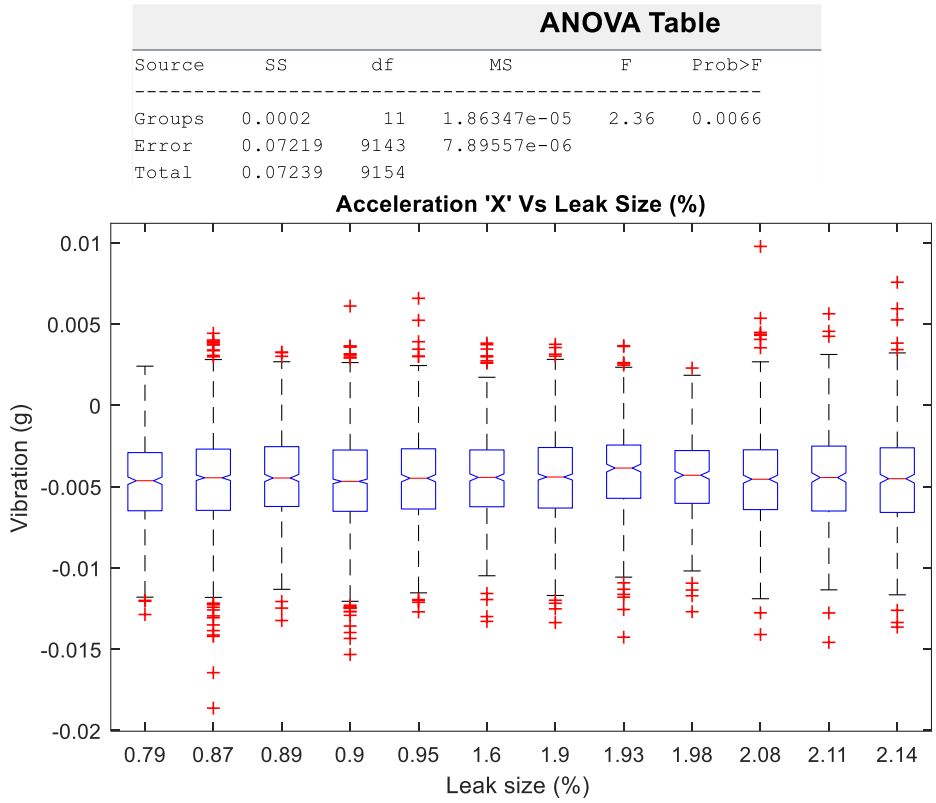

Figure 5.128: Effect of leakage on vibration 'X' under leakage conditions

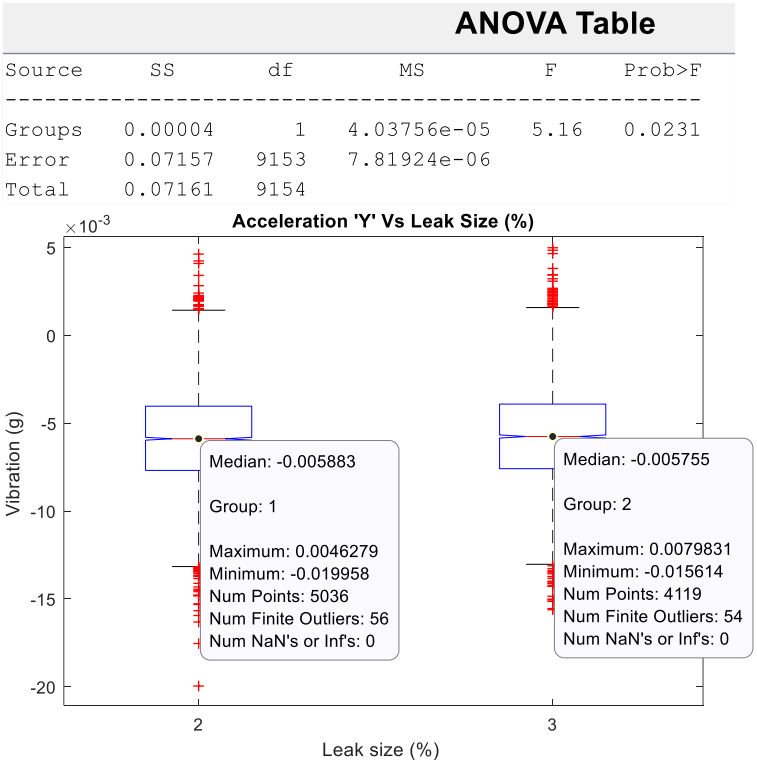

Figure 5.129: Effect of pinhole size on vibration 'Y' under leakage conditions

ANOVA Table

Source	SS	df	MS	F	Prob>F
Groups	0.00027	11	2.43661e-05	3.12	0.0003
Error	0.07134	9143	7.80289e-06		
Total	0.07161	9154			

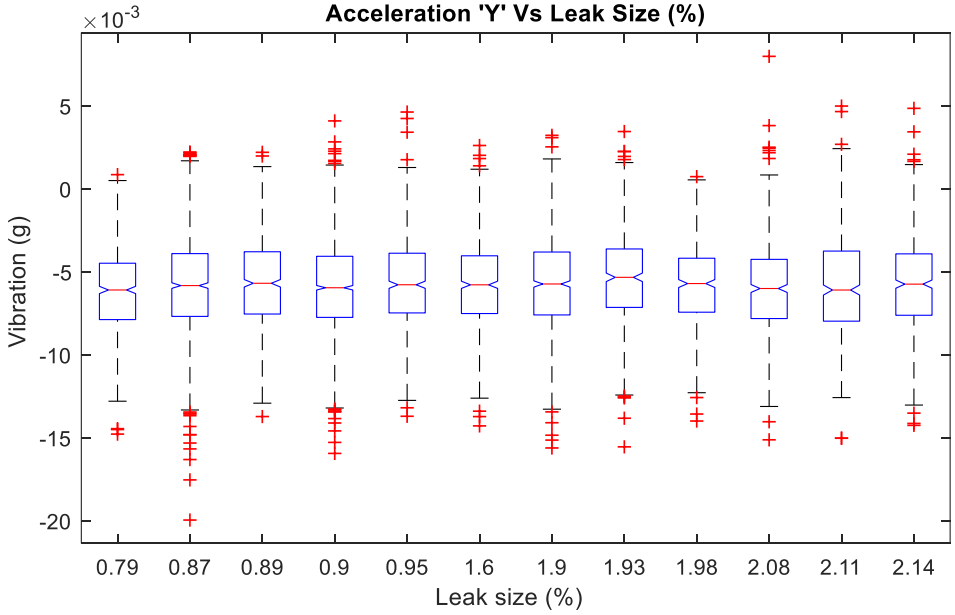

Figure 5.130: Effect of leakage on vibration 'Y' under leakage conditions

ANOVA Table

Source	SS	df	MS	F	Prob>F
Groups	0.00004	1	4.21152e-05	5.44	0.0197
Error	0.07081	9153	7.73573e-06		
Total	0.07085	9154			

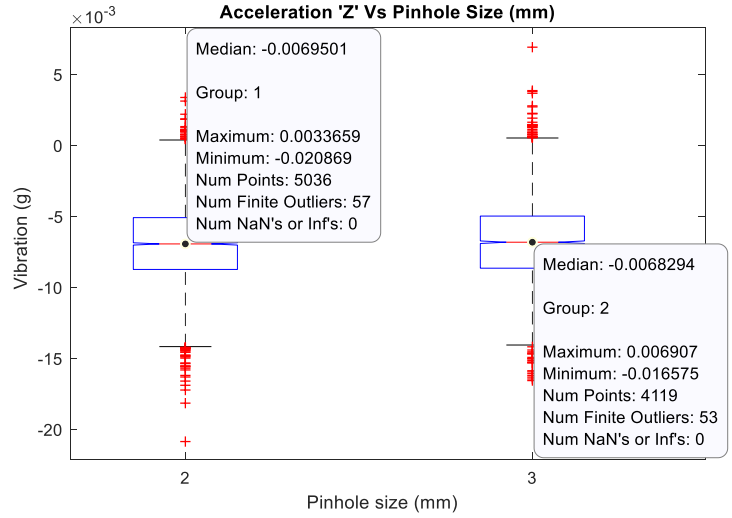

Figure 5.131: Effect of pinhole size on vibration 'Z' under leakage conditions

ANOVA Table

Source	SS	df	MS	F	Prob>F
Groups	0.00019	11	1.70847e-05	2.21	0.0115
Error	0.07066	9143	7.72824e-06		
Total	0.07085	9154			

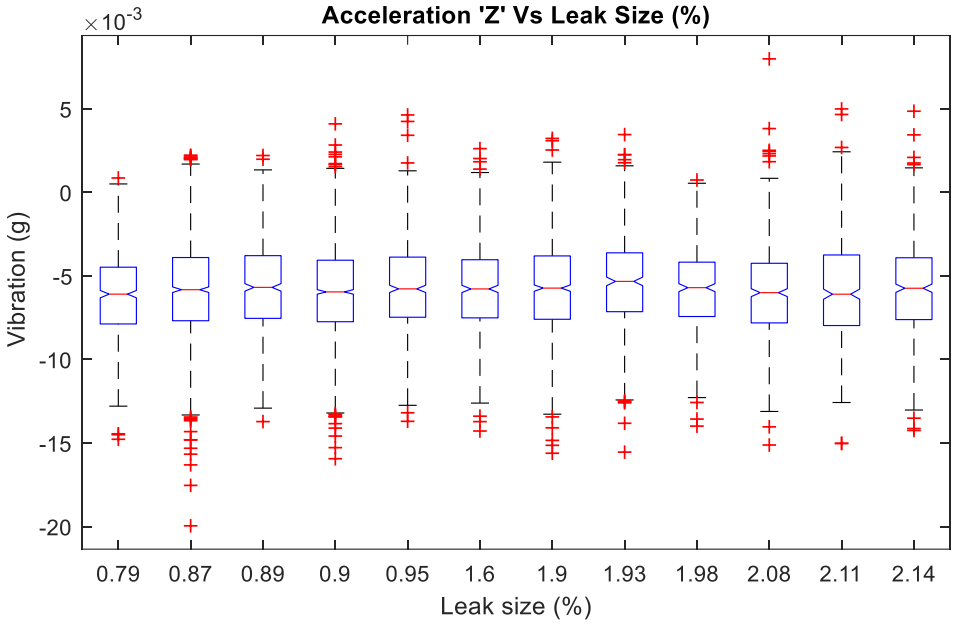

Figure 5.132: Effect of leakage on vibration 'Z' under leakage conditions

The null hypothesis examines the effect of pinhole size and leak size on similar test samples. This hypothesis is that pipe vibration is similar amongst groups; in other words, factors equally affect the output. Factors –leak size and pinhole size- influence pipe vibration, which differs from each group, as demonstrated by all the p-values ≤ 0.05. On the other hand, the accelerometer's low-sensitivity influences the 'means' values because the Fs are close to one.

Chapter 6: Conclusions

6.1 Conclusions

A unique testbed which combines a wide variety of leak detection systems (LDS) employed by the energy pipeline industry has been presented to address the shortcomings in existing leak detection techniques. The testbed's sensor suite was broken down into its elements by principles and methods including dielectric permittivity probes, temperature probes, thermal imaging, pipe vibrations, pressure profiles, and pressure transients. These sensors were presented with technological challenges to map and understand the relationships between responding variables, which are complex and multifactorial.

Soil permeability characterizes the medium's porosity, which is an essential driver for the externally-based LDM, e.g., thermocouple probes. A well-granulated soil has more pore space than one with sparse granulation or one that has been compacted. Thermocouple probes perform inefficiently in black loam. Their readings remained stable although simulant liquids reached the probes due to the reduced pore space resulting in a lower water-holding capacity. Liquids required a longer period to permeate a low porosity medium and reached either substantial lengths of the probe or its measuring (hot) junction – depending on the thermocouple configuration – to sense changes of temperature. However, given their high porosity, thermocouples perform effectively in high-permeable soils such as sand is higher. As a result, the liquids reach greater lengths of the probes faster than low porosity media. Thermocouples are inefficacious to detect leaks in saturated soil – regardless of soil permeability. Because both soil matric suction and its gradient are zero, the only moving forces are gravitational and pressure potential. Therefore fluid moves anisotropically, resulting in lower chances for it to reach the probes.

Transfer of energy from the liquids to the environment should also be considered because in cases of a leak happening in low permeable mediums, the liquids take longer to reach the critical length of the thermocouple and achieve a delta temperature, which diminishes the thermocouple's efficiency. Soil compaction also has the same effect.

Moisture content is also a key driver to the probes' performance as demonstrated through experiments under contrasting conditions such as dry and saturation. Moisture affects the dielectric permittivity of the medium. Dielectric-permittivity probes perform inefficiently in saturated soils because the soil cannot absorb any more liquids, so dielectric permittivity remains stable even if liquids replace liquids out of the leak. However, experiments used water as a simulant liquid with a dielectric permittivity of 80, yielding a dielectric permittivity of saturated soil around 30. Conversely, dielectric permittivity of hydrocarbons is between 2 and 4, so if a leak happens and the leaked liquids reach the probes, then the DP will decrease. However the leaked fluid moves anisotropically because the medium is anisotropic. DP probes are not susceptible to weather seasons because the relation between dielectric permittivity and temperature is inelastic. For example, the DP of water changes from 87 to 73 as its temperature increases from 0 to 40 °C.

Under the experimental conditions, thermal imaging proved to be effective to measure changes in soil temperature due to leaks. Thermal imaging technology does not need to be in touch with liquids or soil to sense their temperature, and is therefore less sensitive to soil permeability, soil compaction or ground surface slope as thermocouples probes are. FLIR's response time is almost instantaneous as opposed to that of thermocouples' which is in the range of several minutes. In extreme conditions, such as during winter, chances of false-negative alarms increase when using FLIRs because by the time the UAV equipped with thermal imaging payload is deployed, the temperature of the leaked liquids on the surface might have cooled. Thermocouples can perform better in this situation because underground soil temperature under any seasonal condition always ranges between 0 to 18 °C at one-meter depth and from 5 to 14 °C at two meters depth, where oil pipelines are buried.

Pressure transients are useful to detect leaks as proven through experiments. In pressure transients, the effect of leakage is compounded by several elements. First, when the pump and the valve are shut off, the transient is created, generating a steep negative wave which reflects at the leak. The ending reflection is visible as a small and abrupt pressure change in the pressure transient at the pump. Second, the leak will cause a disturbance of the pressure peaks, so the shape of the oscillations deteriorates progressively from perfectly

sinusoidal at no leakage conditions to a distorted one under rupture condition. Finally, leakages attenuate the transient pressure oscillations significantly, so the leakage rate relates to the damping ratio of the transient. Moreover, the attenuation effect is more significant the higher the order of the oscillation period. The number of oscillations depends on the pump's inertia. This number is low for current experiments because the pump's inertia is low. The research-pump entirely stops in five seconds, while Jonsson's (1994) does so by around 3 minutes. Experimental data show a straight relationship between pressure transients and whether or not the pipe leaks. In other words, pressure transients successfully detected the leaks. The technique used to pinpoint leaks was the detection of a rarefaction wave generated by the leak.

Experiments resulted in data sets that can be further used to evaluate the whole meta-classifier. Evaluating each component in isolation yielded a better understanding of the uncertainties faced by pipeline systems. As a result, some of the system's technological challenges can be assessed to improve the system's sensitivity, reliability, accuracy, and robustness.

6.2 Framework Limitations

Difficulties in obtaining accurate data may undermine the validity of the results. The current research is limited in its ability to test the technologies which may weaken the data gathered, thus preventing the machine learning from capturing the wide variety of relationships between the responding variables. The centrifugal pump noise is a significant limitation because it conceals the pressure and flow profiles as well as transient pressure data. Although some steps were implemented to minimize the noise in the data, denoising efficiency comes with a signal distortion level, limiting the machine learning performance. Because the pipe loop is too short for having a flow meter at the inlet it is impossible to fully evaluate the transient model-based leak detection system. Therefore the apparatus cannot construct the inlet flow profile. Moreover, this apparatus does not test the mass balance leak detection technique because it can only account for all fluid leaving the pipeline system.

Two accelerometers on pipe fittings can measure and pinpoint a leak by measuring the waves traveling away from the leak source along the pipe wall (as radial vibrations) and through the water column (as pressure waves). The NI-9230 slot that acquires the accelerometer's data has only three inputs, whereas the used accelerometers - Type 4506 B003 - are triaxial, so the apparatus can power up only one accelerometer. Therefore, the apparatus cannot cross-correlate the distinct leak to pinpoint the leak position. Another limitation is the accelerometer's sensitivity, 490 mV/g, which cannot detect the vibrations from small leaks – the accelerometers were only able to measure the transient pressure vibrations.

Thermocouple probes are connected to the NI CDAQ-9178 whereas dielectric permittivity probes are connected to their data logger, so there is a risk of damage to the loggers if an electric short-circuit happens when the probes are fully submerged underwater, as happened once. Consequently, when running experiments under small-leak conditions, the thermocouple probes were lined up with increasing level of water, and when the water table reached the soil surface the dielectric permittivity probes were reallocated by adding saturated soil. This cyclic process was executed as long as the water level increased, resulting in anomalous peaks in their readings. Soil responding variables such as soil temperature and

soil dielectric permittivity were not analyzed under rupture conditions because a 120 Volts solenoid valve recreates pipe fractures, so this creates a significant electric risk to the loggers. Finally, the analysis is limited by using water as a simulant liquid because energy transportation companies convey hydrocarbons through their pipelines. Hydrocarbons have different physical properties than water, so the tested technologies will yield different results when using hydrocarbons.

6.3 Recommendations for future research

In addition to improvements that can address the limitations discussed in 6.2, there are other areas and experiments that can be considered. Instead of using water for simulations, the use of hydrocarbons should be considered because they pose closer parameters to fluids conveyed in pipelines by energy transportation companies. Hence, tested leak detection technologies in laboratory conditions will yield results more accurate.

Machine learning builds a mathematical model based on sample data in order to predict leaks, so additional experiments, including different experimental conditions, are suggested to gather more data. For instance, set the leak source in other directions or to consider pipe cracks or corroded pipes as leak sources. Crafting the leak source under these conditions will yield a better understanding of the relation between local terrain and fluid properties. Another example is to use additional types of soils such as silt and clay. Since soil permeability profoundly influences the liquid-soil relation, the performance of the physical-inspection technologies will also be affected.

Experiments with liquids at different temperatures ought to be considered because a fluid's temperature greatly influences the performance of technologies. Current experiments only considered the critical condition, 38 °C, which is the maximum operational temperature defined by a large energy transportation company. Experimenting using lower temperature yields a smaller gap between soil and liquids temperature. Further work will allow us to see the critical temperature at which technologies such as FLIR and thermocouples stop working. Pipelines usually transport batches of different products, so another advantage of employing different temperatures is to understand their impact over the fluid properties such as specific

gravity, viscosity, and other fluid characteristics. This will provide a better understanding of the sensitivity of the leak detection technologies of unmeasured variables and fluid properties.

Future research should consider the effect of environmental temperature on the soil and its affect on the temperature differential between the oil and the soil. Such research will deliver a more precise time-span effectiveness of UAVs equipped with thermal imaging cameras. Pipelines are buried between 0.91 and 1.83 meters, so the medium's emissivity and absorptivity can hinder the FLIR camera from measuring changes of temperature and detecting leaks.

More experiments considering pipes buried deeper are critical to understand this phenomenon. Current experiments considered a pipe buried 4 inches deep and so the liquids went to either the surface or spread out less than 4 inches beneath the surface. Medium emissivity and the absorptivity played a negligible role under current experimental conditions. This recommendation, paired with employing different soils and simulant liquids will yield a better understanding of their heat capacity effect on the soil temperature when pipe leakage happens. For instance, the specific heat of petroleum and light oil are 2.0 and 1.8 while loam's is 1.5. This means that petroleum (a) requires more energy to increase its temperature and (b) can absorb more energy than light oil or loam. The timespan of convection from the soil-commodity blend to the environment is longer for commodities with higher specific heat. Moreover, temperature delta between the soil-commodity blend area and its surroundings is due to two factors: (a) the energy which is already in the commodity due operations and (b) environmental factors as sunlight. Theoretically, materials with higher specific heat coefficients can absorb more energy, therefore they take longer to cool down due convection than mediums with smaller specific heat coefficients. For example, if a drone with a FLIR payload is deployed at night, it can detect leaks because the soil-commodity blend still has more energy than the dry surrounding soil. On the other hand, after sunrise, the drone will detect a colder spot because the soil-commodity blend takes more time to heat up since its specific heat coefficient is higher. Hence, the temperature curves due to solar radiation using different commodities can be created to have a more comprehensive analysis, and to calculate precisely for how long FLIR is still effective.

Thermal properties of the pipeline surroundings are influenced by ground moisture content while pipeline systems stretch across hundreds of kilometers, resulting in different moisture levels along their surroundings. Current research only considered two conditions: dry and saturation. The present research apparatus is unable to operate with large amounts of soil making it difficult to use batches of soil with different moisture levels simultaneously. Therefore, it is proposed to run experiments while including different moisture levels to make data profiles. If appropriately arranged, these profiles can be employed by artificial intelligence algorithms.

An additional extension of this research is to upgrade the apparatus to dampen the noise of the centrifugal pump, which masks the transient pressure data. Although the present research yields concrete results and straight relations between transients and leaks, dampening this noise will yield better results. Transients have proven to detect leaks under severe transient conditions where other technologies have failed.

Testing sensing cables is a vital extension of this research since their use has grown steadily in the industry because of their comparative advantages over other sensors. For example, since accelerometers have proven inefficient, distributed acoustic sensing (DAS) cable to detect the low-frequency acoustic signals surrounding the pipe may give better results. Test fiber sensor cables that measure the presence of hydrocarbons is another technology to test because detecting the presence of this variable will address some limitations of thermocouples or dielectric permittivity probes.

Another point that deserves more attention is to read batches of thermal images that came out of the current research for processing in machine learning. This data should be used for training, prediction, and classification for leak detection applications. For example, tooling UAVs with sensor payloads and artificial intelligence to detect leaks before they come to the surface by measuring temperature differentials between the oil and the soil, or ground subsidence or ground heave.

References

1. M. B. Abdulla, R. O. Herzallah and M. A. Hammad, "Pipeline leak detection using artificial neural network: Experimental study," 2013 5th International Conference on Modelling, Identification and Control (ICMIC), Cairo, 2013, pp. 328-332.
2. Alberta Agriculture and Forestry. (2018). Agricultural land resource atlas of Alberta - soil groups of Alberta. Retrieved July/22, 2018, from https://www1.agric.gov.ab.ca/$department/deptdocs.nsf/all/agdex10307
3. Agriculture and Agri-Food Canada. (2018). Soil moisture application. Retrieved July/22, 2018, from http://www.agr.gc.ca/atlas/agpv?webmap-en=e749b74eb15c48df8a0198618986db61&webmap-fr=1971a264a6a64957a03f7c824950038f
4. Agwu, O. E., Akpabio, J. U., Alabi, S. B., & Dosunmu, A. (2018). Artificial intelligence techniques and their applications in drilling fluid engineering: A review doi:https://doi.org/10.1016/j.petrol.2018.04.019
5. Antkowiak, M. (2006). Artificial Neural Networks vs. Support Vector machines for skin diseases recognition. Neural Networks.
6. Arifin, B. M. S., Li, Z., Shah, S., Meyer, G., & Colin, A. (2018). A novel data-driven leak detection and localization algorithm using the kantorovich distance. Computers & Chemical Engineering, 108, 300-313. doi:https://doi.org/10.1016/j.compchemeng.2017.09.022
7. API - American Petroleum Institute. (2015). API RP 1162 - public awareness programs for pipeline operators (Second ed.). Washington, DC:
8. API - American Petroleum Institute. (2017). API 1175 pipeline leak detection - program management (Errata: March 2017 ed.). Washington, DC:
9. API - American Petroleum Institute. (Reaffirmed, April 2012). API RP 1130 - computational pipeline monitoring for liquids (First ed.). Washington, DC:
10. Audrey, P., & Yin, X. Internal free swimming pipeline leakage detection technology?smartball doi:doi:10.1061/41202(423)106

11. Badri, L. (2009) Development of Neural Networks for Noise Reduction. The International Arab Journal of Information Technology, Vol. 7, No. 3, July 2010.
12. Baldwin, C. (2018). 8 - fiber optic sensors in the oil and gas industry: Current and future applications. In H. Alemohammad (Ed.), Opto-mechanical fiber optic sensors (pp. 211-236) Butterworth-Heinemann. doi:https://doi.org/10.1016/B978-0-12-803131-5.00008-8
13. Barrios, J., She, Y., Dick, S., & Lipsett, M. (2018). Review of pipeline leak detection techniques and systems: An addendum to "in-situ condition monitoring of pipelines via inferential sensing". Canada: University of Alberta.
14. Beale, M., Hagan, M., and Demuth, H. (2017). Neural Network Toolbox™ User's Guide. [ebook] Boston: MathWorks, Inc.
15. Berk, Z. (2018). In Berk Z. (Ed.), Chapter 2 - fluid flow Academic Press. doi:https://doi.org/10.1016/B978-0-12-812018-7.00002-6
16. Bin, Y., Mingxing, L. and Qiongwei, L. (2017). Ultrasonic Monitoring System for Oil and Gas Pipeline Corrosion - IEEE Xplore Document. [online] Ieeexplore.ieee.org.
17. Campbell, J. E. 1990. Dielectric Properties and Influence of Conductivity in Soils at One to Fifty Megahertz. Soil Sci. Soc. Am. J. 54:332-341. doi:10.2136/sssaj1990.03615995005400020006x
18. Chun-Lin, L. (2010). A tutorial of the wavelet transform. Retrieved from http://disp.ee.ntu.edu.tw/tutorial/WaveletTutorial.pdf
19. CSA Z662-15 - oil and gas pipeline systems (2015). (Seventh ed.). Canada: CSA Group.
20. L. Chiang, B. Lu and I. Castillo, "Advances in big data analytics at The Dow Chemical Company," 2017 6th International Symposium on Advanced Control of Industrial Processes (AdCONIP), Taipei, 2017, pp. 207-208.
21. Datta, S., & Sarkar, S. (2016). A review on different pipeline fault detection methods doi:https://doi.org/10.1016/j.jlp.2016.03.010
22. Dawson C, Inkpen S, Nolan C, Bonnell D. A New Approach to Pipeline Leak Detection Using Electromagnetic Sensing. ASME. International Pipeline Conference, Volume 3: Operations, Monitoring and Maintenance; Materials and Joining ():V003T04A008. doi:10.1115/IPC2016-64371

23. Drumond, G. P., Pasqualino, I. P., Pinheiro, B. C., & Estefen, S. F. (2018). Pipelines, risers and umbilicals failures: A literature review doi:https://doi.org/10.1016/j.oceaneng.2017.11.035
24. Duru, C. & Ani, C. Sādhanā (2017) 42: 1889. https://doi.org/10.1007/s12046-017-0731-8
25. El-Abbasy, M. S., Ahmed, S., Tarek, Z., Laya, P., & Farid, M. (2016). Unpiggable oil and gas pipeline condition forecasting models. Journal of Performance of Constructed Facilities, 30(1), 04014202. doi:10.1061/(ASCE)CF.1943-5509.0000716
26. El-Abbasy, M. S., Senouci, A., Zayed, T., Mirahadi, F., & Parvizsedghy, L. (2014). Artificial neural network models for predicting condition of offshore oil and gas pipelines doi:https://doi.org/10.1016/j.autcon.2014.05.003
27. El-Zahab, S., Mohammed Abdelkader, E., & Zayed, T. (2018). An accelerometer-based leak detection system doi:https://doi.org/10.1016/j.ymssp.2018.02.030
28. Elliott, J., Fletcher, R., & Wrigglesworth, M. (2008, January 1). Seeking the Hidden Threat: Applications of a New Approach in Pipeline Leak Detection. Society of Petroleum Engineers. doi:10.2118/118070-MS
29. Eze, J., Nwagboso, C., & Georgakis, P. (2017). Framework for integrated oil pipeline monitoring and incident mitigation systems doi:https://doi.org/10.1016/j.rcim.2016.12.007
30. FLIR Systems Inc. (2016). User's manual FLIR Exx series FLIR Systems Inc.
31. Food and Agriculture Organization of the United Nations. (2019). Soil permeability. doi:http://www.fao.org/tempref/FI/CDrom/FAO_Training/FAO_Training/General/x6706e/x6706e09.htm
32. Gangl, G., & Navas, R. Leak detection in virtual DMA combining machine learning network monitoring and model based analysis. Amsterdam. (Amsterdam International Water Week)
33. Gargour, C., Gabrea, M. and Ramachandran, V. (2017). A short introduction to wavelets and their applications - IEEE Xplore Document.

34. Gao, Y., Liu, Y., Ma, Y., Cheng, X., & Yang, J. (2018). Application of the differentiation process into the correlation-based leak detection in urban pipeline networks doi:https://doi.org/10.1016/j.ymssp.2018.04.036
35. GE Oil & Gas. (2018). Discover PII pipeline solutions. Retrieved April/11, 2018, from https://www.geoilandgas.com/pipeline-storage/pipeline-integrity-services
36. Gong, J., Png, G. M., Arkwright, J. W., Papageorgiou, A. W., Cook, P. R., Lambert, M. F., et al. (2018). In-pipe fibre optic pressure sensor array for hydraulic transient measurement with application to leak detection.
37. Govind, H., & Clark, J. Pipeline monitoring employing geospatial big data in ArcGIS. Retrieved April/27, 2018, from http://proceedings.esri.com/library/userconf/petrol16/papers/petrol_32.pdf
38. Graps, A. (2017). An introduction to wavelets - IEEE Xplore Document. [online] Ieeexplore.ieee.org.
39. Guzel, E., Canytlmaz, M., & Turk, M. (2011). Application of wavelet-based denoising techniques to remote sensing very low frequency signals (doi 10.1029/2010RS004449). Radio Science -Washington-, 46(2), RS2013.
40. Hemsoth, N. (2018). Oil and gas industry gets GPU, deep learning injection., April/2018, from https://www.nextplatform.com/2018/01/29/oil-gas-industry-gets-gpu-deep-learning-injection/
41. Henrie, M., Carpenter, P. and Nicholas, R. (2016). Pipeline leak detection handbook. 1st ed. Gulf Professional Publishing.
42. Herlinawati, Murdika, U., Elan, G., and Yulianti, T. (2017). Ultrasonic signal denoising based on wavelet Haar decomposition level - IEEE Xplore Document. [online] Ieeexplore.ieee.org.
43. International Organization for Standardization. (2017). ISO 13623 - petroleum and natural gas industries - pipeline transportation systems (Third ed.). Switzerland:
44. Jurado, F., and Saenz, J. (2002). Comparison between discrete STFT and wavelets for the analysis of power quality events, Electric Power Systems Research, Volume 62, Issue 3. Pages 183-190.

45. A. Kadri, A. Abu-Dayya, R. Stefanelli and D. Trinchero, "Characterization of an acoustic wireless sensor for water leakage detection in underground pipes," 2013 1st International Conference on Communications, Signal Processing, and their Applications (ICCSPA), Sharjah, 2013, pp. 1-5.
46. Karray, F., Garcia-Ortiz, A., Jmal, M. W., Obeid, A. M., & Abid, M. (2016). EARNPIPE: A testbed for smart water pipeline monitoring using wireless sensor network doi:https://doi.org/10.1016/j.procs.2016.08.141
47. Kargas, George, and Konstantinos X. Soulis. Performance Evaluation of a Recently Developed Soil Water Content, Dielectric Permittivity, and Bulk Electrical Conductivity Electromagnetic Sensor. 213 Vol. , 2019. Web.
48. Kim, H. J., & Yoon, H. S. (2018). Reynolds number effect on the fluid flow and heat transfer around a harbor seal vibrissa shaped cylinder doi:https://doi.org/10.1016/j.ijheatmasstransfer.2018.05.083
49. Kishawy, H. A., & Gabbar, H. A. (2010). Review of pipeline integrity management practices doi:https://doi.org/10.1016/j.ijpvp.2010.04.003
50. Kizito, F., et al. Frequency, Electrical Conductivity and Temperature Analysis of a Low-Cost Capacitance Soil Moisture Sensor. 352 Vol. , 2008. Web.
51. Kosowatz, J. (2017). Machine learning applies to pipeline leaks. Retrieved April/11, 2018, from https://www.asme.org/engineering-topics/articles/energy/machine-learning-applies-pipeline-leaks
52. Layouni, M., Hamdi, M. S., & Tahar, S. (2017). Detection and sizing of metal-loss defects in oil and gas pipelines using pattern-adapted wavelets and machine learning doi:https://doi.org/10.1016/j.asoc.2016.10.040
53. L, Jonsson. "Leak Detection in Pipelines using Hydraulic Transients." 7.WIT Transactions on Ecology and the Environment (1994): 343. Print.
54. Lam, A. (2010). A conceptual approach to subterranean oil sand fragmentation and slurry transport. Canada: University of Alberta. Retrieved from http://hdl.handle.net/10048/1236

55. Lu, Z. (2017). Investigation into the effects of real-world uncertainties on A computer model-based leak detection system for liquid pipelines . (Master dissertation, University of Alberta).
56. Luz, L. M. d., Francisco, A. C. d., Piekarski, C. M., & Salvador, R. (2018). Integrating life cycle assessment in the product development process: A methodological approach doi:https://doi.org/10.1016/j.jclepro.2018.05.022
57. Mallat, S.G. (1989). A theory for multiresolution signal decomposition: The wavelet representation - IEEE Xplore Document
58. Mallat, S. and Peyre, G. (2009). A wavelet tour of signal processing. Burlington, MA: Academic Press/Elsevier.
59. Mashford, J., De Silva, D., Marney, D., & Burn, S. (2009). An approach to leak detection in pipe networks using analysis of monitored pressure values by support vector machine. Paper presented at the NSS 2009 - Network and System Security, 534-539. doi:10.1109/NSS.2009.38 Retrieved from www.scopus.com
60. Mathworks (2018). Support Vector Machines for Binary Classification. https://www.mathworks.com/help/stats/support-vector-machines-for-binary-classification.html
61. Meter Group, Inc. Ec-5 - Publications.metergroup.com. (n.d.). Retrieved from http://publications.metergroup.com/Manuals/20431_EC-5_Manual_Web.pdf
62. METER Group, Inc. "10HS MANUAL." 2019. Web. <http://publications.metergroup.com/Manuals/20426_10HS_Manual_Web.pdf>.
63. Misiti, M., Misiti, Y., Oppenheim, G. and Poggi, J. (2017). Wavelet Toolbox™ User's Guide. [ebook] Boston: MathWorks, Inc.
64. Modarres, M., Kaminskiy, M., & Krivtsov, V. (2010). Reliability engineering and risk analysis: A practical guide (2nd ed.). Boca Raton, FL: CRC Press.
65. Mohamed, Abdel-Mohsen Onsy, and Evan K. Paleologos. Chapter 6 - Soil-Water Interaction. Eds. Abdel-Mohsen Onsy Mohamed and Evan K. Paleologos. Butterworth-Heinemann, 2018. Web.

66. Murvay, P., & Silea, I. (2012). A survey on gas leak detection and localization techniques. Journal of Loss Prevention in the Process Industries, 25(6), 966-973. doi:https://doi.org/10.1016/j.jlp.2012.05.010
67. National Electrical Code®. National Fire Protection Association (Batterymarch Park, Quincy, Mass. 02210)
68. National Energy Board. (2018). Safety and environmental performance dashboard. Retrieved April/14, 2018, from https://www.neb-one.gc.ca/sftnvrnmnt/sft/dshbrd/dshbrd-eng.html
69. Natural Resources Canada. (2016). Pipelines across canada. Retrieved April/14, 2018, from http://www.nrcan.gc.ca/energy/infrastructure/18856
70. NDT Global. (2018). Our company. Retrieved April/11, 2018, from https://www.ndt-global.com/about/our-company
71. O'Brien, L. (2017). Smart sensors: On the front line of the industrial internet of things. Retrieved April/15, 2018, from https://www.arcweb.com/blog/smart-sensors-front-line-industrial-internet-things
72. P. Guo, et al. "Evaluation of Errors Induced by Soil Dielectric Models for Soil Moisture Retrieval at L-Band". 2016 IEEE International Geoscience and Remote Sensing Symposium (IGARSS). Web.
73. Pesinis, K., & Tee, K. F. (2017). Statistical model and structural reliability analysis for onshore gas transmission pipelines doi:https://doi.org/10.1016/j.engfailanal.2017.08.008
74. PHMSA. Enhancement of the long-range ultrasonic Method for the detection of degradation in buried, unpiggable pipelines. Retrieved March/7, 2018, from https://primis.phmsa.dot.gov/rd/publicabstract12_3_02.htm]
75. Prihtiadi, Hafizh, Azrul Azwar, and Mitra Djamal. "A Simple Method to Determine Leakage Location in Water Distribution Based on Pressure Profiles." AIP Conference Proceedings 1719.1 (2016): 030045. Web.
76. PSI Software AG. (2018). Pipeline leak detection and location. Retrieved April/27, 2018, from http://www.psioilandgas.com/en/pipeline-monitoring/leak-detection-and-location/

77. Qin, J., Yue, H., & and Dunia, R. (1997). Self-validating inferential sensors with application to air emission monitoring. United States: American Chemical Society. doi:10.1021/ie960615y
78. R., Exell. Random Vs. Systematic Error - Umd Physics. (n.d.). Retrieved from https://www.physics.umd.edu/courses/Phys276/Hill/Information/Notes/ErrorAnalysis
79. R.A. van Overmeeren (1994). Georadar for hydrogeology, First Break, pp. 401-408, - earthdoc.org
80. Rebizant W., Szafran J., Wiszniewski A. (2011) Application of Artificial Neural Networks. In: Digital Signal Processing in Power System Protection and Control. Signals and Communication Technology. Springer, London
81. Romano M., Kapelan Z., & Savić D. A. Real-time leak detection in water distribution systems doi:doi:10.1061/41203(425)97
82. Romano, M., Woodward, K., & Kapelan, Z. (2017). Statistical process control based system for approximate location of pipe bursts and leaks in water distribution systems doi:https://doi.org/10.1016/j.proeng.2017.03.235
83. Rioul, O. And Vetierli, M. (2017). Wavelets and signal processing - IEEE Xplore Document. [online] Ieeexplore.ieee.org.
84. Rui, Zhenhua, et al. A New Model to Evaluate Two Leak Points in a Gas Pipeline. 46 Vol. , 2017. Web.
85. S. Saechai, W. Kongprawechnon, & R. Sahamitmongkol. (2012). Test system for defect detection in construction materials with ultrasonic waves by support vector machine and neural network. doi:10.1109/SCIS-ISIS.2012.6505090
86. S. Rashid, U. Akram, S. Qaisar, S. A. Khan and E. Felemban, "Wireless Sensor Network for Distributed Event Detection Based on Machine Learning," 2014 IEEE International Conference on Internet of Things (iThings). doi: 10.1109/iThings.2014.93
87. Sadeghioon, Ali & Metje, Nicole & Chapman, David & Anthony, Carl. (2014). SmartPipes: Smart Wireless Sensor Networks for Leak Detection in Water Pipelines. Journal of Sensor and Actuator Networks. 3. 64-78. 10.3390/jsan3010064.
88. Schön, Jürgen H. Chapter 8 - Electrical Properties. Ed. Jürgen H. Schön. 65 Vol. Elsevier, 2015. Web.

89. Senouci, A., Elabbasy, M., Elwakil, E., Abdrabou, B., & Zayed, T. (2014). A model for predicting failure of oil pipelines. Structure and Infrastructure Engineering, 10(3), 375-387. doi:10.1080/15732479.2012.756918
90. Shukla, A., & Karki, H. (2016). Application of robotics in onshore oil and gas industry—A review part I. Robotics and Autonomous Systems, 75, 490-507. doi:https://doi.org/10.1016/j.robot.2015.09.012
91. Soldevila, A., Fernandez-Canti, R. M., Blesa, J., Tornil-Sin, S., & Puig, V. (2017). Leak localization in water distribution networks using bayesian classifiers doi:https://doi.org/10.1016/j.jprocont.2017.03.015
92. Soldevila, A., Blesa, J., Tornil-Sin, S., Fernandez-Canti, R. M., & Puig, V. (2018). Sensor placement for classifier-based leak localization in water distribution networks using hybrid feature selection doi:https://doi.org/10.1016/j.compchemeng.2017.09.002
93. Soleimani, A. Mahjoob, M.J. and Shariatpanahi, M. (2009). Fault classification in gears using support vector machines (SVMs) and signal processing. - IEEE Xplore Document. [online] Ieeexplore.ieee.org.
94. Sun, Y. Fidge, C., and Ma, L. "Reliability prediction of long-lived linear assets with incomplete failure data," 2011. doi: 10.1109/ICQR2MSE.2011.5976585
95. The American Society of Mechanical Engineers. (2016). Pipeline transportation systems for liquids and slurries, ASME B31.4. United States: ASME.
96. Transportation Safety Board of Canada. "Statistical Summary – Pipeline Occurrences 2011." 2011. Web. <http://www.tsb.gc.ca/eng/stats/pipeline/2011/ss11.html>.
97. Transportation Safety Board of Canada. (2014). Statistical summary – pipeline occurrences 2011. Retrieved July/26, 2018, from http://www.tsb.gc.ca/eng/stats/pipeline/2011/ss11.asp
98. Transportation Safety Board of Canada. (2018). Statistical summary: Pipeline occurrences in 2017. Retrieved from http://www.bst-tsb.gc.ca/eng/stats/pipeline/2017/ssep-sspo-2017.asp
99. Transportation Safety Board of Canada. (2019). Pipeline transportation., 2019, from http://www.tsb.gc.ca/eng/pipeline/index.html

100. Transportation Safety Board of Canada. (2019). Data and statistics on pipeline occurrences. Retrieved from http://www.bst-tsb.gc.ca/eng/stats/pipeline/index.html
101. Yusoff, N., Isa, M. and Hamid, H. (2017). Denoising technique for partial discharge signal: A comparison performance between artificial neural network, fast Fourier transform and discrete wavelet transform - IEEE Xplore Document.
102. Verma, A., Nimana, B., Olateju, B., Rahman, M. M., Radpour, S., Canter, C., et al. (2017). A techno-economic assessment of bitumen and synthetic crude oil transport (SCO) in the canadian oil sands industry: Oil via rail or pipeline? doi:https://doi.org/10.1016/j.energy.2017.02.057
103. Virupakshappa, K. and Oruklu, E. "Ultrasonic flaw detection using Support Vector Machine classification," 2015 IEEE International Ultrasonics Symposium (IUS), Taipei, 2015. pp. 1-4.
104. Williams, G. P.; Gold, L. W. Ground Temperatures - Nrc-irc. *Canadian Building Digest - CBD 180, 1976-07*. N.p., n.d. Web. 20 March. 2019 https://nrc-publications.canada.ca/eng/view/accepted/?id=386ddf88-fe8d-45dd-aabb-0a55be826f3f
105. Wint, D. (2016). Difficult to pig pipelines. United States: Appalachian Underground Corrosion Short Course.
106. Wikipedia. Darcy–Weisbach Equation. (n.d.). Retrieved from https://en.wikipedia.org/wiki/Darcy-Weisbach_friction_factor
107. Zadkarami, M., Shahbazian, M., & Salahshoor, K. (2016). Pipeline leakage detection and isolation: An integrated approach of statistical and wavelet feature extraction with multi-layer perceptron neural network (MLPNN) doi:https://doi.org/10.1016/j.jlp.2016.06.018
108. Zeng, K., Tan, Z., and Dong, M. (2015). Using short-time Fourier transform and wavelet packet transform to attenuate noise from heart sound signal for wearable e-healthcare device. Journal of Mechanics in Medicine and Biology Vol. 15.
109. Zhao, J., Hao, S., Yang, L. and Wang, X. (2010). Study on thickness detection of industrial pipe network by high-frequency ultrasound - IEEE Xplore Document.

Appendix 1: Literature review of LDSs based on AI

Leak detection systems have been discussed in this chapter. The performance of these methods depends on the features and uncertainties of the pipeline systems while deploying new LDSs also depends on resources available (Soldevila et al., 2018).

LDSs are usually pipeline models furnished with hard sensors which read the pipeline responding variables. A SCADA system samples this information. The pipeline's operator defines both the pipeline model and alarm thresholds. The readings are compared to the alarm threshold, and their differences trigger a leak alarm (Abulla et al., 2013).

Artificial intelligence techniques are gaining interest in the industry because they effectively solve problems with several types of uncertainties; they are also cheaper than hard sensing because soft sensors can be "deployed" virtually whereas deploying hard sensors is onerous or unfeasible. Authors have researched applications of artificial techniques to detect leaks in pipelines. For instance, Support Vector Machines were proposed to analyze data obtained by a set of pressure control sensors of a pipeline network to locate and compute the size of a possible leak present in a Water distribution network (Mashford et al., 2009). Soldevila et al. (2016) also proposed the use of k-Nearest Neighbors (k-NN) and Bayesian and neuro-fuzzy classifiers for leak localization purposes.

The alternative being proposed in further studies, machine learning, is essentially a family of non-parametric models (those that do not assume a prior distribution) that are sufficiently flexible and adaptable to capture an extensive variety of relationships between variables, for a broad range of measurement types. Each algorithm works from a very general input-output model, adapting the model's structure and parameters to replicate the input-output behaviors captured in a dataset. The "deep learning" algorithms that have recently gained fame are Artificial Neural Networks (ANNs), which are known generally to be universal approximators. By adopting the structure and parameter of a neural network appropriately, it can be taught to mimic any analytical function to any desired degree of accuracy; statistical models do not have in general this property (Senouci, 2014). Machine learning algorithms are universally very useful as classification algorithms thus they are

common in analytics, examples of these techniques are statistical techniques such as discriminant analysis or machine learning techniques: ANNs, decision trees, k-nearest neighbors, SVMs, etc. (El-Zahab, Abdelkader, and Zayed, 2018). Classifiers map several independent variables -of arbitrary types- to a discrete-valued dependent variable (the "label"). The independent variables would often be sensed data in the LDS context, and the label is commonly an alarm.

Machine learning conceives an LDS -or condition monitoring in general- as an anomaly detection problem: the goal of the learning system is to recognize deviation from the norm. A classifier tool is trained on these feature vectors along with the targeted labels of class, so the classifier determines whether a fault is present in the pipeline by using subsequent features (Rashid et al., 2014).

LDSs based on machine learning acquire data from the sensor network to extract the signal statistical features and finally build a candidate feature set. Different condition tests are performed on these features to qualify for a reduced feature set; hence, a classifier tool is trained on these feature vectors along with the targeted labels of class; therefore they are used to detect failures in pipelines (Rashid et al., 2014).

Implementing artificial neural networks is also cheaper than deploying a sensor suite that can monitor the entire pipeline in real-time because ANNs is a low-cost computational approach which predicts leaks rather than detects them, as sensors suite do. Nowadays the use of soft sensing is increasing steadily in the industry because their potential to understand and gather small leaks data, also because pipeline operators can use already deployed technologies as building blocks (Kosowatz, 2017). In other words, soft sensors can use already deployed technologies as building blocks to infer a more complex system state than the individual sensors can identify.

Soft sensing is also able to identify the type of commodity that pipelines leak: crude and mineral oil, diesel, gasoline, natural gas, or water. Another advantage of this novel technique is that sensors sampling frequencies are lower compared to continuous externally based LDSs, thus saving data logger's battery life when using Wireless Sensor Networks for instance (Romano, Woodward, and Kapelan, 2017).

Examples of artificial intelligence applications in the pipeline industry are, for instance, forecasting the condition of unpiggable oil and gas pipelines in Qatar using ANNs (El-Abbasy, 2016), or when DigitalGlobe employed big geospatial data and machine learning to harvest key features to monitor significant changes around pipelines, preventing accidental damage by third parties (Govind, and Clark, 2018). The energy industry is aware of the potential of AI to detect leaks in pipeline systems as well as in the industry in general. As a result, companies as Baker Hughes is presently investing on a new wave of software products for the industry based on deep learning, where neural networks are touching everything from overall rig optimization to more traditional High-Performance Computing simulation-based areas in resource discovery and production (Hemsoth, 2018). Finally, a fault detection system implemented in a 20-km pipeline in southern Iran (Goldkari-Binak pipeline) deliveries a promising severity and location detectability (a correct classification rate of 92%) as well as a low False Alarm Rate (Zadkarami, Shahbazian, & Salahshoor, 2016).

Artificial intelligence has yet limitations to detect leaks, i.e. there is no a specific machine learning algorithm which outperforms the others (El-Abbasy, 2014) since each AI technique displays its particular strengths and weaknesses (Agwu, Akpabio, Alabi, and Dosunmu, 2018). Additionally, in some cases a trained system under certain conditions gets tripped up in others, meaning, higher false-positive and false-negative alarm rates. Another problem is that operators usually lack pattern recognition knowledge, resulting in choosing poorly the best hyperparameter values for a given dataset; therefore expertise in the machine learning technology is crucial to tune a set of input-output variables efficiently. Soft sensing techniques may be overwhelmed in complex systems because variables and uncertainties might spike. Additionally, data required to train the AI algorithms are currently either scarce or incomplete, and harvesting data from the field is unfeasible.

Appendix 2: Hydraulic analysis

A.2.1) Reynolds number

The proposed apparatus should replicate the hydraulic conditions of pipelines, so controlled variables such as pipe diameter, type of fluid, type of soil, fluid temperature, defines the pipeline operational conditions. Reynolds number is a critical dimensionless parameter used in the pipeline industry because this number encompasses the flow, fluid velocity, cross-sectional area, and diameter of the pipe; it helps to predict flow patterns. Therefore, if the apparatus deliveries a Re similar to the average in the pipeline industry, then the apparatus recreates the required fluid pattern. Kim and Yoon (2018) affirm the Re number equation ($e.1$).

$$Re = \frac{Q * D_H}{v * A} \qquad (e.1)$$

Where:

Q: $Volumetric\ flow\ rate\ (m3/s)$ / DH : $Hydraulic\ diameter\ of\ the\ pipe\ (m)$

v: $Kinematic\ viscosity$ / A: $Pipe's\ cross\ sectional\ area\ (m2)$

A.2.2) Pressure loss in pipelines

The Reynolds number, in addition to the pressure loss deliveries a comprehensive view of pipeline operations. Pressure loss depends on Reynolds number, pipe material, pipe size, and friction factor; Berk (2018) refers the procedure for calculating the pressure drop in a straight pipe of diameter D and length L, carrying a fluid of known viscosity and density at a given volumetric flow rate Q as:

a) Solve the Reynolds number (Equation is aforementioned in e.1)
b) Calculate Re from D, v, ρ, and μ. If Re < 2,000 (equation e.2) assume laminar flow and calculate the pressure drop with the help of Poiseuille's equation. If Re > 2,000 the equation $e.3$ assumes turbulent flow and consult a friction-factor chart to find the value of f corresponding to Re.

$$F_m = \frac{64}{Re}\ ; if\ Re \leq 2{,}000 \qquad (e.2)$$

$$F_m = \frac{1.325}{\left[ln\left(\frac{\text{Ɛ\_}D}{3.7} + \frac{5.74}{Re^2}\right)\right]^2} \; ; \; if \; 2{,}000 > Re > 10^8 \; and \; 50x10^{-6} > \text{Ɛ}_D > 10^{-2} \quad (e.3)$$

Where the relation between Roughness Coefficient and the diameter of the pipe (Ɛ_D):

$$\text{Ɛ}_D = \frac{\text{Ɛ}}{Hydraulic \; diameter \; of \; the \; pipe} \qquad (e.4)$$

Note: Some pieces of literature defines the range 2,000 ≤ Re ≤ 6,000 a transition (neither fully laminar nor fully turbulent) regime flow. The Darcy friction factor is subject to significant uncertainties in this flow regime

c) Calculate the pressure drop ΔP from equation (*e*.5) as follows:

$$\Delta P = F_m * \frac{L}{D} * \frac{v^2}{2g} \qquad (e.5)$$

Equation *e*.5 expresses the pressure loss due to friction in terms of the equivalent height of a column of the working fluid and the Darcy–Weisbach equation in terms of head loss.

A.2.3) R factor

The API 1149 (1993) defines the R factor as a dimensionless parameter that characterizes a series of similar systems, so two pipelines with the same 'R' value and with identical scaled head and flow histories will behave identically in terms of scaled variables. Equation *e*.6 defines the R factor.

$$R = \left(\frac{V_o}{2a}\right) * \left(\frac{L * f}{D_H}\right) \qquad (e.6)$$

Where,

$$V_o: Initial \; velocity \; of \; the \; fluid \; (m/s)$$

$$L: Pipe \; length \; (m) - \quad F: Friction \; factor$$

$$a: Wave \; speed \; (m/s) - D_H \; : \; Hydraulic \; diameter \; of \; the \; pipe \; (m)$$

A.2.4) Volume of fluid leaked through the Pinhole leak

$\boldsymbol{C_d}$: $Discharge\ coefficient$

$= 0.61$; Discharge coefficients depend on: pressure ratio, aspect ratio , Hole geometry

$$\boldsymbol{A_o}: Area\ of\ Pinhole\ (millimeter^2)$$

$$\boldsymbol{Y}: Expansion\ coefficient = 1\ (For\ non - comprensible\ fluids)$$

$$\boldsymbol{\rho}: Density\ of\ the\ fluid\ \left(\frac{Kg}{m^3}\right)$$

$$\boldsymbol{\Delta P} = Pump\ Pressure - \ Atmosphere\ Pressure\ (KPa)$$

$$\boldsymbol{\beta} = \ Ratio\ of\ pipe\ diameter\ to\ orifice\ diameter\ (D_0/D_1)$$

Equation of the volume of fluid leaked through the pinhole leak:

$$Q = C_d * A_o * Y * \sqrt{\frac{2 * \Delta P}{\rho * (1-\beta)^4}} \qquad (e.7)$$

Appendix 3: Selection of soil and moisture level

Pipeline operators deployed their pipeline infrastructure across Canada. These pipelines are buried in several types of soil since the Canadian landmass is diversified and broad; as a result, recreating all these conditions would be impractical because test each type of soil requires 12 tests total. According to Canadian Soil Information Service (2018) Alberta clusters nine types of soil whereas Saskatchewan 11 ones, so if the research simulated the leaks in 11 types of soil, it would be required 132 tests thus 13,200 Kg of soil.

Enbridge pipelines are mainly located in western Canada, being Edmonton and its surroundings a HUB, so when overlapping the Enbridge pipeline layout with these two provinces soil maps the outcome is overall two types of soil: brown and black chernozemic, The apparatus uses black chernozemic and sand because brown chernozemic's properties are similar to black chernozemic's. As a result, using only two types of soil narrows down the number of tests from 132 to 24. Figures A.1, A.2, and A.3 map the soil group of Alberta and Saskatchewan.

The Canadian Soil Information Service describes (2018) the percent-saturated surface soil moisture across Canada and in both the province of Alberta and Saskatchewan where the pipeline crosses, the moisture of soil in experiments for dry conditions is measured but controlled. Experiments with saturated soil are controlled by adding water up to reaching saturation, and this replicates the soil surrounding the pipeline when deployed near or underneath rivers. Figure A.4 details the percent saturated surface soil moisture in Canada as well as where the pipeline system is deployed.

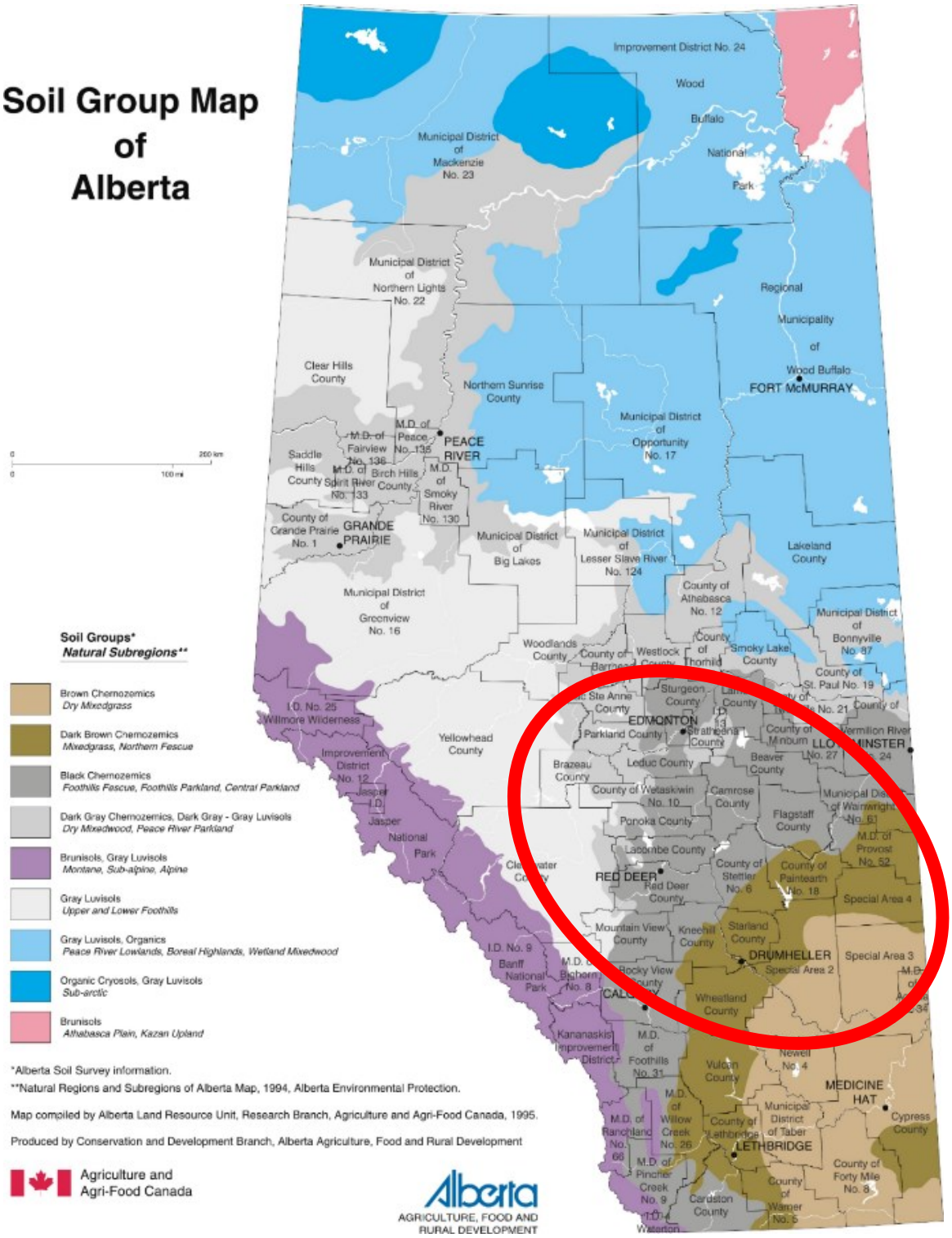

Figure A.1: Soil group map of Alberta

Figure A.2: Soil group map of Saskatchewan

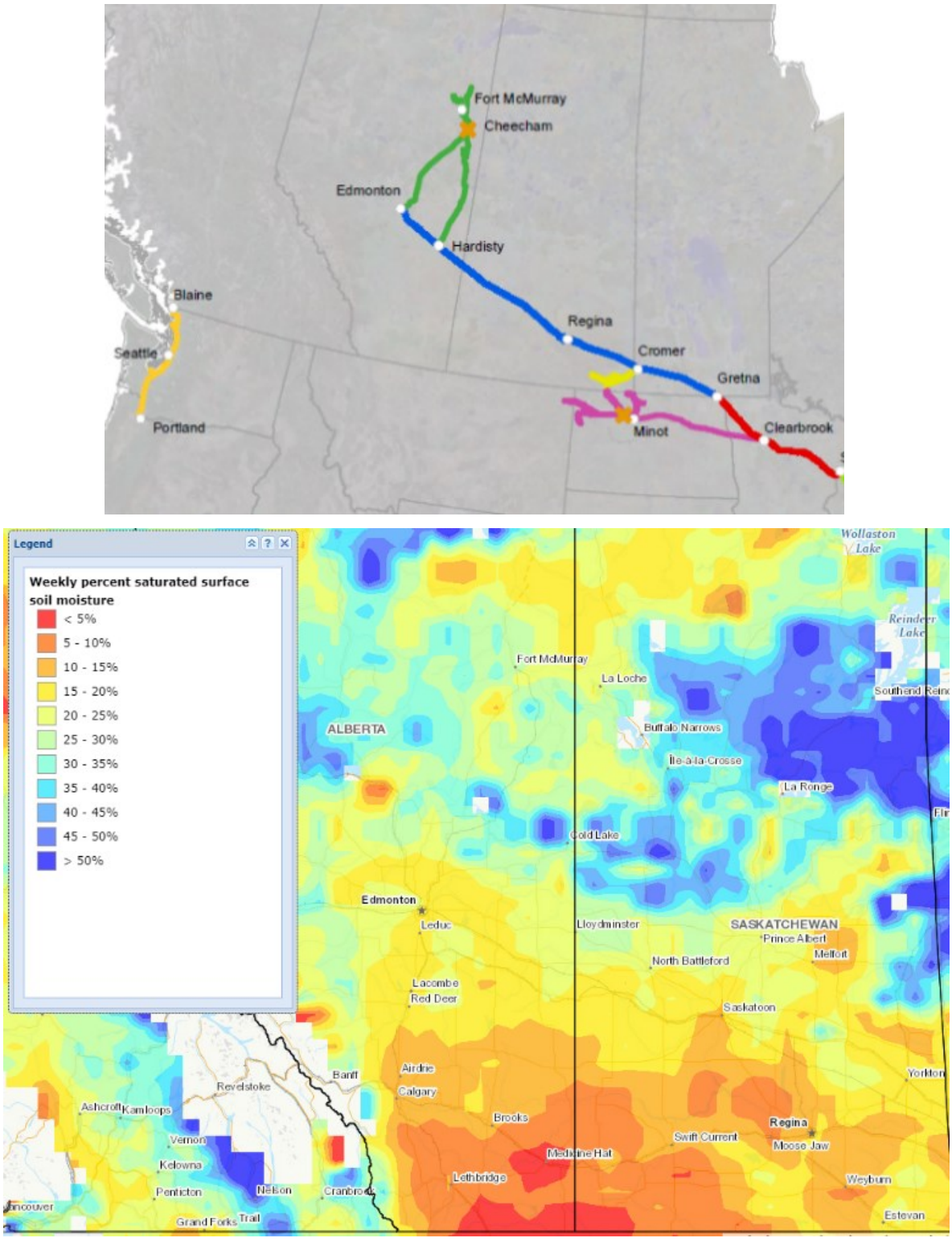

Figure A.3: Soil Moisture (%) in Canada and major operator's pipeline system layout

Appendix 4: Load platform strength analysis

This appendix contents the load cell platform's strength analysis:

Table A.1: Load cell platform physical features

Material	Steel, Mild
Density	0.283599 lbmass/in^3
Mass	59.1636 lbmass
Area	1699.51 in^2
Volume	208.617 in^3
Center of Gravity	x=-12.5 in y=0.337444 in z=-12.5 in

A.4.1) Static Analysis:

Table A.2: Mesh settings

Avg. Element Size (fraction of model diameter)	0.1
Min. Element Size (fraction of avg. size)	0.2
Grading Factor	1.5
Max. Turn Angle	60 deg
Create Curved Mesh Elements	Yes

Table A.3: Load cell platform material

Name	Steel, Mild	
General	Mass Density	0.283599 lbmass/in^3
	Yield Strength	30022.8 psi
	Ultimate Tensile Strength	50038 psi
Stress	Young's Modulus	31908.3 ksi
	Poisson's Ratio	0.275 ul
	Shear Modulus	12513.1 ksi
Part Name(s)	Load Cell Platform	

A.4.2) Operating conditions

Table A.4: Force applied to the load cell

Load Type	Force
Magnitude	441.000 lbforce
Vector X	0.000 lbforce
Vector Y	-441.000 lbforce
Vector Z	0.000 lbforce

A.4.3) Results

Table A.5; Reaction Force and Moment on Constraints

Constraint Name	Reaction Force		Reaction Moment	
	Magnitude	Component (X,Y,Z)	Magnitude	Component (X,Y,Z)
Fixed Constraint:1	441 lbforce	0 lbforce	0 lbforce ft	0 lbforce ft
		441 lbforce		0 lbforce ft
		0 lbforce		0 lbforce ft

Table A.6: Result Summary

Name	Minimum	Maximum
Volume	208.617 in^3	
Mass	59.1636 lbmass	
Von Mises Stress	0.0340557 ksi	54.2816 ksi
1st Principal Stress	-16.517 ksi	45.1631 ksi
3rd Principal Stress	-72.1837 ksi	9.10999 ksi
Displacement	0 in	0.0308831 in
Safety Factor	0.553094 ul	15 ul

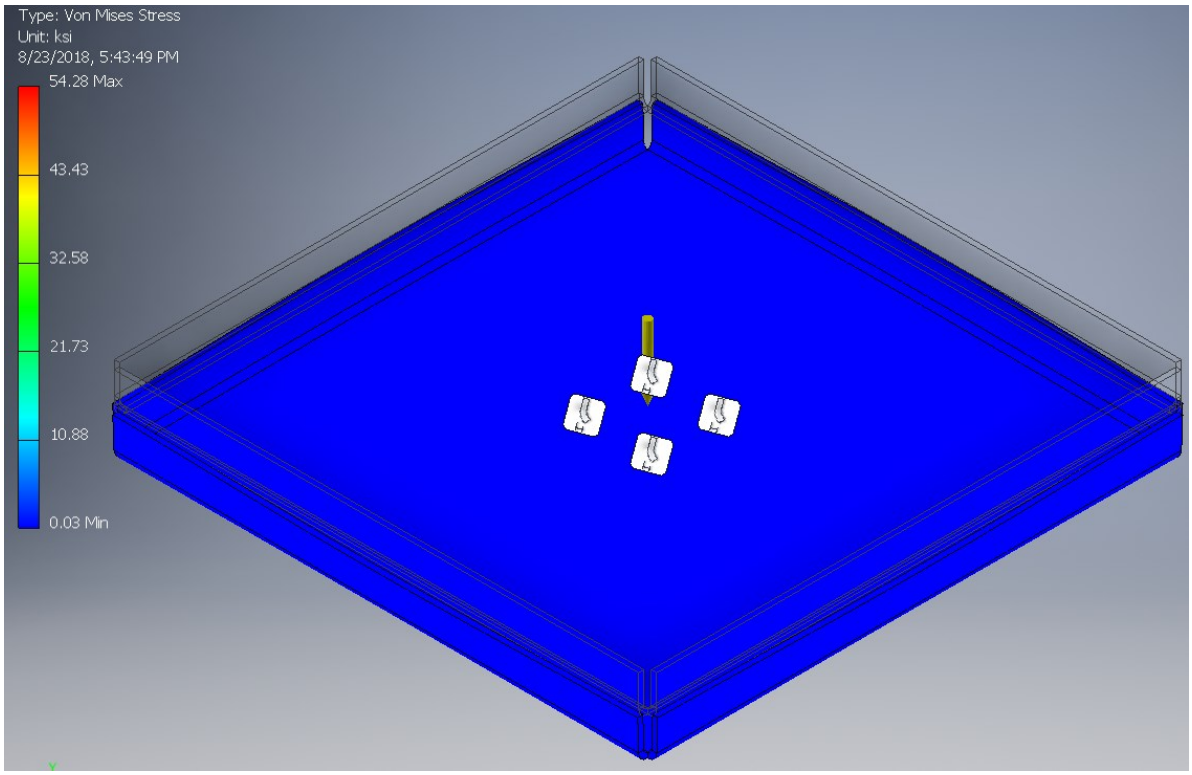

Figure A.4: Von Mises Stress applied to the Platform

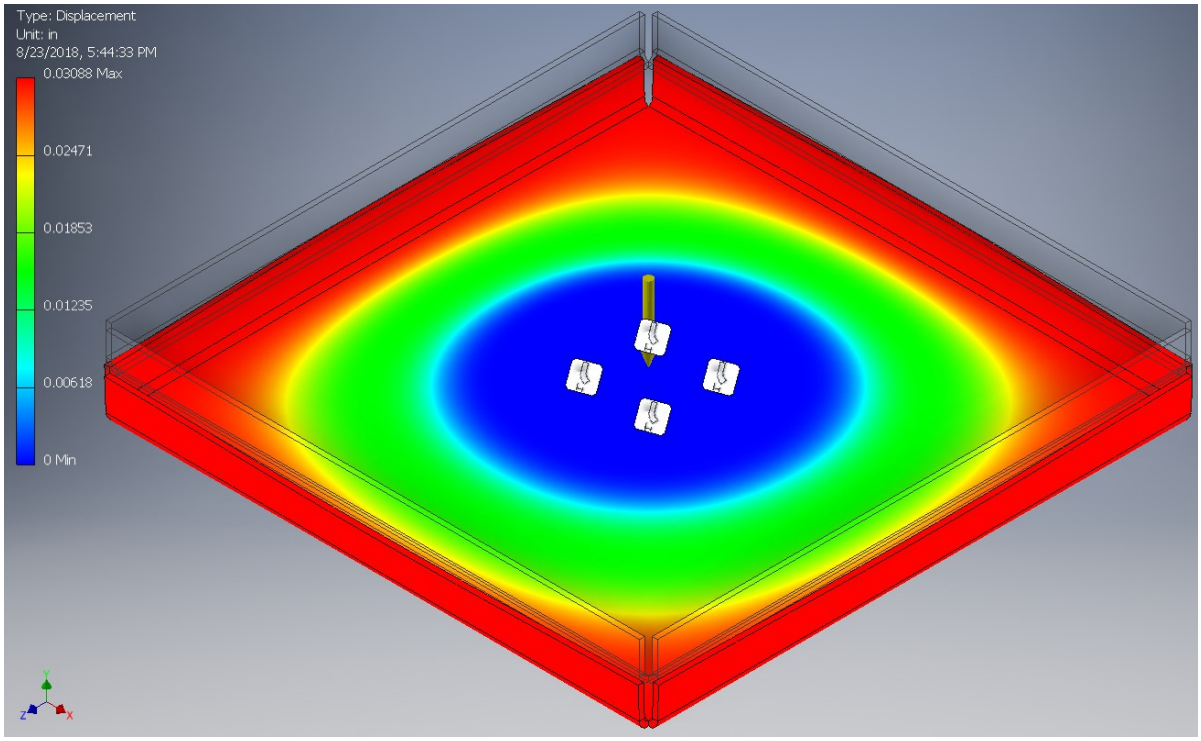

Figure A.5: Platform Displacement

Appendix 5: Centrifugal pump and heater analysis

A.5.1) Centrifugal Pump:

Table A.7: Centrifugal Pump Data Input

Data Input	Voltage (V)	220
	Number of Poles	3
	Motor (KW)	0.75
	Power Factor	0.72

$$I_l = \frac{P}{\sqrt{3} * P_f * V_{LL}} = \frac{750}{\sqrt{3} * 0.72 * 220} = 2.74\ (A)$$

$$I_{3\phi} = 2.74 * \sqrt{3} = 4.75\ (A)$$

Table 44 of the Canadian Electrical Code (CEN) defines an $I_{3\phi} = 4.6\ (A)$ for a motor with the specifications aforementioned. The CEN also states in Table D16 that a breaker of 15 (A) is required between the supply power and the operating device. The National Electrical Code (NEC) in its bullet point 430.109(7)(C) states "for stationary motors rated at 2 hp or less and 300 volts or less, the disconnecting means shall be permitted to be … a general-use switch having an ampere rating not less than twice the full-load current rating of the motor," thus

According to the National Electrical Code (NEC) on Table 250.122 defines that a copper cable size 14 is required for grounding equipment. Based on table 310.15(B)(16) who defines the allowable Ampacities per cable size AWG, and since the pump is operated through a VFD clause 430.122 Conductors - Minimum Size and Ampacity Circuit conductors applies is also considered because "…system shall have an ampacity not less than 125 percent of the rated input current to the power conversion equipment." As a result, Cable AWG 14 is required to operate the apparatus-centrifugal pump. ABB VFD technical data recommends an 18 AWG cable to connect the motor to the VFD

NEC Bullet point 430.73 requires protection of conductors from physical damage. NEC Bullet points 430.124 states that Overload protection of the motor shall be provided

for Adjustable-Speed Drive Systems. The ABB VFD technical data states that the maximum output current allowed is 8.2 (A) for two seconds at start, otherwise as long as allowed by the drive temperature, so based on both CEN bullet point 430.32 (A)(1) and the ABB VFD manual 10 (A) type gG fuses are the short-circuit, overload and phase failures protection element. Table A.8 resumes the circuit diagram electrical components.

Table A.8: Centrifugal Pump Data Output

Data Output	Power cable size	14 AWG - Type TW or UF
	Motor cable size	18 AWG - Type TW or UF
	Grounding cable size	14 AWG - Type TW or UF
	Short-circuit, overload and phase failures protection	• 10 (A) Any brand of J class fast-acting fuse • fuse holder, or a fusible disconnect

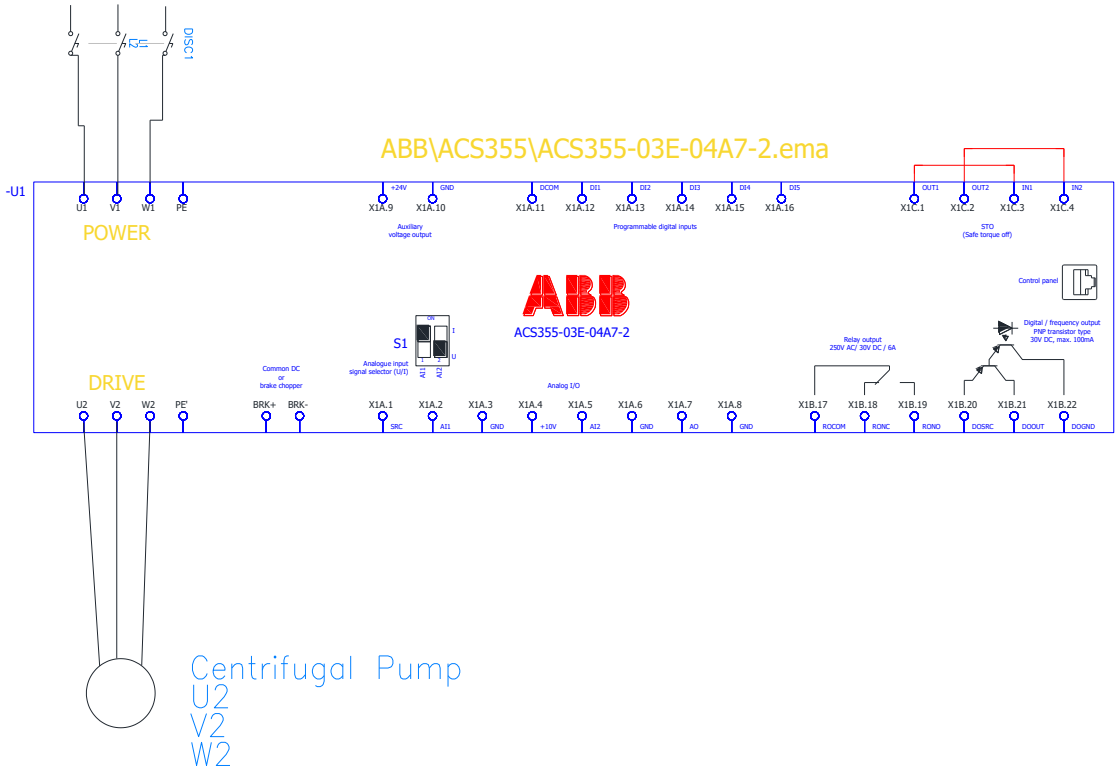

Figure A.6: Centrifugal pump circuit diagram

A.5.2) Heater

Table A.9: Heater Data Input

Data Input	Power (W)	3,000
	Voltage (V)	220
	Power factor	0.95
	Control circuit type	12 Vdc
		30 mA

$$I_{l(Without\ safety\ factor)} = \frac{P}{\sqrt{3} * P_f * V_{LL}} = \frac{3{,}000}{\sqrt{3} * 0.95 * 240} = 7.6\ (A)$$

$$I_l = 7.6 * 1.2 = 9.12\ (A)$$

Schneider LC1D12JD (TeSys D contactor: 3P(3 NO) - AC-3 - 440 V - 12 A - 12 V DC coil) fits the conditions required by the heater. A circuit breaker of 15 (A) works as a disconnecting means. Table A.10 shows the elements to set up the heater.

Table A.10: Heater Data Output

Data Output	Heater cable size	14 AWG - Type TW or UF
	Grounding cable size	14 AWG - Type TW or UF

	Power control	• RELAY SSR 15A 3PH DIN MNT
		  ○ Manufacturer: OMROM
		  ○ Code: G3PE-215B-2N DC12-24
		• 15 (A) circuit breaker

	Box with Mounting Flange	• Box Metal, Lid 7.500" L x 6.250" W (190.50mm x 158.75mm) X 4.750" (120.65mm)

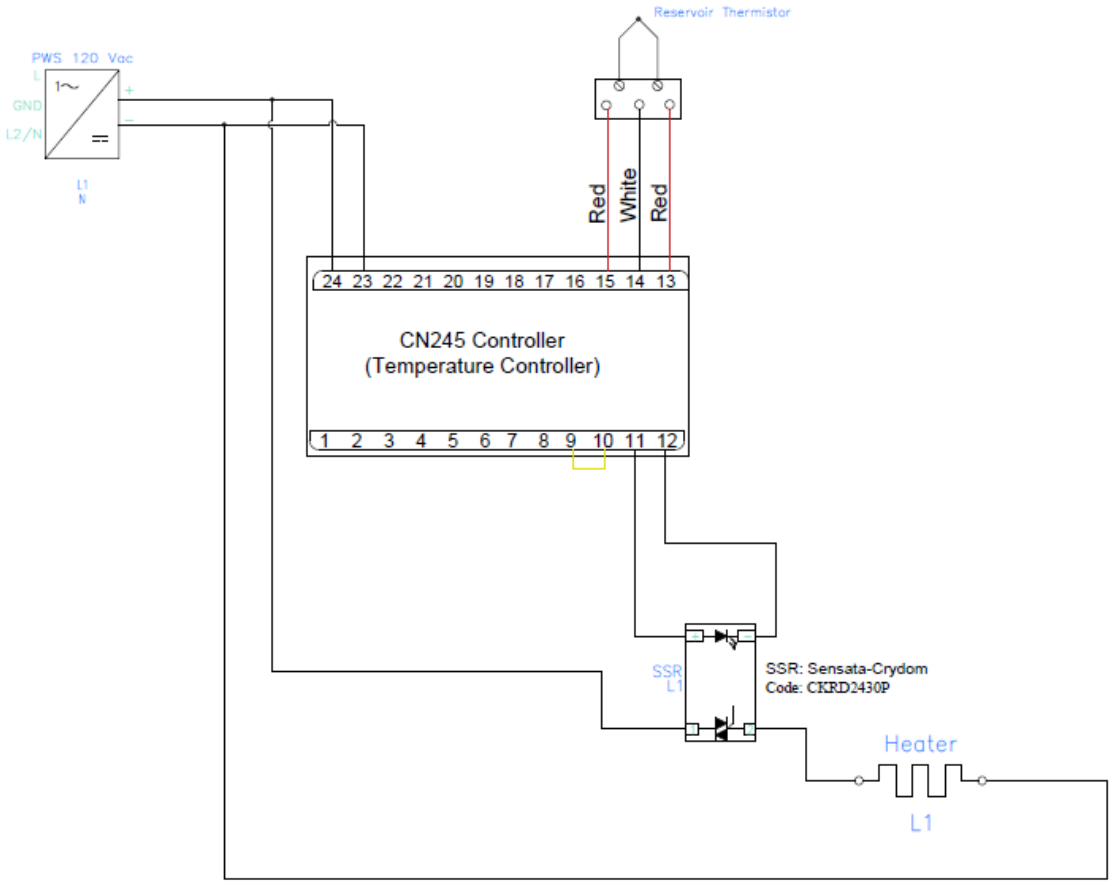

Figure A.7: Heater circuit diagram

Appendix 6: Apparatus P&I diagram

Figure A.8 depicts the apparatus P&I diagram detailing the apparatus that shows the piping and reservoir in the process flow, together with the instrumentation and control devices.

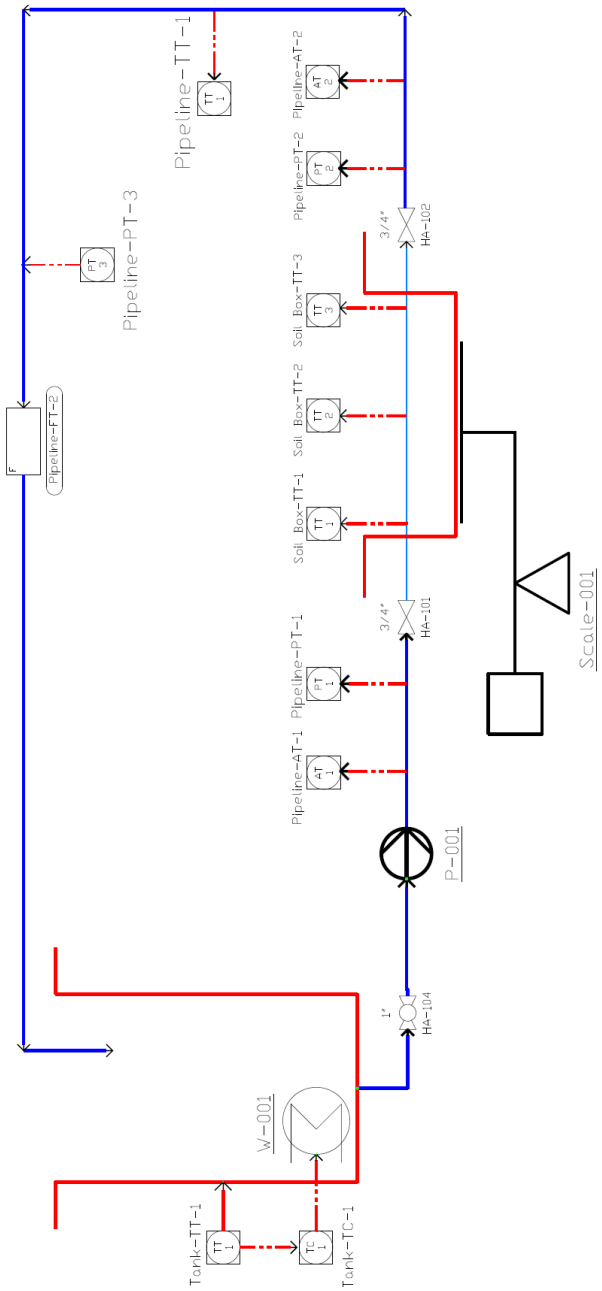

Figure A.8: Apparatus P&I diagram

Appendix 7: Bill of materials

Table A.11 shows the apparatus bill of materials; table A-12 depicts the required sensors.

Table A.11: Apparatus bill of materials N° 1

Material	Specifications	Quantity
Vessel	Vessel from zeebest (Code: OTC-45)	1 unit
Sand Box	Tote box from zeebest (Code: T162426T - 36 gallons)	2 unit
Valve	Spears CPVC Socket/FNPT x Socket/FNPT Ball Valve, Locking Tee, 1" Pipe Size	1 unit
Nipple	1X6" SCH80 PVC NIPPLE	1 unit
Nipple	1 1/2in.X6" SCH80 PVC NIPPLE	1 unit
3/4” / Pipe	3/4in. x 10' CPVC PIPE P/E AQUARISE	≈ 3.35 (m)
1” / Pipe	1 in. x 10' CPVC PIPE P/E AQUARISE	20 ft
11/2” Pipe	1 1/2in.x10' CPVC PIPE P/E AQUARISE	20 ft
Copper Pipe	000389 Copper Type L Water Tube, 3/4 in. X 3 ft.	6 ft
1” 90° Elbow	1 X 90 ELBOW CPVC AQUARISE	2 units
11/2” 90° Elbow	1 1/2 X 90 ELBOW CPVC AQUARISE	5 units
3/4” 90° Elbow	3/4 X 90 ELBOW CPVC AQUARISE	2 units
Reducer 1 x 3/4	1" X 3/4" CPVC Aquarise Reducing Bushing SPxS	1 unit
Reducer 1 1/2 x 3/4	1-1/2" X 3/4" CPVC Aquarise Reducing Bushing SPxS	1 unit
3/4” Tee	3/4in.x3/4in.x1/2in. CPVC RED. TEE SxSxS AQUARISE	2 units
CPVC to brass adapter	1/2 AQUARISE ADAPT FEM BRASS	2 units
CPVC to brass adapter	3/4 AQUARISE ADAPT FEM BRASS	2 units
Brass Threaded Reducer 1/2 X 1/8	1/2" X 1/8" Brass Threaded Bushing	2 units
1 1/2” Tee	1-1/2" x 1-1/2" x 3/4" Aquarise CPVC Reducing Tee SxSxS	1 unit
CPVC to brass adapter	359821 3/4 AQUARISE ADAPT SPG X FIP BRA	1 unit
Brass Threaded Reducer 3/4 X 1/8	3/4" X 1/8" Brass Threaded Bushing	1 unit
Disconnect tool 3/4”	RWC SharkBU712 Plastic Disconnect Clip, 3/4 in.	1 unit
3/4" Connect valve	RWC SharkB24736LF Lead-Free DZR Brass Lever Handle Full Port 2-Piece Inline Slip Ball Valve, 3/4 in., Push to Connect	2 units
CPVC Cement	074139 QUART (946ML) PVC CEMENT BLUE	1 unit

Table A.12: Apparatus bill of materials N° 2

Equipment	Specifications	Quantity
SCADA	Manufacturer: National Instruments, compounded by next slots:	1
	1) NI CDAQ-9178 (One unit)	
	a) Input FIFO size: 127 samples per slot	
	b) Maximum sample rate: Determined by the C Series I/O module or modules	
	c) Timing accuracy: 50 ppm of sample rate	
	d) Timing resolution: 12.5 ns	
	e) Number of channels supported: Determined by the C Series I/O module or modules	
	2) NI9203 (One unit)	
	a) 8-Channel, ±20 mA, 16-Bit Analog Input Module	
	b) Sample rate	
	i) R Series Expansion 192 kS/s max	
	ii) All other Chasis 200 kS/s max	
	3) NI9217 (One Unit)	
	a) 4 RTD, 0 Ω to 400 Ω, 24 Bit, 400 S/s Aggregate, PT100	
SCADA Slot	NI 9217 4-Ch PT100 RTD 24-bit, 100S/s/ch, Analog Input Module	1
Computer	Processor - dual core @ 2.4 GHz (i5 or i7 Intel processor or equivalent AMD) / Operating System - Windows 7	1
PID Controller	DIN Rail Mountable Universal Temperature Process Controller Code: CN245-R1-R2-F3-C4 https://www.omega.ca/pptst_eng/CN245.html	1
Thermistor (to measure the reservoir temperature)	Vibration Tested Thermistor Probe with M12 Connection Code: TH-21D-2252-1/4-0600-M12 / Straight sheath with 1/4 NPT mounting, 1/4" diameter, 6" long, M12 male connector	1
Heater	Screwplug Heater: 2"NPT, 304SS Elements 1500W, 120V, 1ph, 13"Imm. L,	1
Heating circuit control enclosure	Brand: Hammond Manufacturing - Code:CHKO666 Description: BOX STEEL GRAY 6"L X 6"W X 6” H	1
SSR relay to control the heater	Brand: Sensata-Crydom; Model: CKRD2430P; SSR RELAY SPST-NO 20A 24-280V	1
Pressure Transducers	Code: PX359-050AI	3
	Sensor - Span Limit: 50 psi	
	Process Connection: ¼-18 MNPT	
	Electrical Connection: M12 connection	
	Output: 4 ... 20 mA -	
Pressure Transducer cable extension	Code: CA-359-4PC22-5M / 5 m (16') vented cable with M12 connector for PX359 for gage ranges <100 psi	2

Equipment	Specifications	Quantity
Weighing platform	Meter Toledo, Model: PBA220-QD300 · Capacity: 300 (Kg) · Material: Carbon steel	1
Load Cell Input Signal Conditioner	Meter Toledo, Model: 71208076	1
Load Cell Power Supply	POWER SUPPLY 7.5W 24VDC DIN	1
Temperature sensor (fluid temperature within the pipe)	Code: PR-30-PT100A-0250 Pt100 RTD (100 Ω at 0°C) Range: Temperature Range -50 to 200°C (32 to 212°F)	1
Extension cable for the thermistors	Code: M12C-PUR-4-S-F-10 RoHS compliancy undetermined Polyurethane Cable, straight 4-pin M12 female connector one end, flying leads one end, 10 m long	8
PT100 RTD (to measure the soil temperature)	PR-26F-3-100-A-M6-0350-M12-2: Vibration Resistant and Bendable RTD (Pt100) Probe with M12 Connector and Mounting Thread	3
Accelerometers	Manufacturer: Bruel and Kjaer; Model: Type 4506 (Miniature triaxial piezoelectric ccld accelerometer, 100mv/g)	2
Pump	Manufacturer: IWAKI; Model: Mag-Drive PP Centrifugal Pump w/Enclosed Motor; Code: MX-251CV6-2 · (MX) Material of casing: GFRPP · (251) Pump size: 25Ax25A 0.75 KW - Motor: 1 HP\ · (CV) Material of bearing/Spindle/O-ring: Carbon/Alumina ceramic/FKM (EPDM) · (6) Impeller mark: 60 Hz · (2) Motor: 3phase 200/200/220V • Max Discharge Pressure (ft): 75 • Max Flow (GPM): 40 / Max Pressure (psi): 47.6	1
Variable Frequency Drive (VFD)	ABB: ABB machinery drive VACS355 (0.37 to 22 kW/0.5 to 30 hp); Code: ACS355-03X-04A7-2+R1+J400+J402+OPMP-01 · (03X) Construction: 3-phase · (04A7) Size: 1 hp · (2) Voltage range: 200 to 240 V · (R1) Frame Size and Type: Cabinet-mounted drives · (J400) Control panel: Assistant control panel	1
Circuit Breaker	Brand: Altech Corporation - Code: 3G15UM 3 Pole – Thermomagnetic 15 Amp – 480 Vac	1
Fast Acting Fuses	Brand: Littelfuse - Code: JLLS015 Specifications: 15 Amp - Class T - Type: Cartridge Lead Voltage Rating: 600 VAC - Interrupting Rating: 200,000 Amp Features: Fast Acting.	6
Fuse Holder	Brand: LittelFuse~ Code: LFT600303C Specification: Fuse Block - Class T - 3 Pole - 30 Amp - 600V AC	1

Equipment	Specifications	Quantity
	Terminal Type: Box - Max. Wire Size: #24 Copper. DIN Rail Mountable.	
VFD control enclosure	Brand: Hammond Manufacturing - Code: EJ14128 Description: N4,12 enclosure w/panel - 14 x 12 x 8 - Steel/Gray	1
Din Rail	DIN RAIL 35MMX7.5MM SLOTTED 2M	1
Din Clip	DIN CLIP FOR 1427 SERIES	4
Cable 4 conductors for VFD	CABLE 4COND 14AWG BLK SHLD 100'	1
Hose 1.220" id steel 3.28' silvr	Hose 1.220" id steel 3.28' silvr	10
CBL clamp 1/2"	CBL clamp p-type black fastener	10
CBL clamp 1 1/2"	CBL clamp p-type black fastener	1
Cable gland m32	Cable gland 18-25mm m32 nylon	2
Flow Meter	Code: FMG3002-PP Polypropylene/316LSS, 1 1/2" pipe size 4 to 20 mA output	1
Flow Meter Fitting	Code: FP-5310M / 1 1/2" PVC 40 Fitting	1
Power cable hose	Code: PHC 3240848	10 meters
24 VDC Power supply	Power supply unit - UNO-PS/1AC/24DC/30W - 2902991	1
DIN rail adapter	DIN rail adapter - PTFIX-NS35 - 3274054	2

Appendix 8: Denoising signal techniques

The denoising methods required extensive knowledge and understanding of the noise features. The implementation of these methods relies on the frequency and time domain. Some techniques of de-noising are short-time Fourier transform (STFT), fast Fourier transform (FFT), low pass filtering, least mean square approach, Wavelet Transform, artificial neural networks (ANN) and support vector machines (SVM) (Yusoff et al., 2016).

A.8.1) Wavelet transform

The Wavelet Transform (WT) usefully analyzes non-stationary signals (the signal period is variable) because it provides an alternative to the classical Short-Time Fourier Transform (STFT). The fundamental difference between both of them is whereas STFT uses a single analysis window, the WT uses short windows at high frequencies and long windows at low frequencies (Rioul and Vetierli, 2017). In other words, the Wavelet Transform represents a signal as a sum of translations and dilations of a band-pass function called a wavelet (Mallat, 1989). Moreover, whereas the Fourier transform represents a signal in the frequency domain alone, the wavelet transform provides a spatial-frequency representation of a signal.

Moreover, the Fourier transform gives a constant resolution at all frequencies, whereas the wavelet transform uses a multiresolution technique by which different frequencies are analyzed with different resolutions (Guzel et al., 2011). In wavelet analysis, the scale used to look at data plays a unique role. Wavelet algorithms process data at different scales. Large “windows” look at gross signal features whereas small “windows” look at small signal features, so replacing a fixed windows as SFTF does by compressed versions of unique oscillating windows as WT does, then more reliable and accurate results occur (Graps, 2017), yet WT performs well for white noise, but fails for non-white noise (Zeng, 2015).

Figure A.9 shows a windowed Fourier transform, where the window is simply a square wave, and a widowed Wavelet transform, where the window changes according to by the time.

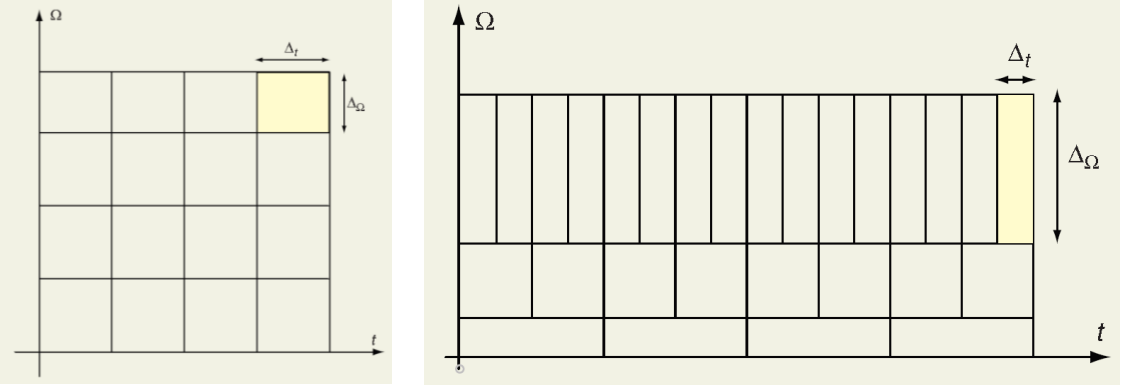

Figure A.9: Time-frequency plane for the STFT and Wavelet Transform

According to Gargour et al. (2017), the Continuous Wavelet Transform (CWT) of a signal x is defined:

$$X_\psi(a,b) = \langle x(t), \psi_{ab}(t) \rangle = \int_{-\infty}^{+\infty} x(t)\psi_{ab}(t)dt$$

$\psi_{ab}(t)$ is a continuous affine transform of the 'mother wavelet' $\psi(t)$

$$\psi_{ab}(t) = \frac{1}{\sqrt{a}}\psi\left(\frac{t-b}{a}\right), a \in R, a \neq 0, b \in R \qquad a, scaling;\ b, time$$

Mallat and Peyré (2009) comprised the equations of wavelet families:

- **Haar Wavelet:**

The Haar wavelet's mother wavelet function $\psi_{ab}(t)$ can be described as

$$\psi_{ab}(t) = \begin{cases} 1 & 0 \leq t < \frac{1}{2} \\ -1 & \frac{1}{2} \leq t < 1 \\ 0 & otherwise \end{cases}$$

Its scaling function $\varphi_{ab}(t)$ can be described as

$$\varphi_{ab}(t) = \begin{cases} 1 & 0 \leq t < 1 \\ 0 & otherwise \end{cases}$$

- **Daubechies wavelets**

There are several Daubechies forms, they like the Haar transform, can be extended to multiple levels as many times as the signal length can be divided by 2. The discrete-time domain representation is (Chun-Lin, 2010):

$$h_{\emptyset}[n] = \frac{\sqrt{2}+\sqrt{6}}{8}\delta[n] + \frac{3\sqrt{2}+\sqrt{6}}{8}\delta[n-1] + \frac{3\sqrt{2}-\sqrt{6}}{8}\delta[n-2] + \frac{\sqrt{2}+\sqrt{6}}{8}\delta[n-3]$$

According to Chun-Lin (2010), the result is the minimum size filter with two vanishing moments, and the corresponding filter size is four. Higher-order Daubechies wavelets are computed similarly.

To denoise a signal using Wavelet Transform denoising is straightforward; thresholding is the basic principle underlying this method. Figure A.10 depicts this process.

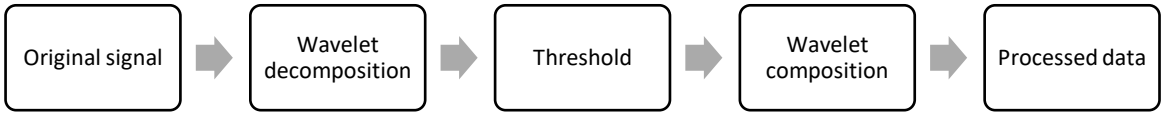

Figure A.10: Wavelet Thresholding Process

Assessment decomposition is the process where a signal is broken in two parts by inserting a wavelet family signal to the system, resulting in many signals, being each one a fraction of the original signal, but they are different from each other in the frequency domain (Herlinawati, 2017). Thresholding eliminates those values of the wavelet decomposition components higher than the predetermined thresholds T_i for each scale S_i. Hard thresholding and soft thresholding are the most used threshold methods. Hard thresholding consists on zeroed any S_i higher than T_i whereas soft thresholding reduces by T_i the signal decomposition components, S_i, greater than the threshold T_i. The inverse wavelet transformation reverses the resulting coefficients to yield a de-noised version of the original signal without unacceptable distortion (Gargour et al., 2017).

Appendix 9: Systematic errors check (Transducer readings)

Leak Detection System Experiments

University of Alberta
MECE 2-17
Date:

1 1/2": V(m/s) x 24.737 = GPM

Experiment Number:	

Type of Fluid	**Type of Soil**	**Initial Moisture Content (%)**	**Orifice Size (mm)**	**Fluid Velocity (m/s)**
Water	Brown chernozemic		0	

Sytematic errors check (Transducer readings)

TReference (^{0}C)	**T1 (^{0}C)**	**T2 (^{0}C)**	**T3 (^{0}C)**

TReference (^{0}C)	**TT_Pipe (^{0}C)**

WReference (Kg)	**Weight (Kg)**

Flow (m/s) - Labview	**Time (s)**	**Volume (Gal)**	**Flow (GPM) - Indirect**	**Flow (m/s) - Indirect**

Notes:

Done by: _____

Appendix 10: Water moisture content curves for black chernozemic soil and sand

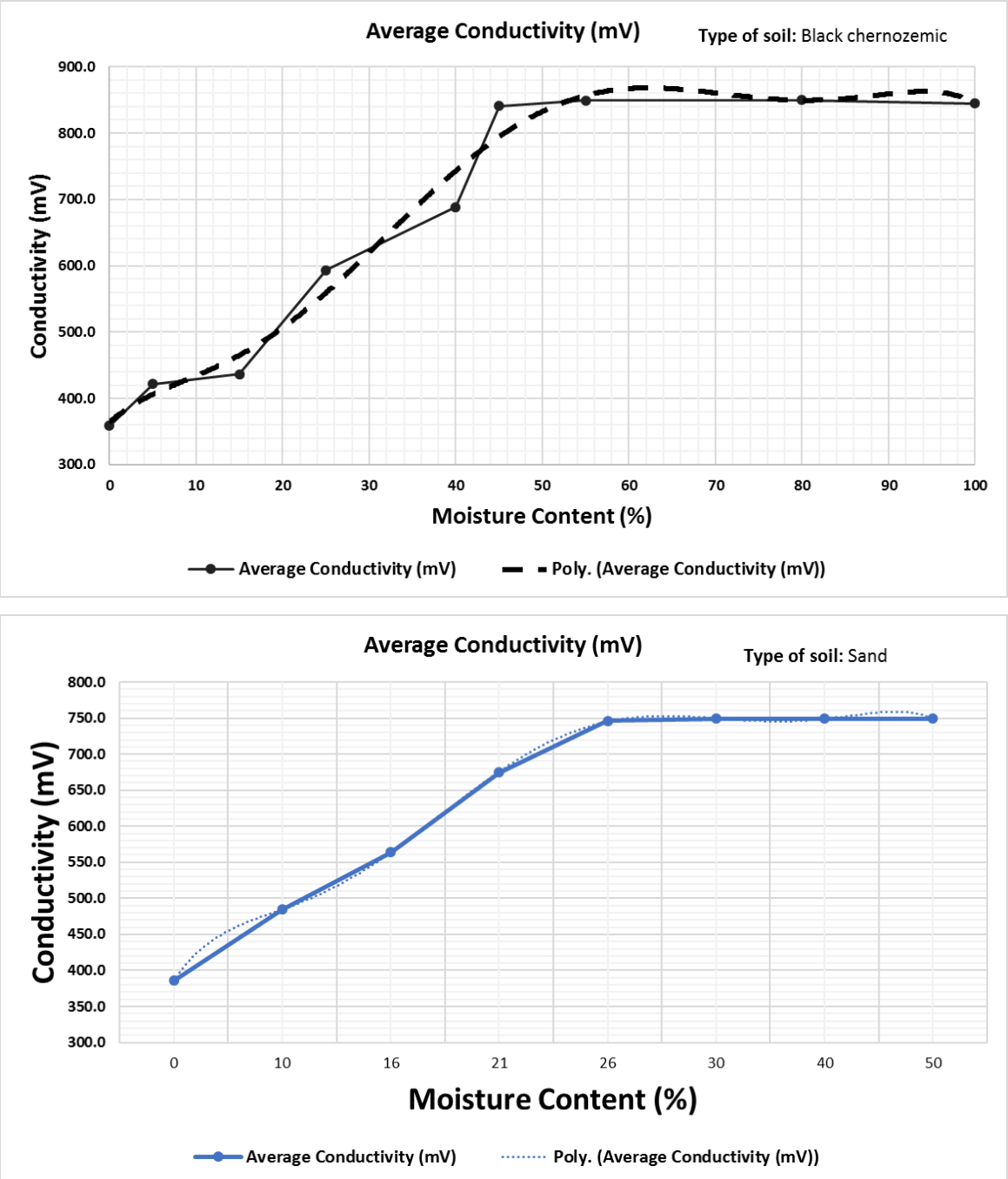

Figure A.-13. Water Moisture content curves for Black chernozemic soil and sand

Appendix 11: Thermal images of steady-state and small leak experiments

Pictures of experiments 1, 16, 23 are chapter #5. Current appendix compresses pictures of otherwise experiments.

- Experiment #1 results (2 % moisture / Sand / no leak / Fluid Velocity: 5 m/s)
- Experiment #16 results (15 % moisture/Black soil/2.2% leak/Fluid Velocity: 5 m/s)

- **Experiment #2 results (2 % moisture / Sand / no leak / Fluid Velocity: 3.5 m/s)**

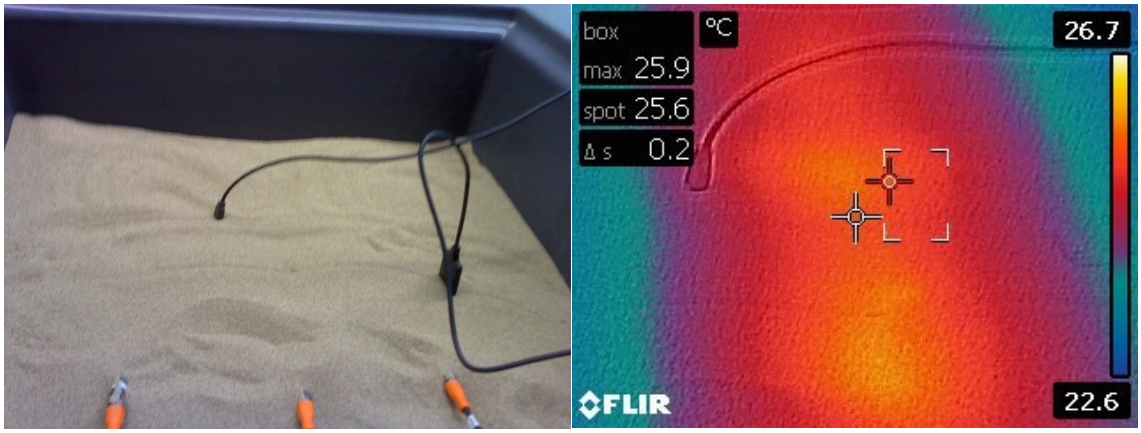

Figure (a): Experimental setup #2 when starting the experiment

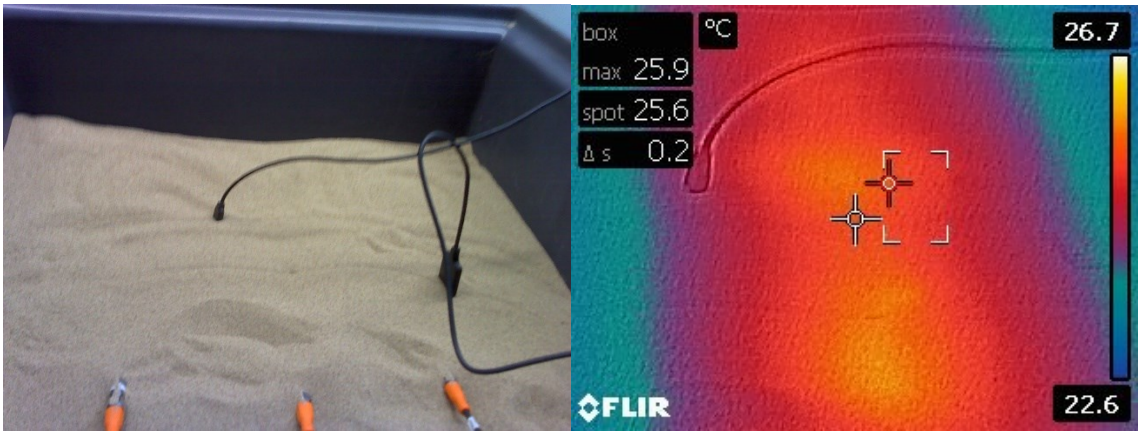

Figure (b): Experimental setup #2 when finishing the experiment

- **Experiment #3 results (15 % moisture / Black soil / no leak / Fluid Velocity: 3.5 m/s)**

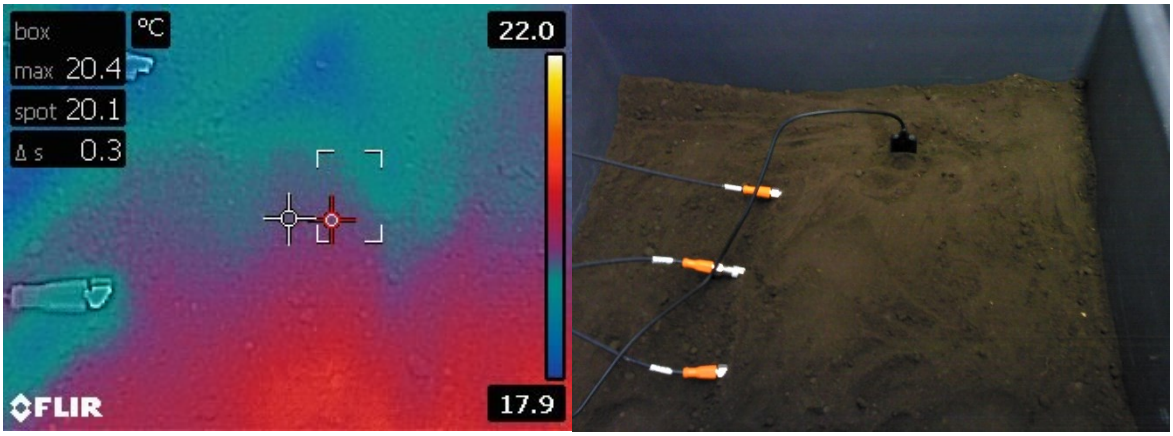

Figure (a): Experimental setup #3 when starting the experiment

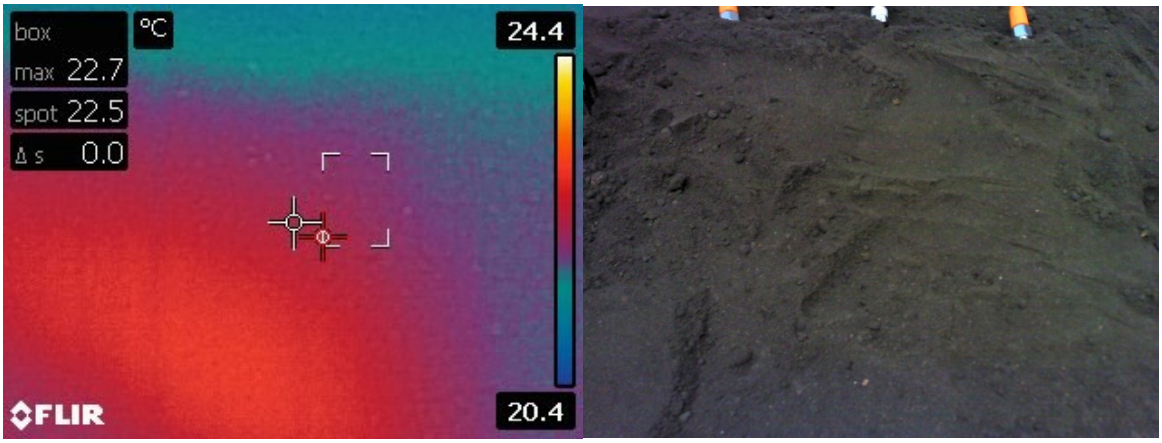

Figure (b): Experimental setup #3 when finishing the experiment

- **Experiment #4 results (15 % moisture / Black soil / no leak / Fluid Velocity: 5 m/s)**

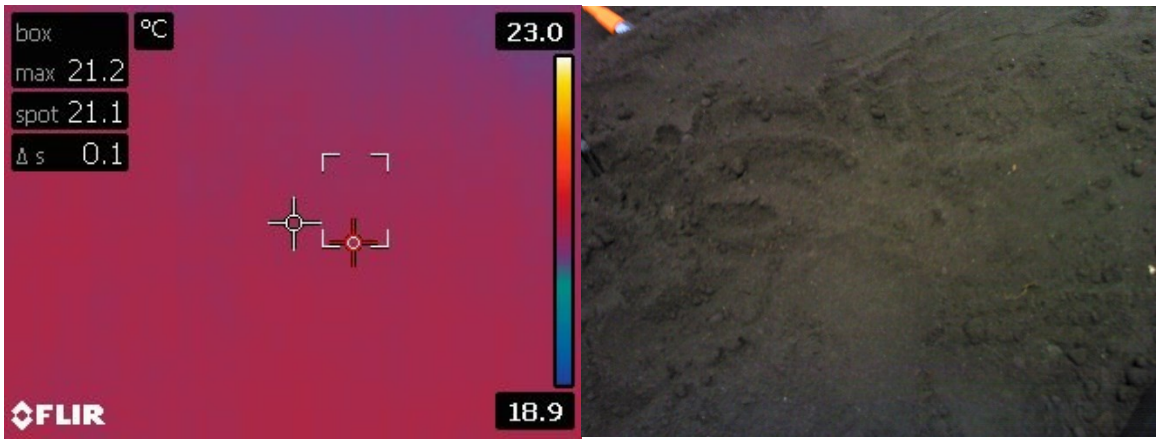

Figure (a): Experimental setup #4 when starting the experiment

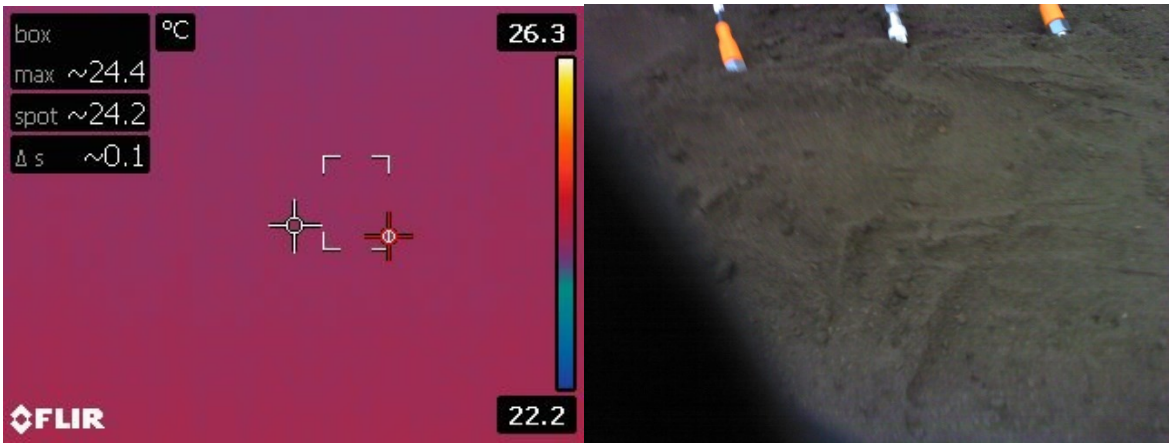

Figure (a): Experimental setup #4 when finishing the experiment

- **Experiment #5 results (15% moisture/Black soil / 0.97% leak / Fluid Velocity: 5 m/s)**

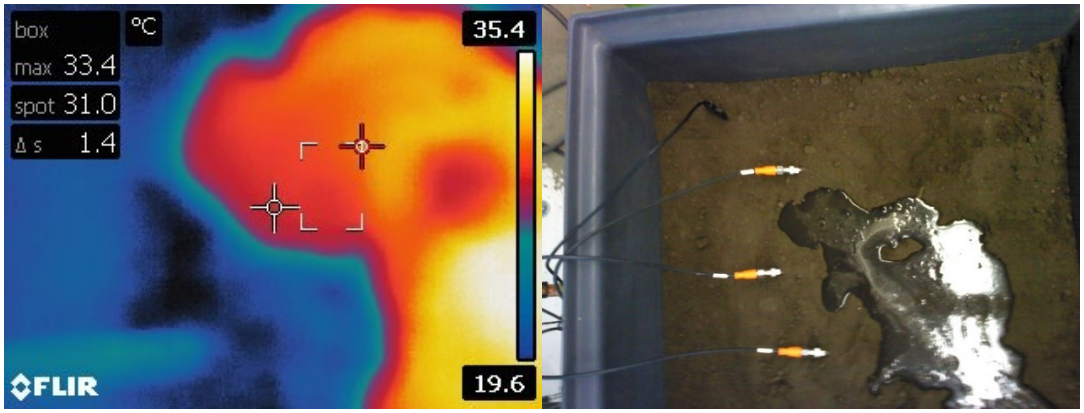

Figure (a): Experimental setup #5 when starting the experiment

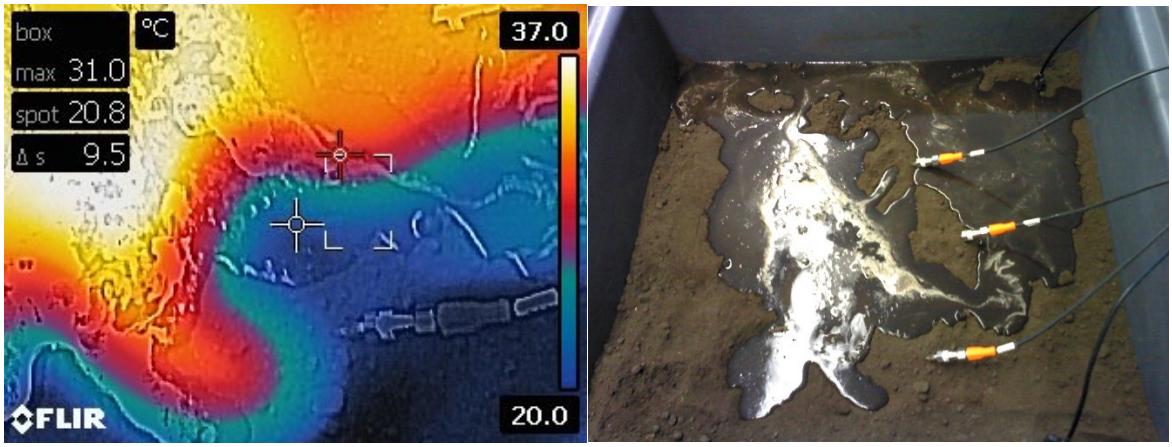

Figure (b): Experimental setup #5 through the running

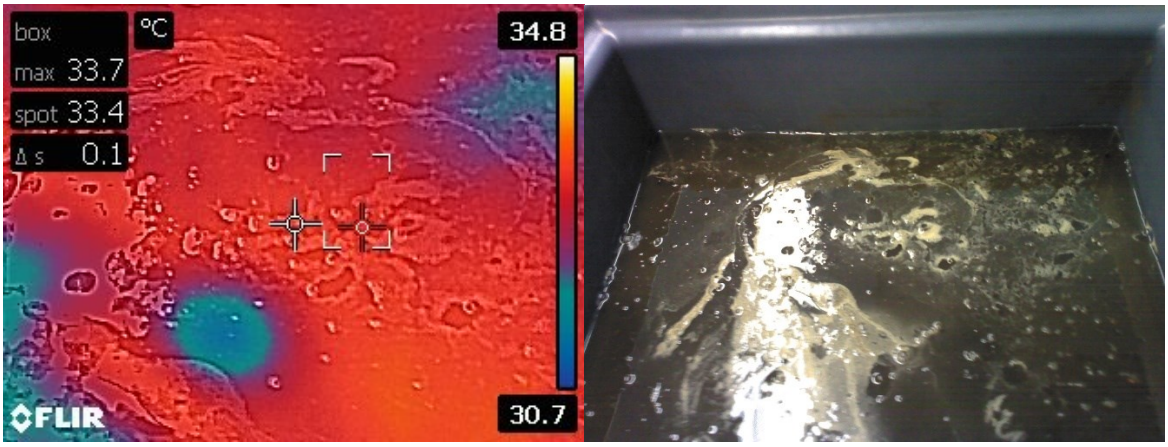

Figure (c): Experimental setup #5 when finishing the experiment

- **Experiment #6 results (45 % moisture /Black soil/0.97% leak/ Fluid Velocity: 5 m/s)**

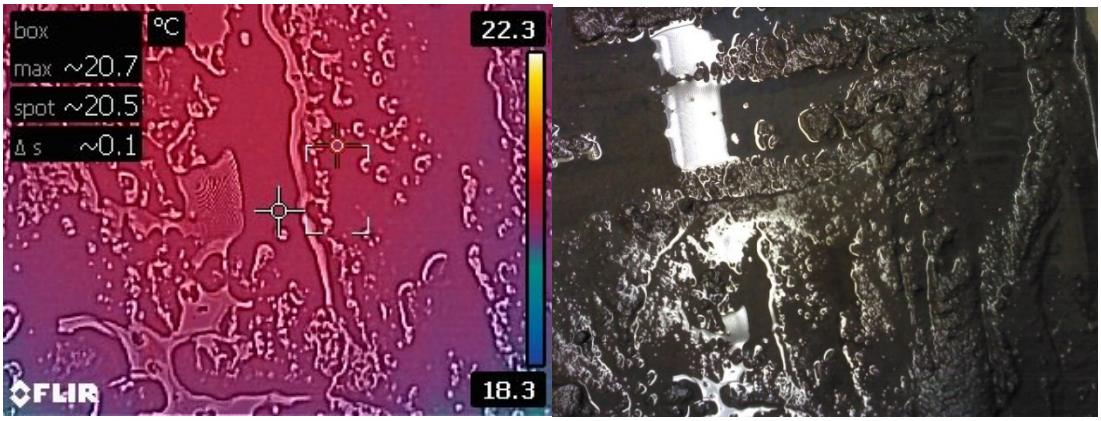

Figure (a): Experimental setup #6 when starting the experiment

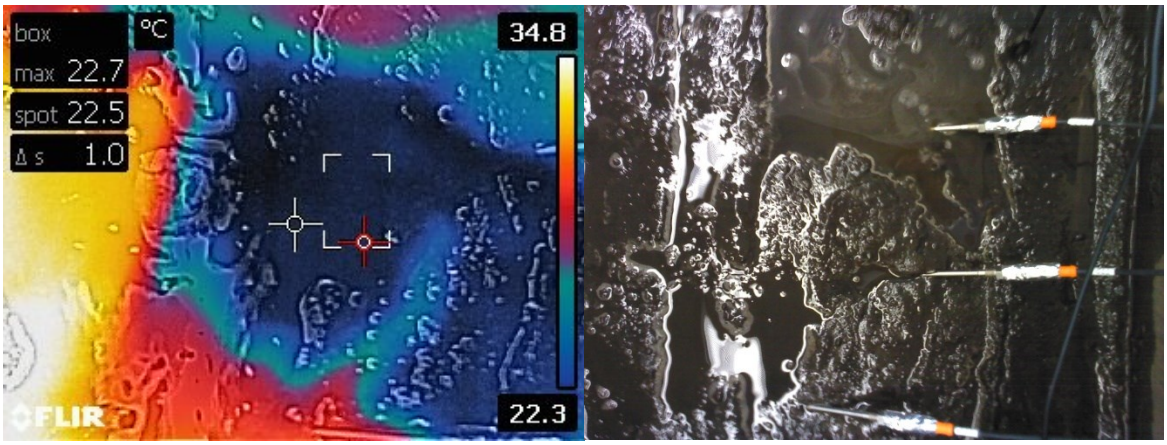

Figure (a): Experimental setup #6 through the running

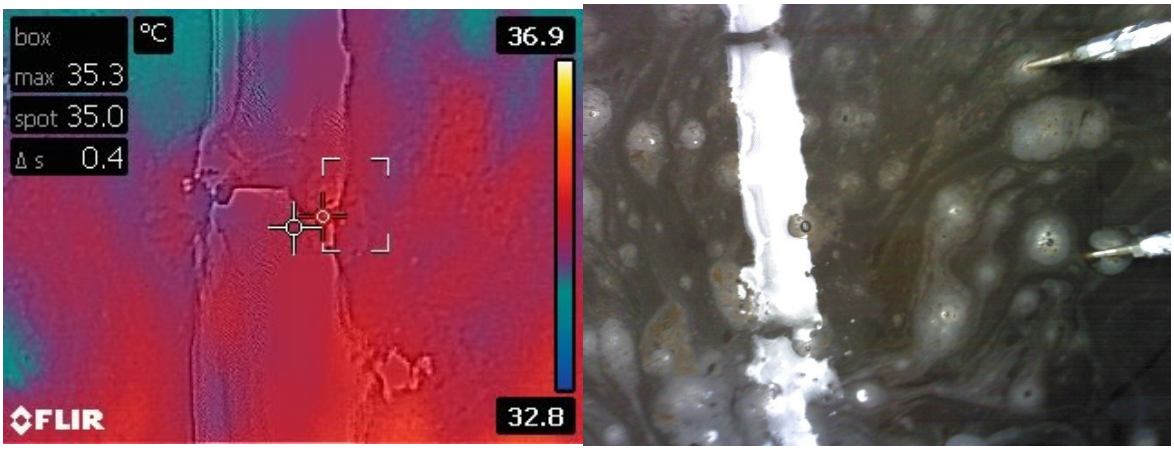

Figure (c): Experimental setup #6 when finishing the experiment

- **Experiment #7 results (45 % moisture/Black soil/0.97% leak/Fluid Velocity: 3.5 m/s)**

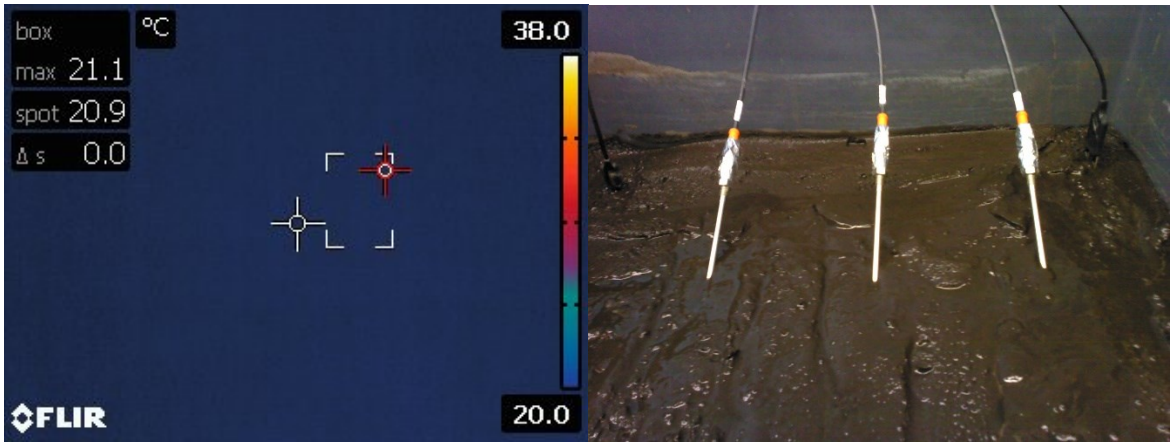

Figure (a): Experimental setup #7 when starting the experiment

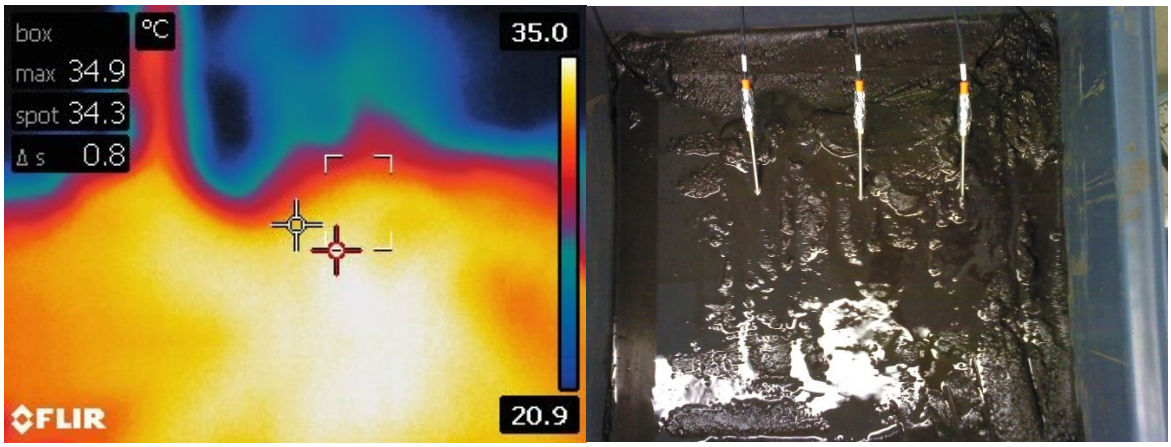

Figure (b): Experimental setup #7 through the running

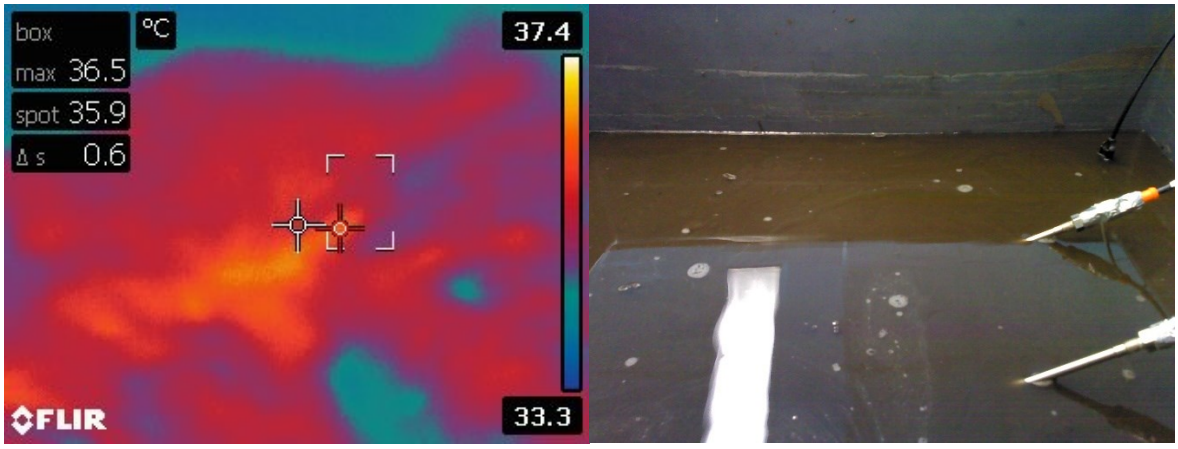

Figure (c): Experimental setup #7 when finishing the experiment

- **Experiment #8 results (2 % moisture / Sand / 0.97% leak / Fluid Velocity: 5 m/s)**

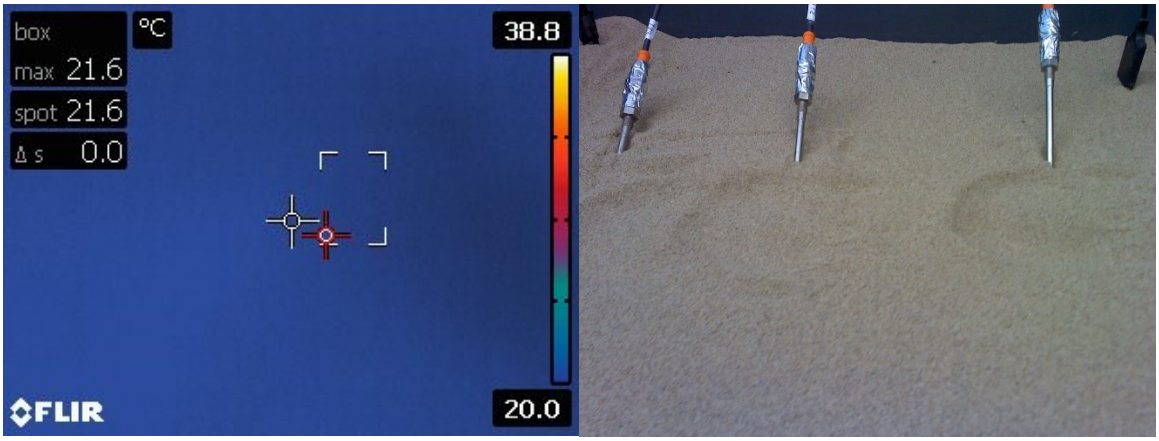

Figure (a): Experimental setup #8 when starting the experiment

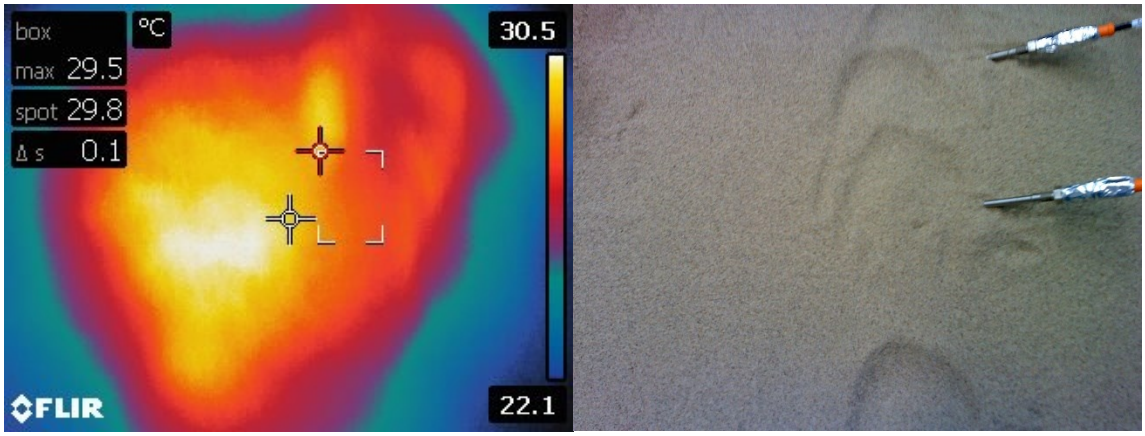

Figure (b): Experimental setup #8 through the running

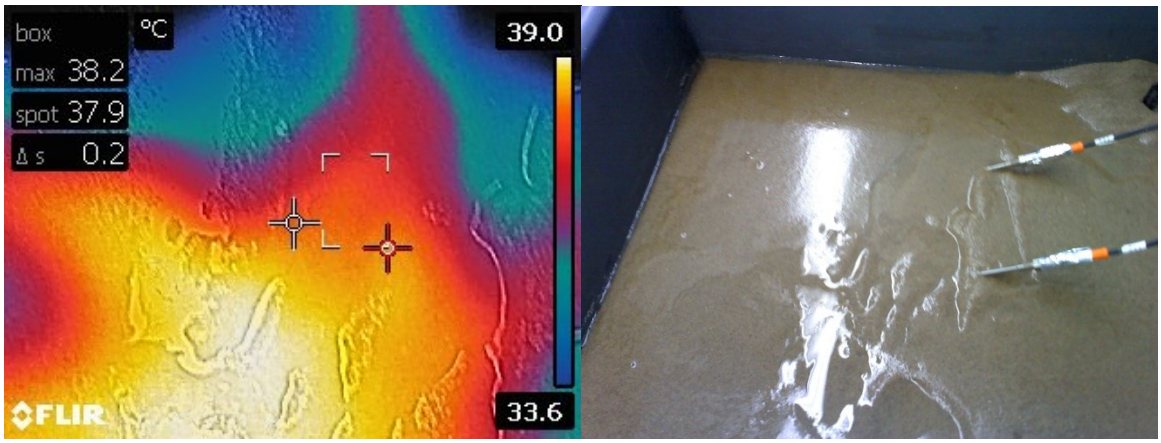

Figure (c): Experimental setup #8 when finishing the experiment

- **Experiment #9 results (26 % moisture / Sand / 0.97% leak / Fluid Velocity: 5 m/s)**

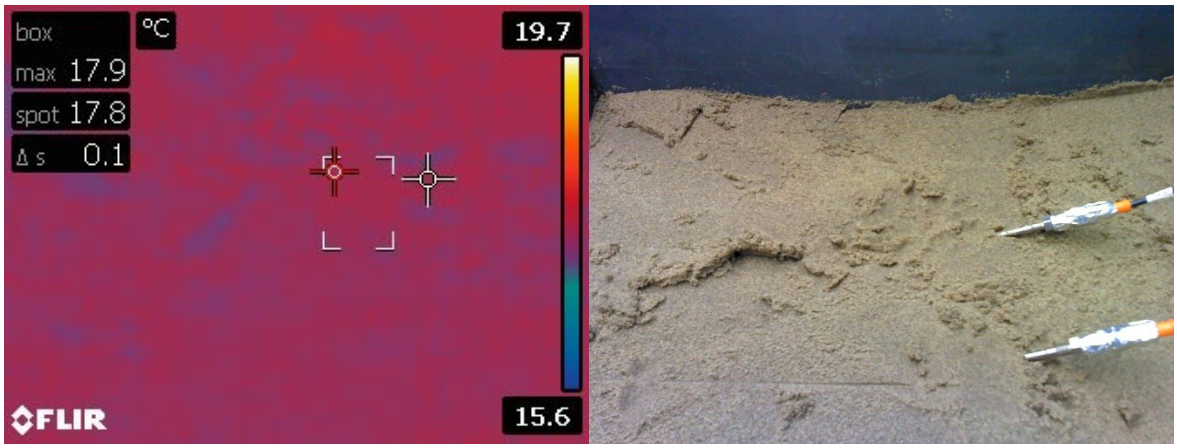

Figure (a): Experimental setup #9 when starting the experiment

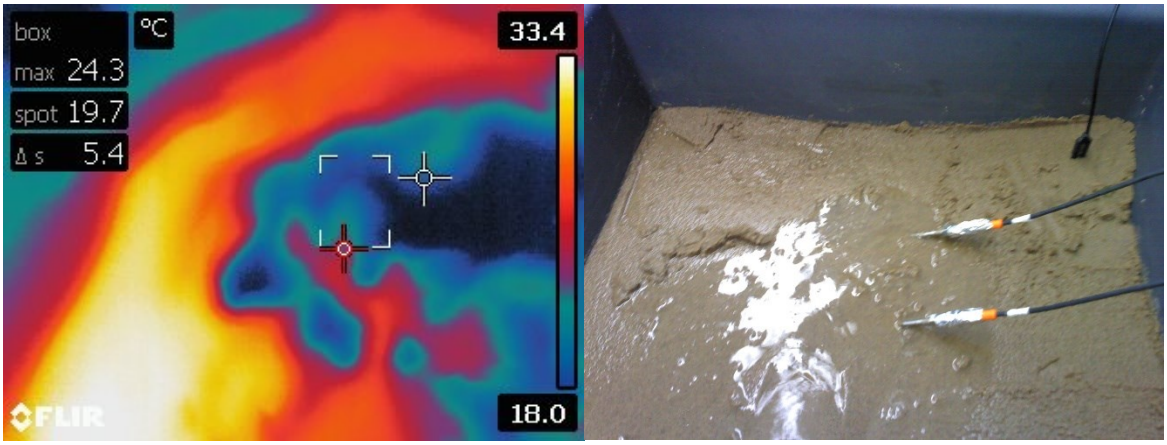

Figure (b): Experimental setup #9 through the running

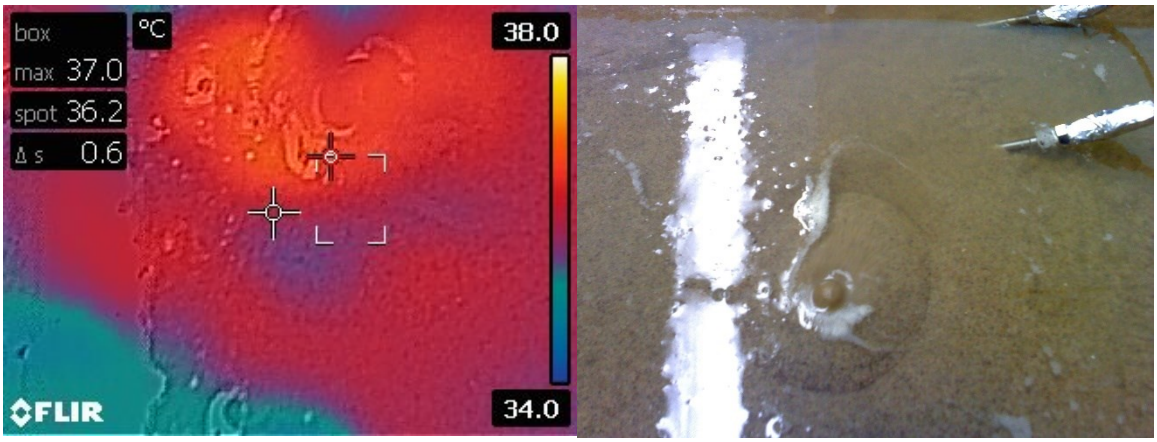

Figure (c): Experimental setup #9 when finishing the experiment

- **Experiment #10 results (26 % moisture /Sand/0.97% leak / Fluid Velocity: 3.5 m/s)**

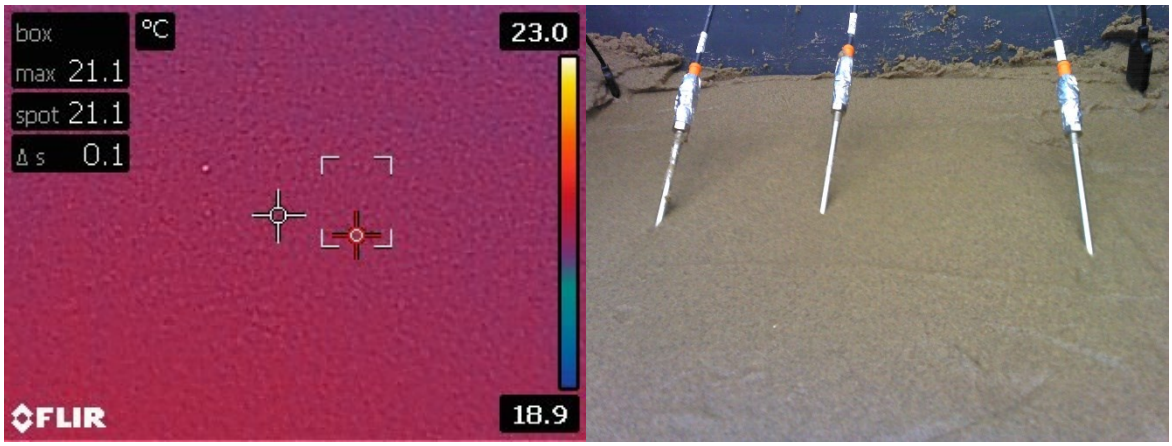

Figure (a): Experimental setup #10 when starting the experiment

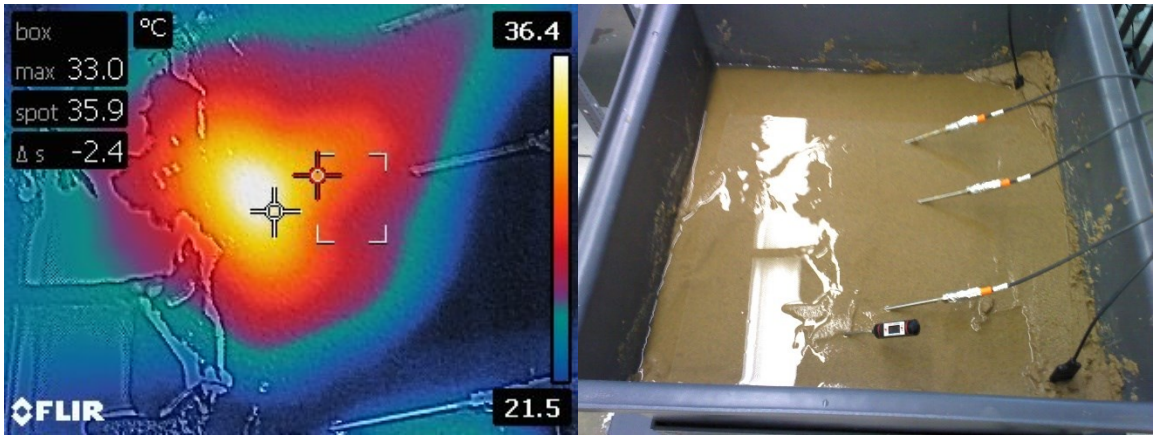

Figure (b): Experimental setup #10 through the running

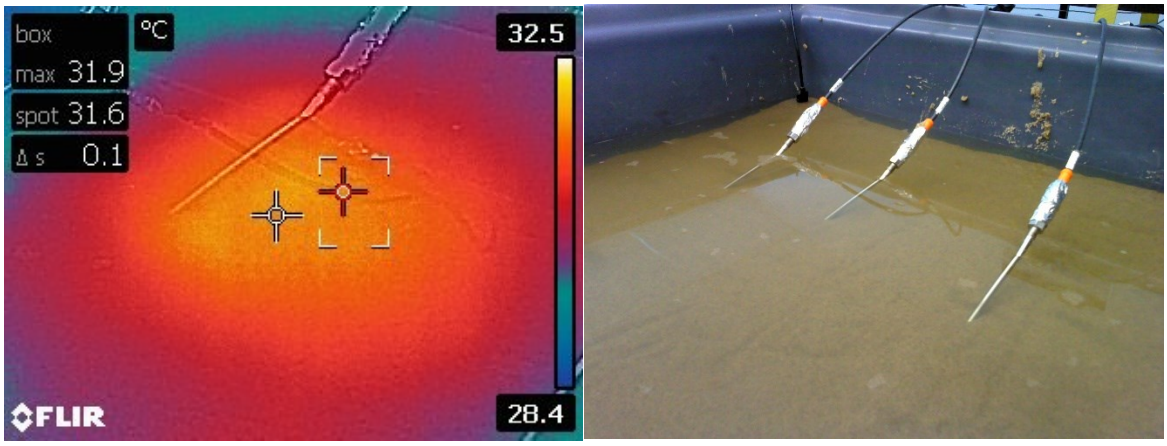

Figure (c): Experimental setup #10 when finishing the experiment

- **Experiment #11 results (26 % moisture / Sand / no leak / Fluid Velocity: 5 m/s)**

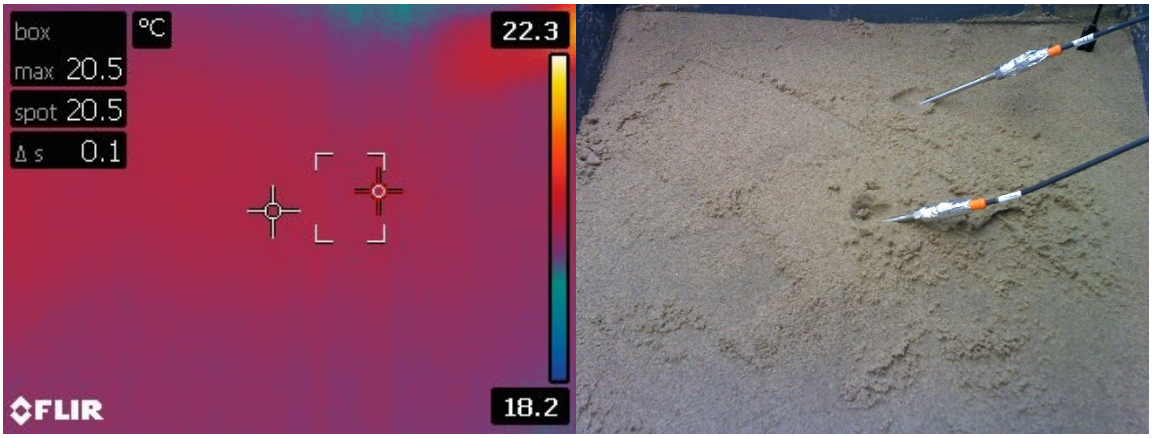

Figure (a): Experimental setup #11 when starting the experiment

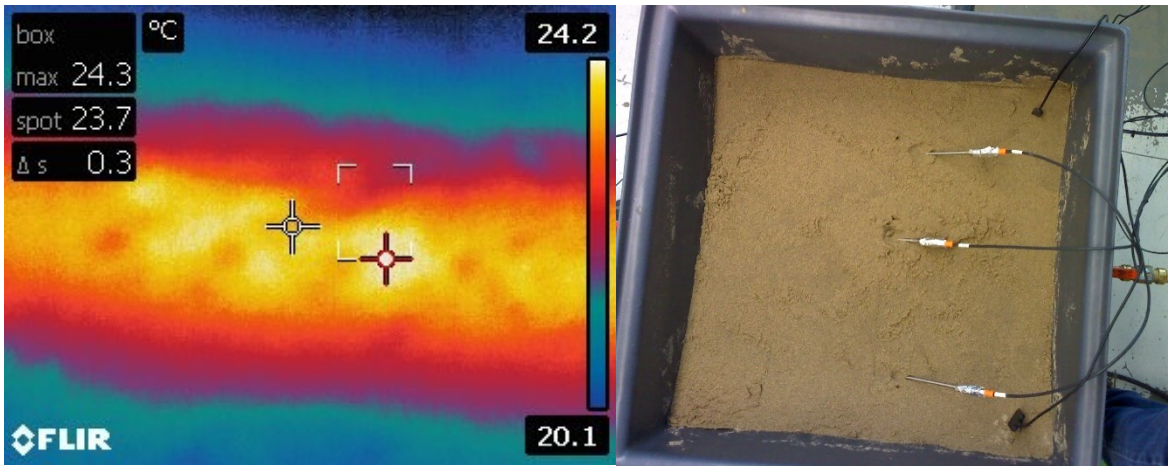

Figure (b): Experimental setup #11 when finishing the experiment

- **Experiment #12 results (26 % moisture / Sand / no leak / Fluid Velocity: 3.5 m/s)**

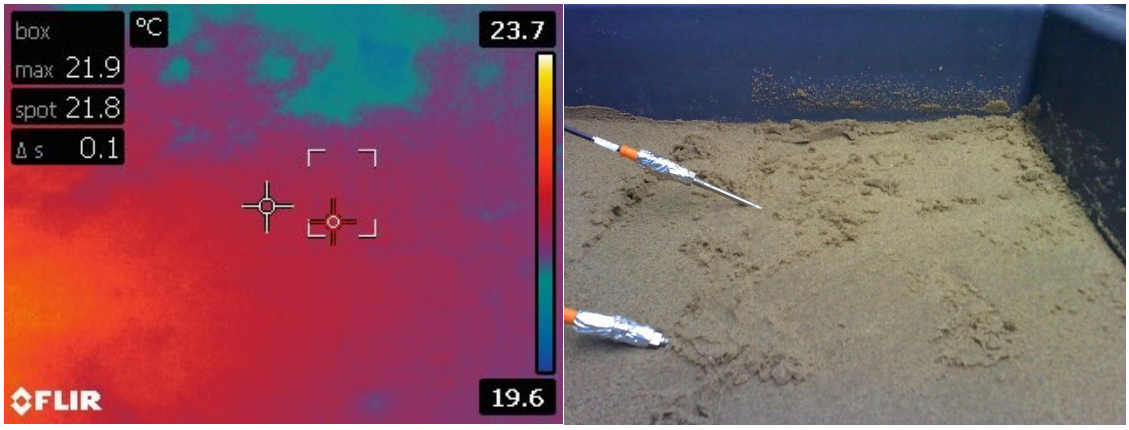

Figure (a): Experimental setup #12 when starting the experiment

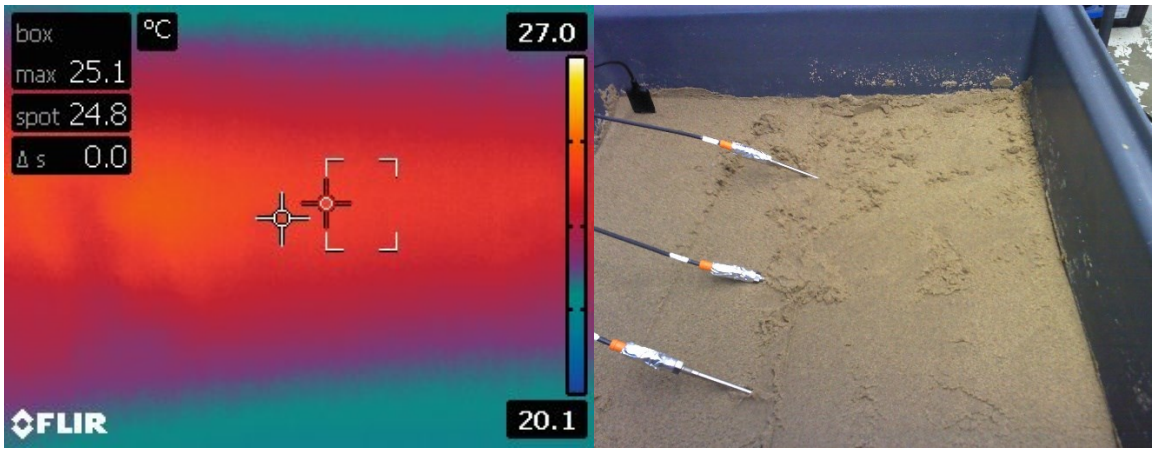

Figure (b): Experimental setup #12 when finishing the experiment

- **Experiment #13 results (2 % moisture / Sand / 0.97% leak/Fluid Velocity: 3.5 m/s)**

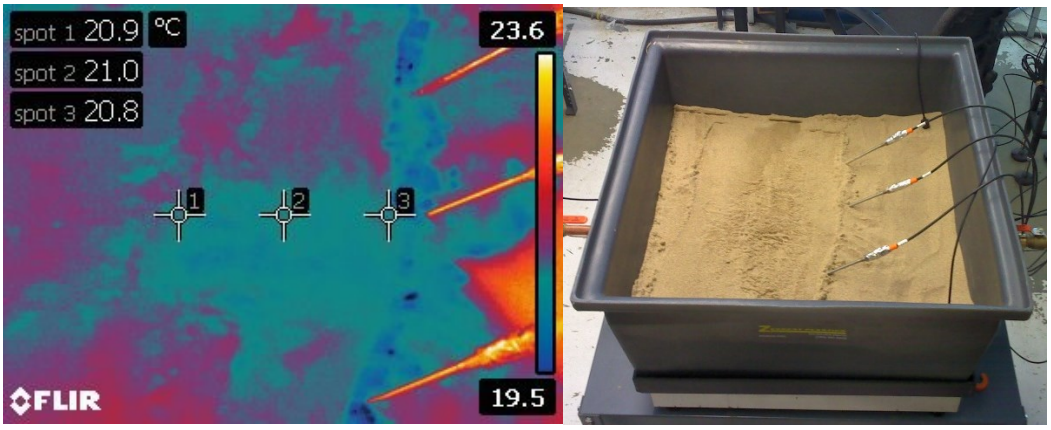

Figure (a): Experimental setup #13 when starting the experiment

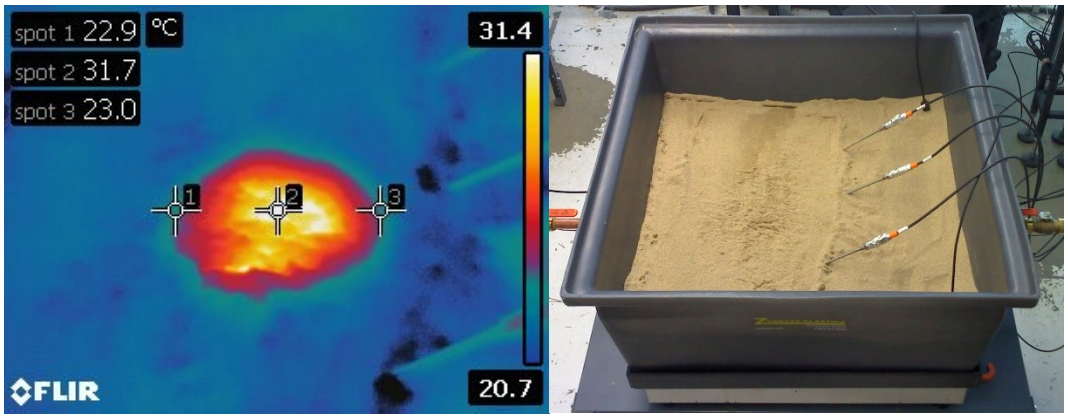

Figure (b): Experimental setup #13 through the experimental running

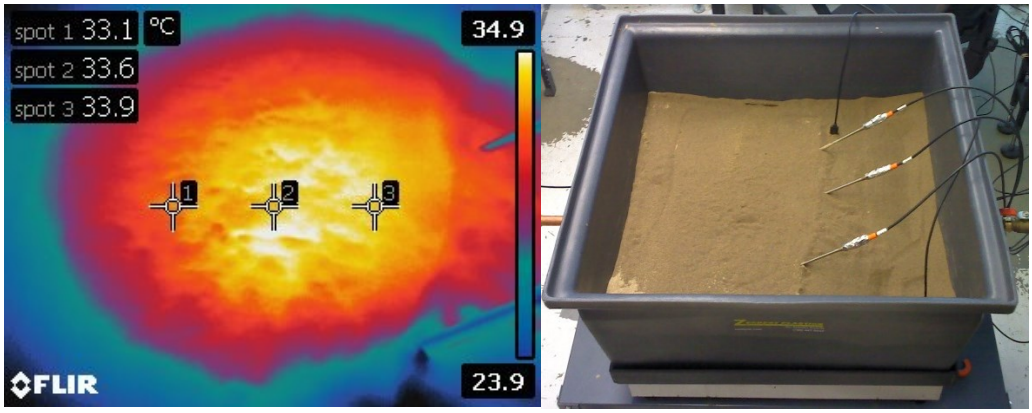

Figure (c): Experimental setup #13 when finishing the experiment

- **Experiment #14 results (26 % moisture / Sand / 2.2% leak / Fluid Velocity: 5 m/s)**

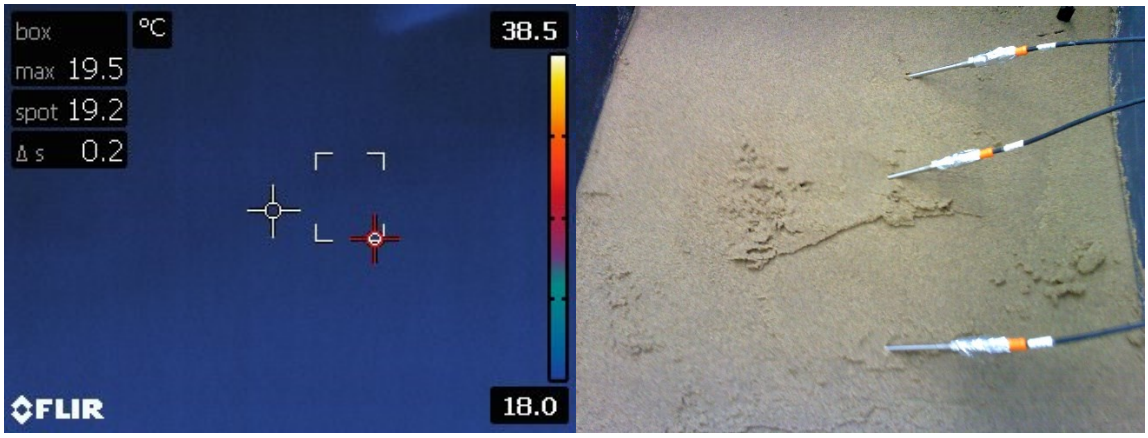

Figure (a): Experimental setup #15 when starting the experiment

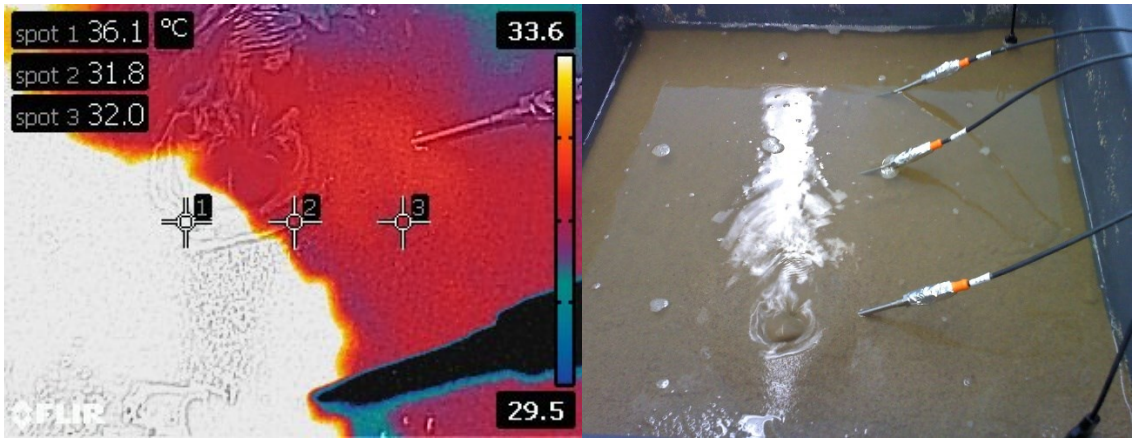

Figure (b): Experimental setup #15 through the experimental running

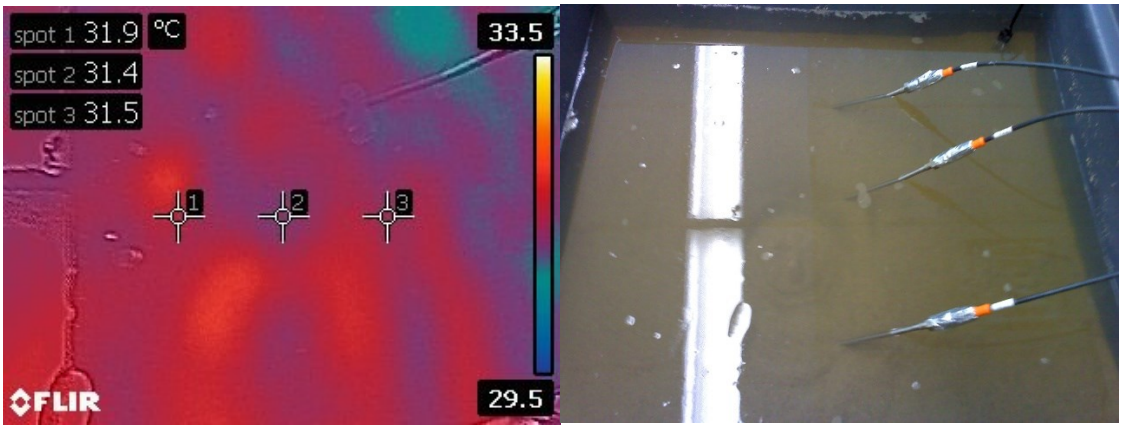

Figure (c): Experimental setup #15 when finishing the experiment

- **Experiment #15 results (26 % moisture / Sand / 2.2% leak/Fluid Velocity: 3.5 m/s)**

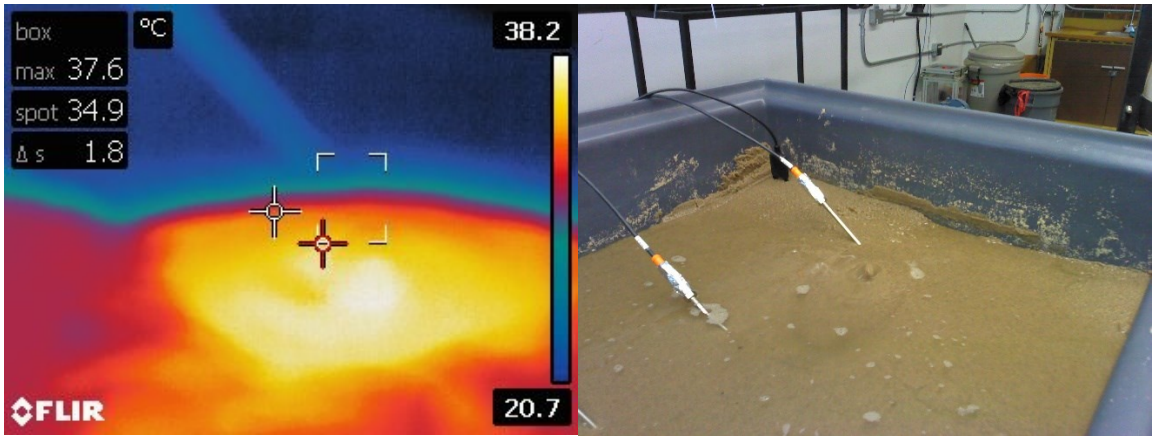

Figure (a): Experimental setup #8 when starting the experiment

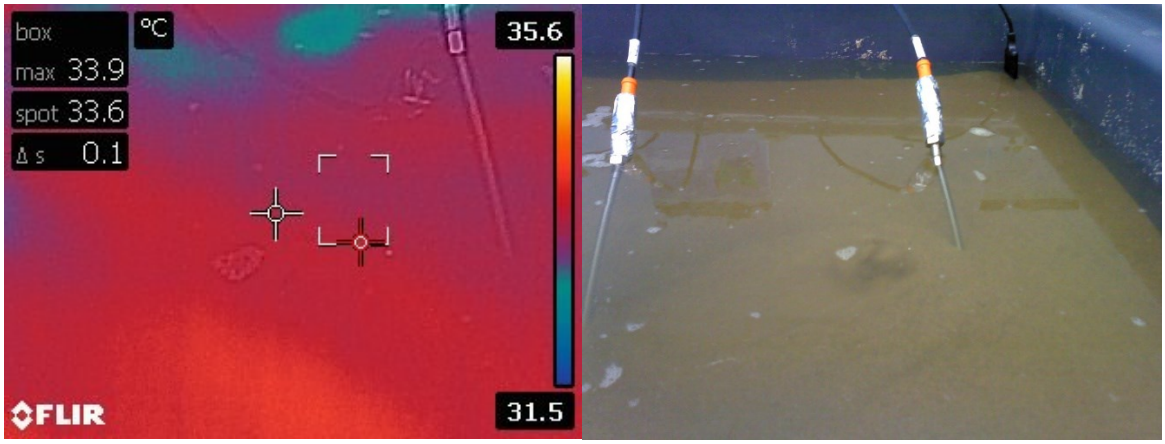

Figure (b): Experimental setup #8 when finishing the experiment

- **Experiment #17 results (45 % moisture/Black soil/2.2% leak/Fluid Velocity: 5 m/s)**

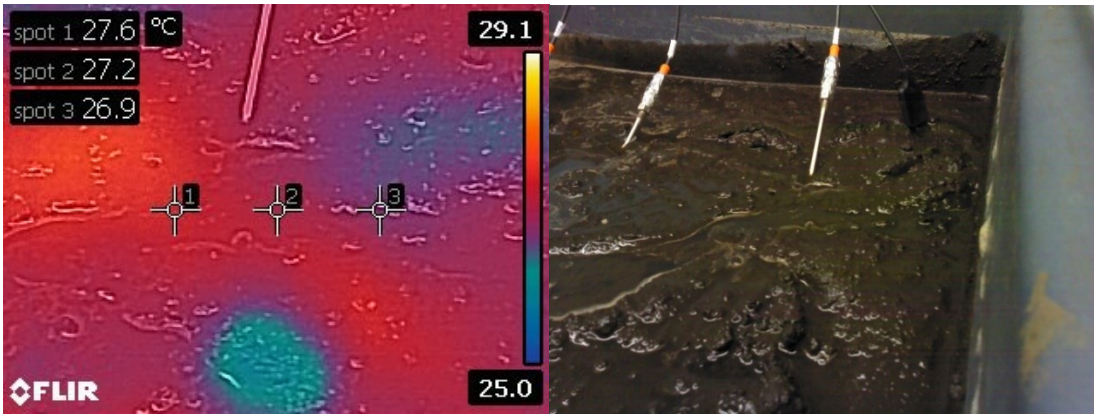

Figure (a): Experimental setup #17 when starting the experiment

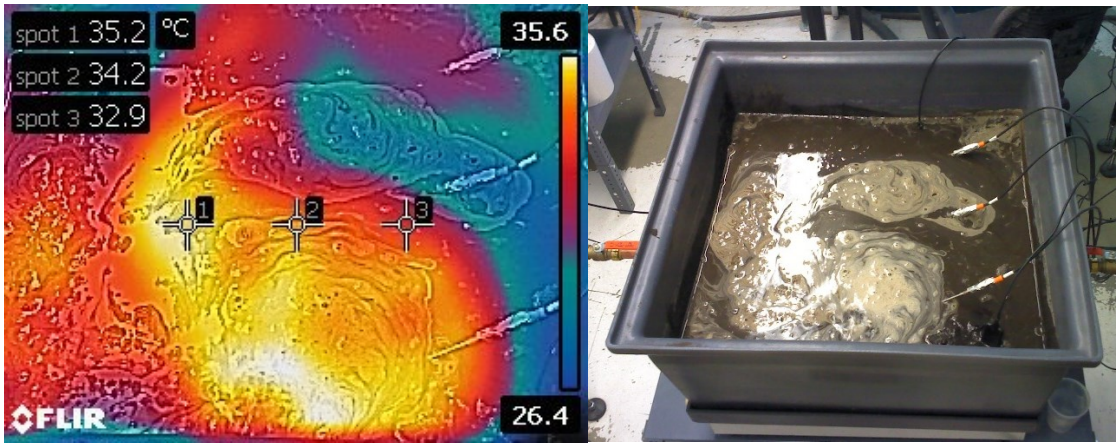

Figure (b): Experimental setup #17 through the experimental running

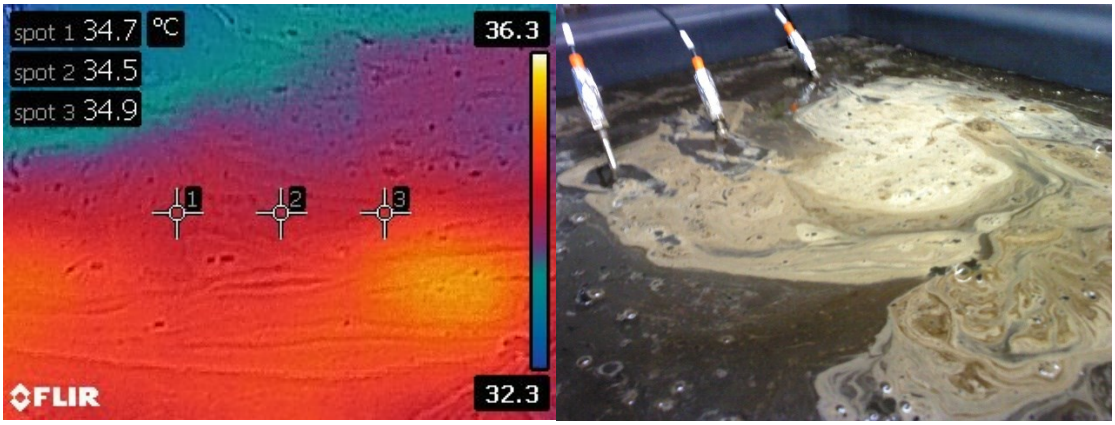

Figure (c): Experimental setup #17 when finishing the experiment

- **Experiment #18 results (15% moisture / Black soil / 2.2% leak / Fluid Velocity: 3.5 m/s)**

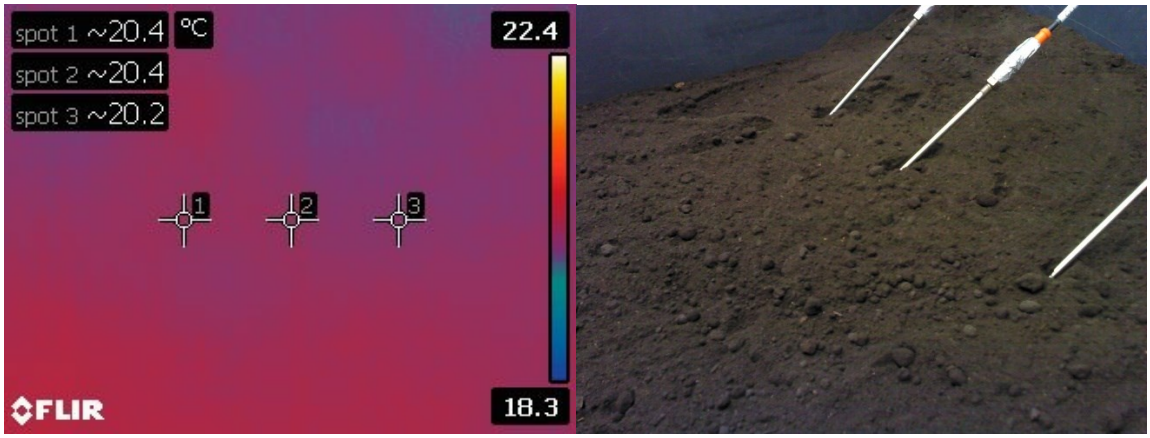

Figure (a): Experimental setup #18 when starting the experiment

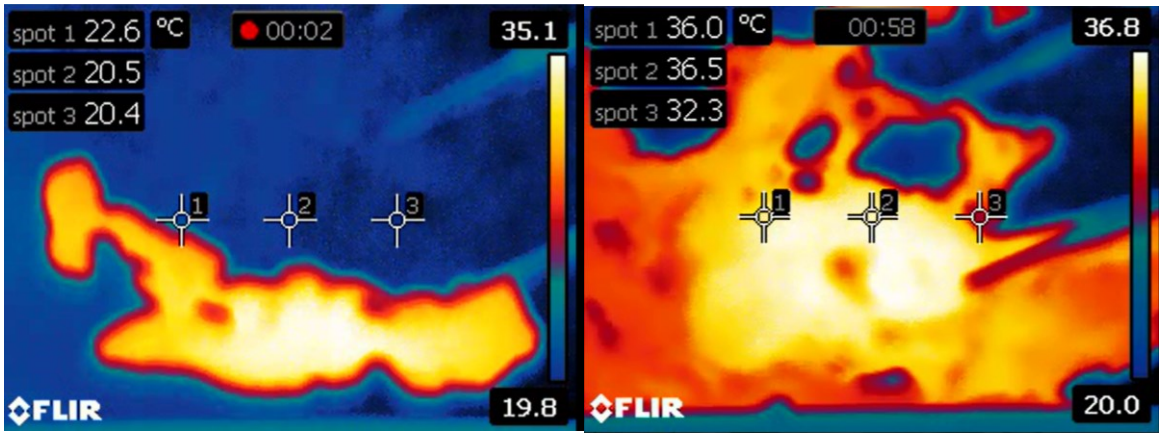

Figure (b): Experimental setup #18 through the experimental running

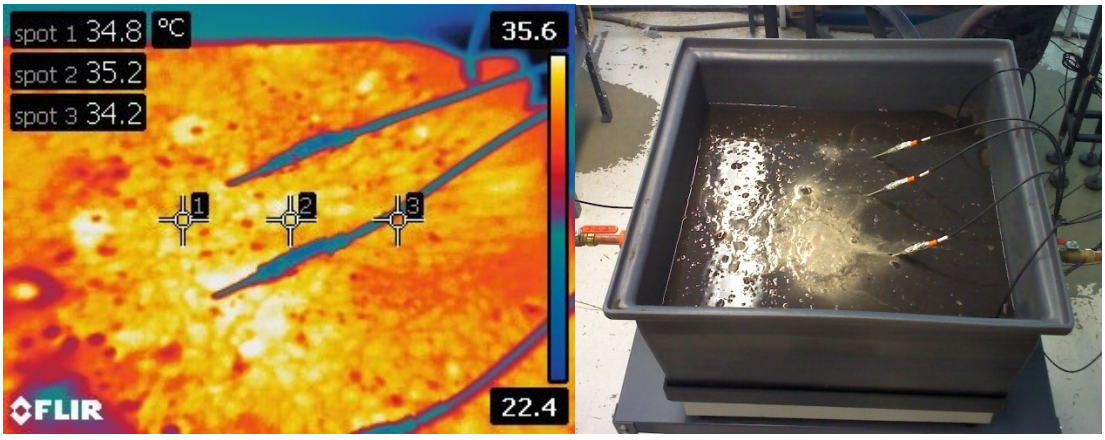

Figure (c): Experimental setup #18 when finishing the experiment

- **Experiment #19 results (45% moisture / Black soil / 2.2% leak / Fluid Velocity: 3.5 m/s)**

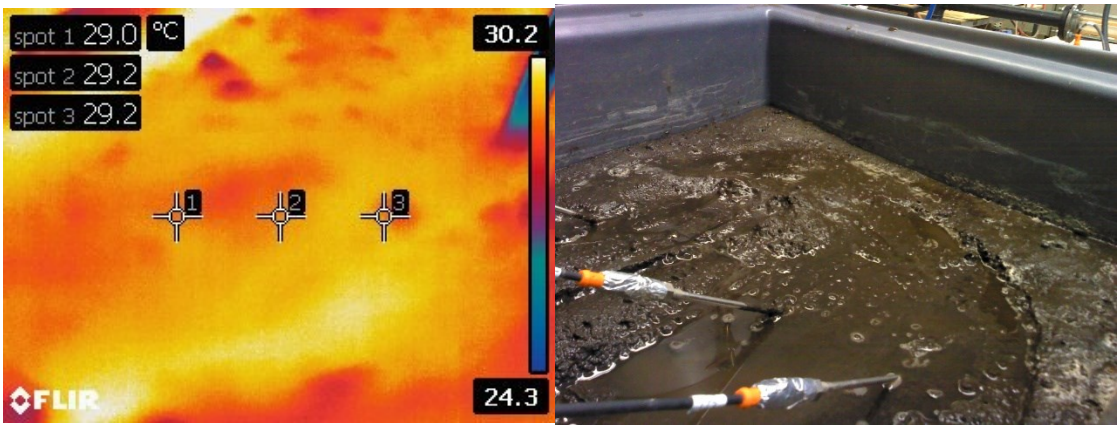

Figure (a): Experimental setup #19 when starting the experiment

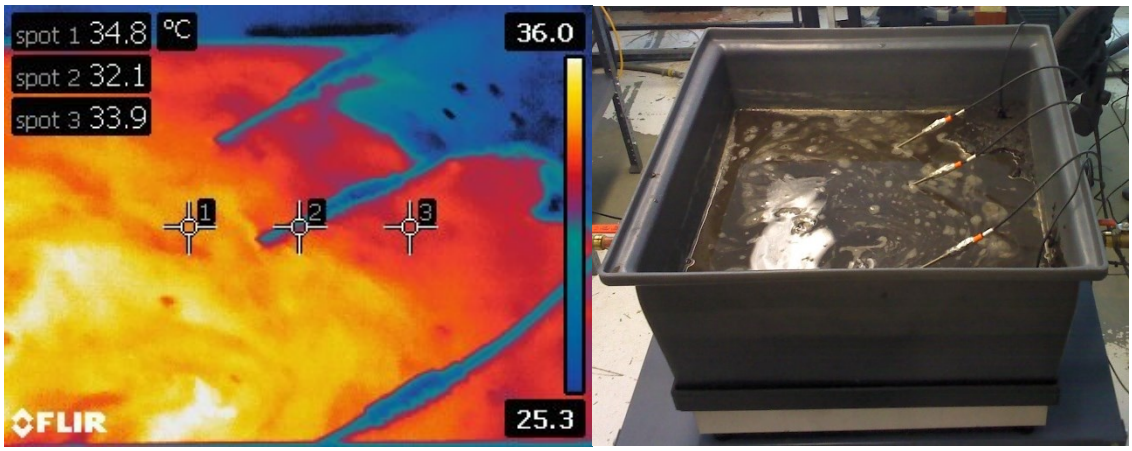

Figure (b): Experimental setup #19 through the experimental running

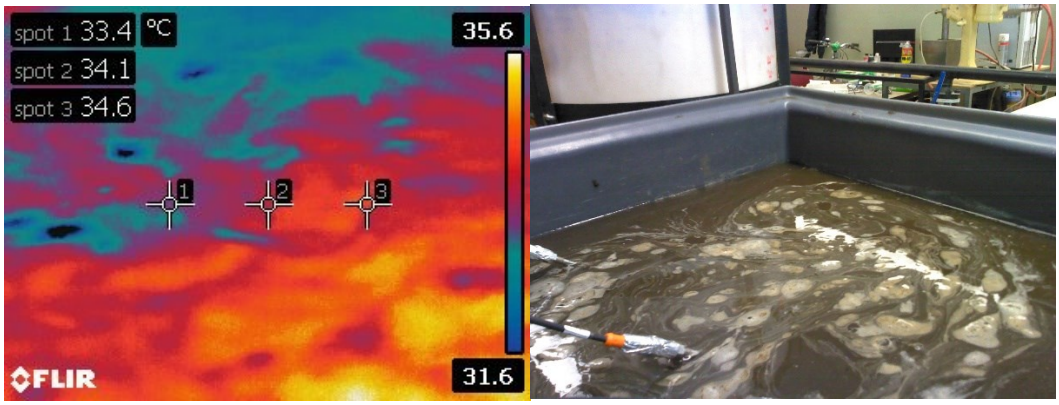

Figure (c): Experimental setup #19 when finishing the experiment

- **Experiment #20 results (15% moisture / Black soil / 0.97% leak / Fluid Velocity: 3.5 m/s)**

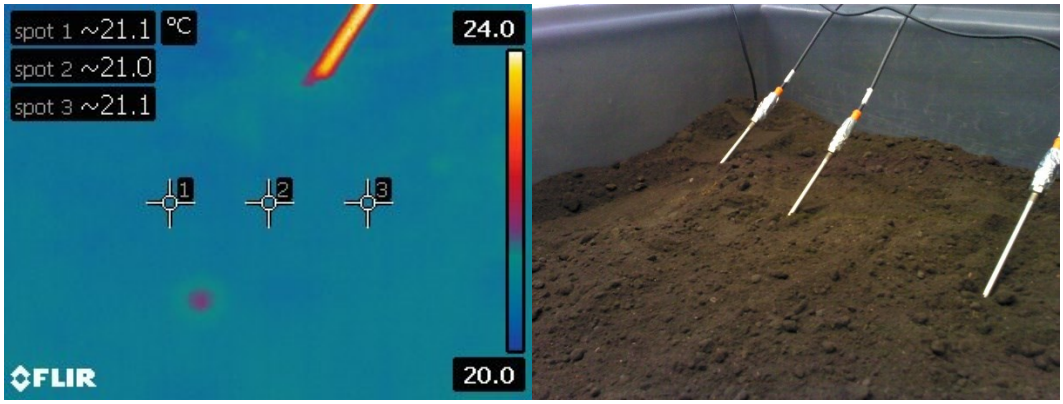

Figure (a): Experimental setup #20 when starting the experiment

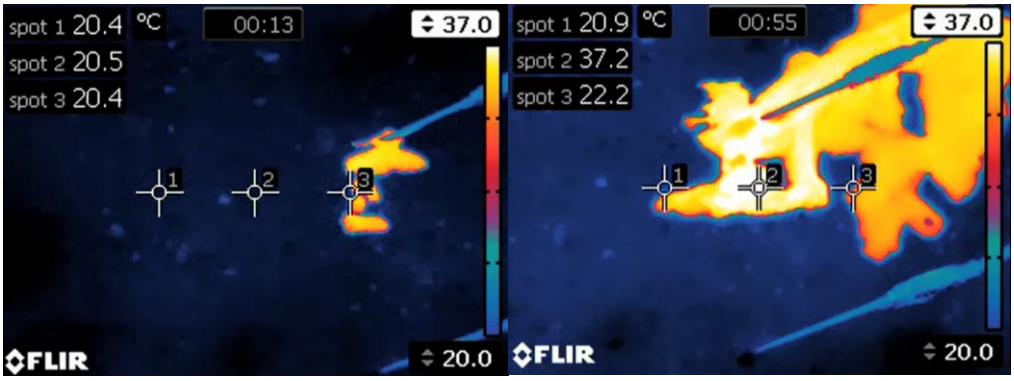

Figure (b): Experimental setup #20 through the experimental running

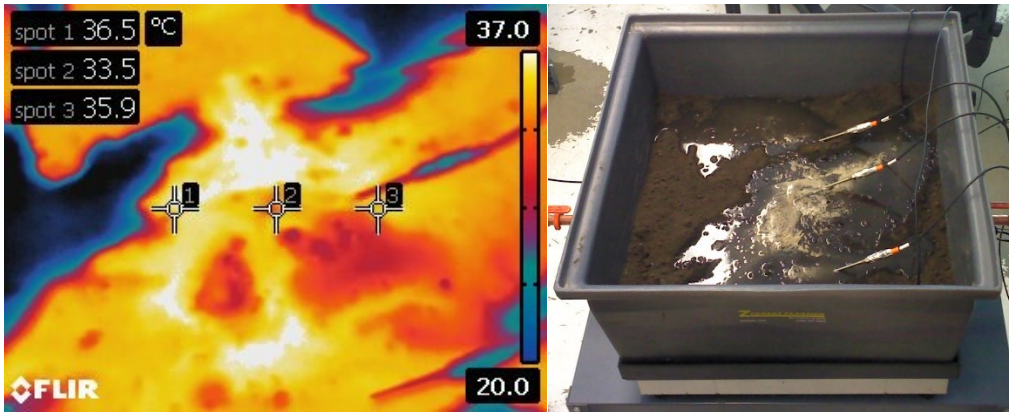

Figure (c): Experimental setup #20 when finishing the experiment

- **Experiment # 21 results (45% moisture/ Black soil /no leak/Fluid Velocity: 5 m/s)**

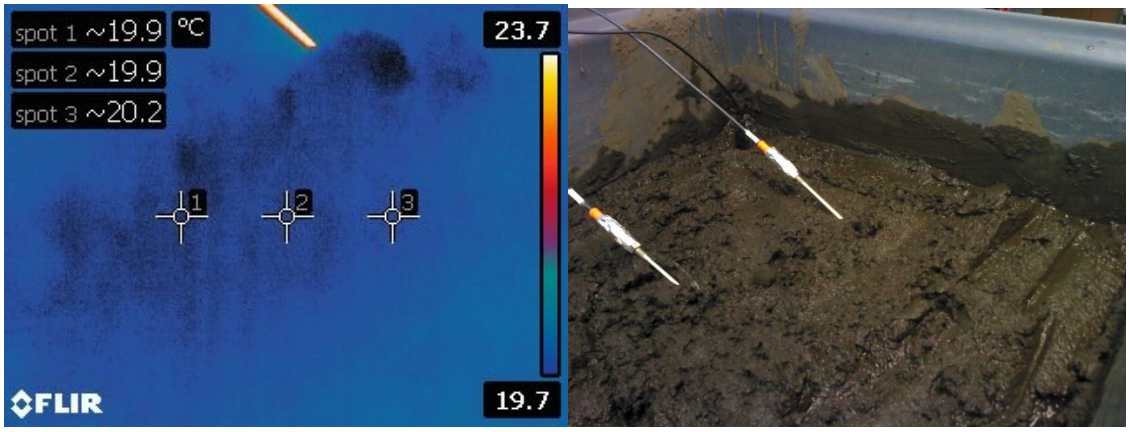

Figure (a): Experimental setup #21 when starting the experiment

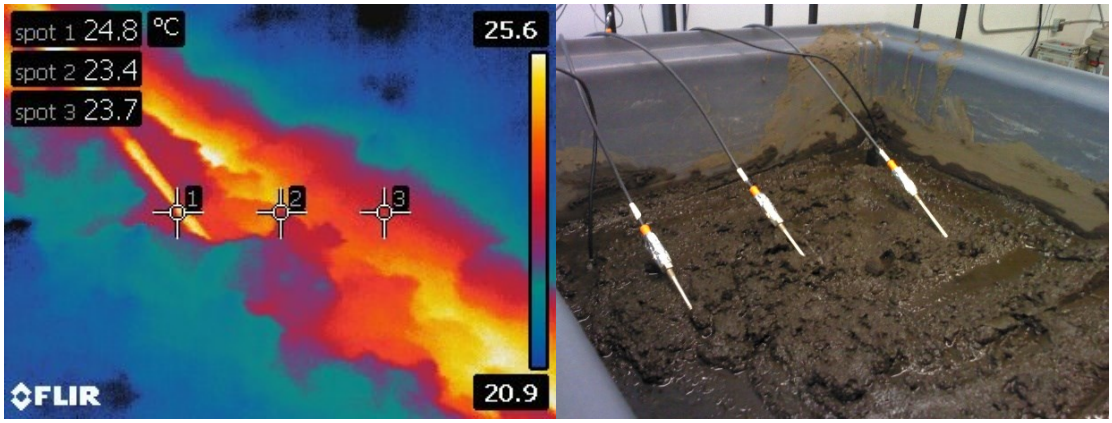

Figure (b): Experimental setup #21 when finishing the experiment

- **Experiment # 22 results (45% moisture/ Black soil /no leak/Fluid Velocity: 3.5 m/s)**

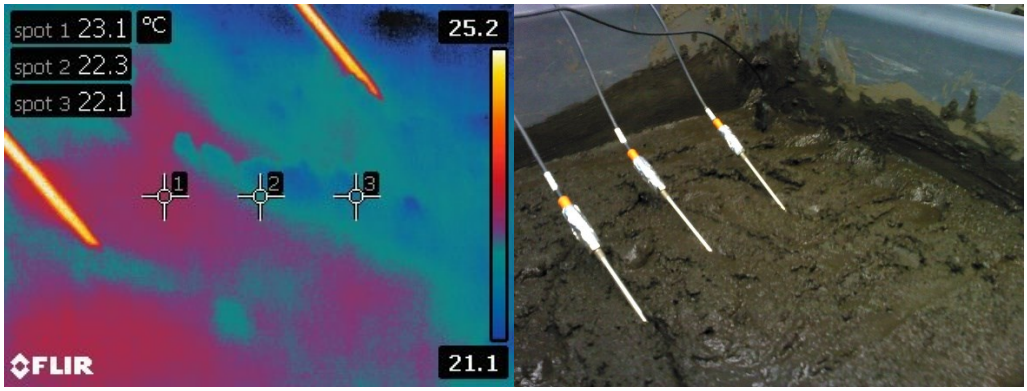

Figure (a): Experimental setup #22 when starting the experiment

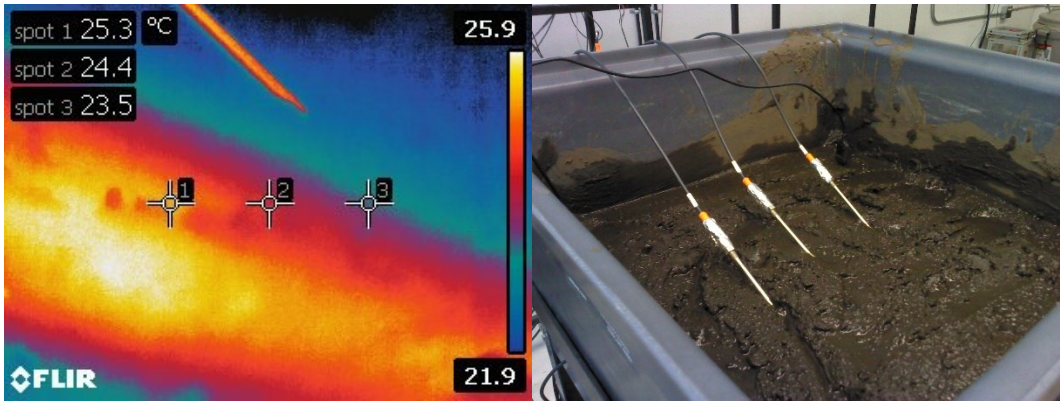

Figure (b): Experimental setup #22 when finishing the experiment

- **Experiment # 23 results (2% moisture/ Sand / 2.2 % leak / Fluid Velocity: 5 m/s)**

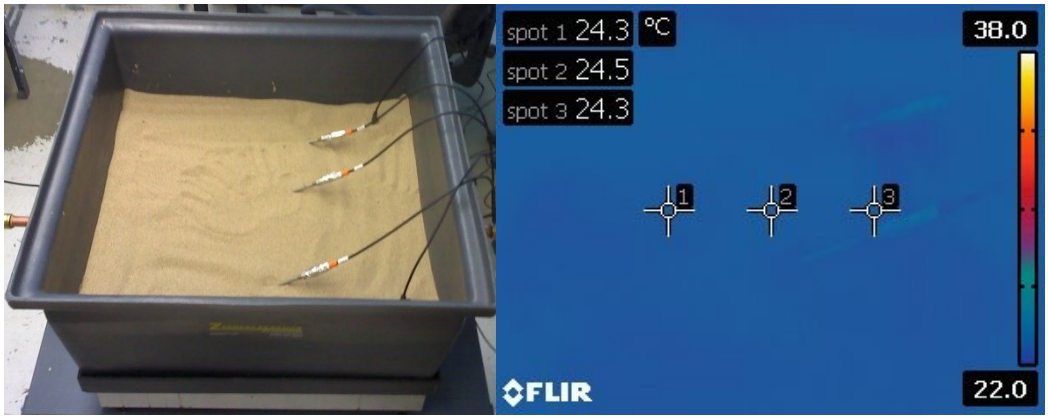

Figure (a): Experiment #23 (2nd Round) when starting (4:11 pm)

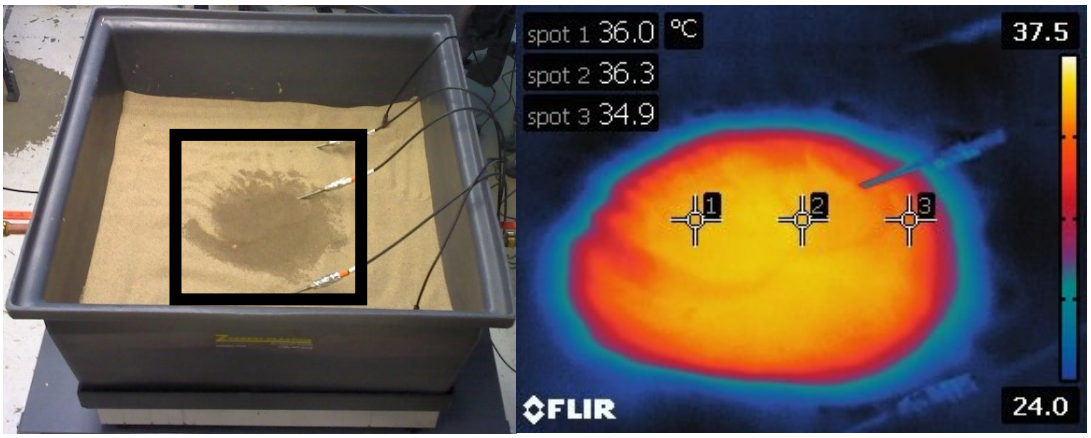

Figure (b): Experiment #23 (2nd Round) after 5 minutes (4:16 pm)

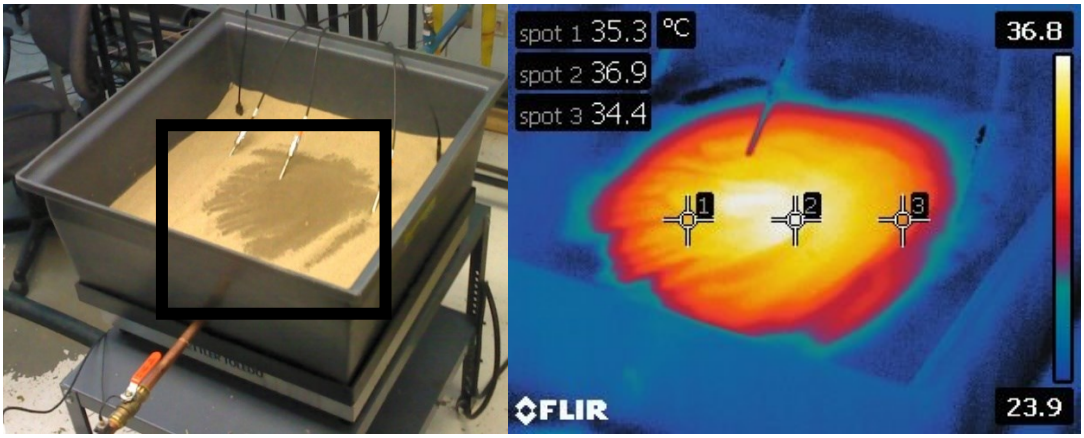

Figure (c): Experiment #23 (2nd Round) after 12 minutes (4:23 pm)

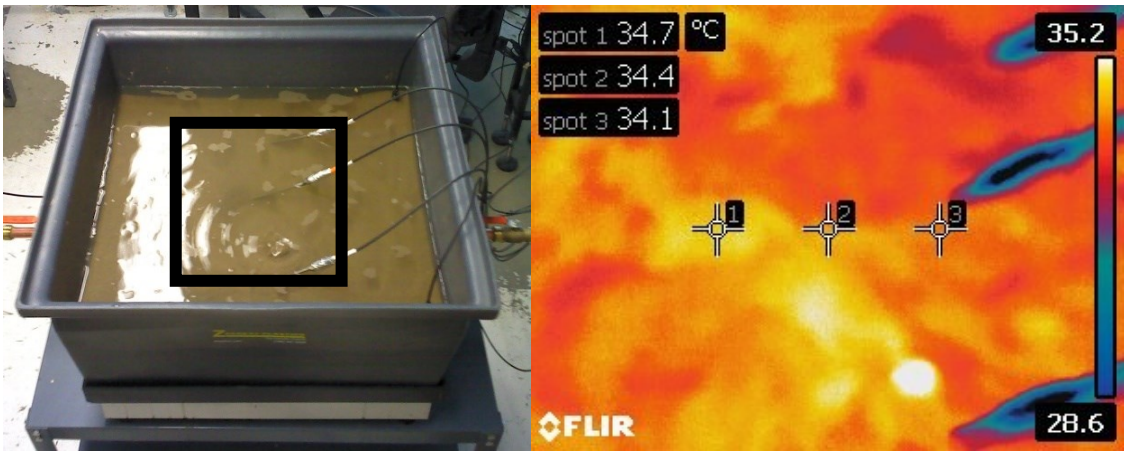

Figure (d): Experiment #23 (2nd Round) when ending after 26 minutes (4:37 pm)

- **Experiment # 24 results (2% moisture/ Sand / 2.2 % leak / Fluid Velocity: 3.5 m/s)**

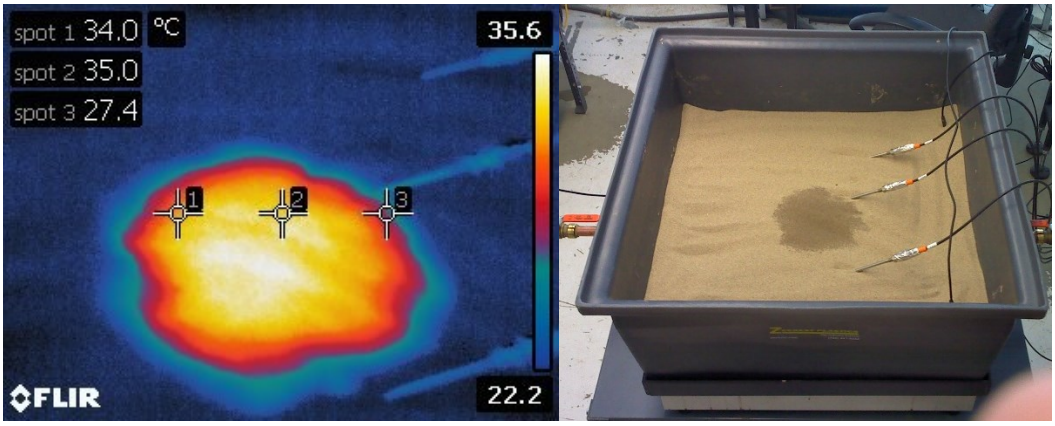

Figure (a): Experimental setup #20 when starting the experiment

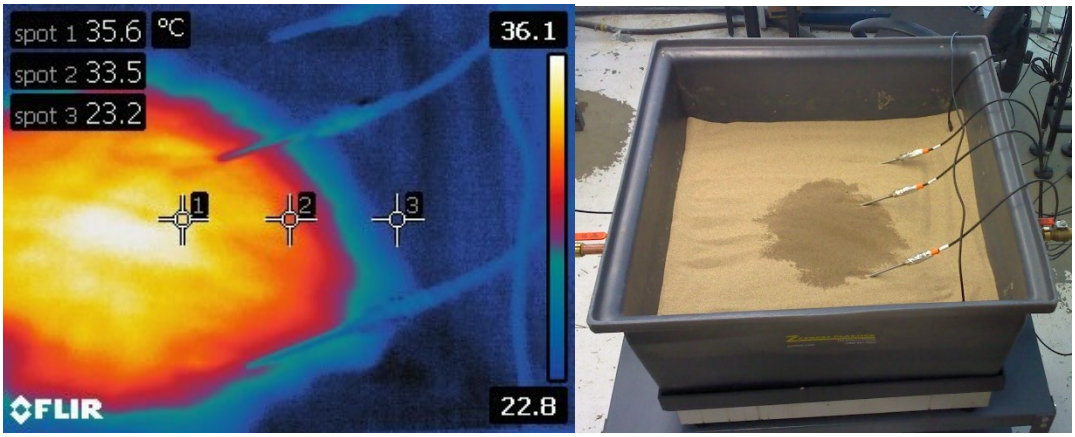

Figure (b): Experimental setup #20 through the experimental running

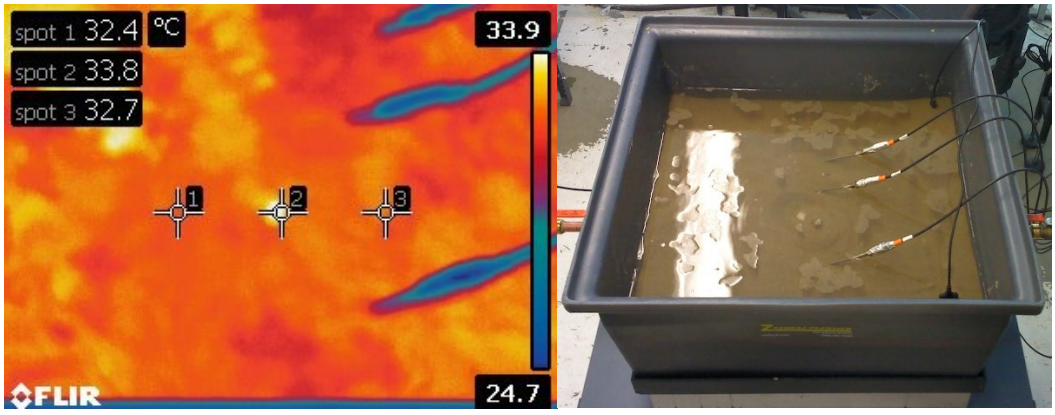

Figure (c): Experimental setup #20 when finishing the experiment

Appendix 12: Denoising parameters

Test	Variable	Type of Wavelet	Level	Denoising Method	Threshold Rule	Noise	Additional denoising
Test9 (Round 2): FV: 5 m/s - Dry black soil - 0.82% Leakage	TT_1_Celsius	db10	15	Bayes	Soft	Level Dependent	Not Applicable
Test9 (Round 2): FV: 5 m/s - Dry black soil - 0.82% Leakage	TT_2_Celsius	db10	15	Bayes	Soft	Level Dependent	Not Applicable
Test9 (Round 2): FV: 5 m/s - Dry black soil - 0.82% Leakage	TT_3_Celsius	db10	15	Bayes	Soft	Level Dependent	Not Applicable
Test9 (Round 2): FV: 5 m/s - Dry black soil - 0.82% Leakage	TT_Pipe_Celsius	db10	15	Bayes	Soft	Level Dependent	Not Applicable
Test9 (Round 2): FV: 5 m/s - Dry black soil - 0.82% Leakage	TP_1_Psi	db5	13	Bayes	Soft	Level Dependent	Not Applicable
Test9 (Round 2): FV: 5 m/s - Dry black soil - 0.82% Leakage	TP_2_Psi	db5	13	Bayes	Soft	Level Dependent	Not Applicable
Test9 (Round 2): FV: 5 m/s - Dry black soil - 0.82% Leakage	TP_3_Psi	db5	13	Bayes	Soft	Level Dependent	Not Applicable
Test9 (Round 2): FV: 5 m/s - Dry black soil - 0.82% Leakage	Flow_ms_7500	db10	12	Bayes	Soft	Level Dependent	Gaussian smoothing method
Test9 (Round 2): FV: 5 m/s - Dry black soil - 0.82% Leakage	Flow_ms_1500	db10	12	Bayes	Soft	Level Dependent	Gaussian smoothing method
Test9 (Round 2): FV: 5 m/s - Dry black soil - 0.82% Leakage	MT_Kilograms	db10	18	Universal Threshold	Soft	Level Dependent	Gaussian smoothing method
Test9 (Round 2): FV: 5 m/s - Dry black soil - 0.82% Leakage	Acceleration_1_X	db5	10	Bayes	Soft	Level Dependent	Not Applicable

Test	Variable	Type of Wavelet	Level	Denoising Method	Threshold Rule	Noise	Additional denoising
Test9 (Round 2): FV: 5 m/s - Dry black soil - 0.82% Leakage	Acceleration_1_Y	db5	10	Bayes	Soft	Level Dependent	Not Applicable
Test9 (Round 2): FV: 5 m/s - Dry black soil - 0.82% Leakage	Acceleration_1_Z	db5	10	Bayes	Soft	Level Dependent	Not Applicable
Test9 (Round 2): FV: 5 m/s - Dry black soil - 0.82% Leakage	Re	db10	12	Bayes	Soft	Level Dependent	Not Applicable
Test23 (Round 2): FV: 3.5 m/s - Dry Sand - 0.89% Leakage	TT_1_Celsius	db10	15	Bayes	Soft	Level Dependent	Not Applicable
Test23 (Round 2): FV: 3.5 m/s - Dry Sand - 0.89% Leakage	TT_2_Celsius	db10	15	Bayes	Soft	Level Dependent	Not Applicable
Test23 (Round 2): FV: 3.5 m/s - Dry Sand - 0.89% Leakage	TT_3_Celsius	db10	15	Bayes	Soft	Level Dependent	Not Applicable
Test23 (Round 2): FV: 3.5 m/s - Dry Sand - 0.89% Leakage	TT_Pipe_Celsius	db10	15	Bayes	Soft	Level Dependent	Not Applicable
Test23 (Round 2): FV: 3.5 m/s - Dry Sand - 0.89% Leakage	TP_1_Psi	db5	13	Bayes	Soft	Level Dependent	Not Applicable
Test23 (Round 2): FV: 3.5 m/s - Dry Sand - 0.89% Leakage	TP_2_Psi	db5	13	Bayes	Soft	Level Dependent	Not Applicable
Test23 (Round 2): FV: 3.5 m/s - Dry Sand - 0.89% Leakage	TP_3_Psi	db5	13	Bayes	Soft	Level Dependent	Not Applicable
Test23 (Round 2): FV: 3.5 m/s - Dry Sand - 0.89% Leakage	Flow_ms_7500	db10	12	Bayes	Soft	Level Dependent	Gaussian smoothing method
Test23 (Round 2): FV: 3.5 m/s - Dry Sand - 0.89% Leakage	Flow_ms_1500	db10	12	Bayes	Soft	Level Dependent	Gaussian smoothing method

Test	Variable	Type of Wavelet	Level	Denoising Method	Threshold Rule	Noise	Additional denoising
Test23 (Round 2): FV: 3.5 m/s - Dry Sand - 0.89% Leakage	MT_Kilograms	db10	15	Universal Threshold	Soft	Level Dependent	Gaussian smoothing method
Test23 (Round 2): FV: 3.5 m/s - Dry Sand - 0.89% Leakage	Acceleration_1_X	db5	10	Bayes	Soft	Level Dependent	Not Applicable
Test23 (Round 2): FV: 3.5 m/s - Dry Sand - 0.89% Leakage	Acceleration_1_Y	db5	10	Bayes	Soft	Level Dependent	Not Applicable
Test23 (Round 2): FV: 3.5 m/s - Dry Sand - 0.89% Leakage	Acceleration_1_Z	db5	10	Bayes	Soft	Level Dependent	Not Applicable
Test23 (Round 2): FV: 3.5 m/s - Dry Sand - 0.89% Leakage	Re	db10	12	Bayes	Soft	Level Dependent	Not Applicable
Test12 (Round 2): FV: 3.5 m/s - Saturated soil - 0.90% Leakage	TT_1_Celsius	db10	15	Bayes	Soft	Level Dependent	Not Applicable
Test12 (Round 2): FV: 3.5 m/s - Saturated soil - 0.90% Leakage	TT_2_Celsius	db10	15	Bayes	Soft	Level Dependent	Not Applicable
Test12 (Round 2): FV: 3.5 m/s - Saturated soil - 0.90% Leakage	TT_3_Celsius	db10	15	Bayes	Soft	Level Dependent	Not Applicable
Test12 (Round 2): FV: 3.5 m/s - Saturated soil - 0.90% Leakage	TT_Pipe_Celsius	db10	15	Bayes	Soft	Level Dependent	Not Applicable
Test12 (Round 2): FV: 3.5 m/s - Saturated soil - 0.90% Leakage	TP_1_Psi	db5	13	Bayes	Soft	Level Dependent	Not Applicable
Test12 (Round 2): FV: 3.5 m/s - Saturated soil - 0.90% Leakage	TP_2_Psi	db5	13	Bayes	Soft	Level Dependent	Not Applicable
Test12 (Round 2): FV: 3.5 m/s - Saturated soil - 0.90% Leakage	TP_3_Psi	db5	13	Bayes	Soft	Level Dependent	Not Applicable

Test	Variable	Type of Wavelet	Level	Denoising Method	Threshold Rule	Noise	Additional denoising
Test12 (Round 2): FV: 3.5 m/s - Saturated soil - 0.90% Leakage	Flow_ms_7500	db10	12	Bayes	Soft	Level Dependent	Gaussian smoothing method
Test12 (Round 2): FV: 3.5 m/s - Saturated soil - 0.90% Leakage	Flow_ms_1500	db10	12	Bayes	Soft	Level Dependent	Gaussian smoothing method
Test12 (Round 2): FV: 3.5 m/s - Saturated soil - 0.90% Leakage	MT_Kilograms	db10	15	Universal Threshold	Soft	Level Dependent	Gaussian smoothing method
Test12 (Round 2): FV: 3.5 m/s - Saturated soil - 0.90% Leakage	Acceleration_1_X	db5	10	Bayes	Soft	Level Dependent	Not Applicable
Test12 (Round 2): FV: 3.5 m/s - Saturated soil - 0.90% Leakage	Acceleration_1_Y	db5	10	Bayes	Soft	Level Dependent	Not Applicable
Test12 (Round 2): FV: 3.5 m/s - Saturated soil - 0.90% Leakage	Acceleration_1_Z	db5	10	Bayes	Soft	Level Dependent	Not Applicable
Test12 (Round 2): FV: 3.5 m/s - Saturated soil - 0.90% Leakage	Re	db10	12	Bayes	Soft	Level Dependent	Not Applicable
Test2 (Round 2): FV: 5 m/s - Saturated black soil - 1.93% Leakage	TT_1_Celsius	sym4	16	Bayes	Medium	Level Independent	Not Applicable
Test2 (Round 2): FV: 5 m/s - Saturated black soil - 1.93% Leakage	TT_2_Celsius	sym4	16	Bayes	Medium	Level Independent	Not Applicable
Test2 (Round 2): FV: 5 m/s - Saturated black soil - 1.93% Leakage	TT_3_Celsius	sym4	16	Bayes	Medium	Level Independent	Not Applicable
Test2 (Round 2): FV: 5 m/s - Saturated black soil - 1.93% Leakage	TT_Pipe_Celsius	sym4	16	Bayes	Medium	Level Independent	Not Applicable
Test2 (Round 2): FV: 5 m/s - Saturated black soil - 1.93% Leakage	TP_1_Psi	db5	13	Bayes	Soft	Level Dependent	Not Applicable
Test2 (Round 2): FV: 5 m/s -	TP_2_Psi	db5	13	Bayes	Soft	Level Dependent	Not Applicable

Test	Variable	Type of Wavelet	Level	Denoising Method	Threshold Rule	Noise	Additional denoising
Saturated black soil - 1.93% Leakage							
Test2 (Round 2): FV: 5 m/s - Saturated black soil - 1.93% Leakage	TP_3_Psi	db5	13	Bayes	Soft	Level Dependent	Not Applicable
Test2 (Round 2): FV: 5 m/s - Saturated black soil - 1.93% Leakage	Flow_ms_7500	db10	12	Bayes	Soft	Level Dependent	Gaussian smoothing method
Test2 (Round 2): FV: 5 m/s - Saturated black soil - 1.93% Leakage	Flow_ms_1500	db10	12	Bayes	Soft	Level Dependent	Gaussian smoothing method
Test2 (Round 2): FV: 5 m/s - Saturated black soil - 1.93% Leakage	MT_Kilograms	db10	15	Universal Threshold	Soft	Level Dependent	Gaussian smoothing method
Test2 (Round 2): FV: 5 m/s - Saturated black soil - 1.93% Leakage	Acceleration_1_X	db5	10	Bayes	Soft	Level Dependent	Not Applicable
Test2 (Round 2): FV: 5 m/s - Saturated black soil - 1.93% Leakage	Acceleration_1_Y	db5	10	Bayes	Soft	Level Dependent	Not Applicable
Test2 (Round 2): FV: 5 m/s - Saturated black soil - 1.93% Leakage	Acceleration_1_Z	db5	10	Bayes	Soft	Level Dependent	Not Applicable
Test2 (Round 2): FV: 5 m/s - Saturated black soil - 1.93% Leakage	Re	db10	12	Bayes	Soft	Level Dependent	Not Applicable
Test24 (Round 2): FV: 3.5 m/s - Saturated Sand - 0.95% Leakage	TT_1_Celsius	sym4	16	Bayes	Mean	Level Independent	Not Applicable
Test24 (Round 2): FV: 3.5 m/s - Saturated Sand - 0.95% Leakage	TT_2_Celsius	sym4	16	Bayes	Mean	Level Independent	Not Applicable
Test24 (Round 2): FV: 3.5 m/s - Saturated Sand - 0.95% Leakage	TT_3_Celsius	sym4	16	Bayes	Mean	Level Independent	Not Applicable
Test24 (Round 2): FV: 3.5 m/s - Saturated Sand - 0.95% Leakage	TT_Pipe_Celsius	sym4	16	Bayes	Mean	Level Independent	Not Applicable

Test	Variable	Type of Wavelet	Level	Denoising Method	Threshold Rule	Noise	Additional denoising
Test24 (Round 2): FV: 3.5 m/s - Saturated Sand - 0.95% Leakage	TP_1_Psi	db5	13	Bayes	Soft	Level Dependent	Not Applicable
Test24 (Round 2): FV: 3.5 m/s - Saturated Sand - 0.95% Leakage	TP_2_Psi	db5	13	Bayes	Soft	Level Dependent	Not Applicable
Test24 (Round 2): FV: 3.5 m/s - Saturated Sand - 0.95% Leakage	TP_3_Psi	db5	13	Bayes	Soft	Level Dependent	Not Applicable
Test24 (Round 2): FV: 3.5 m/s - Saturated Sand - 0.95% Leakage	Flow_ms_7500	db10	12	Bayes	Soft	Level Dependent	Gaussian smoothing method
Test24 (Round 2): FV: 3.5 m/s - Saturated Sand - 0.95% Leakage	Flow_ms_1500	db10	12	Bayes	Soft	Level Dependent	Gaussian smoothing method
Test24 (Round 2): FV: 3.5 m/s - Saturated Sand - 0.95% Leakage	MT_Kilograms	db10	15	Universal Threshold	Soft	Level Dependent	Gaussian smoothing method
Test24 (Round 2): FV: 3.5 m/s - Saturated Sand - 0.95% Leakage	Acceleration_1_X	db5	10	Bayes	Soft	Level Dependent	Not Applicable
Test24 (Round 2): FV: 3.5 m/s - Saturated Sand - 0.95% Leakage	Acceleration_1_Y	db5	10	Bayes	Soft	Level Dependent	Not Applicable
Test24 (Round 2): FV: 3.5 m/s - Saturated Sand - 0.95% Leakage	Acceleration_1_Z	db5	10	Bayes	Soft	Level Dependent	Not Applicable
Test24 (Round 2): FV: 3.5 m/s - Saturated Sand - 0.95% Leakage	Re	db10	12	Bayes	Soft	Level Dependent	Not Applicable
Test7 (Round 2): FV: 5 m/s - Saturated black soil- 0% Leakage	TT_1_Celsius	sym4	16	Bayes	Mean	Level Independent	Not Applicable
Test7 (Round 2): FV: 5 m/s - Saturated black soil- 0% Leakage	TT_2_Celsius	sym4	16	Bayes	Mean	Level Independent	Not Applicable
Test7 (Round 2): FV: 5 m/s -	TT_3_Celsius	sym4	16	Bayes	Mean	Level Independent	Not Applicable

Test	Variable	Type of Wavelet	Level	Denoising Method	Threshold Rule	Noise	Additional denoising
Saturated black soil-0% Leakage							
Test7 (Round 2): FV: 5 m/s - Saturated black soil-0% Leakage	TT_Pipe_Celsius	sym4	16	Bayes	Mean	Level Independent	Not Applicable
Test7 (Round 2): FV: 5 m/s - Saturated black soil-0% Leakage	TP_1_Psi	db5	13	Bayes	Soft	Level Dependent	Not Applicable
Test7 (Round 2): FV: 5 m/s - Saturated black soil-0% Leakage	TP_2_Psi	db5	13	Bayes	Soft	Level Dependent	Not Applicable
Test7 (Round 2): FV: 5 m/s - Saturated black soil-0% Leakage	TP_3_Psi	db5	13	Bayes	Soft	Level Dependent	Not Applicable
Test7 (Round 2): FV: 5 m/s - Saturated black soil-0% Leakage	Flow_ms_7500	db10	12	Bayes	Soft	Level Dependent	Gaussian smoothing method
Test7 (Round 2): FV: 5 m/s - Saturated black soil-0% Leakage	Flow_ms_1500	db10	12	Bayes	Soft	Level Dependent	Gaussian smoothing method
Test7 (Round 2): FV: 5 m/s - Saturated black soil-0% Leakage	MT_Kilograms	db10	15	Universal Threshold	Soft	Level Dependent	Gaussian smoothing method
Test7 (Round 2): FV: 5 m/s - Saturated black soil-0% Leakage	Acceleration_1_X	db5	10	Bayes	Soft	Level Dependent	Not Applicable
Test7 (Round 2): FV: 5 m/s - Saturated black soil-0% Leakage	Acceleration_1_Y	db5	10	Bayes	Soft	Level Dependent	Not Applicable
Test7 (Round 2): FV: 5 m/s - Saturated black soil-0% Leakage	Acceleration_1_Z	db5	10	Bayes	Soft	Level Dependent	Not Applicable